ABSTRACT

Title of Document:	CONTROLLING NANOSTRUCTURES FOR *IN-SITU* TEM CHARACTERIZATION
	Hanna Magdalena Nilsson, Doctor of Philosophy, 2015
Directed By:	Professor John Cumings, Department of Material Science and Engineering

Low dimensional nanostructures, such as nanotubes and 2D sheets, have unique and promising material properties both from a fundamental science and an application standpoint. Theoretical modelling and calculations predict previously unobserved phenomena that experimental scientists often struggle to reproduce because of the difficulty in controlling and characterizing the small structures under real-world constraints. The goal of this dissertation is to present advancements in controlling these structures so that nanostructures can be characterized *in-situ* in transmission electron microscopes (TEM) allowing for direct observation of the physical responses of the materials to different stimuli. Of most interest to this work are the thermal and electrical properties of carbon nanotubes, boron nitride nanotubes, and graphene.

The first topic of the dissertation is using surfactants for aqueous processing to fabricate, store, and deposit the nanostructures. More specifically,

thorough characterization of a new surfactant, ammonium laurate (AL), is provided and shows that this new surfactant outperforms the standard surfactant for these materials, sodium dodecyl sulfate (SDS), in almost all tested metrics.

New experimental set-ups have been developed by combining specialized *in-situ* TEM holders with innovative device fabrication. For example, electrical characterization of graphene was performed by using an STM-TEM holder and depositing graphene from aqueous solutions onto lithographically patterned, electron transparent silicon nitride membranes. These experiments produce exciting information about the interaction between graphene and metal probes and the substrate that it rests on. Then, by adding indium to the backside of the membrane and employing the electron thermal microscopy (EThM) technique, the same type of graphene samples could be characterized for thermal transport with high spatial resolution.

It is found that reduced graphene oxide sheets deposited onto a silicon nitride membrane and displaying high levels of wrinkling have higher than expected electrical and thermal conduction properties. We are clearly able to visualize the ability of graphene to spread heat away from an electronic hot spot and into the substrate.

CONTROLLING NANOSTRUCTURES FOR *IN-SITU* TEM CHARACTERIZATION

by

Hanna Magdalena Nilsson

Dissertation submitted to the Faculty of the Graduate School of the
University of Maryland, College Park, in partial fulfillment
of the requirements for the degree of
Doctor of Philosophy
2015

Advisory Committee:

Professor John Cumings, Chair
Professor Robert Briber
Professor Oded Rabin
Professor YuHuang Wang
Professor Bao Yang, Dean's Representative

Dedication

To Professor Daniel Strickland, for his inspiration and support to start this degree and for the strength his example gave me to succeed.

Acknowledgements

I would like to thank my advisor, Dr. John Cumings for all of his guidance and exciting ideas throughout my time as a doctoral student at the University of Maryland. He has an inspiring love of knowledge and has a talent for passing on that passion. The members of the Cumings' group have also been great sources of support and inspiration. Dr. Merinjte Bronsgeest and Dr. Norvik Voskanian were very helpful when I first started in the group and guided me to get my research started. The other members, Jasper Drisko, Jeremy Ticey, Dr. Khim Kharki, and Dr. Kai He, have helped me in immeasurable ways, not in the least with their friendships.

Second, I want to thank the Eva Olsson Group at Chalmers University, where I spent the last year of my studies thanks to an NSF GROW collaboration. Dr. Olsson and her group were incredibly welcoming and guided me both in research and on a personal level. I would especially like to thank Dr. Ludvig de Knoop and Dr. Lunjie Zeng for passing on their vast knowledge and experience with *in-situ* TEM work.

Thank you to my committee members; Dr. YuHuang Wang, Dr. Oded Rabin, Dr. Robert Briber, and Boa Yang. I have appreciated your support on the direction of my work.

Last but not least, a big thank you to my family for their love and support always, no matter what goal I am trying to reach.

Table of Contents

Dedication…….....ii
Acknowledgements…….....iii
Table of Contents…….....iv
List of Tables…….....…vi
List of Figures……...…….....vii
1 Introduction and background…….....1
1.1 Nanostructure properties and structures…….....1
1.1.1 Electrical transport..…….....2
1.1.2 Thermal transport…….....4
1.1.3 Carbon and boron nitride nanotubes…….....5
1.1.4 Graphene…….....9
1.2 Transmission electron microscopy.....12
1.2.1 History……....12
1.2.2 Operating principles……...13
1.2.3 *In-situ* transmission electron microscopy..……....15
1.2.4 Thermal characterization techniques……16
1.3 Surfactants for processing of nanostructures……...24
1.3.1 Types of surfactants……...25
1.3.2 Successes in surfactant development……26
1.4 Goal of dissertation……..27
1.5 Structure of dissertation……...32
2 Suspension of nanomaterials in solution…….33
2.1 Boron nitride nanotubes …….....33
2.2 Multi-walled carbon nanotubes.... …….....39
2.3 Single-walled carbon nanotubes.……60
2.4 Graphene …….....69
2.4.1 Solution suspended reduced graphene oxide…….....70
2.4.2 Graphite exfoliated to graphene in solution……...77
3 Electrical characterization at the nanoscale …….....82
3.1 Biasing of metal heater wires……...82
3.2 Localized graphene biasing…….93
4 *In-situ* transmission electron microscopy thermal characterization at the nanoscale.....116
4.1 Methods for *in-situ* transmission electron microscopy heating…….....……..116
4.2 Indium for thermal measurements …….....118
4.3 Boron nitride nanotube device……..….137
4.4 Thermal stability of multi-walled carbon nanotubes.……..……..144
4.5 Graphene……..……147
4.6 Thermal stability of graphene…….....……..159

5 Summary and future work……..161
References……..164

List of Tables

Table 2.2.1. Description of the result of combining different ionic constituents to form surfactant suspended CNTs……...……56

Table 2.4.1. Summary of the differences between the two approaches that were used for solution processing of graphene…….....……69

Table 2.4.1.1. Typical raman spectra for AL and SDS deposited graphene flakes on SiN……...…….81

Table 2.4.2.1. Average raman frequencies and intensity ratios for the graphene exfoliated in AL…….…75

List of Figures

Figure 1.1.3.1. Atomic structure of boron nitride nanotubes……...…..6

Figure 1.2.2.1. Electron sources created by a) thermionic and b) field-emission…….13

Figure 1.2.2.2. Schematic showing the electron source focused and limited before hitting the sample by two condenser lenses and aperture…….…….14

Figure 1.2.2.3. Schematics of different TEM imaging modes……..15

Figure 2.1.1. Molecular structure of three different liquids used for suspending BNNTs……...34

Figure 2.1.2. Optical images of BNNT solutions…….34

Figure 2.1.3. Photograph showing that solution of BNNTs is homogeneous…...35

Figure 2.1.4. Zeta potential results for BNNTs in ethanol and isopropyl alcohol…….……...36

Figure 2.1.5. HRTEM image of individual BNNTs deposited via ethanol onto a SiN membrane…….…….…….37

Figure 2.1.6. LRTEM image of BNNTs deposited by leaving sample in an ethanol solution…….……..…38

Figure 2.1.7. TEM images showing long and undamaged BNNTs even after the sonication procedure…….…….……39

Figure 2.2.1. Schematic of the molecular structure of surfactant system used to suspend and deposit MWCNTs……...……..42

Figure 2.2.2. Schematic showing the APTES evaporation jar and the structure of the molecule……..…….43

Figure 2.2.3. TEM images showing the resulting MWCNTs after extended probe sonication……..45

Figure 2.2.4. Images of MWCNTs in aqueous solutions…….……46

Figure 2.2.5. Raw absorbance data from 300 to 800 nm for the MWCNT surfactant solutions over time……...48

Figure 2.2.6. Chart showing the drop in optical absorption of a different set of 1.0 wt.% solutions over 11 days…….49

Figure 2.2.7. Typical TEM images at different magnifications of MWCNTs deposited on APTES treated SiN membranes……..50

Figure 2.2.8. Control TEM images at different magnifications of a pristine SiN membrane prior to any processing……51

Figure 2.2.9. AFM images SDS (a) and AL (b) deposited on silicon chips after APTES treatment (without CNTs)……52

Figure 2.2.10. TEM images at different magnifications of MWCNTs deposited from 1.0 wt.% SDS solution onto APTES treated SiN membranes…….53

Figure 2.2.11. Raman spectra of MWCNTs deposited through surfactant solutions……54

Figure 2.2.12. TEM images of CNTs deposited on SiN membranes after suspension in different combinations of surfactants……57

Figure 2.2.13. Results for measurements of zeta potential for surfactant solutions with different pH……..59

Figure 2.2.14. Results for measurements of zeta potential for surfactant solutions with different pHs for 3 consecutive runs…….60

Figure 2.3.1. TEM image of SWCNTs deposited through AL solution on to carbon grids……...61

Figure 2.3.2. Absorbance measurement results for SWCNT solutions of different surfactants……..62

Figure 2.3.3. PL data showing the preference of AL vs SDS so hold certain chirality SWCNTs in solution……64

Figure 2.3.4. PL data for the same AL SWCNT solution 6 months apart……65

Figure 2.3.5. 1 kV SEM images showing the improved electrical conductivity of AL deposited CNTs……...…67

Figure 2.4.1.1. Optical images of AL and SDS solutions containing suspended graphene flakes……..72

Figure 2.4.1.2. Absorbance data recorded over the course of a month……73

Figure 2.4.1.3. TEM images of graphene flakes deposited on silicon nitride through surfactant solutions……..74

Figure 2.4.1.4. Typical raman spectra for AL and SDS deposited graphene flakes on SiN……...76

Figure 2.4.1.5. TEM image of *in-situ* electrical characterization of SDS deposited graphene……77

Figure 2.4.2.1. Chart comparing absorbance data for the suspended and the exfoliated graphene sheets in AL……..79

Figure 2.4.2.2. TEM images of graphene flakes exfoliated in AL via simple probe sonication……...80

Figure 2.4.2.3. Typical Raman spectra for graphene exfoliated in AL showing low defect densities and a sharp G peak……81

Figure 3.1.1. A 4-probe in-situ TEM biasing holder built in the Cumings group……..84

Figure 3.1.2. Close up of a patterned SiN sample in the 4-probe holder in contact with the wire leads……84

Figure 3.1.3. Image of the Nanofactory Optical Holder……...85

Figure 3.1.4. Magnified optical image of a patterend SiN membrane assembled with a gold STM tip in a Nanofactory STM holder……..85

Figure 3.1.5. Optical microscope image of a sample after the developing an electron-lithography write……87

Figure 3.1.6. Images comparing FIB and EBID deposited Pt heater wires……..89

Figure 3.1.7. AFM image of a FIB deposited Pt heater wire……....89

Figure 3.1.9. Image of lines patterned by writing in resist using dual-beam FIB patterning software…….90

Figure 3.1.10. Images showing the problems with wire bonding…….92

Figure 3.2.1. TEM image of graphene flakes in contact with a gold electrode…96

Figure 3.2.2. Schematic of the side view of the experimental set-up when the probe is contacting graphene that is lying on silicon nitride…….97

Figure 3.2.3. Schematic of the side view of the experimental set-up when the probe is contacting graphene that is lying on the gold electrode……..97

Figure 3.2.4. TEM images of graphene flakes with different orders of wrinkling with labeled local measured resistance values……...……99

Figure 3.2.5. Plot of measured graphene resistance values as a function of wrinkles in the measured area……...……...……100

Figure 3.2.6. TEM image of graphene sheets that are anchored to the Au electrode using EBID Pt……...…102

Figure 3.2.7. TEM image of graphene sheets that have been anchored to silicon nitride using EBID Pt……...……103

Figure 3.2.8. Sequence of TEM images of using the STM probe to drag the graphene to increase the surface area in contact with the probe……..105

Figure 3.2.9. IV curves for the images in the previous figure showing the decrease in resistance with increased contact between the probe and the graphene sheet…….106

Figure 3.2.10. TEM images of another graphene flake tested for location dependent electrical properties……108

Figure 3.2.11. TEM images of a fold on a graphene sheet……..…109

Figure 3.2.12. Plot adopted from reference [201] of contact resistance as a function of sheet resistance for CVD grown graphene.....……..…111

Figure 3.2.13. Plot of measured resistance as a function of probe-electrode distance.....……..…112

Figure 3.2.14. Log-log plot of measured resistance as a function of probe-electrode distance …….....…….…113

Figure 4.1.1. Image of a Philips Heating Holder PW 6592/05……...117

Figure 4.2.1. TEM image of indium islands encapsulated in oxide shells deposited thermally on the backside of SiN membranes.....119

Figure 4.2.2. A series of TEM images captured at an accelerating voltage of 120 kV demonstrating the melting of indium nanoislands on the backside of SiN membranes……...121

Figure 4.2.3. A series of TEM images captured at an accelerating voltage of 200 kV demonstrating the melting of indium nanoislands on the backside of SiN membranes……...122

Figure 4.2.4. TEM images at 200 kV with the heating holder set to 200 C showing that some, but not all of the indium islands are melted…….123

Figure 4.2.5. Plots showing the IV data for a heater wire collected under beams with different accelerating voltages. The difference in resistance is just 1%.....125

Figure 4.2.6. TEM images of island melting for the same device under different accelerating voltages……126

Figure 4.2.7. Image of a 250x250 μm^2 silicon nitride membrane after an EBL pattern has been developed in dual layers of PMMA……..128

Figure 4.2.8. Image of a silicon nitride membrane after an EBL pattern has been etched out using RIE……128

Figure 4.2.9. TEM image showing the dimensions of a slit etched via RIE…..129

Figure 4.2.10. SEM image of 2 trenches in a SiN membrane with indium deposited on the backside of the membrane……130

Figure 4.2.11. DF TEM image of a 100 nm wide trench in a SiN membrane…131

Figure 4.2.12. SEM image of a FIB fabricated slit on a SiN membrane……132

Figure 4.2.13. TEM image of a slit fabricated in SiN membranes using FIB…132

Figure 4.2.14. Bright field TEM image of a SiN membrane with a heater wire and an etch trench…….....……133

Figure 4.2.15. Results from the thesis of Norvik Voskanian showing that the thermal conductivity of the silicon nitride effectively increases further away from the heater wire……..134

Figure 4.2.16. Plot of the change in the effective thermal conductivity of the silicon nitride as a function of distance away from the heater wire…….135

Figure 4.2.17. Three examples of TEM images and COMSOL modeled results for different melting scenarios caused by changing the voltage applied to the heater wire……136

Figure 4.2.18. Plots showing the agreement between the *in-situ* melting results and the COMSOL modeled results……..137

Figure 4.3.1 TEM image of a BNNT suspended over a slit in a SiN membrane…….139

Figure 4.3.2. Dark field TEM image of the completed device……...140

Figure 4.3.3. Sequence of dark field TEM images of the BNNT device as the voltage across the wire is increased……141

Figure 4.3.4. CAD drawing of the system as modeled in COMSOL……142

Figure 4.3.5. Images of the FEA modeled results of the tested device with different effective thermal conductances for the BNNT…….144

Figure 4.4.1. TEM images of MWCNTs before and after annealing at different temperatures…….146

Figure 4.5.1. Top-down view of the experimental set-up showing graphene deposited on a SiN membrane with Au electrodes……..148

Figure 4.5.2. Side view of the experimental set-up showing graphene deposited on a SiN membrane with Au electrodes……..149

Figure 4.5.3. STM probe used to bias a large Au electrode……150

Figure 4.5.4. Bright field TEM image of graphene with overlaid melting contours……151

Figure 4.5.5. Bright field TEM image of graphene with overlaid melting contours……152

Figure 4.5.6. STM probe used to bias graphene in contact with a grounded Au electrode……..154

Figure 4.5.7. Subtracted dark field TEM images to clarify the path of the melting islands……..155

Figure 4.5.8. Bright field TEM image of graphene with overlaid melting contours……156

Figure 4.5.9. COMSOL model similar to the tested graphene joule heated systems…….157

Figure 4.5.1.1. TEM images of a graphene sheet before and after biasing to high enough temperatures to cause migration of indium and gold…….160

Figure 4.5.1.2. TEM images of a graphene sheet before and after biasing to high enough temperatures to remove the indium and recrystallize the gold……...160

Chapter 1: Introduction

1.1 Nanostructures and their properties

Nanostructured materials are those with dimensions on the order of 10^{-9} m. The interest in these structures first appeared in the 1980s after nanometer resolution characterization tools started to become a reality.[1] Nanometer sized structures are unique from larger sized structures because their surface atoms affect the overall behavior of the structure. There are also some transport phenomena that are more pronounced at smaller length scales. In one example, a nanometer sized structure can have drastically larger conductance properties than a corresponding bulk counterpart or vice versa depending on how the atoms on the outside of the structure interacts with its surroundings. In the early 1990s nanostructures such as fullerenes[2] and carbon nanotubes[3] were experimentally produced and this led to an explosion in nanoscale research.

Now, 25 years later, the momentum for research is still strong. There have been many advances in growing and manipulating nanostructure properties to fit the needs of different applications, but there is still a lot of fundamental understanding missing of why nanostructures behave the way that they do. This is part of the reason why the inclusion of nanomaterials in industrial applications is still fairly limited. The next subsections will explore the changes in electrical and thermal transport at the nanoscale and then give an overview of the three nanomaterials that have been researched as a part of this dissertation.

1.1.1. Electrical transport

At the nanoscale the electronic transport in materials changes due to several effects including quantum confinement,[4] quantum size effects,[5] charge quantization,[6] and change in transitions between energy bands. Quantum confinement leads to, among other things, correlation between nanowire diameters and their corresponding bandgaps.[7] However, the results vary widely because surface strain, passivation, and reconstruction have an effect on the confinement. In thin metallic films (on the order of the de Broglie wavelength of electrons) quantum size effects are prevalent. One effect is that electrons in the film get trapped in a quantum well and another is that electrons passing through the film can scatter off of these quantum wells and lead to transmission resonance.[8] Charge quantization phenomena have led to an interest in fabricating single electron pumps.[9] By controlling materials it is possible to make devices with electrically tuned potential barriers.[10]

A combination of these effects in nanoscale devices leads to unpredictable behavior. Once materials with dimensions comparable to the inelastic scattering length for a material are incorporated into a device, the power dissipation can no longer be predicted to follow the classical, diffusive $P=IV$. The local power dissipation is less than this equation estimates in the quasi-ballistic case because there are not enough inelastic scattering events to equilibrate the lattice and instead hot carriers are dissipated at other locations, such as the contact points.[11, 12] Therefore, the dissipated power cannot be calculated straight from IV data, but is dependent on the dimensions of the system and the mean free path of the scattering. These values are not always straightforward to measure, making quantitative analysis of the system difficult. In addition, tunneling or thermionic transmission across barriers leads to asymmetric heating in devices due to effective cooling at one side of the barrier.[13]

In order to make efficient systems at the nanoscale, it is critical to be able to engineer the contact between interfacing materials to reduce additional resistances. Between metals and semiconductors the energy levels at the interface must be well-aligned, but once nanostructures such as nanotubes are integrated into devices, the geometry of the contacts also becomes very important to get dependable behavior.[14] In some cases, it is as trivial as increasing the contact area between the structure and the contact.[15] However, many other studies have focused on creating novel systems with functionalized or engineered interfaces to control the electronic transport.[16]

1.1.2. Thermal Transport

Classically, it is said that heat is transported via conduction, convection, and radiation. There have been several papers showing that heat conduction does not follow Fourier's Law (that the heat transfer rate through a material is proportional to the negative temperature gradient and the area) in many nanoscale systems.[17, 18, 19, 20] There may be several reasons for this, but the most common explanation is that the thermal conductance at interfaces is not well defined, especially at the nanoscale.[21] For insulating materials, only phonons conduct heat, so at the interfaces the question is how much phonon scattering occurs. There are two popular models of phonon scattering, one that only looks at the longitudinal phonons and assumes that there is no scattering and the other assumes maximal scattering from mismatched vibration between the two solids.[22] The first is called the acoustic mismatch model (AMM) and the second the diffusive mismatch model (DMM). AMM is a good approximation at lower temperatures, but at room temperature and above it does not capture actual material behavior well. The DMM generally underestimates the actual conductance, but it has been a good basis for working on ways to engineer materials to improve conductance, for example by inserting thin materials between two solids that are poorly matched.[23] Convection is generally not discussed as an important mechanism in the electronics industry where many devices are surrounded by a solid phase, but it is of course a relevant mechanism in nanofluids.[24]

In the systems discussed in this thesis, which contain solids that are electrically conducting, mechanisms that cause interactions between heat-carrying electrons, photons, and phonons all become important. Classically, radiation deals with photons transferring

heat between two bodies that are far apart. However, there is also a radiation effect that is *near-field*, caused by evanescent electromagnetic energy. In the last 5 years, the interest in this type of transfer has become increasingly popular as a field.[25, 26] The research has provided results that near-field radiation can be orders of magnitude stronger than far-field at the nanoscale.[27, 28] One type of electromagnetic energy is surface waves that can be caused by a coupling between electromagnetic waves and surface electrons (i.e., plasmons) or optical phonons, called plasmon-polaritons and phonon-polaritons, respectively. The effects are difficult to measure because they are often small unless the surfaces are so close that the waves can reach the opposing surface, however there have been several successful studies of the effect.[29, 30, 31] The results in this thesis show length dependent thermal transport for some materials giving further evidence to this phenomena.

1.1.3. Carbon and boron nitride nanotubes

Carbon nanotubes (CNTs) were discovered by Iijima in 1991 when he modified the recipe for arc discharge growth of fullerenes.[3] This article has since been cited over 26,000 times. CNTs are composed of rolled up sheets of hexagonally bonded carbon atoms. A review paper, 10 years after the discovery, touted that this material was the strongest, stiffest, most resilient material known and that the outlook for applications for the 21st century was tremendous.[32] Along with these mechanical properties, the discovery of high thermal conductivity[33] and unique electrical properties[34] had also attracted interest. Yet, 15 years after that review paper there are only a few items commercially

available containing CNTs and these exclusively utilize their mechanical properties. The leading application is for composites in sports equipment by Zyvex Performance Materials.[35] Another is an epoxy resin named Hybtonite. However, CNTs have not yet become part of commercial electronic devices,[36] neither for their electronic properties nor for their thermal properties as heat spreaders. Understanding of the properties, to a point where they can reliably be predicted in real world systems, and reliable, large scale production methods are both still lacking despite immense effort by researchers.

Structurally, boron nitride nanotubes (BNNTs) are analogous to CNTs. However, as the names suggest, BNNTs are made up of alternating boron and nitrogen atoms, as can be seen in Figure 1.1.3.1 . While theoretical evidence of CNTs was published in 1952,[37] BNNTs were not even predicted until 1994.[38] This is part of the reason why CNTs have been much more extensively researched, but a more important reason is that large scale synthesis of BNNTs was more difficult to achieve than for CNTs.

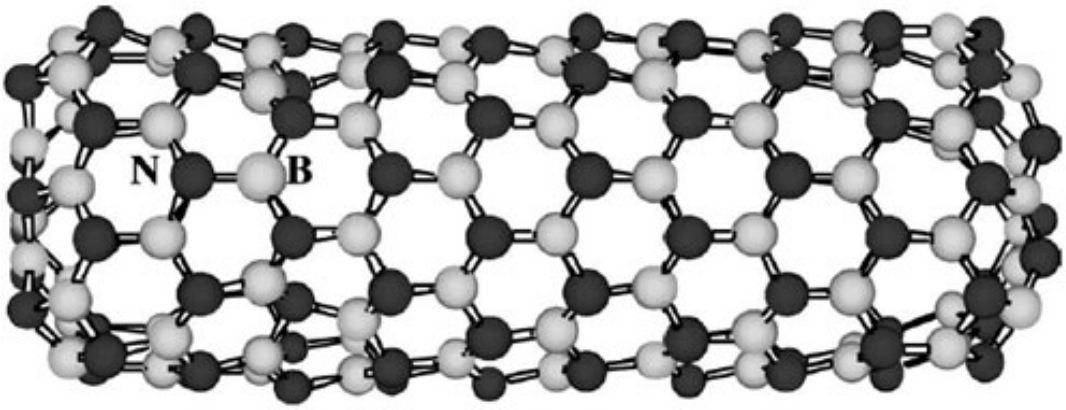

Figure 1.1.3.1. Atomic structure of boron nitride nanotubes

BNNTs were first grown in 1995 via arc-discharge.[39] Several other low-yield techniques were developed shortly after; variations on the arc-discharge technique, [40, 41,

[42] laser heating of BN targets,[43, 44, 45] ball milling annealing,[46, 47] and chemical vapor deposition (CVD).[48, 49] The limitations in mass production of pure high-quality BNNTs are slowly being overcome. The most promising techniques are boric oxide CVD (BOCVD)[50] and pressurized vapor/condenser (PVC) method.[51] This progress has led to ideas of commercial viability of BNNTs; the company BNNT, LLC was recently established to realize this.

Phonon dispersion relation calculations for BNNTs show strong similarities to CNTs and both types of NTs are predicted to have theoretical thermal conductivities around 6,000 W/mK.[33, 52] Many experiments have been performed to measure the thermal conductivity of CNTs, fewer for BNNTs, but results from both are varied. Nonetheless, both types of NTs show promise for use in high thermal conductivity applications. In this area, BNNTs have an advantage over CNTs, because they show structure and property stability in air up to 950 ^{0}C, while CNTs break down at 500 ^{0}C.[53] Another phenomenon that is unique to BNNTs is the isotope effect on thermal conductivity, which drastically changes depending on the boron isotope concentration.[54] It is not surprising that the thermal conductivity changes with isotope concentration since this affects the phonon dispersion relation. However, the 50% increase in thermal conductivity that is observed for BNNTs with 99.5% ^{11}B as compared to isotopically pure BNNTs is significant.

Electronic properties make up the major difference between CNTs and BNNTs. While CNTs' electrical properties strongly depend on chirality and size, BNNTs have a stable band gap for most conditions. CNTs can be either semiconducting or metallic.

BNNTs are always insulating, unless significant modifications are made to their structure.

The electrical properties and phenomena of CNTs are complex. Since SWCNTs are composed of a rolled-up single sheet of graphene they can act either as metals or as semiconductors depending on the direction of the rolling (chirality).[55] Another interesting way to control the electronic properties of SWCNTs is to fill their hollow core with another material.[56, 57] MWCNTs are composed of many layers of rolled-up graphene sheets which can all have different chiralities meaning that there are seldom fully metallic MWCNTs.[58] However, the sheets interact only very weakly with each other and the majority of the current passes through the outer shell in most cases since this is generally the only one physically in contact with the metal contacts.[34, 59] The tube diameter can vary from tens to hundreds of nanometers, which means that they can be either smaller or larger than the elastic mean free path and phase coherent length of the electrons. This means that MWCNTs can be ballistic, semi-ballistic, or diffusive depending on the size.[60]

While there are applications that benefit from the insulating properties of BNNTs there has been work dedicated to testing if the electrical resistance can be decreased so that the BNNTs can be used as electrical conductors or field emitters. A recent paper by Ghassemi et al. shows that the electrical properties of BNNTs are highly strain dependent[61]. The results showed that the electrical resistance could be tuned from 2000 Ω to 769 MΩ by induced strains up to 2.5%. Tests were performed on individual BNNTs inside a TEM using a probe to mechanically deform the BNNTs. They theorize that it is the change in the radius of curvature of the BNNT that changes the electron transport

through the tube. They show that while the mobility decreases, the electron concentration increases. Overall, the resistance decreases, which leads to the assumption of a reduced band gap. There have also been several projects that add material such as carbon or gold to the BNNTs to improve their conduction behavior.[62, 63, 64]

1.1.4 Graphene

Graphene consists of a single sheet of hexagonally bonded carbon atoms. Since all of the atoms in the structure are surface atoms, it leads to very interesting properties that are influenced heavily by the graphene environment and contact with other materials. Graphene, like its nanotube counterparts, has high electrical[65] and thermal conductivity,[66] along with remarkable mechanical strength[67] that can be tuned by altering growth parameters and their system integration.

Graphene was first experimentally and intentionally produced by Andre Geim and Kostya Novoselov in 2003,[68] a discovery that they earned the Nobel Prize for in 2010. After it was understood that a single atomic layer of carbon atoms is stable in ambient conditions the race began to find large scale production methods. There have been notable successes both with arc-discharge[69] and chemical vapor deposition (CVD) [70] techniques, but there are still not large enough quantities being produced for industrial applications. CVD graphene can be grown with high quality and few defects and a standard transfer method has been developed, but it requires depositing polymer on to the

graphene and etching away the growth-substrate, usually copper.[71] This transfer step is far from economically and environmentally sustainable. More recently focus has turned to production via mechanical exfoliation in liquid and thus far this seems promising because of the possibility of using safe and economically viable solutions and ease of scaling.[72, 73] Along with strong support from researchers, graphene has captured the attention of politicians, at least in the European Union, who have given the material some focused attention and funding in the Graphene Flagship Project that will span from 2013 to 2023 in hopes of aiding graphene in entering the industrial market.[74]

Graphene has interesting electronic properties because of its band structure. It is considered a semi-metal because the valance and conduction band touch in just two distinct points in the Brillouin zone.[68] At room temperature graphene has the highest carrier mobility of any known material.[75] Due to the nature of the material, where all atoms are surface atoms, graphene is extremely sensitive to its environment and the electrical properties can change drastically from functionalization.[76] However, this can be a strength in cases where the properties need to be tuned. For example, graphene can be changed to act as an n-type or p-type semiconductor simply by contacting it with metals of different workfunctions because of its susceptibility to charge transfer and re-align its Fermi level simply by contacting metal.[14]

Graphene has just as promising thermal properties with a measured thermal conductivity above 3,000 W/mK at room temperature.[66, 77, 78] The first experimental results of the thermal conductivity of graphene were performed with the optothermal technique, which relies on a shift in the Raman G peak of graphene with temperature

change.[77, 79, 80] These experiments led to the discovery that there is almost an order of magnitude difference in the in-plane thermal conductivity between supported and suspended graphene.[79, 81] Putting graphene on a substrate lowers the thermal conduction of graphene because of dampening of the out of plane phonon mode. Phonon scattering at the interface, as well as off of defects and impurities in the substrate, also play an important role. However, the values of thermal conductivity for supported graphene are still higher than those for commonly used metals, such as silver and copper.[82] The exact conductivity of graphene depends strongly on what kind of graphene that is used. Impurities, grain boundaries, edge roughness, lateral dimensions, and strain have all been shown to play a role.[83, 84, 85, 86] However, the results of these studies vary and there is still great debate over how heat is transferred in graphene, for example which acoustic phonon modes; *LA* (in-plane longitudinal), *TA*(in-plane transverse), or *ZA* (out of plane) contribute the most.[87, 88] Though there are many theoretical investigations of heat transport in graphene there are still only about 15 experimental investigations and these are difficult to compare because they vary in measurement method, layer thickness, substrate support, and fabrication methods. Nonetheless, work continues now on to enhancing the thermal transport of graphene with its surroundings by using functionalizations and composite systems.[89, 90]

1.2 Transmission electron microscopy

Transmission electron microscopes (TEMs) are an important tool for furthering the knowledge of the nanostructures described in the previous sections. The work in this dissertation has been performed mainly with two different TEMs; the JEOL JEM 2100 LaB6 at the University of Maryland and the FEI Tecnai T20 LaB6 at Chalmers University.

1.2.1 History

The first electron microscope was built in 1931 by Ernst Ruska and Max Knoll for which they won the Nobel Prize in 1986.[91] Closing in on a century from the first microscope, there have been incredible advancements throughout the years. Thanks to strong efforts at the start of the millennium with work on aberration correction, the resolution of transmission electron microscopes (TEMs) has improved significantly. For example, the double-corrected TEAM1 microscope at the Molecular Foundry at Berkeley Lab has a 50 pm resolution.[92] Recently, the community has shifted its focus to versatility and adapting the instruments to a wider variety of samples. Electron imaging in high vacuum conditions is harsh on many specimens, especially biological samples. By creating microscopes that have higher resolution even at lower accelerating voltages[93] and at higher pressures (named environmental transmission electron microscopes, ETEM)[94] it is possible to investigate samples that have traditionally been off-limits for electron microscopy investigations.

1.2.2 Operating principles

Transmission electron microscopes operate on similar principles as optical microscopes, with the main difference in the source of the imaging waves; electron versus photons. The electron source, commonly called electron gun, can be realized using a heated filament or by field emission from a sharp tip. Thermal emission sources are generally made of tungsten or LaB6. LaB6 is more expensive as a filament, but it has a lower work function (2.4 eV vs 4.5 eV) so there are more electrons emitted at a given temperature which improve the brightness, energy spread, and lifetime.[95] Field emission sources improve on these parameters even further because the electrons tunnel through the barrier but are more expensive and require stable vacuum below 10^{-8} Pa.[95] Figure 1.2.2.1 shows the main differences between the thermionic and field-emission sources.

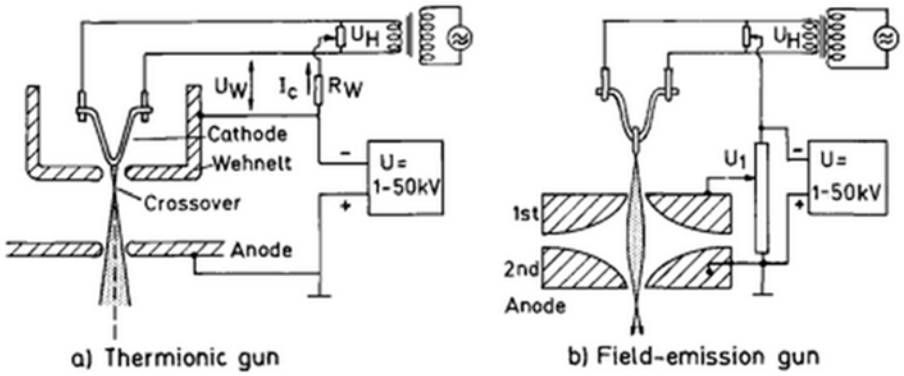

Figure 1.2.2.1. Electron sources created by a) thermionic and b) field-emission.[96]

The electron beam created by the source is focused by two sets of condenser lenses. The spatial coherence at the specimen is controlled by inserting a condenser aperture above the sample as can be seen in Figure 1.2.2.2.

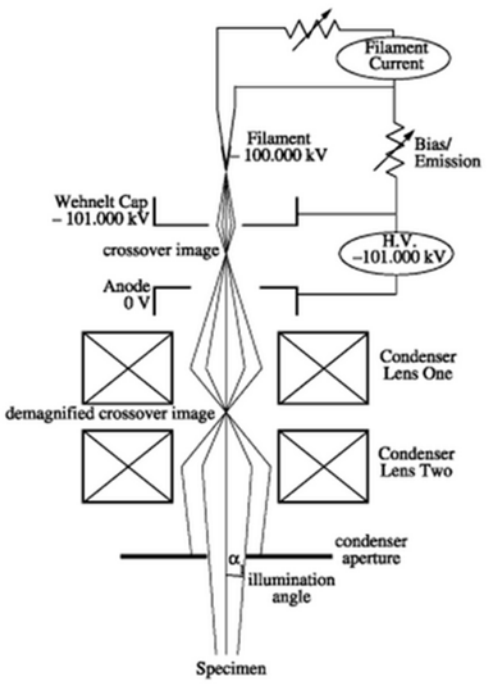

Figure 1.2.2.2. Schematic showing the electron source focused and limited before hitting the sample by two condenser lenses and aperture.[97]

After interacting with the specimen the electron beam is then focused by the objective lens and aperture before spreading out to become an image. There are two main imaging modes, bright field and dark field. These are shown in figure 1.2.2.3. For bright field imaging an objective aperture is used to look at the electrons that have gone directly through the specimen. The image is therefore a summary of the change in the direct beam electron's energy as they interacted with the specimen. This gives information about things such as the sample mass and thickness. The second imaging mode, dark field, on the other hand looks at the electrons that are scattered at angles other than 0^{o} when they pass through the specimen. This gives different information about the sample, for example planar defects, stacking faults, and phase changes, that cannot be seen in the non-scattered beam. A dark field image can be acquired in two ways, either by moving

the objective aperture, called off-axis dark field, or by tilting the beam before it hits the specimen, called on-axis dark field.

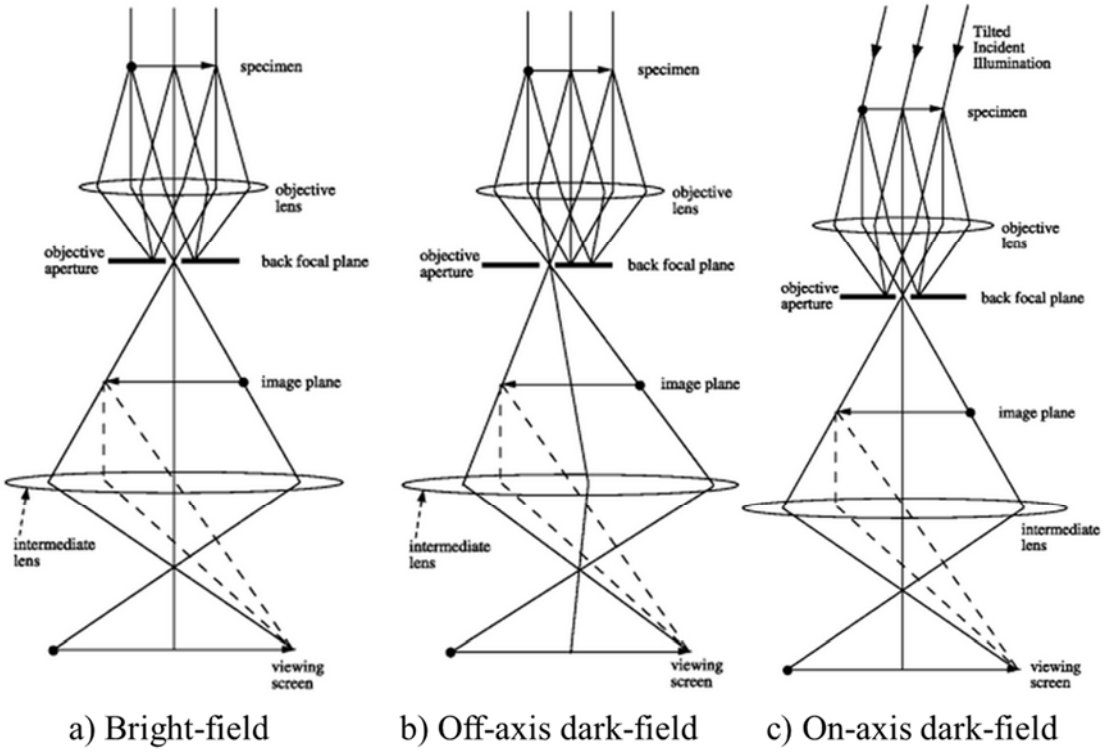

Figure 1.2.2.3. Schematics of different TEM imaging modes.[97]

1.2.3 *In-situ* TEM

While there are many ways to use TEMs to obtain information about a material, the one that is most relevant for this dissertation is *in-situ* TEM. *In-situ* microscopy simply means that a physical process can be observed in real-time. This generally requires inputting some sort of stimulus, such as heat, bias, or physical agitation, to initiate a change. This requires the use of specialized holders that are compliant with the strict space, cleanliness, and electrical requirements inside of the TEM. The market for

holders has grown despite the manufacturer of a couple of the holders used for this project, Nanofactory, entering into bankruptcy. Most of the microscope manufacturers are producing their own line of holders, but there are also dedicated holder manufacturers such as Hummingbird,[98] Protochips,[99] and DENSsolutions. However, in some cases it can be more effective to build a holder that is made specifically for a project's requirement. This is often the approach that the Cumings Group has taken.[100]

In-situ TEM experiments have led to impressive results such as the observation of tensile tests of individual CNTs[101] and observations of lithiation of nano-sized battery systems.[102] Thanks to the current trend in making the microscopes themselves more versatile, such as increasing the space between the pole pieces and allowing gas flow, the next generation of *in-situ* TEM experiments will thus have a lot more versatility.

1.2.4 Thermal characterization techniques

Traditional methods for measuring the thermal conductivity of solids include the transient plane source method and the laser flash method.[21, 103] Unfortunately, these methods can only be used with bulk structures. Electron microscopy techniques have helped in this area, but there are more characterization techniques for the thermal transport of nanostructures that do not rely on electron microscopy. One technique is called scanning thermal microcopy (SThM). This technique relies on localized interactions between a sharp probe tip and the surface of the sample.[104] By placing a temperature sensor at the end of the probe it is possible to generate accurate temperature

maps of a sample. Recent advancements in this technique have shown 50 nm lateral resolution.[105] One advantage of this technique is that it is not limited to high vacuum conditions. The disadvantage that limits this technique is the speed of capture of information. Because the probe has to capture information at each location along the sample one point at a time, the technique is unable to capture time dependent information about nanoscale heat transfer. For example, it has recently been showed that CNT-heating occurs within tens of picoseconds.[106] This means that SThM is better suited to investigate steady-state thermal systems.

Another method for thermal measurements is thermoreflectance microscopy. This technique uses the relationship between the reflectance coefficient of a material and its temperature.[107] This technique offers ~10 mK temperature sensitivity. The downsides are that the resolution is currently limited to ~1 micron and that image capture pixel by pixel can take minutes to hours depending on the system. This means that this technique also cannot capture transient heat transfer events. This technique is mostly applicable to thin films that have uniform surface roughness.

Raman spectroscopy has also been used in various ways to investigate the change in temperature of a system by the changes in the Raman spectra. This technique has been successfully used to track temperature along a joule heated CNT, but the spatial resolution is also limited to ~1 micron and the temperature resolution is only ~10 K, depending on the system used.[108] While this technique has better time resolution than the two techniques above, the spatial and temperature resolution are not good enough to

accurately determine the thermal conductivity and contact resistance of nanoscale systems.

Though the techniques outlined above have brought many scientific advancements, I will introduce electron microscopy techniques that have been used for thermal characterization in more detail as a comparison to the technique that has been used in this thesis work. Many of these techniques, like our own, rely on observing the phase change of deposited materials at a known temperature as a probe of the temperature of the rest of the system. More recently, there have also been developments of using analytical TEM methods like electron energy loss spectroscopy (EELS) to characterize temperature.

The first paper to be published on the topic of using the phase change of a material with a known temperature as a thermometer for an entire system was "Probing Nanoscale Solids at Thermal Extremes" by Begtrup et al. in October 2007.[109] This group used gold nanocrystals deposited on and around a joule heated carbon nanotube to measure the temperature of the substrate. The gold particles were generally less than 10 nm in diameter and the group followed the melting front of those at 6 nm. At this diameter, gold particles are known to have a melting temperature of 1275 K.[110] Their experiments shows that the sample becomes hottest around the center of the CNT when it is Joule heated. Ultimately, they were interested in discovering how high temperature CNTs could withstand before becoming unstable. They found that the CNT was still completely stable in vacuum at an estimated temperature of 2175 K by observing when the membrane starts to disintegrate. From their modeling of the heat front of the

evaporating gold they estimate that their CNT reaches a temperature above 3200 K before becoming unstable. The problem with this technique is that the gold particles may not actually be melting, but rather diffusing out to the sides of the membrane. Diffusion would take place at a much lower temperature. Secondly, they do not consider the effects of radiation in their modeling of the heat front which is valid at lower temperature, but at 3200 K it would be expected to play a significant role.

Just a few months later, the Cumings group published the first paper introducing a thermal measurement technique called electron thermal microscopy (EThM).[111] This technique is the basis for the thermal characterization performed in this thesis. The technique utilized indium nanoislands deposited on the backside of silicon nitride (SiN) membranes to measure the temperature of the sample. In the original study, tungsten heater wires were used to heat up the substrate. Indium has a much lower melting temperature (430 K) and vapor pressure at melting than gold so it allows for thermal characterization closer to room temperature. Rather than evaporating or diffusing like the gold particles, the indium nanoislands melt, but keep their shape because they are enclosed in an oxide layer. The phase transition is visible in specific dark field conditions. The technique has been demonstrated down to <100 nm resolution and video-rate speed imaging. Another advantage to this technique over gold evaporation is its reversibility. The indium nanoislands do not move as long as the temperature is below the diffusion temperature of indium through indium oxide. If this constraint is kept, it is possible to watch island melting and solidification repeatedly. The fact that the phase change front is at a lower temperature means that there are fewer complexities in

modeling the behavior. The disadvantage is that higher temperature systems cannot be explored.

In 2009 Reuger et al. published a paper demonstrating the concepts presented by the Zettl and Cumings group to determine the contact resistance between a heater wire and a substrate.[112] They look at the crystallization of the silicon nitride membrane and use the profile they have determined for the change in the temperature of the membrane with applied electrical power to investigate the preferred growth temperature of silicon nanowires. They used a tungsten heater wire on a silicon nitride membrane like the Cumings group and gold nanoparticles for temperature sensing like the Zettl group. They even focused on the 6 nm gold particles like the Zettl group. However, unlike the Zettl group, the Dallaporta group performs EDX on their samples directly after heating experiments to ensure that the gold particles are in fact evaporating and not just diffusing to the outside of the sample. They claim that their technique is easier to analyze than the Zettl technique and that it allows for deposition on a thinner membrane (50 nm vs 100 nm) than the Cumings group technique.

In 2011 the Goldberg group published two papers exploring the thermal properties of CNTs using two unique TEM techniques. The first is titled "Thermal stability of carbon nanotubes probed by anchored tungsten nanoparticles" and—as the title suggests—the group attached a tungsten nanoparticle to the side of a CNT and watched its movement and melting as the CNT is Joule heated.[113] Unlike the papers discussed so far, this technique focuses on the behavior of a single 60 nm tungsten particle. The melting temperature of this particle is about 3400 K so the stability of the

CNT can be explored up to previously unattained temperatures (recall that the Zettl group claimed to have reached 3200 K in 2007). The second result that the Golberg group published involves filling a CNT with a sublimable material to determine the temperature inside the CNT based off of the sublimation front of the material inside the CNT.[114] The CNTs were Joule heated by gold probes. The CNTs were grown directly with $Zn_{0.92}Ga_{0.08}S$ inside the carbon shell. Because of the unconventional growth method these CNTs had much large outer diameter (~130 nm) than pristine CNTs. This means that the research results are not applicable to all or even most CNTs, but their method does provide an interesting TEM method for monitoring temperature within nanostructures. The $Zn_{0.92}Ga_{0.08}S$ sublimates at 928 K and they are able to see this temperature front, not only axially, but also radially within the CNT, which they claim is the first time that this has ever been observed.

In the same year, Santini et al. published a paper with a novel qualitative method of observation of thermal behavior of CNTs using *in-situ* TEM.[115] Like Wei et al. they deposit nanoparticles directly onto the CNT and use the melting and movement of these particles to analyze the temperature of the CNT. The difference is that they use many nickel particles with diameters ranging from 20 to 35 nm. These particles have a melting temperature of about 1730 K. The CNTs are brought to mechanical breakdown by Joule heating with titanium nitride electrodes. The fact that the nickel particles have melted at this point allows for the conclustion that the temperature at breakdown of CNTs is above 1730 K. Electrical experiments are performed both in air and in high vacuum conditions and it is found that failure occurs at three times lower current density than in air. Failure is attributed to oxidation in air and annealing of the CNTs to the contacts at high

temperature vacuum conditions. Unfortunately, the ambient condition experiments cannot be viewed *in-situ* so they cannot do much more than speculate as to why the CNTs break so much earlier in air. For the *in-situ* TEM experiments the position of the mechanical breaking point along the CNT has to do with the contact resistance at each contact. The temperature of the CNT will be higher at one end if the contact resistance is higher at that end. This will lead to the breakdown occurring closer to that contact. Lastly, they conclude that the thermal conductivity of the CNTs is greatly improved with the addition of the nickel particles. Thermal conductivity above 1730 K is estimated to be 30 to 200 $WK^{-1}m^{-1}$ for the pristine CNTs and as high as 680 $WK^{-1}m^{-1}$ for those with nickel particles.

Since the Cumings group introduced their EThM technique in 2008, two other works have been published showing the utility of the method.[15, 116] The first shows that EThM can be used to calculate the thermal conductivity and even begin to put limits on the thermal contact resistance between CNTs and their substrate. A palladium heater wire is used to passively heat an individual MWCNT. There is no asymmetry in the melting of the indium nanoislands, unless the opposite end of their CNT is anchored by a palladium pad. The palladium pad acts to reduce the contact resistance between the CNT and the substrate. However, even with the addition of the palladium pad, the asymmetry is only slight and it is only thanks to the high spatial resolution of the EThM technique that it is possible to see the difference between the two cases. By modeling the results, the thermal contact resistance of the unanchored CNTs can be estimated as greater than 250 KmW^{-1} and by anchoring the CNTs the contact resistance value can be brought down to 2-10 KmW^{-1}.

In the second paper, contacts are patterned on to the ends of the CNTs in order to Joule-heat the CNT and then characterize the dissipation to the substrate. Once again, thanks to the high spatial technique of the EThM technique, it was possible to observe a previously unseen phenomenon, remote Joule heating. It is found that despite the high thermal contact resistance between the CNT and the substrate when compared to the CNT and the contact pads, the CNT dissipates the majority of the heat directly onto the substrate beneath the center of the CNT. According to the obtained results, it seems that the dominant heat transport mechanism of CNTs is remote scattering.

More recently, a few groups have combined analytical TEM techniques with *in-situ* experiments. Most notably electron energy loss spectroscopy (EELS)[117, 118] and electron backscatter diffraction (EBSD).[119, 120] These methods utilize the fact that the energetics of electron interactions are different at different temperatures for many materials, especially metals. Vendelbo et al., looked at the EELS spectra of platinum wires as they were Joule heated so that they could calibrate a change in spectra with resistive heating.[118] This work helped to prove that one of the commonly used resistive heating holder systems, made by Protochips, has spatially dependent heating. Mecklenburg et al., look at the plasmon energy change of aluminum heater wires. This is a promising technique to use for looking at the temperature and thermal transport of nanodevices, but it will take some time before the community reaches a consensus on the expected energy shifts with temperature for many materials. Lastly, in this section it is worth mentioning the development of a new *in-situ* TEM heating system that allows the temperature to be raised above 2000 C.[121] The development of new hardware in

combination with innovative analysis techniques will lead the way to great progress in the understanding of thermal transport in nanostructures in the future.

In conclusion, the importance of thermal characterization has led to the development of many unique characterization techniques. Many of these techniques are created to address a particular limitation or advantage of a specific material or structure. A challenge that remains is to prepare nanoscale samples for characterization that is more universal and allows for direct comparisons of results. One solution to the preparation challenge can be solution processing development.

1.3 Solution processing of nanostructures

Solution processing of materials can include several parts of the fabrication procedure, but most common are filtering[122] and deposition[123]. For CNTs, solutions have been developed in order to solve the problem of tube bundling so that individual and/or well aligned tubes can be achieved. For graphene, solutions have shown promise as a medium where graphite can be converted to graphene by use of mechanical agitation to separate the layers.

Depending on the material and the application there is a wide variety of solutions that can be used. In some cases it may be desirable for the solution to change the properties of the nanostructure for a certain application, but in other instances, such as when we want to study the intrinsic properties of individual nanostructures it is undesirable for the solution to cause change to the nanostructure.

1.3.1 Types of solutions and surfactants

The type of solution to use depends on the material and the application, but even for one material and one application there are many different options. One common option is to use organic polar solvents, such as dimethylformamide (DMF) and *N*-methylpyrrolidene (NMP), which have shown success in both dispersing CNTs[124] and exfoliating graphene[125]. However, this category of solutions often is less than ideal from a safety, environmental, and economical standpoint. There have also been novel approaches like using DNA molecules[126] and developing superacids[127] for specific applications. The most common option may be to use a tension reducing agent, known as a surfactants in aqueous solutions. Since all of the nanostructures mentioned in the previous sections are very hydrophobic they cannot be processed with any sort of aqueous solution unless surfactants are used to help them form stable colloids with hydrophilic interfaces. Surfactants fall in to one of four categories; nonionic, anionic, cationic, and zwitterionic. Examples of nonionic surfactants are octyl phenol ethoxylate (Triton X-100), alkylphenolethoxylate (IGP), and the TWEEN family (Polysorbate 20, TWEEN 60, etc.). Cationic surfactants include dodecyl trimethylammonium bromide (DTAB) and cetrimonium bromide (CTAB). The most common category for nanostructure suspension has been anionic surfactants, often containing sodium, such as sodium octanoate (SOCT), sodium dodecyl sulfate (SDS), and sodium dodecyl benzene-sulfate (SDBS).

1.3.2 Successes in surfactant development

Four of the main goals for solution processing of nanostructures are (1) high dispersion limits, (2) stability, (3) even dispersions or separations of material, and (4) control/predictability of nanostructure properties. About 5-10 years ago there was a strong effort in surfactants development led by the desire to separate and deposit CNTs.[128, 129, 130, 131] Out of this effort came well-characterized solution systems with SDS as the practical winner. Now with the new push for graphene development, the desire to work on surfactant development has resurfaced. The last couple of years have again seen successful characterization of graphene solution systems. Thus far the community has re-characterized the winners of the CNT research, mainly SDS[132] and NMP.[133] However, there have also been some more creative approaches which give hope that something new will be developed that can be used even for CNTs.[134]

1.4 Goal of dissertation

Low-dimensional materials, such as nanotubes and graphene, have incredibly interesting behaviors from a scientific standpoint and many possibilities for applications, especially in the growing electronics industry. However, we are far from understanding all of the properties of these materials which can facilitate or prevent their use in applications. This dissertation is composed of a few different projects, all with specific challenges, approaches, and measurement metrics. Each will be addressed separately below.

The first goal of this dissertation, addressed in Chapter 2, is to present a new surfactant to suspend, store, and deposit carbon nanostructures. Previously, none of the surfactants available offered the stability, selectivity, and cleanliness required to be able to deposit individual carbon nanotubes (CNTs) on to a substrate without residue and at a high yield. From approximately 2000 to 2010, there was intense research focus on CNTs and on developing surfactants to aid in working with them. The surfactant sodium dodecyl sulfate (SDS) came out as the *de facto* winner and emerged as the standard for solution processing of CNTs. However, as is shown in this dissertation, there is a much better alternative, ammonium laurate (AL). We developed this surfactant and have characterized its performance extensively in comparison to SDS. This dissertation shows that for multi-walled CNTs (MWCNTs) AL is more stable over time, more selective in suspending individual nanotubes, and produces cleaner depositions. Stability is measured by observing the solutions over time and more quantitatively by measuring the change in optical absorbance of the solutions over time. Cleanliness and quality of the depositions

is measured using transmission electron microscopy (TEM) imaging and more quantitatively using Raman spectroscopy. For solutions of single-walled CNTs (SWCNTs) the results show that in addition to all of the benefits described for MWCNTs, there is also evidence of selective suspension of specific chiralities as well as a lower contact resistance between the tubes when deposited. It is well known that SWCNTs properties depend strongly on chirality, which is why it is important to develop methods to separate and control the chirality of tubes for specific applications. Lastly, this surfactant was used to create stable solutions of graphene. Graphene, as is described in detail earlier in the introduction, has very promising characteristics for a variety of applications. Yet, again, there is missing knowledge on how to environmentally and economically fabricate, store, and deposit this material controllably. Without this development and knowledge, graphene cannot be incorporated into industrial applications. The dissertation shows that AL is a viable candidate to solve some of these problems. It has been used to suspend, store, and deposit graphene oxide sheets with results that again outperform SDS. Preliminary results also show that it can be used to fabricate high quality graphene from natural graphite using mechanical exfoliation in the AL solution. In addition to the characterization methods named above, probe testing of the electrical conductivity of the deposited graphene shows that AL deposited graphene has much high electrical conductivity than SDS deposited graphene. This is an essential benefit if the electronic properties of graphene are to be utilized in future electronic devices.

The second goal of this dissertation, addressed in Chapter 3, is to correlate the electronic behavior of graphene with its structure (e.g. wrinkles) and its interactions with

other materials (e.g. at interfaces). More specifically, the electrical resistance of reduced graphene oxide deposited onto substrates has been characterized with respect to contact resistance and local structure influences. In the field broadly, there is a strong effort to understand the complex electronic transport within graphene. The complexity comes in part from the sensitivity of the properties to defects in the material, interactions between layers, and the substrate properties. The work here directly addresses these issues by using a characterization method that provides local electrical measurements of graphene deposited on a substrate using a method that allows the contact between the electronic probe and the graphene to be manipulated, at the same time that the structure is observed. Previous theoretical and experimental work in the field has indicated that wrinkles in graphene lower the electrical conductivity. Our results provide evidence to the contrary. We see no systematic correlation between levels of wrinkling and measured electrical resistance. On the contrary, wrinkling helps to reduce contact resistance, apparently because it provides more contact area with the electrodes. This is an important result, because graphene's mechanical properties cause it to wrinkle naturally when deposited on a substrate. The fact that we can instead utilize this natural behavior to make devices with lower resistance may indicate a pathway to improved graphene electronics.

The final goal of this dissertation, addressed in Chapter 4, is to present progress made on the Electron Thermal Microscopy (EThM) technique and its application to the nanomaterials studied. This technique was developed by the Cumings Group in 2008 and has since been successfully used to characterize the thermal properties of CNTs. In comparison to other nanoscale thermal characterization techniques, this method provides high spatial and time resolution. It allows for direct observation of heat spreading by and

through nanostructures. With all characterization techniques, it is important to understand how the measurement itself affects the behavior of the measured system. This dissertation presents important characterization of the technique itself and how it is influences by the beam parameters used when performing the experiments. In addition, the thermal conductivity of the supporting substrate, here thin silicon nitride membranes, was characterized. The findings by previous researchers using this technique as well as those performing work focused solely on thermal transport in polar substrates have found interesting dependences of the thermal conductivity on parameters such as the distance from the heat source. Again, before materials can be incorporated into new industrial applications it is important that we understand how they behave in different environments. For these studies, fabrication methods were developed to control the thermal spread through the silicon nitride membranes using slits and trenches to provide greater range in experiment design. The results of these experiments are in agreement with recent theoretical modelling work showing that long wavelength phonon modes on the surface of silicon nitride membranes control a large portion of the thermal transport. Next, a measurement, using the newly-developed fabrication methods, of the thermal conductivity of an individual boron nitride nanotube is presented. The resulting conductivity value is an importing contribution to a field of research that has a large spread in the reported values. Lastly, the EThM technique has been modified to look at the thermal transport through graphene. As with the electrical characterization of graphene described above, local measurements were performed on wrinkled graphene sheets resting on a substrate. In this field, it has been proposed that graphene's 2D nature and high thermal conductivity be used as a heat spreading material to replace copper in

the electronics industry where hot spots are a growing problem. Here, we create local hot spots using an STM tip *in-situ* and observe the graphene's ability to transport the heat away and into the substrate that it rests upon. The literature on thermal conductivity of graphene shows a clear trend that thermal conduction is reduced when the material is placed on a substrate. This is caused by the dampening of the out-of-plane phonon mode (ZA) by the substrate contact. Some results show that the reduction in thermal conductivity is as much as a factor of ten. Here we show that the thermal conductivity of this wrinkled graphene is on the order of thousands of W/mK, which is much higher than most reported values, and it is certainly higher than the currently used material, copper. We believe that the wrinkles and concomitant overlapping sheets in these samples, create a semi-suspended case where the phonon conduction is controlled less by the presence of the substrate. This hypothesis has support from recent models showing the amount of conformity between the graphene and the substrate is an important factor in reducing the thermal conductivity. This work also finds that the less the graphene conforms to the substrate, the less the thermal conductivity is reduced as compared to a completely suspended case. This dissertation presents important experimental evidence of the ability of graphene to spread heat away from hot spots and transport it in to a supporting substrate.

In conclusion, the goal of this dissertation is to show that progress has been made in several different areas on the pursuit to understand and utilize nanostructures for future applications.

1.5 Structure of dissertation

The dissertation is composed of four chapters, each with several sections. Chapter 1 gives background and motivation to working with nanostructures, specifically BNNTs, CNTs, and graphene. The focus is on thermal and electrical properties. The first chapter also introduces the concepts of solution processing nanomaterials and the use of TEM to characterize them. Chapter 2 deals with the results of suspension, storage, and deposition of nanostructures. Most of the attention is given to the surfactant, AL, which was fabricated and characterized for the first time as a part of this dissertation work. Results are presented for BNNTs, MWCNTs, SWCNTs, and graphene. The third chapter presents results of electrical characterization performed by *in-situ* TEM experiments. Most of the attention focuses on the results of localized graphene probing via STM *in-situ*. The last chapter focuses on thermal characterization using TEM. The progress that has been made to the EThM technique during this work is presented as well as exciting results of thermal property characterization of BNNTs and graphene.

Chapter 2: Suspension of nanomaterials in solution

2.1 BNNTs

In order to take advantage of the desirable properties of BNNTs, it is necessary to be able to control their deposition onto a desirable substrate. One method for doing this is through suspension in liquid. This has been a popular method for storing and depositing nanomaterials.[135] BNNTs are hydrophobic meaning that they will not suspend or even associate with water without modification to the water or the nanotubes.[136] Here we show evidence that such functionalization is not necessary for making stable solutions of BNNTs. Instead, pure ethanol in combination with light sonication can be used to create stable suspensions for depositions of unbundled nanotubes onto desired substrates either by immersion, drop-casting, or spin-casting. The BNNTs used in this work were grown in the Golberg group using chemical vapor deposition (CVD).[137]

Figure 2.1.1 shows the molecular structure of the three main liquids; water, ethanol, and isopropyl alcohol, that are tested for suspending BNNTs. Figure 2.1.2 shows what initially happens when a clump of BNNTs is placed in a vial of the three different liquids. In deionized water the BNNT clump simply sits on the surface of the liquid. In ethanol the BNNT clump becomes fully infiltrated and sinks to the bottom of the liquid. In isopropyl alcohol the BNNT clump immerses in the liquid, but prefers to stick to the glass of the vial rather than sinking to the bottom. These initial results give a strong indication of the usefulness of each of the liquids for suspending BNNTs.

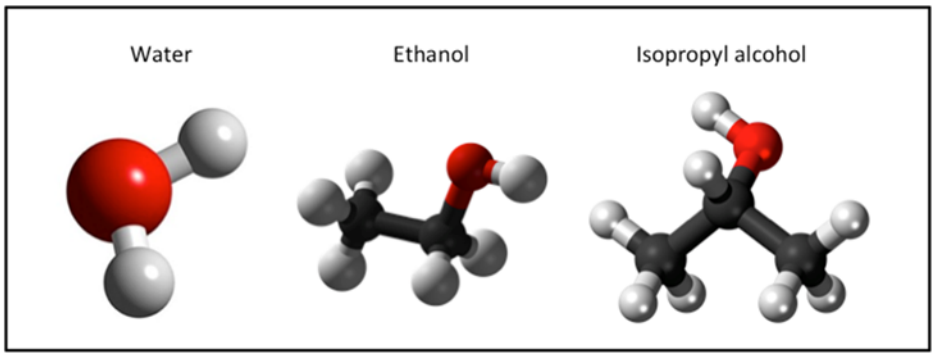

Figure 2.1.1. Molecular structure of three different liquids used for suspending BNNTs.

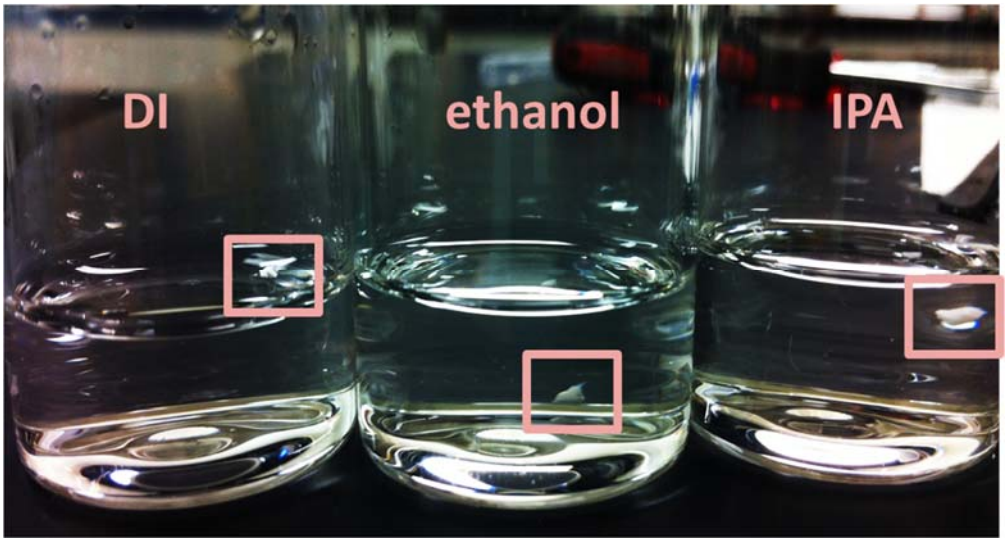

Figure 2.1.2. Clumps of BNNTs placed in three different liquids (DI, ethanol, IPA, from left to right) to show an initial indication of the usefulness of each for making stable and homogenous solutions of BNNTs. Notice that the BNNTs stay on top of the DI while they sink directly in to the ethanol.

In order to create homogeneous and stable suspensions of BNNTs, the vials in figure 2.1.2 are bath-sonicated at 70 W for 30 minutes. This procedure does not do anything for the water sample where the BNNT clump sticks to the side of the glass. The isopropyl alcohol sample initially creates a homogeneous solution, but it is not stable for more than a few hours while the ethanol solutions are stable for months. Figure 2.1.3 shows further evidence of the homogeneity of the ethanol BNNT solutions; by shining a light through the solution and observing orange light on the other side it is possible to

conclude that Rayleigh scattering occurs, which is strong evidence of nanosized particles individually suspended in the solution.[138]

Figure 2.1.3. Photograph of a solution of BNNTs in ethanol showing the passing of light through the solution to show its homogeneous nature. The orange color of the light is evidence of Rayleigh scattering through homogeneous nanoparticles.

Another method for determining the stability of particles in liquids is through electrophoresis zeta potential measurements.[139] Though these types of measurements are most reliable for spherical particles, some information can be gained from comparative studies of non-spherical particles in liquids. Figure 2.1.4 shows a plot of consecutive zeta potential measurements for BNNTs in ethanol and isopropyl alcohol. Water is not included since the BNNTs do not immerse. Li et al. recently published zeta potential results of functionalized BNNTs that were at the most -15 mV.[140] Our results show much higher zeta potential for BNNTs sonicated in ethanol, as high as -25 mV. The results also show that the potential has an upward trend for consecutive measurements showing that

the nanotubes align and stabilize with applied potential. No such trend is seen for the BNNTs in isopropyl alcohol.

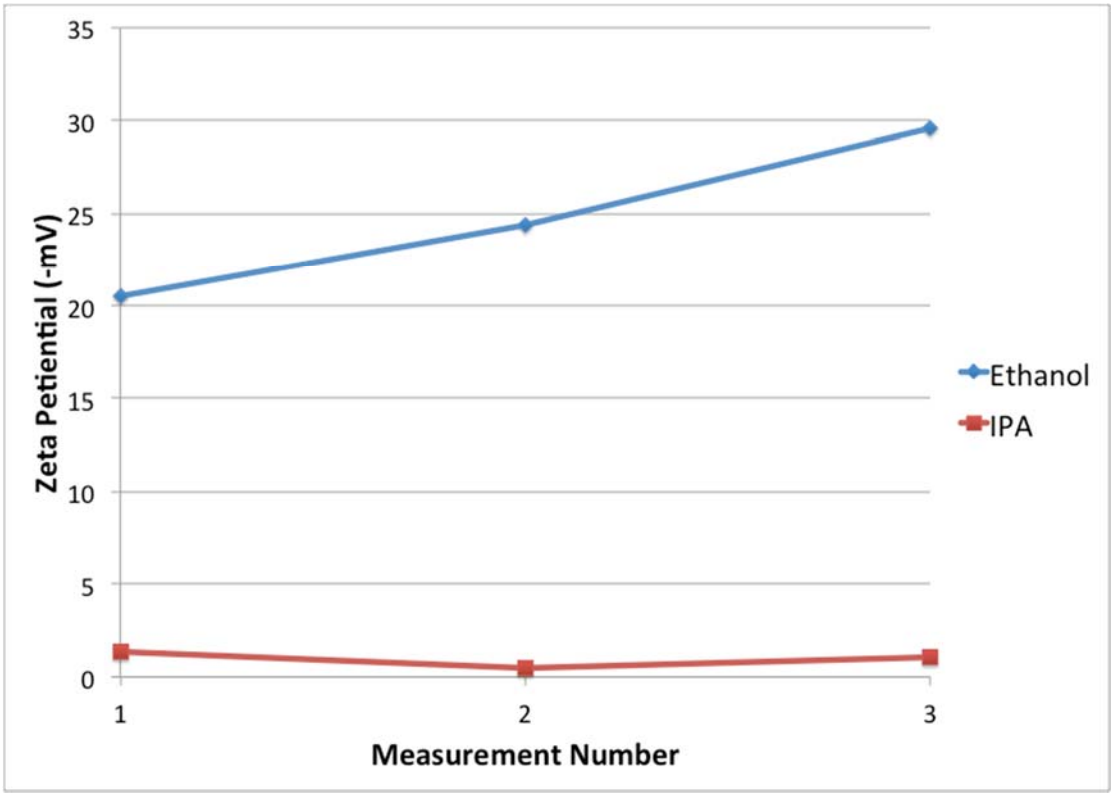

Figure 2.1.4. Zeta potential results for BNNTs in ethanol and isopropyl alcohol. The ethanol solutions show greater stability that increases with measurement iterations because of alignment in the solution.

Once stable solutions have been made the next step is to deposit the nanotubes on to a desired substrate. Here we are working with extremely thin silicon nitride membranes in order to perform TEM analysis of the resulting depositions. Figure 2.1.5 shows a typical HRTEM image of two individual BNNTs. The periodic dark contrast areas along the walls of the tube are caused by the Bragg condition from the helical nature of the tubes which are well documented for pristine BNNTs.[141] The bottom tube shows an example of a tube that has flattened into a ribbon and proves that there is no contrast or defects in the sheets themselves.

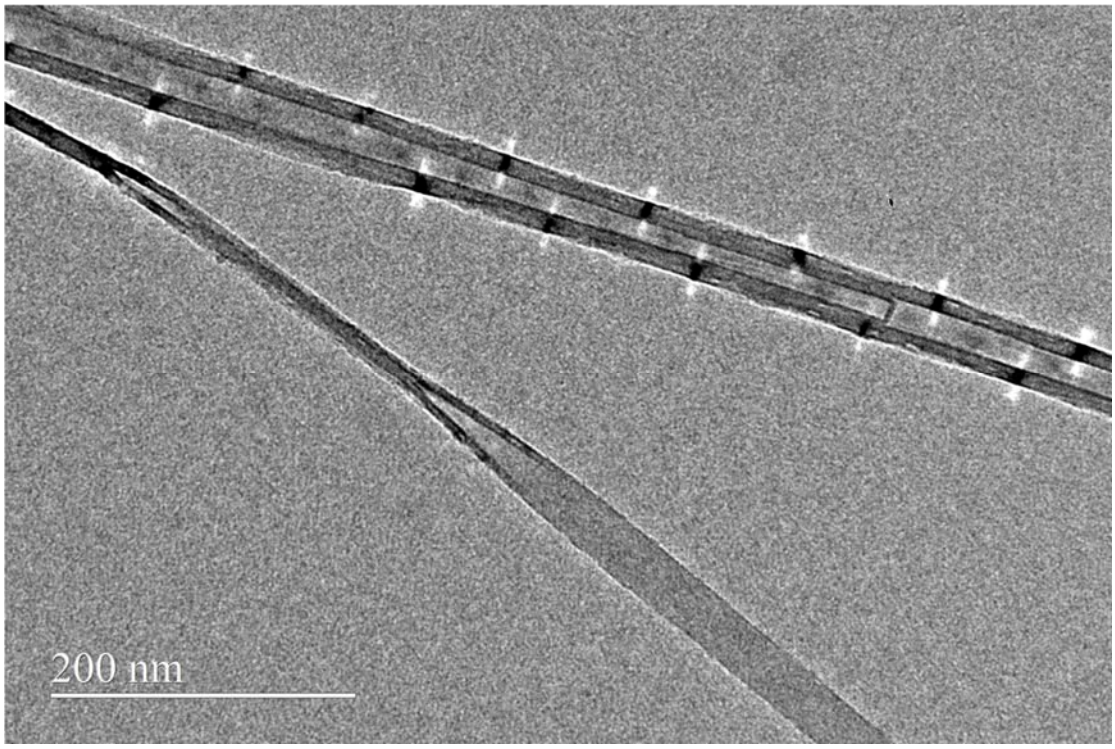

Figure 2.1.5. HRTEM image of individual BNNTs deposited via ethanol onto a 50 nm thick SiN membrane.

Depending on the desired density of the deposited BNNTs, the solutions can be spin-cast or drop cast on to the substrates. Alternatively, since the solutions are very stable and keep the tubes from bundling it is possible to get high density and well-dispersed depositions by leaving substrates in solutions for multiple days. Figure 2.1.6 shows a substrate that was left in a BNNT ethanol solution for 3 days and then lifted out and dried with nitrogen gas. The image shows mostly straight, clean and well-dispersed tubes and very little bundling.

Figure 2.1.6. LRTEM image of BNNTs deposited by leaving the sample in an ethanol solution for 3 days. The tubes are well dispersed and show very little bundling.

Another concern when making solutions with the aid of sonication is the damage that this causes the nanotubes.[142] In comparison to many sonication procedures,[143] the one developed here is very gentle, requiring only 30 minutes in a 70 W bath, meaning low power density since the bath is 10x10 cm^2. Figure 2.1.7 shows that the BNNTs are still long and undamaged even after the sonication procedure.

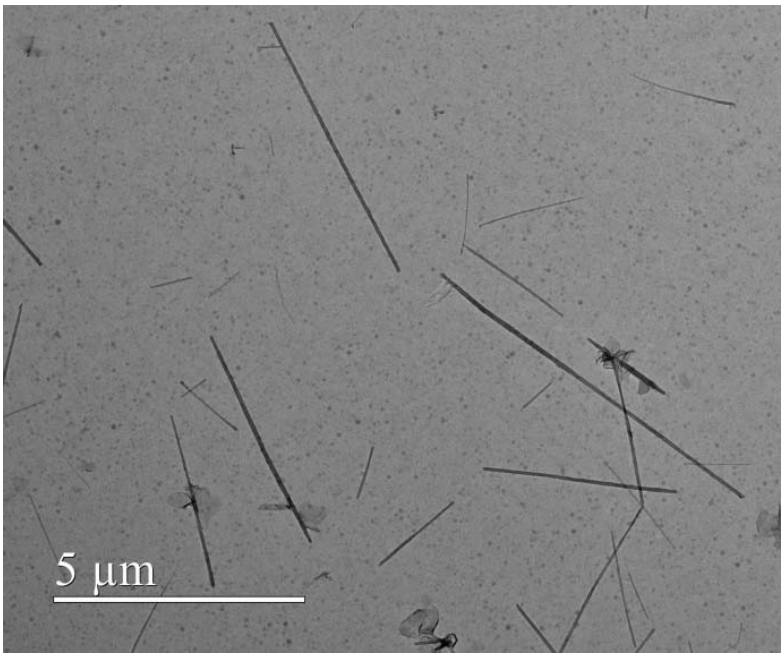

Figure 2.1.7. TEM images showing long and undamaged BNNTs even after the sonication procedure.

Though some previous work with BNNTs has used ethanol as part of the processing,[144] this is the first time that solutions of BNNTs in simple solvents have been characterized. The results provide strong evidence that ethanol is a stable and clean option for suspending, storing, and depositing BNNTs.

2.2 MWCNTs

The initial goal of this research was to find a method to cleanly and reliably separate out individual MWCNTs from bulk powders in order to perform thermal and electrical characterization experiments. This goal was so successfully reached that a complete study on the developed method was performed. Initially, the Cumings group used isopropyl alcohol (IPA) to suspend MWCNTs in solution and then used spin-casting

of the solution to deposit tubes on to SiN membranes for TEM experiments.[15] The method produces clean depositions without altering the nanotube properties. However, the suspensions are not stable for more than one deposition and it is very difficult to achieve individual nanotube depositions.

Within the MWCNT community there are a few different approaches used to solve this problem. Most of these also include suspending the MWCNTs in solution and later depositing them on a test substrate. However, many of the solutions end up changing the properties of the MWCNTs, making them ineffective for use in research of fundamental properties.[145, 146] Of course researchers have tried to develop methods to clean the altered MWCNTs and substrates after the fact,[147, 148] but it is a better strategy to keep the nanotubes contamination-free to begin with.

Since CNTs are hydrophobic they cannot be suspended in most solvents without significant bundling. One option is to alter the CNTs themselves to make them more receptive to suspension, such as oxidation,[149] functionalization,[150] or molecular wrapping.[126] However, this approach again requires work after the deposition in order to return the tubes to their pristine condition. Significant effort has been put into developing surfactants that effectively keep CNTs nicely separated in a solution and there has been some progress, but many researchers have as of the last five years settled with solutions that are less than ideal. Common approaches start with polar organic solvents such as *N*-methylpyrrolidene (NMP) and dimethylformamide (DMF), however these can be toxic, dangerous and generally do not produce suspensions with a stable shelf-life.[124, 151, 152]

More common are surfactant molecules that can be added to water to bridge the hydrophobic-hydrophilic gap. These molecules can be nonionic, anionic, cationic, or zwitterionic. The literature has examples of each,[128, 153] but anionic have been the most successful.[130, 131] Of these, sodium dodecyl sulphate (SDS) is the one that appears most commonly in literature. It has become the standard and point of reference for research with MWCNTs despite many drawbacks.

The project described here introduces and optimizes a new surfactant that outperforms SDS in many of the most important metrics including cleanliness and stability. This new surfactant, ammonium laurate (AL), has similar structure to SDS, including the same length hydrocarbon tail, but it has a different ionic end group and cation (See figure 2.2.1.). However, the change in head group and change from ammonia to sodium gives drastically different results for the interaction between the tubes and the deposition onto (3-aminopropyl)triethoxysilane (APTES) prepared substrates.

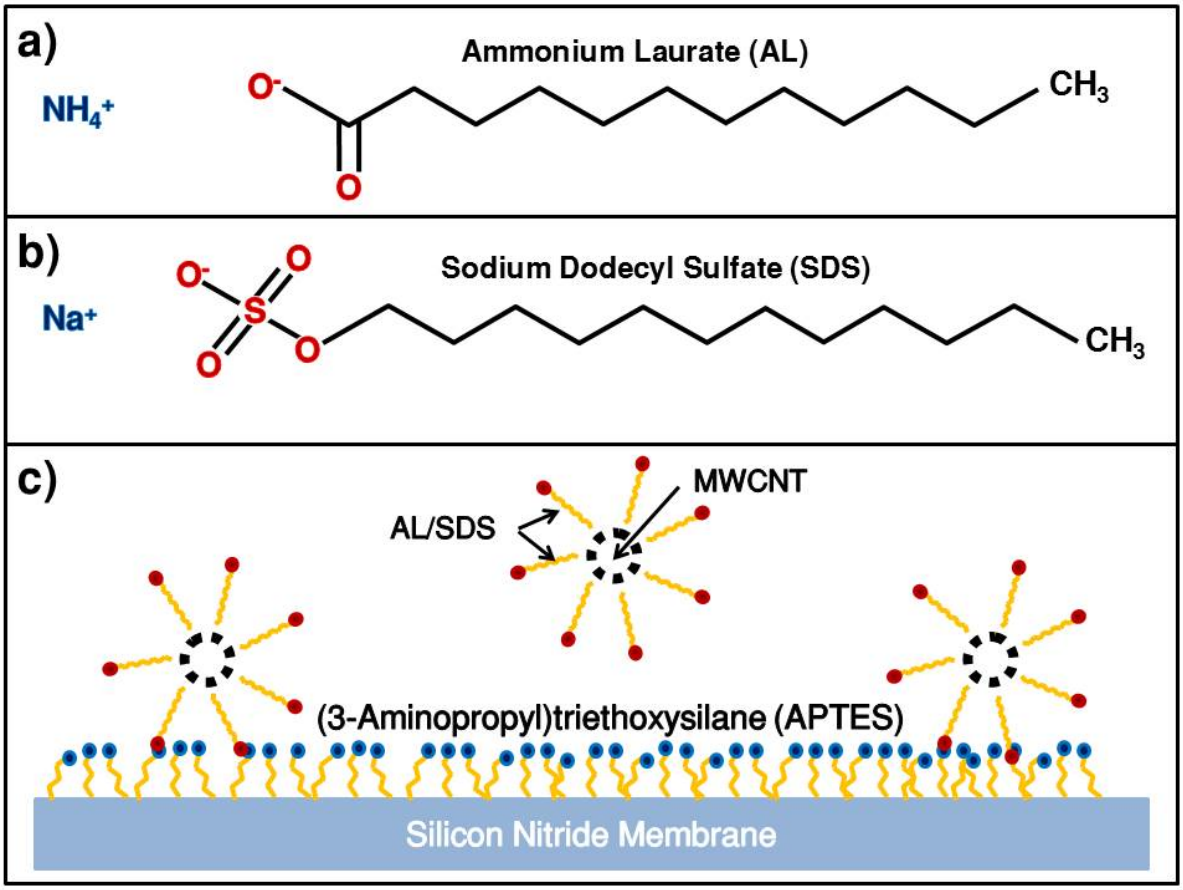

Figure 2.2.1. Schematic of the molecular structure of surfactant system used to suspend and deposit MWCNTs. (a) AL surfactant, (b) SDS and (c) MWCNTs encapsulated in surfactant micelles and their attraction to APTES treated silicon nitride membrane.

In order to improve the results of depositions, the first step is to begin with clean, hydrophilic sample surfaces. The substrates used for all of these tests are silicon nitride membranes, which are often hydrophobic as/prepared. One method that works well to make the surface hydrophilic is to perform an oxygen cleaning plasma treatment prior to nanotube deposition. This cleans the membranes well and gives good enough results in some cases, but if high nanotube density with good adhesion is desired, the surface can be optimized instead with a self-assembled monolayer (SAM).[154] We chose to functionalize using the silane molecule APTES. I did this with a simple evaporation from liquid in a homemade vacuum bell jar and a mechanical pump. Figure 2.2.2 shows the

evaporation set-up and the structure of APTES, the silane molecule that was used. After evaporation for 7 minutes, the membranes are baked for 30 minutes at 120 C, dipped in 37% hydrochloric acid for 5 seconds, to protonate the amino end group, and then transferred to DI water for 1 minute prior to being placed in the nanotubes solutions.

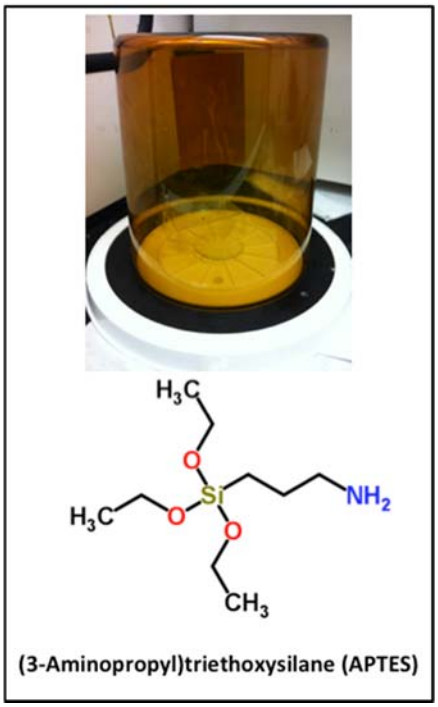

Figure 2.2.2. Schematic showing the APTES evaporation jar and the structure of the molecule. The SAM procedure increases the adhesion between the substrate and the MWCNTs.

Many combinations of concentrations and ionic constituents were compared in this study in order to ensure that the solutions were optimized. The main comparisons were made between SDS and AL ranging in surfactant concentration from 0.5% to 2.0%. The surfactants were prepared in 20 mL glass vials. The appropriate amounts of powder surfactant were weighed out, either SDS (Sigma Aldrich ReagentPlus, >98.5% (GC)) or dodecanoic acid ((>99% (GC/titration)) and then 10 mL of deionized (DI) water was added. In the case of AL, ammonium hydroxide was added dropwise until the pH reached

11 in order to convert the lauric acid to AL. The next step is to add MWCNT powder. Arc-discharge tubes purchased from Sigma-Aldrich (in unprocessed boule form) were used for all studies.[155] These tubes are very pure as confirmed by Thermogravimetric analysis (TGA) data from the supplier. Manually crushed fibers from the boule center are added to the solutions and then bath-sonicated at low power (70 W) for 20 minutes in order to form an even solution. However, in order to separate the bundles of MWCNTs in the solution, more aggressive agitation is required. The solutions are probe-sonicated (Sonics Vibra Cell VC 505) for 2 minutes at 100 W with a 13 mm circular tip, at intervals of 1 second on and 1 second off. This separation procedure is much gentler than many used to suspend MWCNTs in solution where hours of sonication are used.[143, 156] As an aside, we performed longer probe sonication just to test how our nanotubes would be affected by this. Figure 2.2.3 shows the results of longer probe sonication. The MWCNTs are shortened and have damaged ends, and the resulting depositions do not show any improvements in terms of bundling or cleanliness.

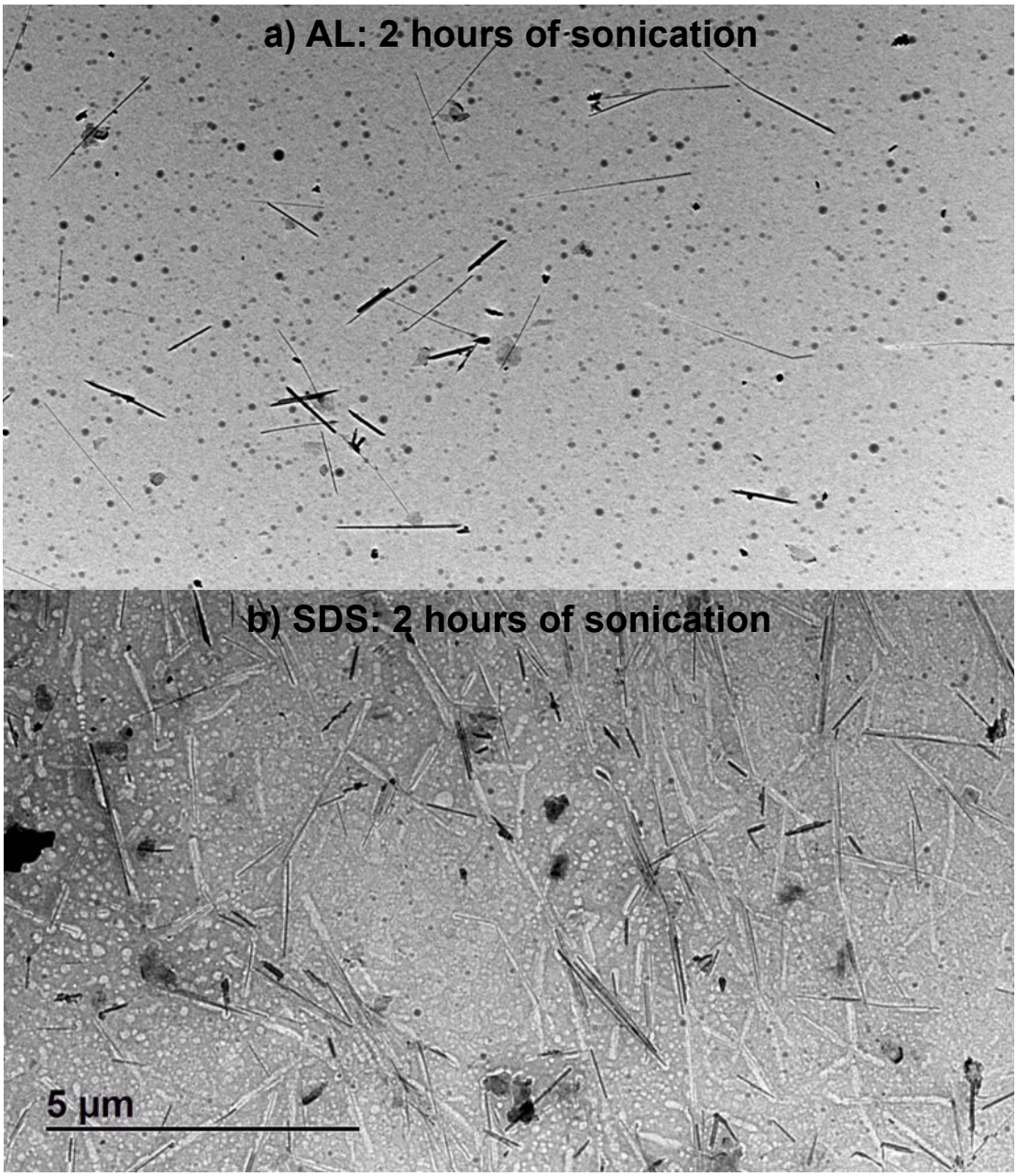

Figure 2.2.3. TEM images showing the result of extended (2 hours) probe sonication. a) is of an AL solution and b) is of an SDS solution. As compared to other images presented in this work which were all probe sonicated for 2 minutes, it is evident that the extended probe sonication does not change the cleanliness of the SDS deposition and additionally it damaged/shortens the MWCNTs.

After sonication the solutions are centrifuged at 1,000 g for 30 minutes to separate out the heavier unwanted carbon particles from the solution. The part of the solution that appears homogeneous is decanted by pipet to form the final solutions. Figure 2.2.4 shows the final solutions over time. On day 1 the higher surfactant concentration solutions show bubbling from the sonication and pouring process. The differences in MWCNT concentrations that are evident in the pictures is dependent on the amount of MWCNTs that remain in solution during the centrifugation process. It is evident from the darker colored solution that the higher concentration AL solutions retain the most MWCNTs.

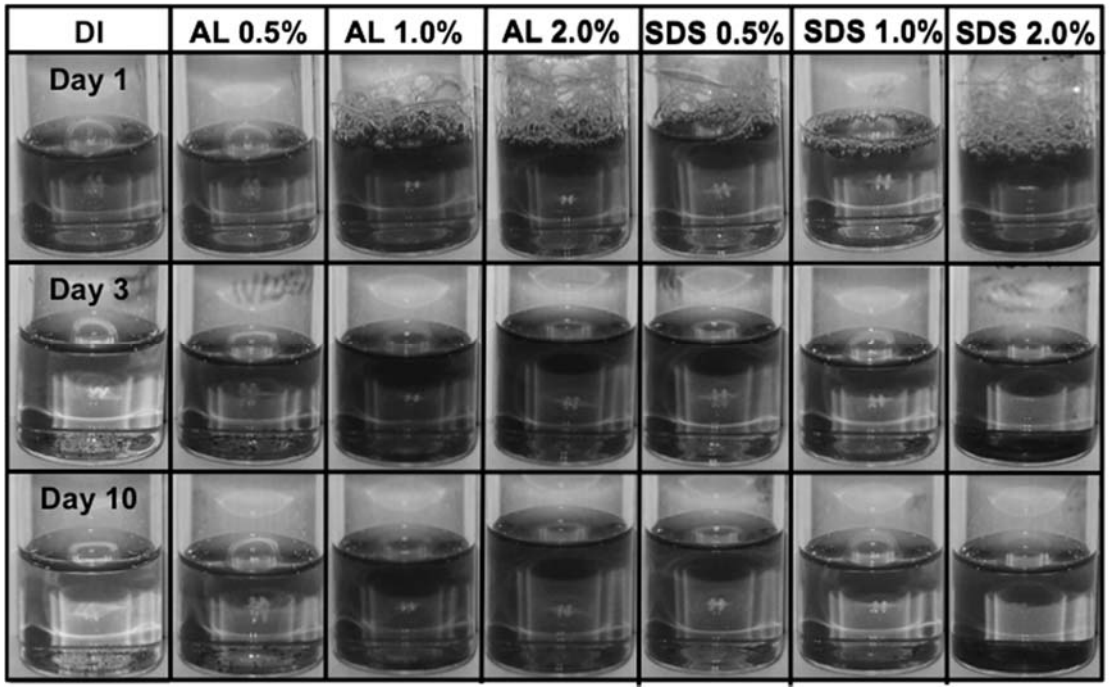

Figure 2.2.4. (a) Images of multiwalled carbon nanotubes (MWCNTs) in aqueous solutions. The first column shows MWCNTs in deionized water (DI) without any surfactant. The MWCNTs quickly drop out of solution without surfactant and can be seen at the bottom of the container. The second column shows a 0.5 wt.% solution of AL, at such a low concentration the MWCNTs are not stable and tend to drop out of the solution over time. The 1.0 and 2.0 wt.% AL are stable over the course of 10 days and they are also dark showing that less MWCNTs dropped out of solution during the centrifugation process. The 0.5 and 1.0 wt.% SDS solutions are also stable over the course of 10 days. The 2.0 wt.% SDS solution shows less stability than the lower concentrations.

Another metric that can be used to characterize the MWCNT retention in solution over time is optical absorbance. Measurements are performed using a Lambda 1050. This spectrometer has a photometric reproducibility of 0.00016 which gives error bars within the point markers in the figures. Figure 2.2.5 shows raw absorbance data for 1% surfactant concentration MWCNT solutions as well as for an AL solution without MWCNTs and a solution without surfactant. These measurements were performed by Brendan Meany. The latter two absorbance lines can be seen at the bottom of the plot, just slightly above 0 for all wavelengths from 300 to 800 nm. For the surfactant solutions with MWCNTs, the lines for day 1 are higher for both solutions, but the drop per day is greater for SDS, meaning that more tubes fall out of suspension. In addition, the overall absorbance value is higher for AL than for SDS for all days showing that AL solutions hold more tubes.

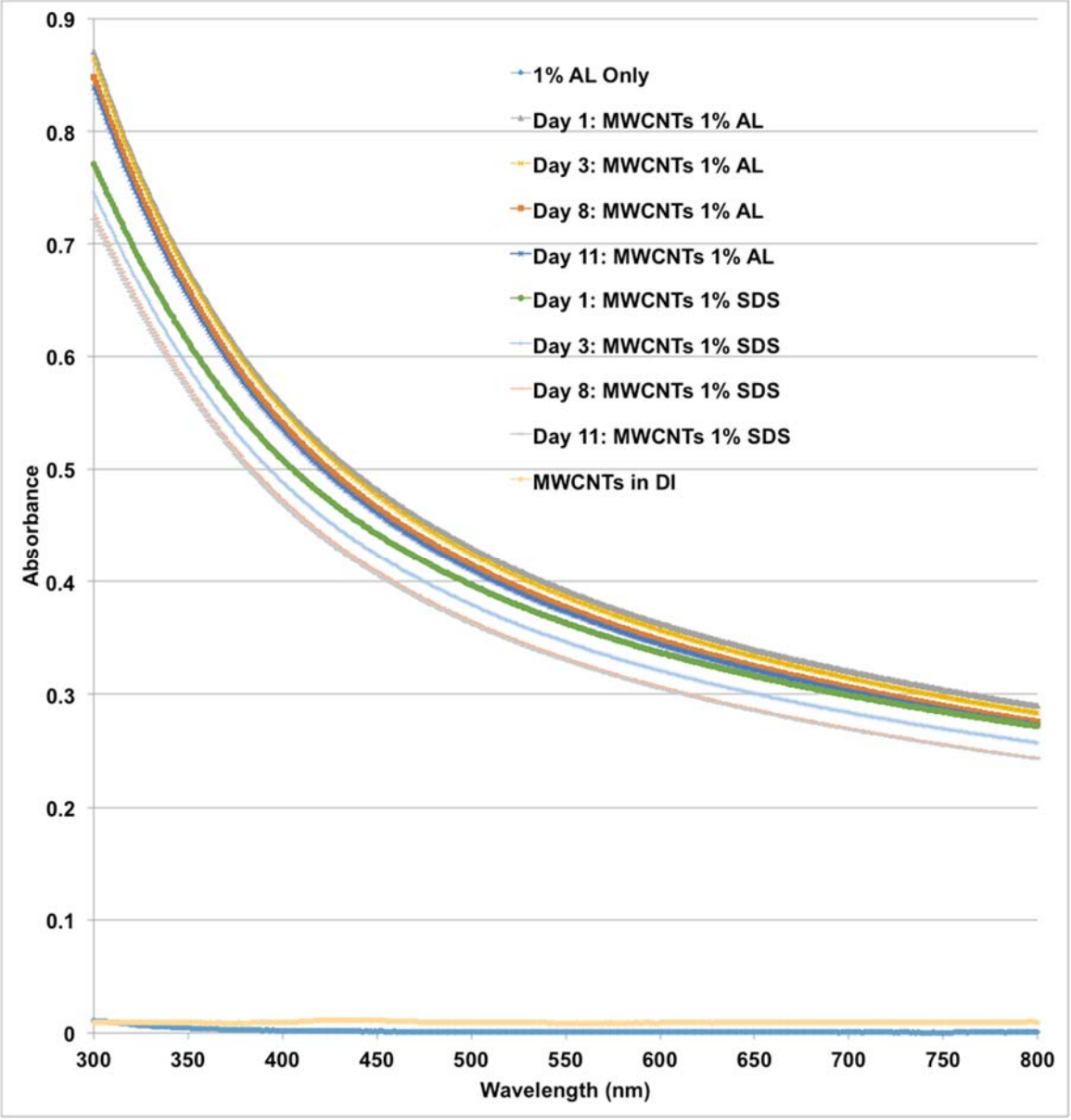

Figure 2.2.5. Raw absorbance data from 300 to 800 nm for the MWCNT surfactant solutions over time including the baseline absorbance of a solution without MWCNTs and a solution of MWCNTs in DI water. Credit: Brendan Meany

The absorbance data is shown in a simplified manner in Figure 2.2.6 that makes it evident that the AL solutions are much more stable than the SDS solutions over the course of 11 days. The figure shows the average absorption value from 300 nm to 800 nm as a percentage of the day 1 percentage for each solution.

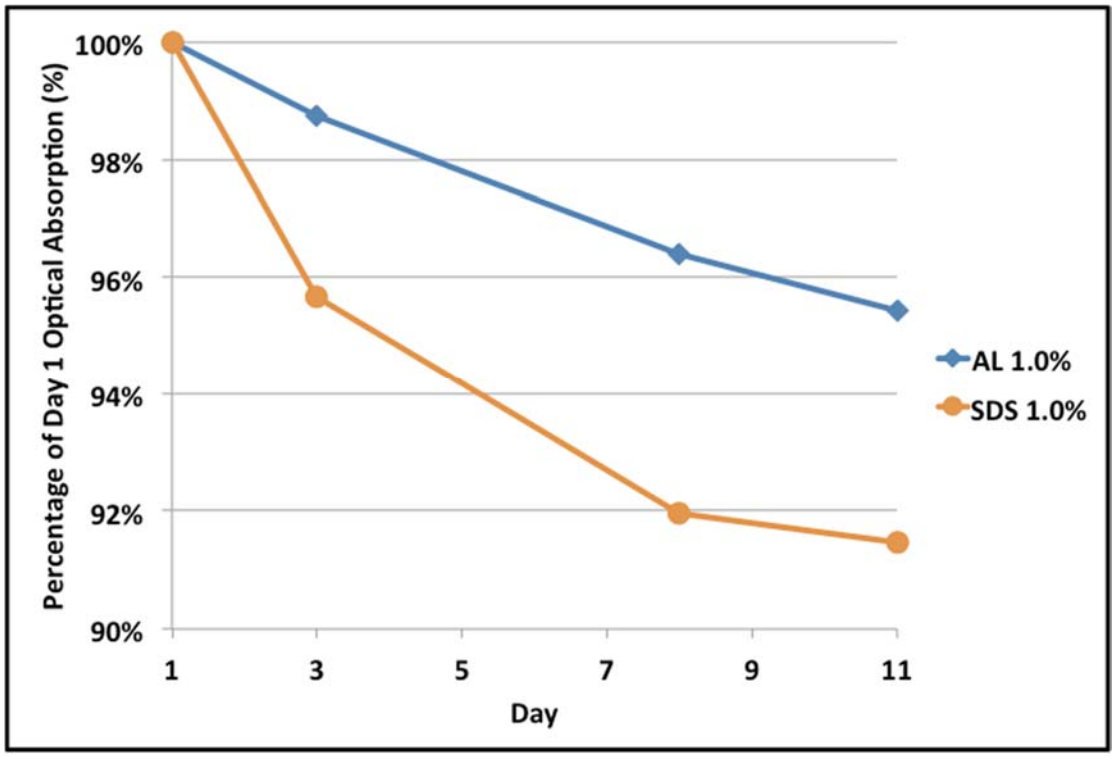

Figure 2.2.6. Chart showing the drop in optical absorption of a different set of 1.0 wt.% solutions over 11 days. The data points are the average absorption from wavelengths of 300 nm to 800 nm as compared to the absorption on the day that the solutions were made. On Day 1, the absorbance for AL is 8% higher than SDS, but this chart shows the absorbance normalized to Day 1, for ease of comparison. Credit: Brendan Meany

The most important and compelling evidence for AL over SDS is TEM images of the deposited MWCNTs, which can be seen in Figure 2.2.7. The images on the left are of AL and those on the right are of SDS. Those on the top are of a lower magnification than those at the bottom. For both magnifications it is evident that the AL deposition is cleaner than the SDS deposition. The SDS has reformed salts on the substrate. Another important observation is that the AL depositions shows more individual, unbundled MWCNTs and less unwanted carbon particles.

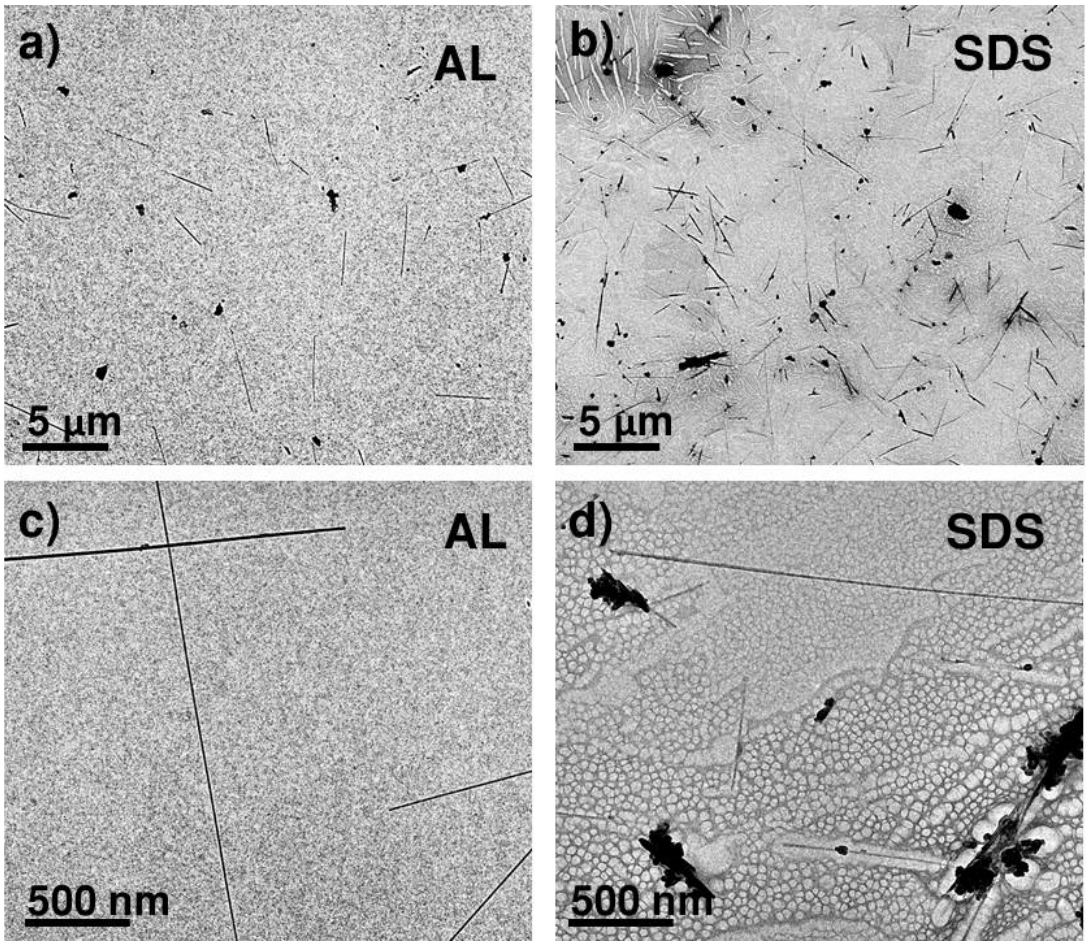

Figure 2.2.7. Typical TEM images at different magnifications of MWCNTs deposited on APTES treated SiN membranes. (a) and (c) are of MWCNTs that have been suspended in 1.0 wt.% AL prior to deposition. (b) and (d) are of MWCNTs that have been suspended in 1.0 wt.% SDS prior to deposition. The AL depositions do not show any surfactant residue and the MWCNTs are deposited individually without much bundling. The SDS depositions on the other hand show surfactant residue and there is notable presence of unwanted non-nanotube carbon deposits alongside the MWCNTs.

As a point of comparison, figure 2.2.8 is provided to show what the pristine, unprocessed SiN membranes look like. TEM images used for all MWCNT images were captured using a JEOL JEM 2100 TEM at 200 kV. This microscope has a point resolution of 0.23 nm. All substrates used for MWCNT experiments were 100 nm thick SiN membranes.

Figure 2.2.8. Control TEM images at different magnifications of a pristine SiN membrane prior to any processing.

In order to confirm that the residue shown in the TEM images of deposited SDS MWCNTS in Figure 2.2.7 is indeed reformed surfactant, atomic force microscope (AFM) measurements were performed to characterize the heights of the residue. It is known from literature that anhydrous SDS has a double layer structure with a bilayer lamellar thickness of approximately 3.9 nm depending on the hydration.[157] The AFM results (see Figure 2.2.9.) show stepwise height changes that are indeed about 4 nm, which gives evidence that the TEM images are showing SDS structures along with the MWCNTs. The maximum height difference that was found was 16 nm indicating 4 bilayers of SDS on the substrate. As a comparison, the substrate that was left in an AL solution, shows no stepwise height differences, giving evidence that there is no layer of surfactant reformed on the substrate after it is taken out of the solution.

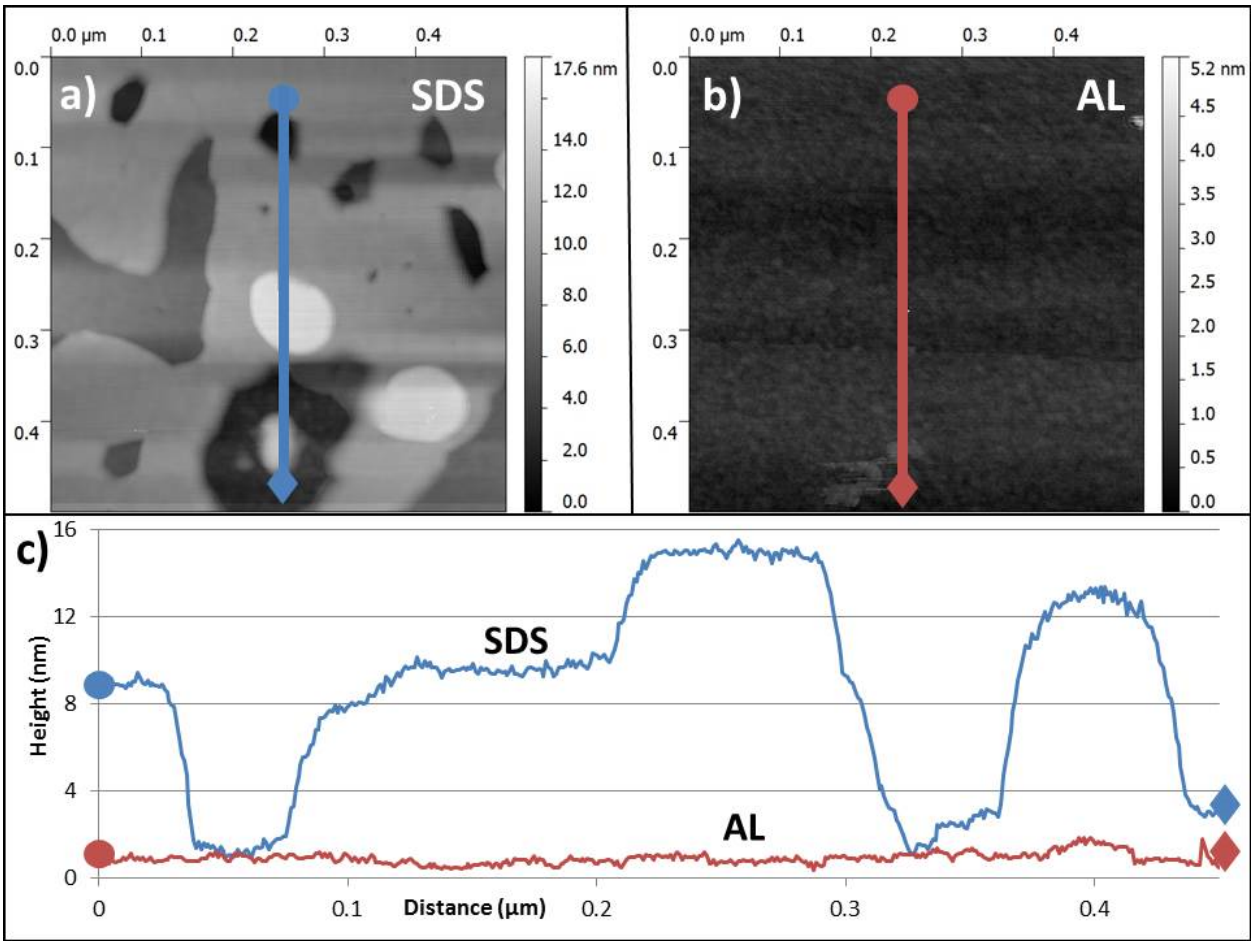

Figure 2.2.9. AFM images SDS (a) and AL (b) deposited on silicon chips after APTES treatment (without CNTs). SDS shows inhomogeneous layering of the micelles throughout the sample area. AL shows a comparatively smooth surface. (c) Line height profiles of the deposited surfactants show that the height difference between areas on the SDS sample differ in steps of about 4 nm. It is known that the bilayer thickness of SDS is approximately 4 nm, therefore a maximum height of 16 nm indicates up to 4 bilayers of SDS.

Cleaning membranes with DI water helps to remove a large percentage of the SDS residue. However, the removal of the surfactant still leaves behind unwanted carbon particles indicated with white arrows in Figure 2.2.10. There is also still some residue of the surfactant even when the majority of the micelles are removed as can be seen by the black arrows in the figure. This leads to the conclusion that SDS depositions can be improved by an additional cleaning step, but that the resulting deposits are still far from

as clean and pristine as those seen in Figure 2.2.7a) and c) deposited through AL without any extra cleaning.

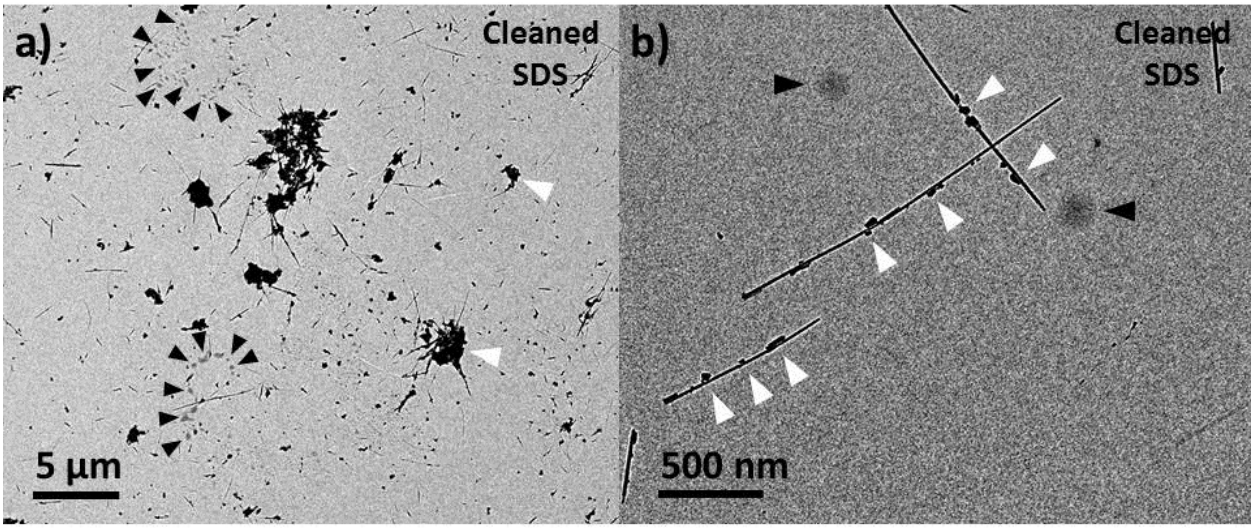

Figure 2.2.10. TEM images at different magnifications of MWCNTs deposited from 1.0 wt.% SDS solution onto APTES treated SiN membranes. After deposition, the membranes were cleaned by deionized water to remove the surfactant residue. Most, but not all of the SDS residue was removed through this process, and unwanted carbon onions (indicated by white arrows) are still visible in the high resolution image (b). In both images, black arrows indicate examples of surfactant residue and white arrows indicate carbon contamination (mostly fullerene onions).

Raman spectroscopy was used to quantify the amount of ordered pristine MWCNTs versus unwanted disordered carbon particles in the different depositions. Raman spectra have long been used to characterize the crystallinity of carbon structures. A common metric is the ratio of the D-band intensity around 1350 cm^{-1} and G-band intensity around 1582 cm^{-1}.[158] Typical spectra for AL and SDS depositions are shown in Figure 2.2.11, but the characterization was done with many spectra over a multiple locations on the sample. The spectra shown in this figure were obtained with the help of Jeremy Ticey. Roughly the D-band signifies defects and the G-band signifies ordered layers so a high I_D/I_G value signifies high disorder and many defects. For my depositions,

I found that the average I_D/I_G was 0.65 for depositions made without surfactant in DI water. For SDS the value was 0.27 and for AL 0.16 meaning that the resulting depositions with AL are more crystalline than those with SDS. The reason for this improvement may have to do with the shape of the micelles in the different surfactants. SDS has more spherical micelles, meaning that it may be more effective at suspending spherical carbon particles while the oval AL particles may more effectively suspend tubes.[159]

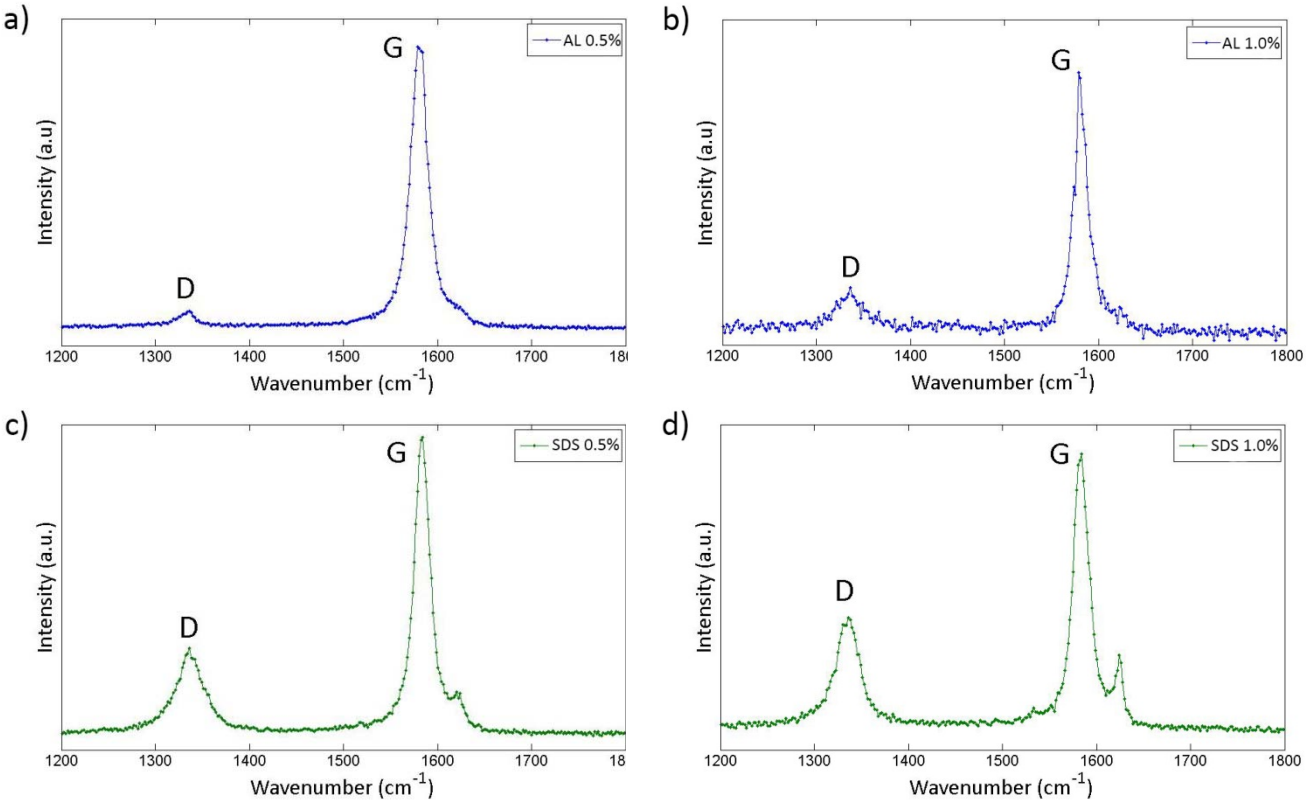

Figure 2.2.11. Raman spectra of MWCNTs prepared with varying concentrations of ammonium laurate (a,b) and sodium dodecyl sulfate (c,d). Spectra were taken on silicon nitride TEM membranes using a 633nm He-Ne laser at room temperature. Credit: Jeremy Ticey

The next part will review the results of combining a variety of different salts and lipids in order to confirm that the combination of lauric acid and ammonium hydroxide indeed is the optimal surfactant for suspending and depositing MWCNTs. The results are outlined in Table 2.2.1 and Figure 2.2.12. The conclusion of these tests is that SDS reforms into thick salt residue even when combined with ammonium hydroxide or sodium hydroxide to bring the pH up to 11. Lauric acid with sodium hydroxide also shows residue formation.

Sample	Base salt/lipid	Added base	pH	What happens?	How does it look?
1	None	None	7	Solution is not stable, cannot centrifuge without NTs dropping out of the solution	Samples are clean, but there are mostly clumps of graphitic particles, not individual nanotubes
2	Sodium dodecyl sulfate	None	4.5	Stability and dispersion are good, but the samples are very dirty	Layers of SDS are easily seen all over the membranes even where there are no tubes or particles
3	Sodium dodecyl sulfate	Ammonium hydroxide	11	Stability similar to plain SDS, lower dispersion density	Lots of residue on the membrane, but it looks different from plain SDS, rather than forming layers evenly across the membrane there are clumps of thick residue
4	Sodium dodecyl sulfate	Sodium hydroxide	11	Very similar both in stability and dispersion to plain SDS	Residue almost identical to plain SDS
5	Lauric Acid	None		Doesn't dissolve in water	Don't have images because it doesn't dissolve so you can't get NTs dissolved in there
6	Lauric Acid	Ammonium hydroxide	11	Stability and dispersion very good, no visible residue	No visible residue, lots of individual NTs, not much junk particles
7	Lauric Acid	Sodium hydroxide	11	Very difficult to disperse, formed cloudy clumps until I probe sonicated	Very odd residue on the samples, pretty good single nanotube dispersion

Table 2.2.1. Description of the result of combining different ionic constituents to form surfactant suspended CNTs.

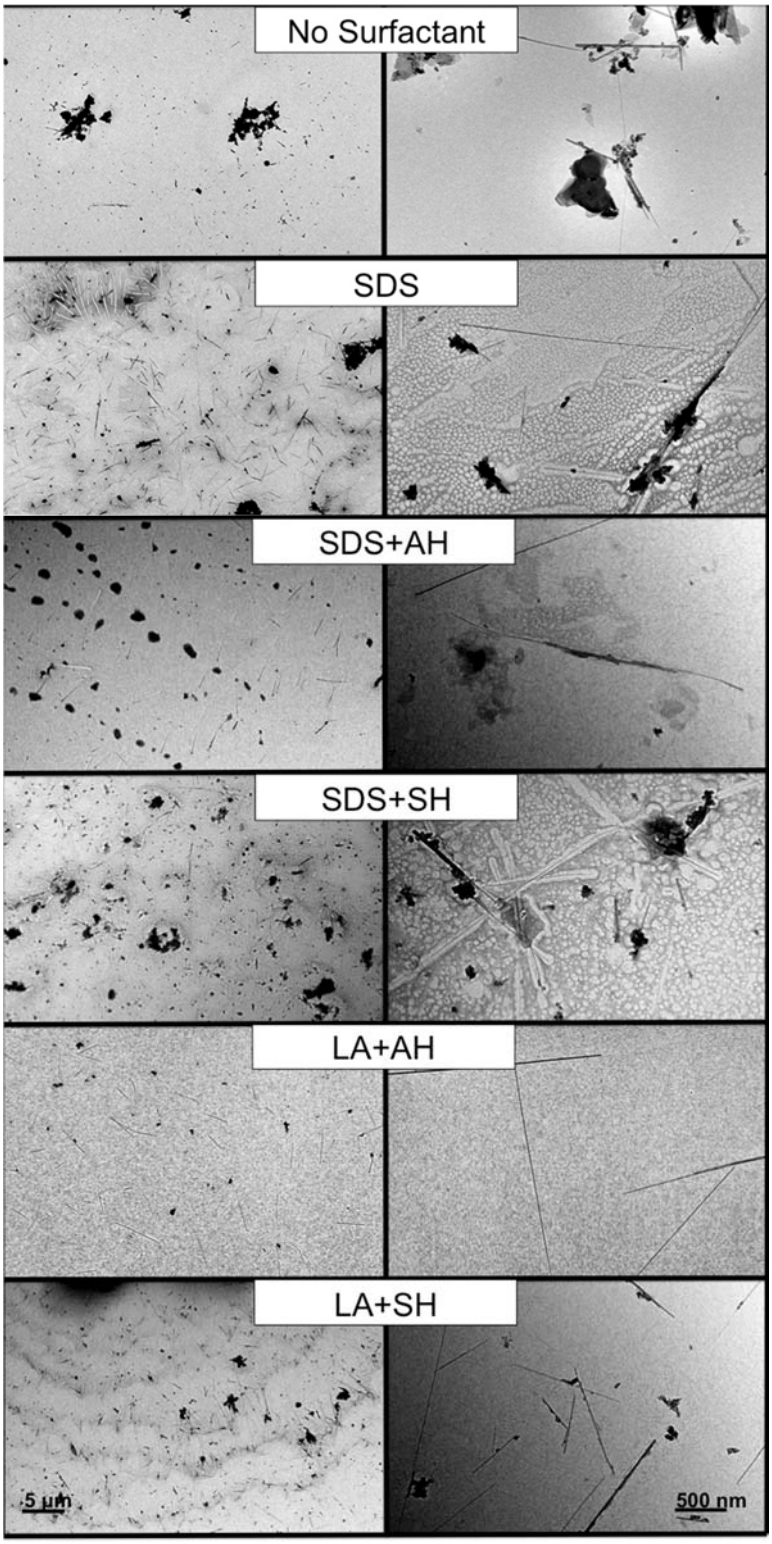

Figure 2.2.12. TEM images of CNTs deposited on SiN membranes after suspension in different combinations of surfactants. Images on the left are the same magnification and those on the right are the same magnification.

In order to investigate the behavior of the surfactant micelles in solution, electrophoresis zeta potential measurements were performed. Zeta potential measurements can give quantitative results for the stability of solutions with spherical particles. Here the particles are mostly cylindrical so the zeta potential values are only valuable in terms of comparison between the solutions presented here. That said, it is common to refer to zeta potential values in the literature even for nanotube studies. [128] The zeta potential value gives an indication of the charge between the particles and therefore the ability of the nanotubes to stay unbundled. A higher absolute value potential signifies a more stable solution. The pH of the solution can of course affect the value since it changes the amount of charges in the solution. Both SDS and AL were tested at different pH values in order to get a better understanding of the ionic behavior of the micelles. The results are shown in Figure 2.2.13. These and those in the following figure were obtained with the help of Zois Tsinas. The first thing that is clear is that the absolute value of the zeta potential is higher for AL at all pH values. For both solutions the trend is also that the zeta potential decreases with increasing pH. The change is more drastic for AL with more than a 50% reduction in potential from a pH of 9 to the working condition pH that was used in this study 11. It may seem as if it would be better to work with AL at lower pH to improve stability, but it is more important to make sure that the AL molecule is in an un-dissociated polar state without much ionic character so that it does not re-associate once the water is removed. Even at this lower zeta potential state, the stability of the AL far outperformed SDS at its highest zeta potential.

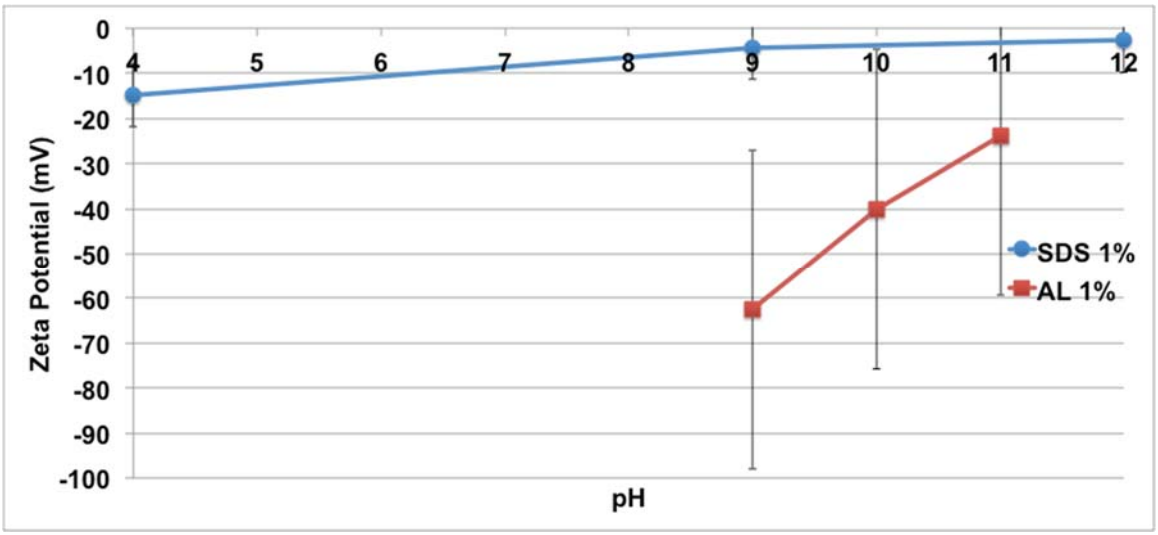

Figure 2.2.13. Results for measurements of zeta potential for surfactant solutions with different pH in order to look at the effect of pH on the measurements and to explore the behavior of the ionic constituents of the surfactants with applied potential. These solutions do not contain any MWCNTs. The values are the averages for 3 consecutive runs of the same solutions. The lauric acid requires a pH of 9 to dissolve so lower values are not shown. Typically SDS is used at a pH around 4; this is the condition when no additional acid is added. Credit: Zois Tsinas

Another thing to keep in mind when performing these measurements on ionic solutions is that the repeated applied electrophpresis potential leads to ordering of the micelles in the solution which increases the resulting measurement value. The values in Figure 2.2.13 are an average over the 3 consecutive runs that can be seen in Figure 2.2.14. Here it is also evident that the change to the AL solutions is greater with repeated measurements meaning that those solutions have a stronger tendency toward aligning stably in solution.

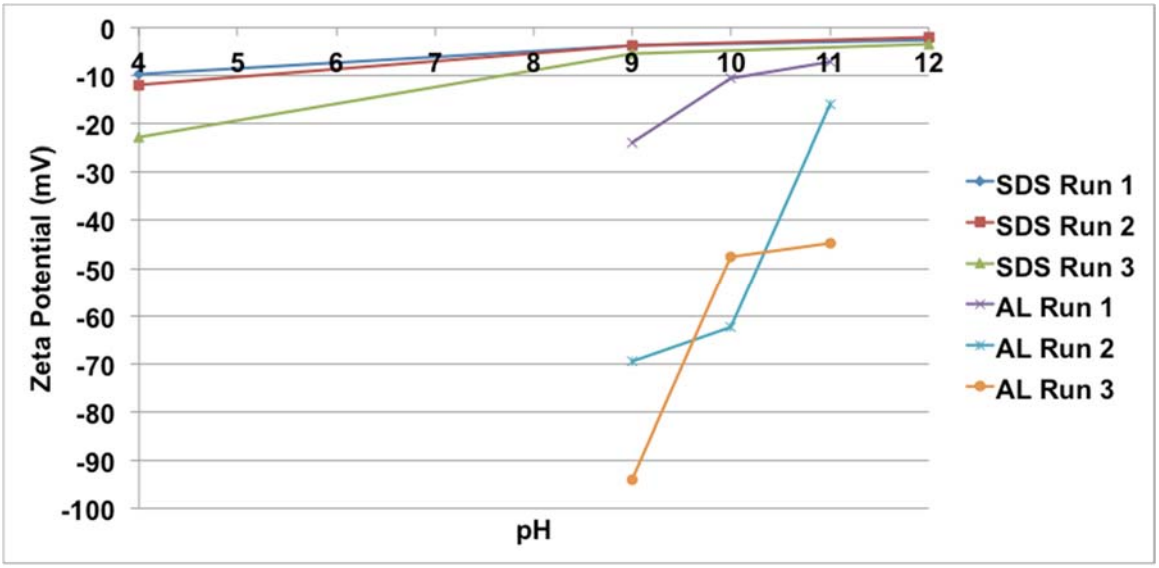

Figure 2.2.14. Results for measurements of zeta potential for surfactant solutions with different pH values for the 3 consecutive runs that were averaged in Figure 2.2.13. Credit: Zois Tsinas

The overall conclusion from this work is that AL outperforms SDS in all of the tested metrics; most significantly, in cleanliness, stability, and selectivity. An important implication of this work is that SDS, which is so extensively used in CNT research, is by far, not the best solution. While we did explore and present a few other combinations of surfactant molecules, there are endless other possibilities and perhaps this research can motivate continued efforts to optimize surfactants for CNT solution processing.

2.3. SWCNTs

AL has proven to be a unique and worthwhile surfactant for single-walled carbon nanotubes (SWCNTs) as well. TEM mages of SWCNTs deposited using AL on to carbon grids can be seen in Figure 2.3.1. SWCNTs are as the name suggests carbon nanotubes with just one sheet of carbon atoms rolled in to a tube. Their properties strongly depend on their chirality and diameter.[160] As with MWCNTs, the results of our study show that

AL solutions of SWCNTs are very stable. The advantage of characterizing surfactant solutions with SWCNTs is that there are multiple characterization methods that are more valuable for SWCNTs compared to MWCNTs. These include absorbance, photoluminescence, and low voltage SEM charge contrast imaging.[161, 162]

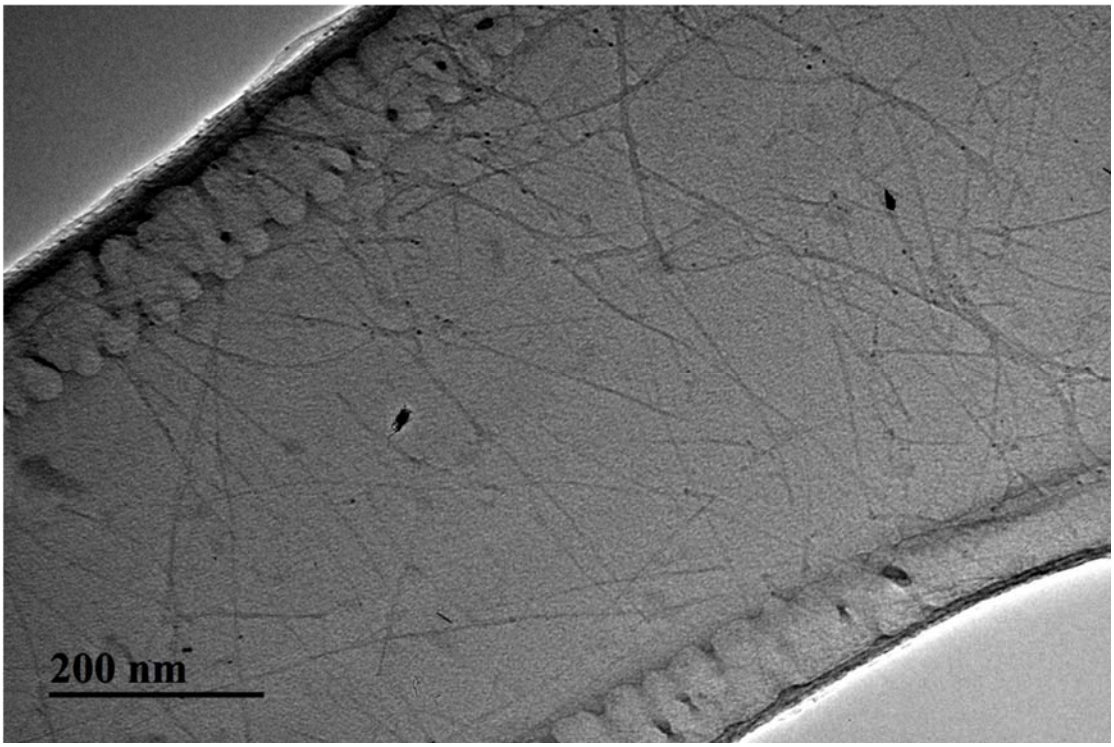

Figure 2.3.1. TEM image of SWCNTs deposited through AL solution on to carbon grids.

For absorbance measurements of MWCNTs it is possible to look at the average value of the absorbance over a certain range to get general information about the concentration of MWCNTs in the solution, however for SWCNTs, absorbance values give information about the chirality and diameter of the SWCNTs suspended in the solution.[160] The most relevant areas to look at are wavelengths from 400 nm to 1400 nm. These measurements were performed by Brendan Meany. Figure 2.3.2 shows the results of measurements that were performed for SWCNT solutions with AL and SDS with

different acids to increase the pH up to the same level as AL. The reason for this is that it is well known that the results of absorbance measurements are pH dependent, with higher pH giving more pronounced optical absorbance peaks.[163] Our results show the same trend, which is why only solutions with a pH of 10 were compared. When looking at those results it is evident that the AL solution more effective at suspending SWCNT compared to SDS, but the effect is much more pronounced at the larger wavelengths, meaning larger diameter SWCNTs.

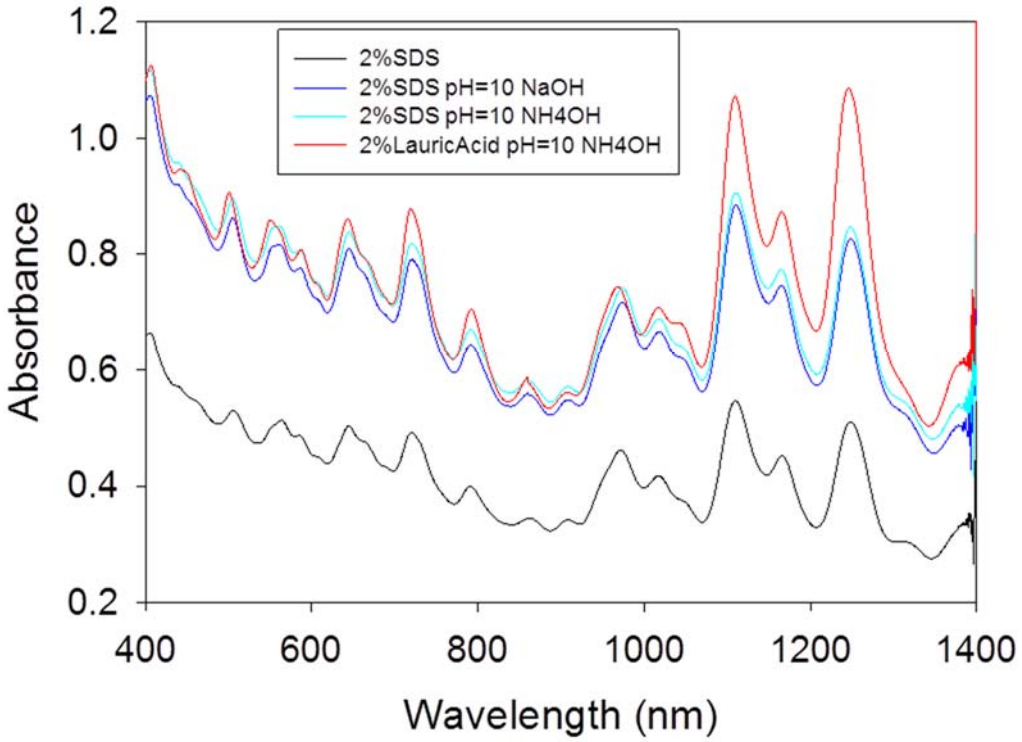

Figure 2.3.2. Absorbance measurement results for SWCNT solutions of different surfactants. It is known that pH affects absorbance results so only those with the same pH should be used for analysis. It can clearly be seen that the AL solution has higher absorbance compared to SDS, but the effect is more pronounced at greater wavelengths, which correspond to larger diameter SWCNTs. Credit: Brendan Meany

To further investigate the diameters and chiralities of the SWCNTs in the solutions, PL measurements are performed. It is well documented which combinations of

emission and excitation wavelengths that signify certain chiralities and diameters.[164, 165] Figure 2.3.3 shows the result of the measurement of the SWCNT surfactant solutions in their typical pH working conditions because the results of the higher pH SDS solutions showed that these solutions were not stable enough to give clear results. Note that the legends show different values for the different solutions, with the AL solution having higher values, perhaps related to the higher pH. What is clear is that each solution has a difference tendency towards which chirality SWCNTs are more prevalent in the solutions. In SDS, the (6,5) chirality with 0.757 nm diameter is most prevalent while in AL the (8,4) chirality with 0.840 nm diameter is most prevalent. When comparing the two results it is also evident that AL has a much stronger percentage of (7,6) and (9,4) chiralities with 0.895 nm and 0.916 nm diameters respectively. Just like the optical absorbance results, these show that AL solutions are most successful at suspending large diameter SWCNTs. There have been many recent studies which focus on finding ways to separate SWCNTs of certain chiralities and sizes and AL may be a valuable aid in achieving these types of result.[166, 167, 168]

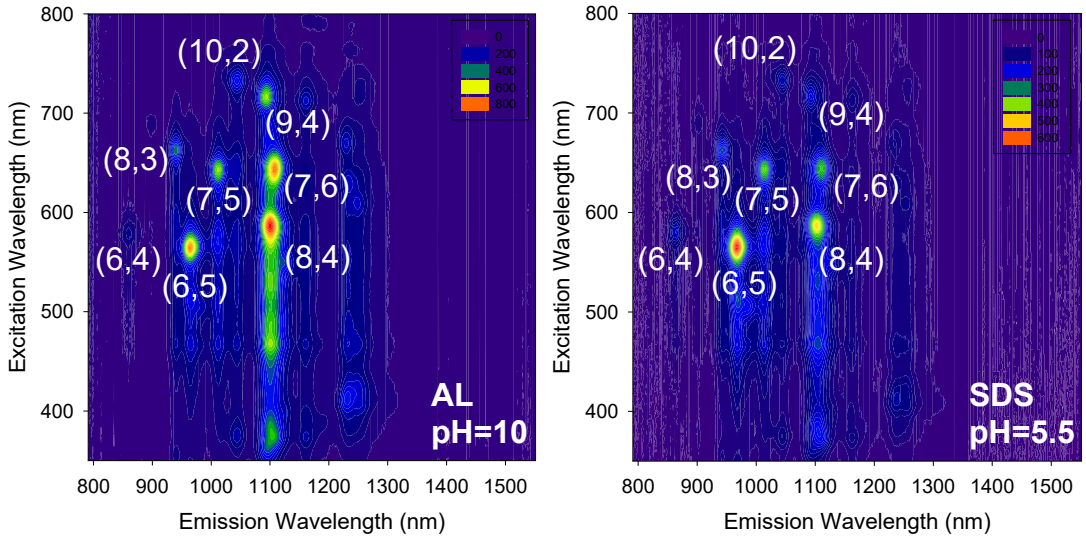

Figure 2.3.3. PL data showing the preference of AL vs SDS so hold certain chirality SWCNTs in solution. AL has a preference toward larger diameter tubes. Credit: Brendan Meany

In addition, PL is a useful tool for analyzing the stability of the solutions over time. By looking at the PL response over time it is possible to see if the tubes bundle or fall out of solution. Figure 2.3.4 shows that the AL solutions are completely stable for 6 months. There is no evident change in the PL intensity or preference towards chirality even when the solution has been sitting for 6 months.

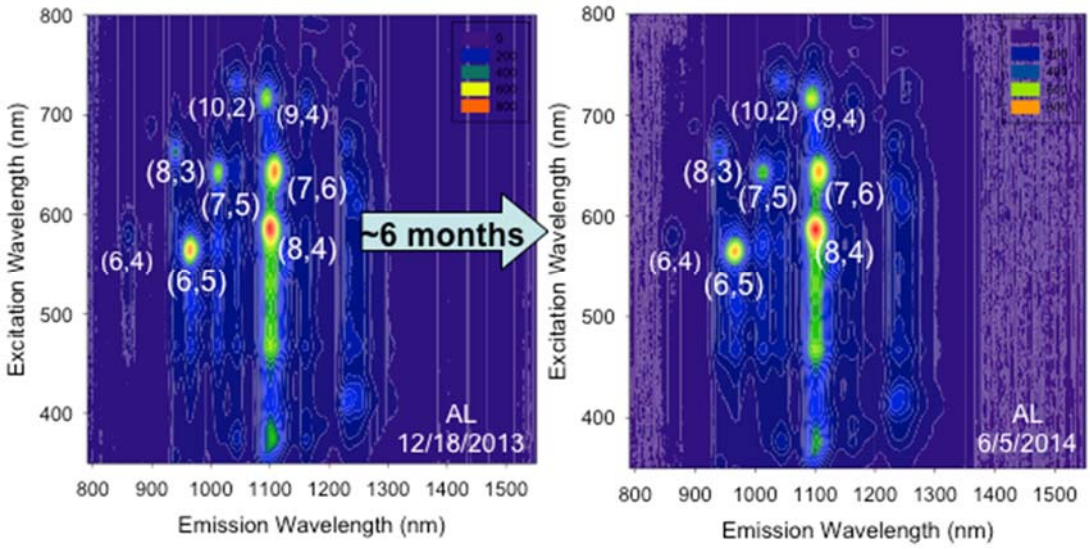

Figure 2.3.4. PL data for the same AL SWCNT solution 6 months apart showing that the solution is completely stable and without any nanotubes dropping out of solution during this time period. Credit: Brendan Meany

Lastly, in order to prove that the improvements in cleanliness lead to improvements for the proposed applications for CNTs we use a technique developed by Brintlinger et al.,[169] to demonstrate that the electrical contact resistance of CNTs with metal is lower for CNTs suspended and deposited via AL as compared with SDS. More information about this technique can be found in further references[162, 170, 171]. The basic mechanism is that a low kV (in this case 1 keV) beam is used to charge Au deposited on part of the sample, and candidate CNTs adjacent to the gold contact are observed for secondary electron contrast differences. CNTs with low electrical contact resistance with the Au will show bright contrast as compared to CNTs not in contact with the Au, in the same field of view. These samples were prepared by Jeremy Ticey and the imaging was performed by Jasper Drisko. Figure 2.3.5 shows the results for both SWCNTs and MWCNTs deposited in AL and in SDS. SWNT are synthesized by arc discharge, from Carbon Solutions, and MWNT are from Sigma Aldrich. A) is of MWCNTs in 1 wt.%

AL, B) of MWCNTs in 0.5 wt.% SDS, C) of SWCNTs in 0.5 wt.% AL, and D) of SWCNTs in 0.5 wt.% SDS. These images are typical results, representative of numerous observed locations and multiple deposition attempts. The microscope utilized is a Raith e-Line, with Zeiss/LEO Gemini electron column. For all images, the InLens SE detector is used. The working distance is 6 mm and the aperture is 20 um, resulting in approximately 15 pA beam current. The suspensions were prepared with high CNT concentration, as described in the main text. Figure 2.3.5c), as compared to 2.3.5d), is an especially clear example of how well the charges from the Au transfer to CNTs when the contact resistance is low.

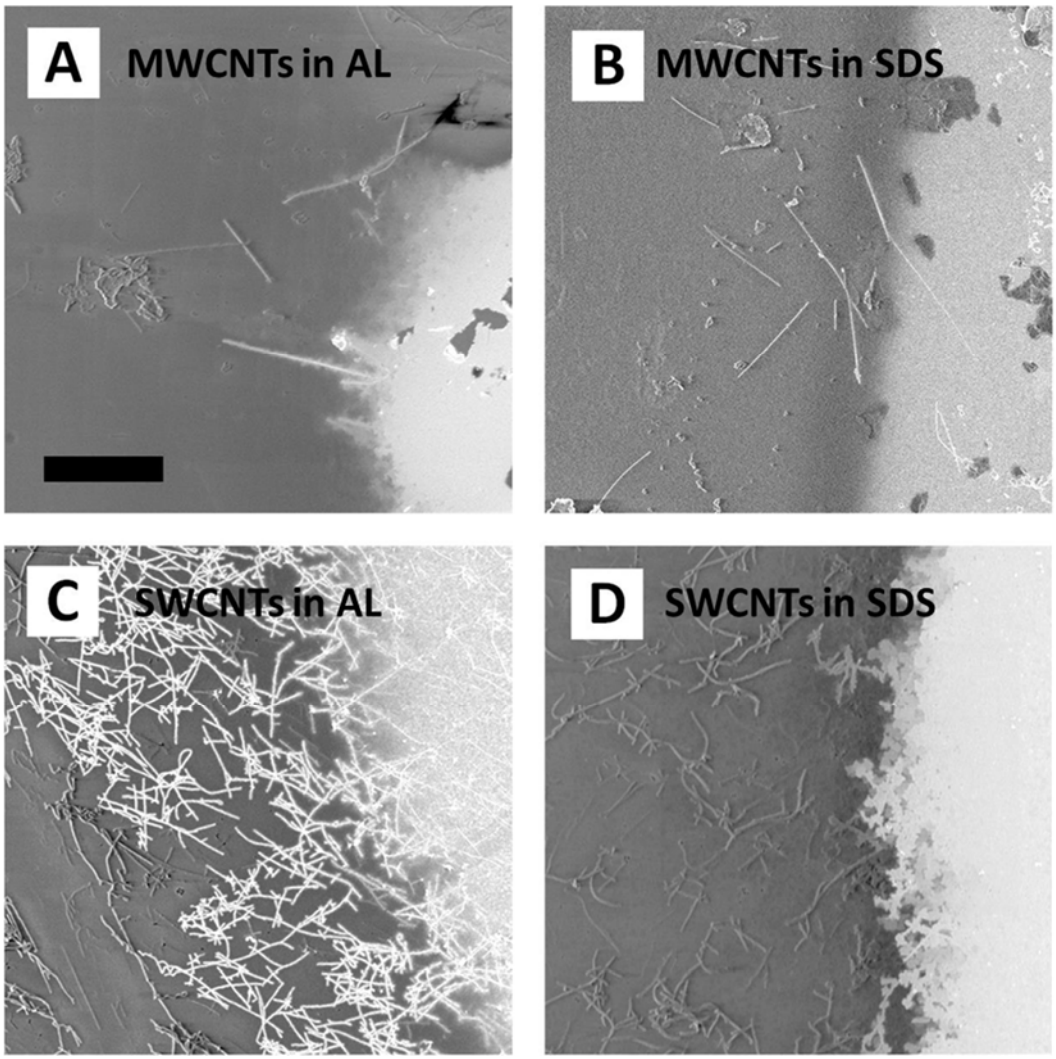

Figure 2.3.5. 1 kV SEM images showing the improved electrical conductivity of AL deposited CNTs. On the right side of all images Au has been deposited. High density MWCNTs and SWCNTs solutions were prepared and deposited as described in the main manuscript. A) MWCNTs from 1 wt.% AL B) MWCNTs from 0.5 wt.% SDS C) SWCNTs from 0.5 wt.% AL D) SWCNT from 0.5 wt.% SDS. The scale bar in A, which applies in all cases, is 3 μm. The larger contrast difference between the nanotubes in contact with Au on the AL samples shows that the electrical resistance is lower between the Au and the AL-deposited NTs compared to the SDS-deposited NTs. Credit: Jeremy Ticey and Jasper Drisko

The SWCNT work with AL leads to the same conclusions as for the previous section with MWCNTs; that AL is a stable and clean way to suspend and deposit SWCNTs. However, the characterization led to further important findings, that the AL shows distinct preference toward certain chiralities of SWCNTs. This kind of selectivity

is important in work with SWCNTs where the chirality of a tube determines its properties. Lastly, the electronic measurements give clear proof that the processing of the NTs, even when using surfactants that do not bond covalently, strongly affects the properties. In the case shown here, the AL processing leads to much better electrical conductivity between tubes than does SDS.

2.4. Graphene

This section is divided in two parts because two different approaches were explored for solution processing of graphene. Table 2.4.1 summarizes the differences between the two approaches. The first approach was to start with pre-fabricated reduced graphene oxide in powdered form. The manufacturer claims that the powder contains few layered flakes of graphene with micron sized lateral dimensions. The oxygen content in the material aids in the suspension in aqueous surfactant. The second approach was to start with natural graphite in bulk powder form and use the surfactant solution as a medium to mechanically exfoliate the graphite into graphene layers.

	"Suspended"	**"Exfoliated"**
Source Material	Reduced graphene oxide (Angstrom Materials)	Natural graphite (Alfa Aesar)
Carbon content	95%	99.8%
Starting Dimensions	Micron-sized flakes, <3 layers	Millimeter-sized, millions of layers
Suspension Process	Oxygen content aids with aqueous suspension	Probe agitation used to separate in to graphene layers
Quality of final product	Defects caused by initial chemical processing reduces some desirable properties	Few defects, nearly pristine graphene

Table 2.4.1. Summary of the differences between the two approaches that were used for solution processing of graphene.

2.4.1. Solution suspended reduced graphene oxide

A natural extension for the use of AL is to use it to suspend graphene flakes. There have recently been several successful suspensions of graphene in SDS,[132, 172, 173] so it is likely that AL will be similarly successful in suspending graphene with similar benefits that are seen for suspending CNTs with AL compared to SDS. The graphene used for this was purchased from Angstrom Materials and is advertised as being flakes with less than 3 layers and having lateral dimensions less than 10 μm. Though they do not disclose exact fabrication method they claim that the product has less than 2.5% oxygen and C/O ratio of 38 so it is far from graphene oxide,[174] but the fact that there is some residual oxygen leads to the conclusion that the graphene was produced via some sort of electrochemical oxide reduction process.[175] This is important to note because high oxygen content in graphene naturally facilitates its suspension in aqueous solutions.[176] This is both because graphene oxide is hyrophilic[177] and because charged carboxylic acid and hydroxyl groups from the ionization form stable colloids in aqueous solution.[178] Graphene oxide however, does not share the same high electrical conductivity as pure graphene so for many applications graphene oxide cannot be used in place of graphene.[179] However, as will be shown in subsequent chapters, the slight oxygen content in these sheets makes the graphene p-doped with low sheet resistance.

AL and SDS are prepared as described in previous sections. For the graphene flakes a surfactant concentration of 6 times the CMC is found to allow for high concentration suspension without causing excess residue of the depositions. Large amounts of graphene flakes are added to the surfactant solutions and then probe sonicated

for 10 minutes (1 second on/1 second off) at 100 W to distribute the graphene in the solution. Next the solutions are centrifuged at 4000 rpm for 15 minutes in order allow excess carbon material to drop out of solution. The top 50% of the solution is decanted after the centrifugation step. This means that the color and concentration of the solutions vary depending on how well the solutions are able to hold the graphene in solution.

Figure 2.4.1.1 shows optical images of the solutions. It is clear that the AL solution has a higher concentration of graphene than does SDS. Over the course of the 5 days that the images show, both solutions appear to be stable. This is confirmed by absorbance measurements which is a commonly used indication of the graphene content and stability.[176] Figure 2.4.1.2 shows the average absorption intensity from 300-800 nm over the course of a month. The absorbance data backs up the optical images in showing that the AL has a higher graphene concentration. The absorption data shows that the SDS solution is completely stable over the course of the measurements while the AL solution shows a slight dip around 20 days, but then remains stable at that level. Solution stability is important for industrial application where solutions may be an option for storing graphene until it is needed for production. Depending on the application and the type of industry, the time requirements are different, but here we show stability for a month which we believe should be a basic requirement for the industrial use of graphene solutions. While other work has achieved higher graphene concentrations initially, their concentrations deteriorate even after 1 hour after dispersion and continues to drop off continuously until there is nearly nothing left in solution after a year.[172]

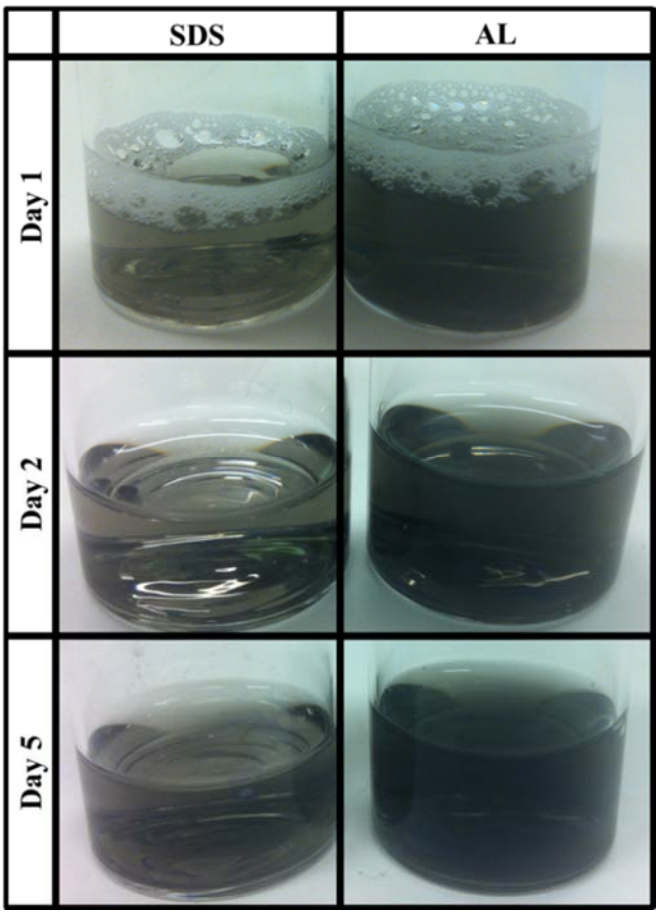

Figure 2.4.1.1. Optical images of AL and SDS solutions containing suspended graphene flakes. The darker color of the AL solution indicate that it has a higher graphene concentration than does the SDS solution.

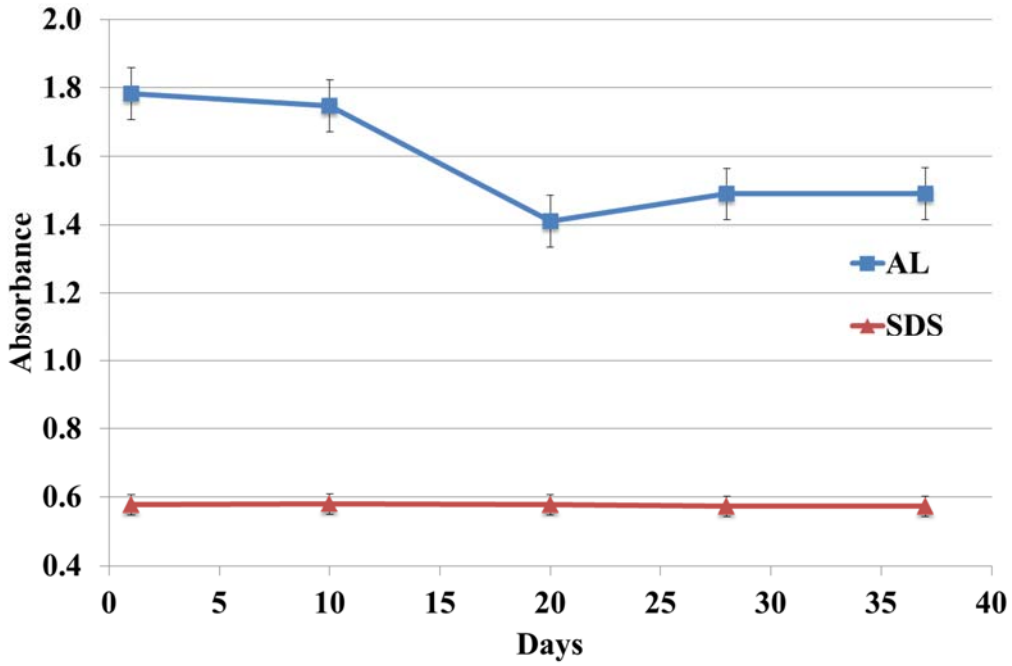

Figure 2.4.1.2. Absorbance data recorded over the course of a month to show the stability of the graphene solutions. The absorbance intensity reported is the average value from wavelengths 300-800 nm on each day. The tool measurement error is within the size of the data point, but 5% error bars have been added to account for errors is sample selection.

The graphene is deposited on to silicon nitride membranes for TEM observations by leaving plasma cleaned membranes in solution over night. The membranes are taken out of solution and dipped in IPA to clean them prior to drying with nitrogen gas. The resulting depositions can be seen in figure 2.4.1.3. This leads to several important observations. The first, is as expected, that the AL deposited samples are much cleaner from surfactant residue as compared to the SDS samples. Another important note is that the flakes are very wrinkled and folded on the substrate. Lastly the lateral dimensions are much less than the 10 μm that the manufacturer reports, which may be a result of (1) the probe sonication process, (2) that the solutions suspend small flakes while large flakes drop out, or (3) that the starting materials did not contain as large sheets as the manufacturer claims.

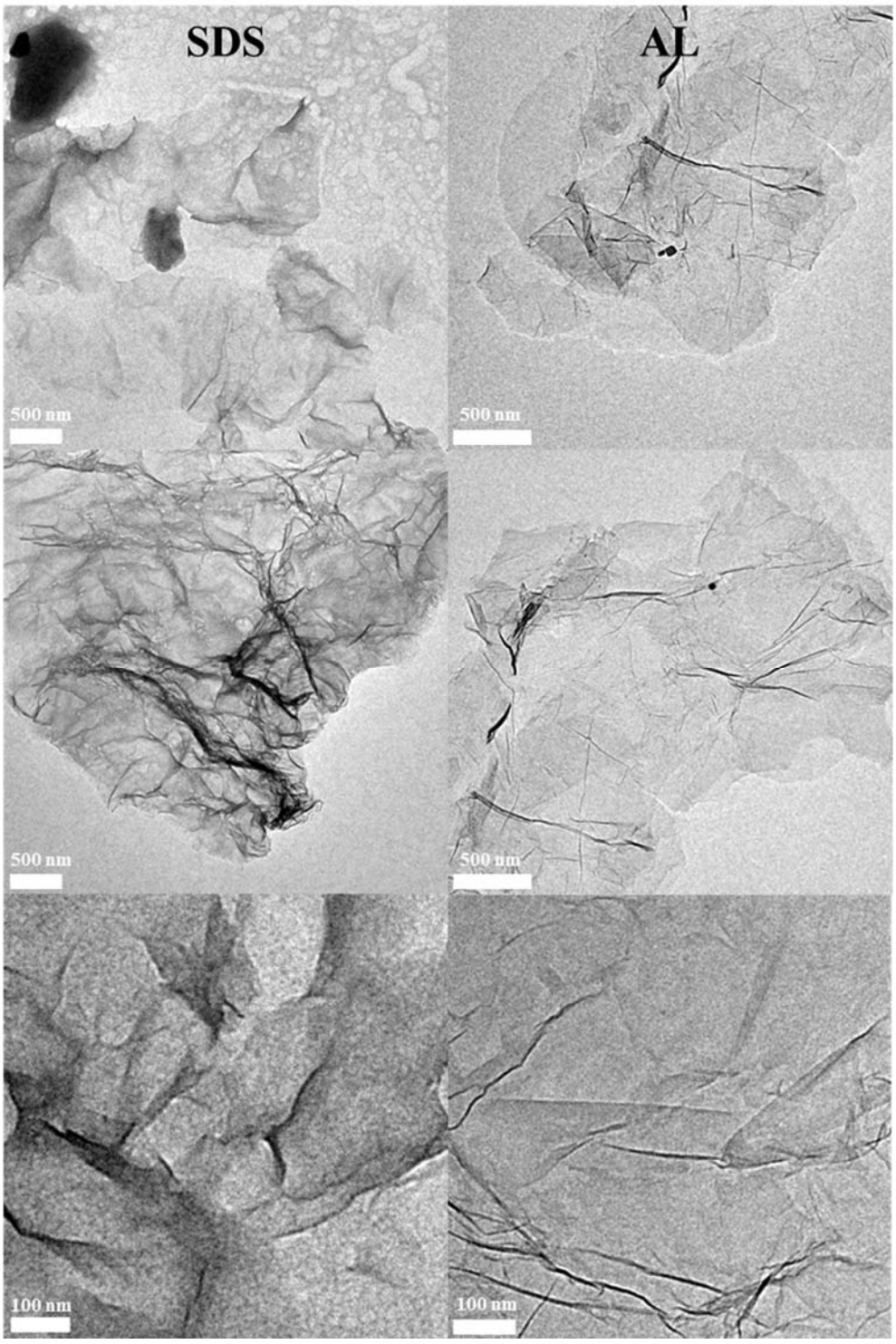

Figure 2.4.1.3. TEM images of graphene flakes deposited on 50 nm thick silicon nitride through surfactant solutions.

As is standard, Raman spectroscopy is used to characterize the graphene depositions.[180] The results are shown in figure 2.4.1.4 and table 2.4.1.1. The results presented in the table are averages from samples deposited from different solutions and many different locations on those samples. Interesting first observations are that the signals from the AL samples are stronger than from the SDS samples. This is most likely caused by the excess surfactant residue on the SDS sample dampening the signal. The locations of the disorder peaks can vary quite a bit depending on the laser wavelength used and the substrate that the sample rests on,[180] but in general the D peak is a 1350 cm^{-1} and G is at 1580 cm^{-1} for pure graphene[181] Due to the small size of the flakes it is likely that much of the Raman signal for these samples is coming from the edges of the graphene and this is part of the reason why the D peak is so strong.[182] However, in general the shape of the peaks shown are rather characteristic of reduced graphene oxide.[177] This includes the defect ratio, I_D/I_G, which is about 1.2-1.3 and the location of the D and G peaks which for graphene oxide are known to fall at 1325 cm^{-1} and 1595 cm^{-1} respectively.[174] There does seem to be a significant difference between AL and SDS when it comes to where these peaks are located however the reason for this could be as simple as that the residue of the SDS sample are changing the Raman signal, or it may have something to do with the actual graphitic particles in the different solutions. It may be the case that the AL has a higher concentration of graphene in solution, but that it also has a higher amount of disordered graphitic particles.

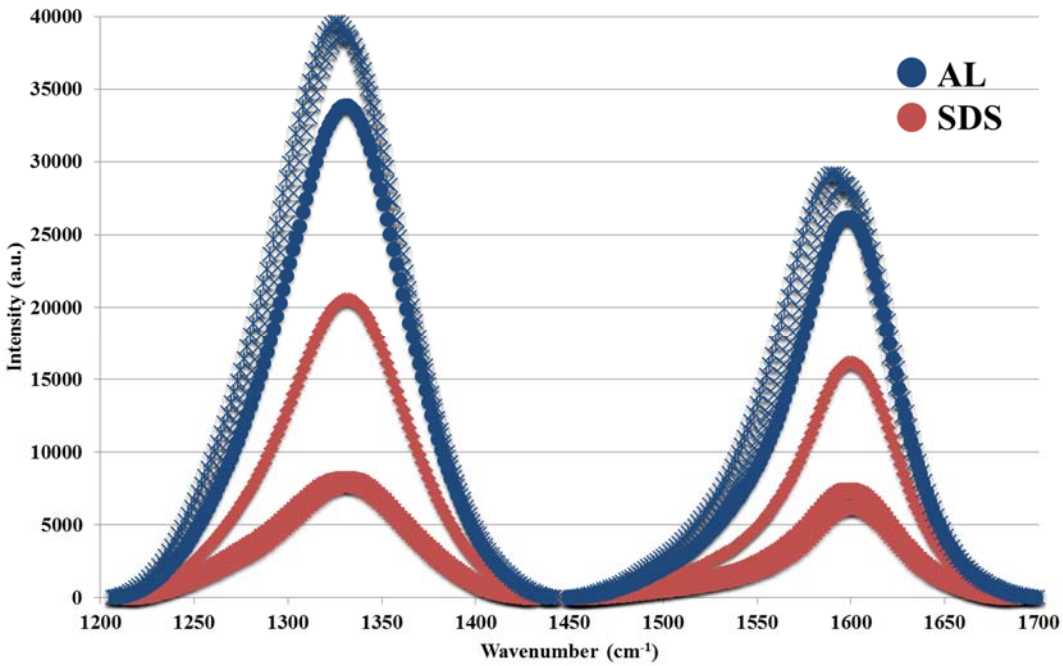

Figure 2.4.1.4. Typical raman spectra for AL and SDS deposited graphene flakes on SiN.

Average	D frequency	G frequency	I_D/I_G
SDS	1331 cm^{-1}	1599 cm^{-1}	1.22
AL	1327 cm^{-1}	1593 cm^{-1}	1.33

Table 2.4.1.1. Typical raman spectra for AL and SDS deposited graphene flakes on SiN.

Extensive electrical and thermal characterization was performed on the AL deposited graphene flakes. This will be discussed in later chapters, but it is relevant to mention here that the SDS deposited graphene was completely insulating as can be seen in figure 2.4.1.5 while the AL deposited graphene showed linear IV characteristic with resistance on the order of 10s of kΩ including contact resistances. The reason for the insulating behavior of the SDS deposited graphene is most likely that the STM probe used during electrical characterization cannot get through all of the SDS residue on the sample in order to get to the graphene.

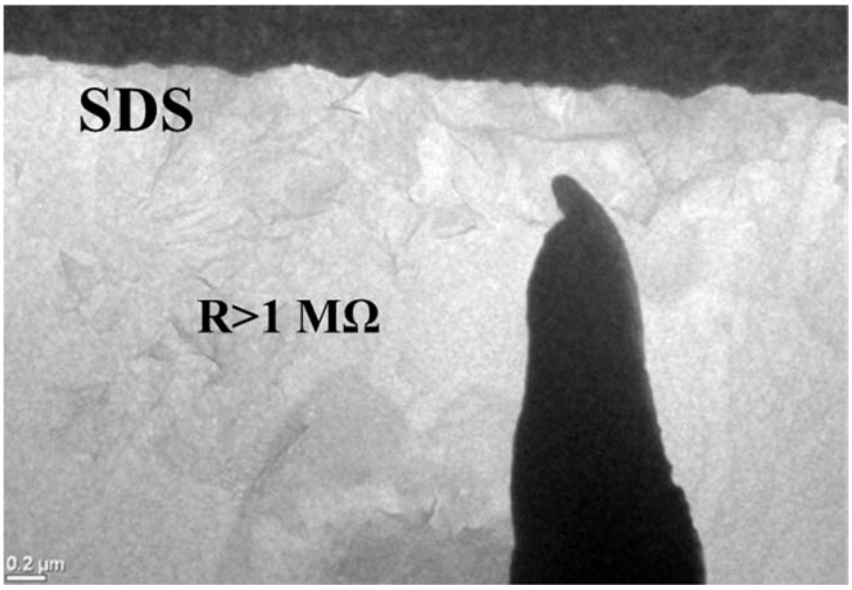

Figure 2.4.1.5. TEM image of *in-situ* electrical characterization of SDS deposited graphene labeled with the measured resistance showing that the SDS depositions are insulating because of the residue on the graphene.

2.4.2. Graphite exfoliated to graphene in solution

The next challenge for AL is to see if it is possible to use it as an aid in mechanical exfoliation of graphite into graphene in solution. Non-oxidized graphite has previously been mechanically sheared into few layered sheets of graphene using different sonication methods with varying results.[125, 132, 133, 134, 183, 184] Four of these studies employ less than environmentally safe and friendly solvents such as N-methyl-pyrrolidone (NMP) and sometimes require complicated and time-consuming preparation procedures.[125, 133, 183, 184] Another uses SDS, but has to use alcohols to reduce the surface tension in order to get more than 0.2 mg ml^{-1} graphene concentration.[132] There is one very recent study that

found a method for producing high concentration (100 mg ml^{-1}) with 95% of the graphene having thickness less than 1 nm using microwave sonication for just 30 minutes in oligomeric ionic liquids.[134]

The method that I use is similar to that which I use to suspend already prepared flakes, however, the sonication time and power are increased to 20 minutes and 175 W inorder to induce separation of the thick graphite layers. The absorbance results show disappointingly low graphene concentrations, but the combined Raman and TEM investigations show low defect, high purity, and few layered graphene sheets from the deposited solutions.

The absorbance results that indicate the low dispersion are shown in figure 2.4.2.1. The plot compares the results of the suspended AL solutions from the previous subsection with graphene exfoliated from pure graphite in AL and in DI water. The exfoliated solutions show much lower absorbance values, but the AL exfoliated solution shows great stability over the course of the 2 weeks where measurements were performed. The low concentration may be improved if several iterations of exfoliation are performed in the same solution. However, for our application of *in-situ* TEM characterization of individual flakes, low concentration is not a problem.

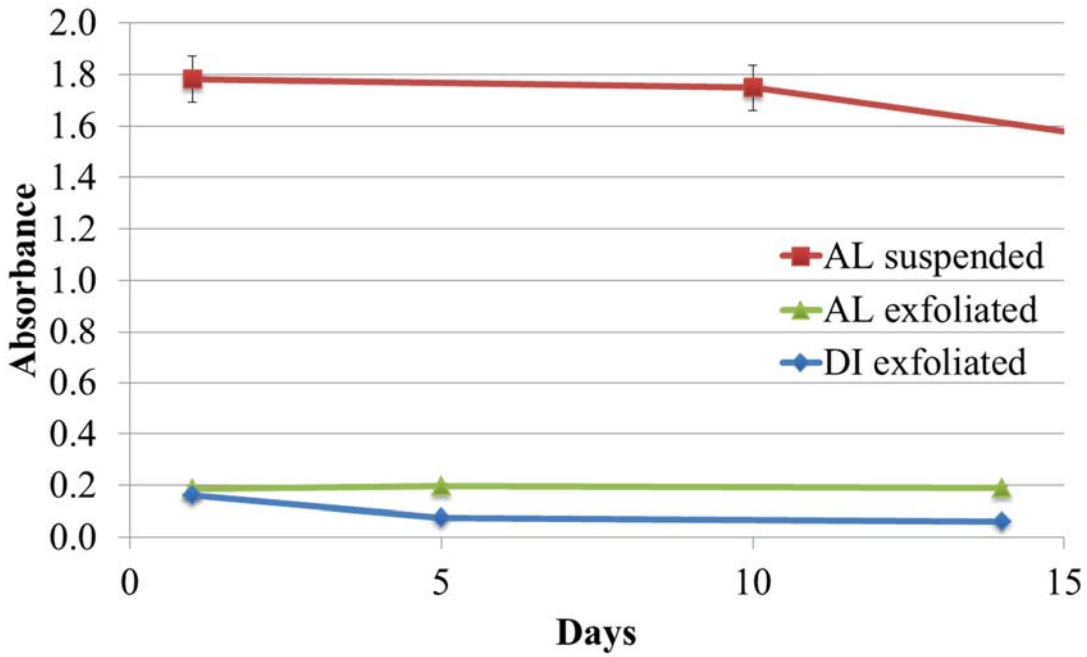

Figure 2.4.2.1. Chart comparing absorbance data for the suspended and the exfoliated graphene sheets in AL. The exfoliated solutions have much lower concentration than the suspended flakes. The tool measurement error is within the size of the data point, but 5% error bars have been added to account for errors when solution was selected for measurement.

The TEM investigation of the structure of the exfoliated graphene shows that the solutions do indeed contain mostly multi-layered graphene (figure 2.4.2.2). Compared to the suspended graphene flakes, the exfoliated graphene has larger lateral dimensions. The depositions are clean and free from surfactant residue. The graphene seems to be crystaline however the periodicity that can be seen in some of the HRTEM images is not that of the atomic spacing of graphene, but rather Fresnel contrast which indicated that the samples are crystalline. Looking at the Raman spectra in figure 2.4.2.3 and table 2.4.2.1, it is obvious that the deposited graphene has properties that are very different from the suspended graphene characterized in figure 2.4.1.4 and table 2.4.1.1. The data very closely resembles that obtained in the Matsumoto et al.[134] work described earlier where they come to the conclusion that their graphene is high purity with few defects and

contains mostly flakes with less than 1 nm thicknesses. The graphite that we are starting with here is natural 325 mesh graphite from Alfa Aesar with carbon content of 99.8%. The Raman spectra backs up that there is no oxidation. The location of the D2 peak around 2663 cm^{-1} is evidence that the sheets are between 2 and 10 layers thick.[185]

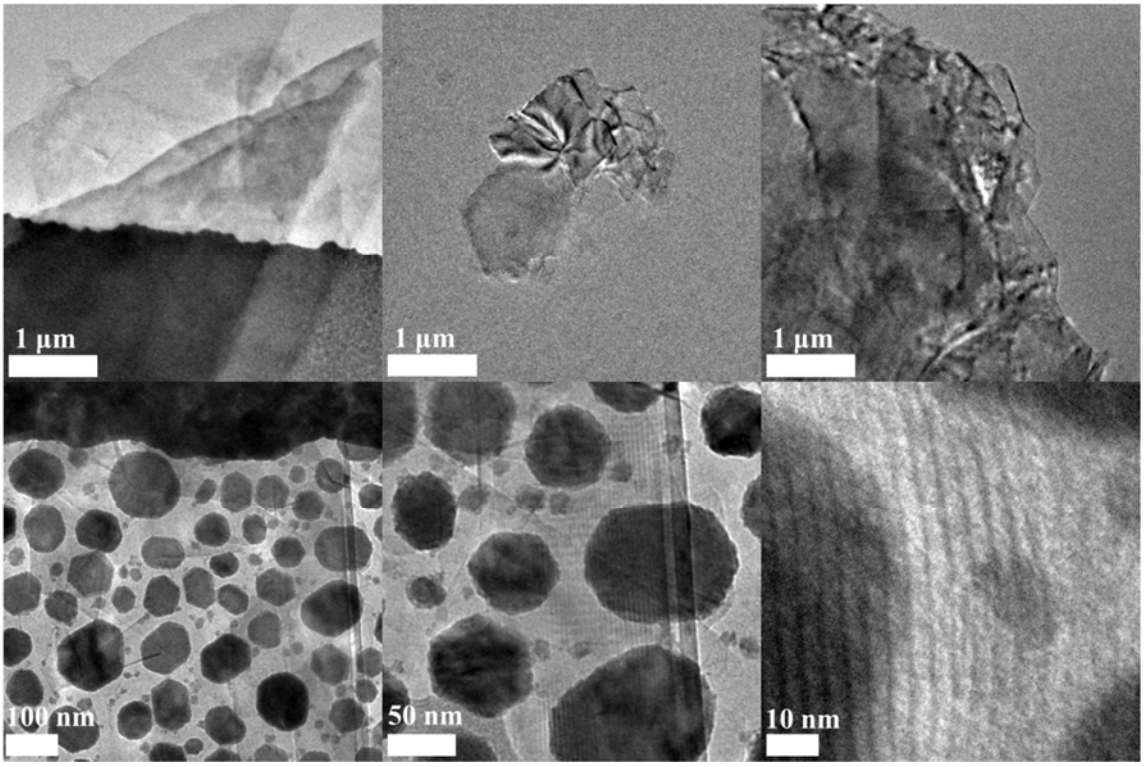

Figure 2.4.2.2. TEM images of graphene flakes exfoliated in AL via simple probe sonication. The images confirm that the bulk graphite is separated into multi-layered graphene flakes during the processing. The bottom row of images is of graphene deposited on SiN membranes with indium islands on the backside. These images show periodic contrast from Fresenel edges, indicating that the samples are crystalline.

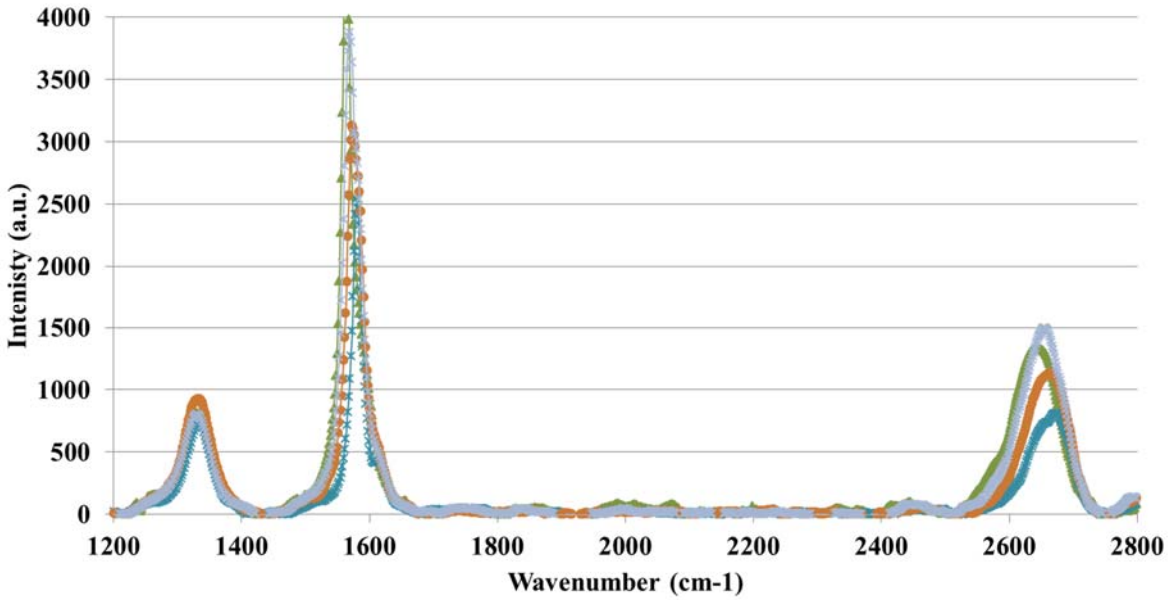

Figure 2.4.2.3. Typical Raman spectra for graphene exfoliated in AL showing low defect densities and a sharp G peak.

Average	D frequency	G frequency	D2 frequency	I_D/I_G	I_{D2}/I_G
AL (exfoliated graphite)	1334 cm^{-1}	1574 cm^{-1}	2663 cm^{-1}	0.24	0.36

Table 2.4.2.1. Average raman frequencies and intensity ratios for the graphene exfoliated in AL.

The results of these experiments are very promising for the use of AL for graphene processing. Fabrication and deposition on to a desired substrate are among the largest challenges for working with graphene and here we have been able to show a great solution for clean deposition of two different types of graphene on to a very fragile and difficult to work with substrate. The solutions suffer from low concentration, but there is optimization that can be performed in this area by changing the surface tension of the solutions.[132]

Chapter 3: *In-situ* TEM electrical characterization at the nanoscale

3.1. Biasing metal heater wires

As part of this work, the fabrication and electrical characterization of metal nanowires were investigated in-depth. The goal is to fabricate nanometer scale metal wires with predictable joule heating behavior. Wires are fabricated using a few different approaches; lithography in combination with thermal or electron beam evaporation, electron induced beam deposition (EBID), and focused ion beam (FIB) deposition. The metals that are tested are gold, palladium, platinum, and tungsten.

Joule-heating in a metal nanowire depends on its dimensions and the material properties. For the EThM experiment, we want to be able to raise the temperature of the sample locally by about 200 C using approximately 1 V of applied bias. We can generally control the dimensions of the wire, but we are limited in length to about 2 μm by the TEM viewing area during experimentation, to no less than 100 nm in width by the fabrication, and to about 30 nm in thickness in order to be able to see the indium islands

under the wires. This means that we are targeting a certain resistance in order to melt the indium islands. The resistance of a pure metal wire is:

$$R = \frac{\rho L}{A}$$

Where L is the length of the wire, A is the cross-sectional area, and ρ is the resistivity. This means that for the dimensions mentioned above, and for the known resistivity of pure platinum, 1.06E-7 Ωm,[186] the resistance would be expected to be just 35 Ω. However, the actual resistance that we measure is much higher and varies from sample to sample depending on the fabrication method used. Devices have shown values spanning from 1E2 to 1E6 Ω. We have found that devices with resistance on the order of 1E3 Ω perform the best.

The measurements are performed with *in-situ* TEM holders with biasing capabilities. Three different holders of this kind, but with varying capabilities, have been used for this project. The first is a 4-probe holder built in the Cumings group. It can been seen in Figure 3.1.1. The placement of the sample in the holder can be seen in Figure 3.1.2. The advantage of this holder is that a patterened SiN chip can simply be placed on to the wire leads and then clamped in to place to achieve electrical contact.

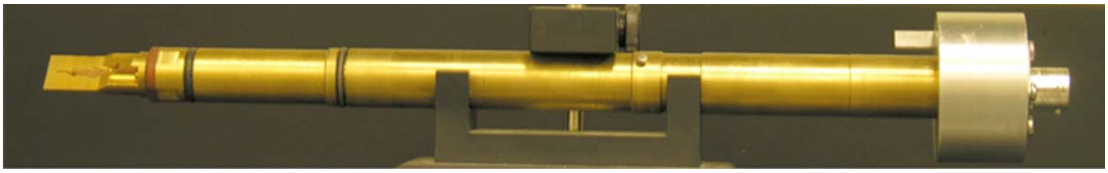

Figure 3.1.1. A 4-probe *in-situ* TEM biasing holder built in the Cumings group

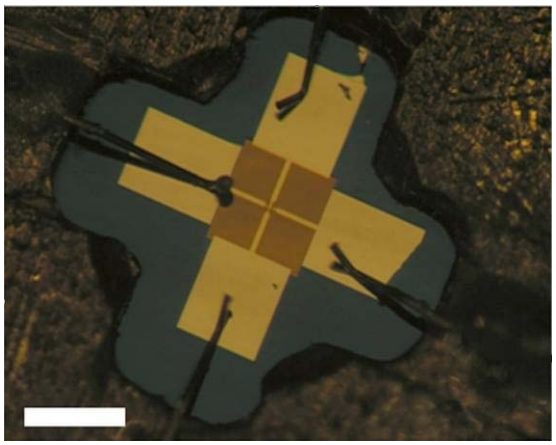

Figure 3.1.2. Close up of a patterned SiN sample in the 4-probe holder in contact with the wire leads. The scale bar is 1 mm.

The other two holders that were used for biasing were Nanofactory holders. The first one is a so-called optical holder, named so because of an optical wire that allows for photons to be introduced in to the TEM chamber. This functionality was not needed for our experiments, but the biasing capabilities were. Figure 3.1.3 shows an image of this holder. This holder requires the sample to be glued and then wire-bonded onto a chip carrier. This proved to be a difficult procedure for our samples because they have thin layers of metal that easily scratch off when contacted with the metal wedge bonder. In many cases, the abrupt electrical current sent through the device as part of the bonding procedure caused failure of the device. Examples of this will be provided later in this section.

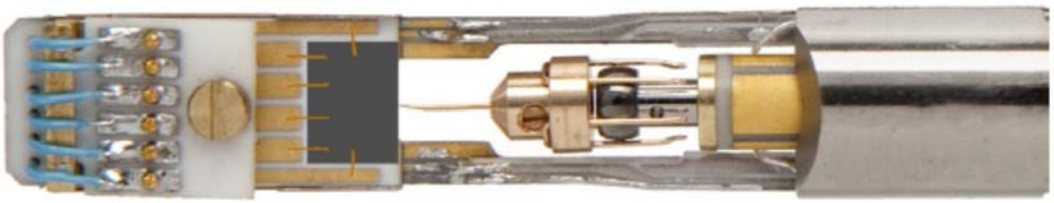

Figure 3.1.3. Image of the Nanofactory optical holder which allows for 6-probe biasing, but requires problematic wire bonding of the sample to a chip carrier.

The second Nanofactory holder was the scanning tunneling microscopy (STM)-TEM holder seen in Figure 3.1.4. In this holder the sample is electrically grounded to the holder using a metal post and silver epoxy. On the other end of the holder, an STM tip is attached that allows for current to be passed through the sample, in addition to allowing for mechanical manipulation of the sample, with picometer precision. The disadvantage is that 4-probe tests cannot be performed the way that the holder is currently set-up. However, the local control of the STM tip allows for valuable information to be collected from the sample that is not otherwise available.

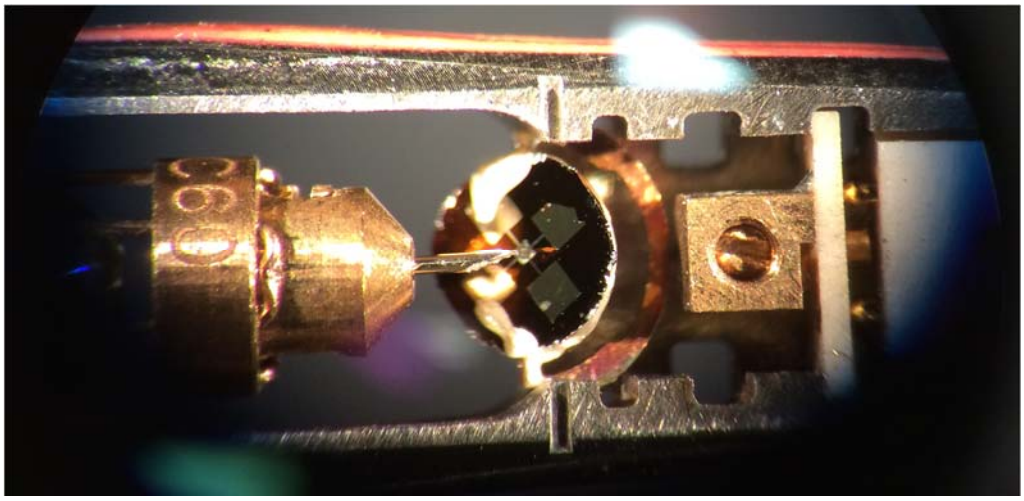

Figure 3.1.4. Magnified optical image of a patterned SiN membrane assembled with a gold STM tip in a Nanofactory STM holder. The tip can be used to locally manipulate and pass current through the sample.

For all of the aforementioned TEM holders, SiN membranes must be uniquely patterned for the holder and the planned experiment. The standard fabrication method is electron beam lithography. While optical lithography gives high enough resolution for the pads and the majority of the structures that are needed for experiments, the most critical features required for local heating of the nanostructures are on the order of tens of nanometers which cannot be achieved with optical lithography. Process development was performed on several different electron beam lithography tools to fabricate devices for this project. These include a Raith e_Line, a JEOL 6400 with Nabity, a Philips XL30 with Nabity, and a JEOL JBX-9300FS. The first three are all operated at 30 kV. The JEOL JBX-9300FS tool is operated at 100 kV, which requires a different process sequence and parameters in order to be successful on thin SiN membranes. In order to have successful metal lift-off, of high-resolution features, it is important to have resists with specific properties. Here one layer of methyl methacrylate (MMA) spun at 4500 rpm followed by one layer of poly methyl methacrylate) PMMA spun at 6000 rpm is used. Each layer is baked separately in an oven at 180 C for at least 40 minutes. Lastly, a layer of a conductive polymer such as e-spazer or Aquasave is spun at 6000 rpm in order to prevent problems with charging during the e-beam writing process. It is important to perform all of the steps within a short time frame. Especially important are the time between writing and developing and the time between metal deposition and lift-off. For these, less than an hour is preferable. For the other steps; from baking to writing and developing to metal deposition, a time frame of a couple days should be aimed for. Developing is done with 1:3 MIBK:IPA for 60-70 seconds. Lift-off is done with acetone

and/or PRX. Figure 3.1.5 shows an optical microscope image of a sample after it has been developed, but before metal has been deposited.

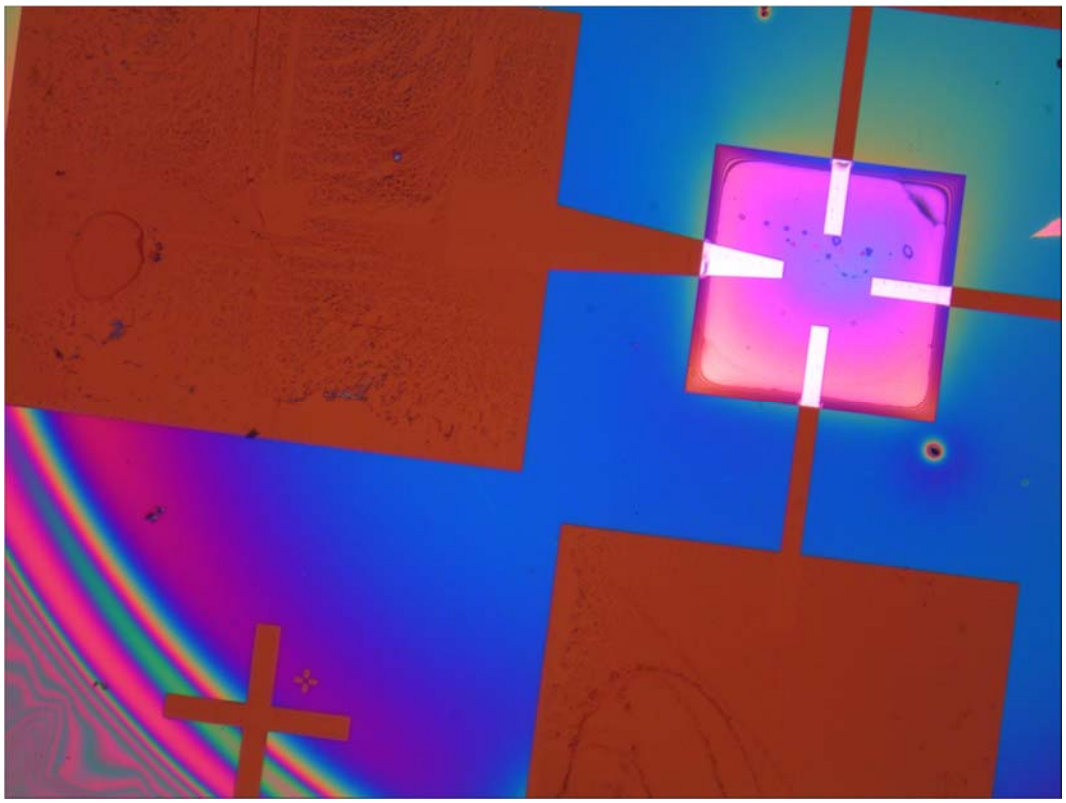

Figure 3.1.5. Optical microscope image of a sample after the developing an electron-lithography write. The square in the upper right of the image is the SiN membrane (50 nm thick and 250x250 μm^2 in lateral dimensions).

For the first lithography step on a pristine SiN sample the only feature that can be used to align the write is the membrane. However, the membrane is very electron sensitive so it is important to avoid unnecessary exposure during the alignment. During the first write alignment marks like those seen in the lower left part of Figure 3.1.5 are added in order to improve the alignment and overlay of later writes.

Another approach that was used to fabricate devices was to purchase pre-patterned optical lithography made gold pads and then use focused ion beam (FIB) metal

deposition or electron beam induced deposition (EBID) to directly deposit thin metal heater wires via a gas precursor on to the SiN membrane. The problem with this method is that it is difficult to get low enough resistance of the metal in order to use them for predictive heating. The precursor used for platinum deposition is especially high in carbon content and ends up with an impure metal. The tungsten precursor is slightly better, but still results in a much higher resistance than pristine tungsten.[187] One method for reducing the electrical resistivity is to anneal the deposited structures in an inert environment in order to remove organic species,[188] however since our samples have temperature sensitive gold pads this is not an alternative. The second problem is that the ion beam easily damages the SiN membrane and leaves the sample with gallium ion implantation that changes the properties of the system as can be seen in the AFM image of figure 3.1.7. Figure 3.1.6 compares FIB and EBID deposited Pt wires. The EBID deposited wire appears more uniform, but has higher resistance values compared to the FIB deposited wire. The inset in the figure also shows that the FIB deposition method can also remove material from the Au electrode which can affect the overall resistance of the system.

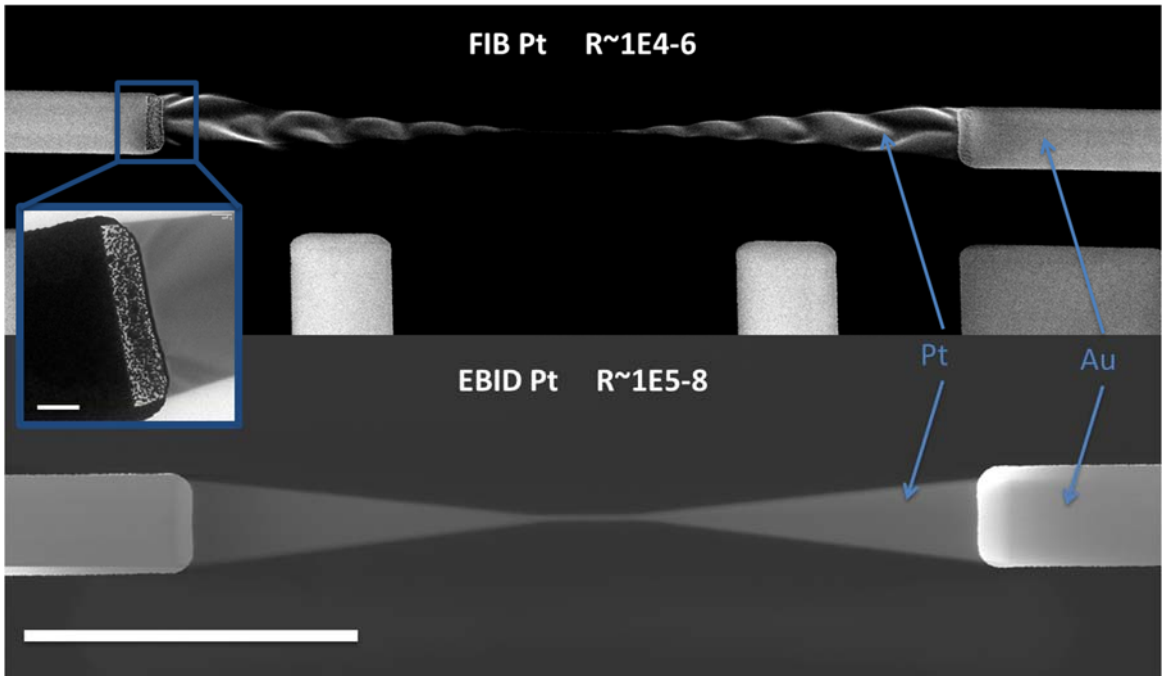

Figure 3.1.6. Images comparing FIB and EBID deposited Pt heater wires. FIB wires show more damage to the SiN substrate and the Au electrode (see TEM inset, 2 μm scale bar), but have lower resistance than EBID deposited wires. Scale bar is 30 μm.

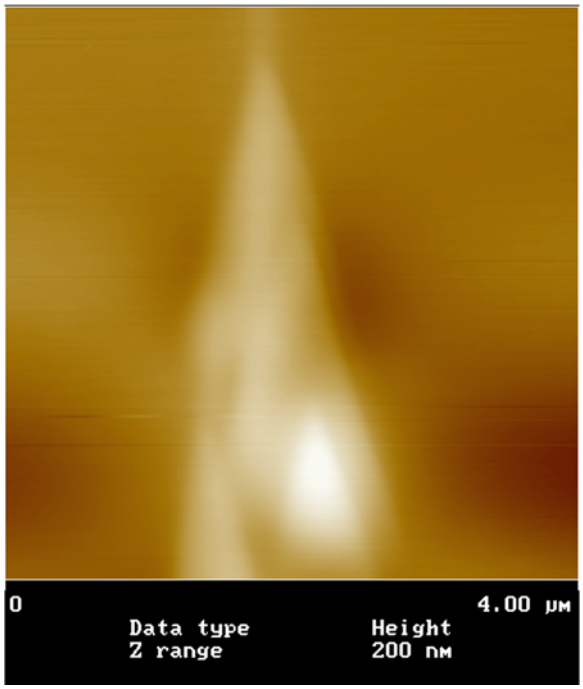

Figure 3.1.7. AFM image of a FIB deposited Pt heater wire. The lighter areas represent greater height. The darker areas next to the wire are an indication that the ions are removing SiN material near the deposition sites.

A last process that was developed, was electron lithography using dual-beam FIB software. This meant depositing resist on the samples and then using the software on the dual-beam FIB to make patterns in the resist with the electron beam. The problem with this technique was that the beam blanker on the tool that was used (FEI Strata 235) was not fast enough to make lines without causing additional features. Lift-off was also difficult because the working area always had to be exposed a little bit in order to do the write.

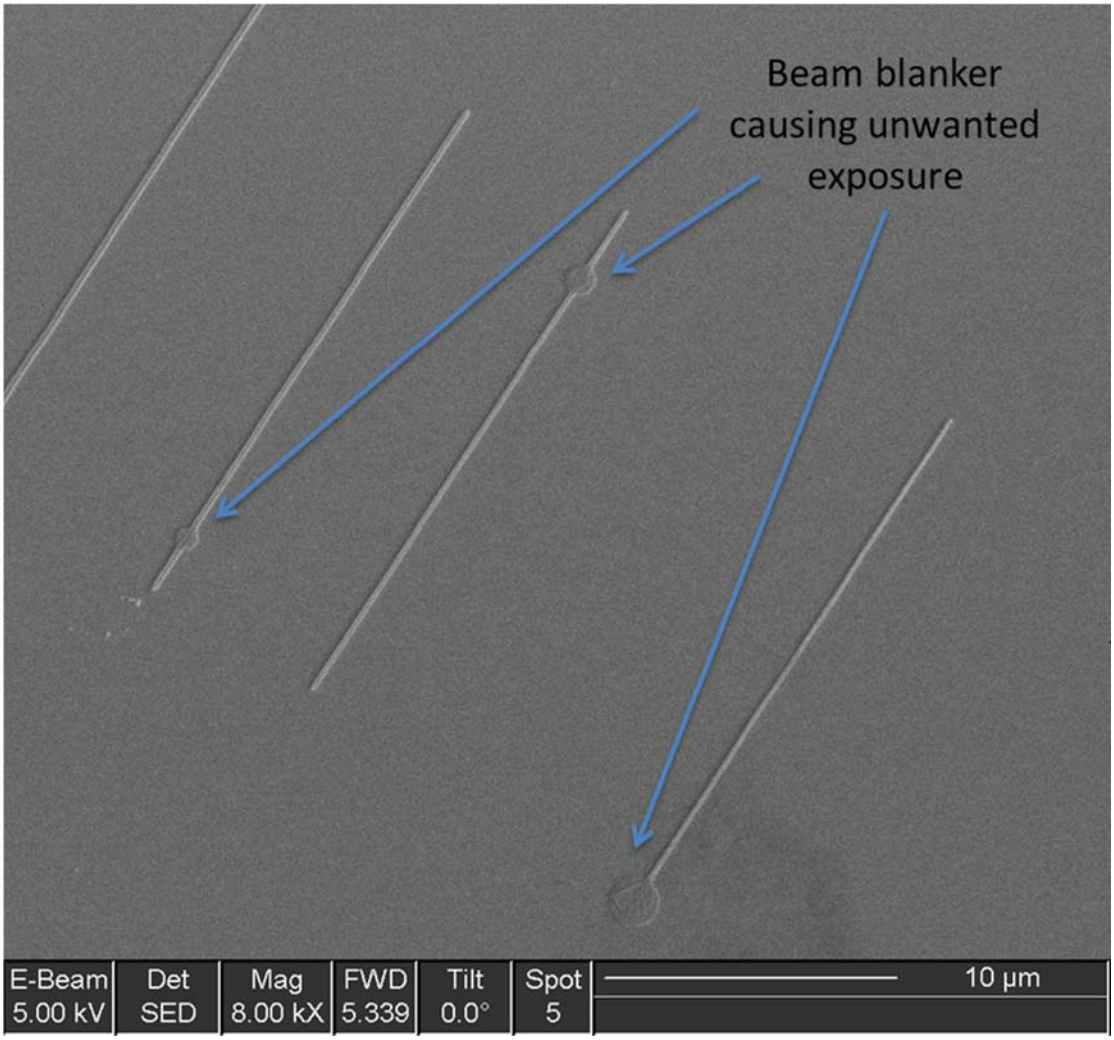

Figure 3.1.9. Image of lines patterned by writing in resist using dual-beam FIB patterning software. The beam blanker is not fast enough to avoid unwanted exposure.

A last consideration is how the sample is to be mounted. As was mentioned above, wire bonding is problematic for these samples because of the high localized resistance and the poor adhesion between the metal and the SiN. Figure 3.1.10 shows examples of what happens to heater wires when exposed to the wire bonding process. Wires that were deposited using lithography and evaporation had such poor adhesion to the substrate that they were completely removed from the substrate when exposed to the high current densities of the bonding shocks as can be seen in figure 3.1.10b. FIB fabricated wires over-heated to the point where the SiN melted as can be seen in figure 3.1.10a and d.

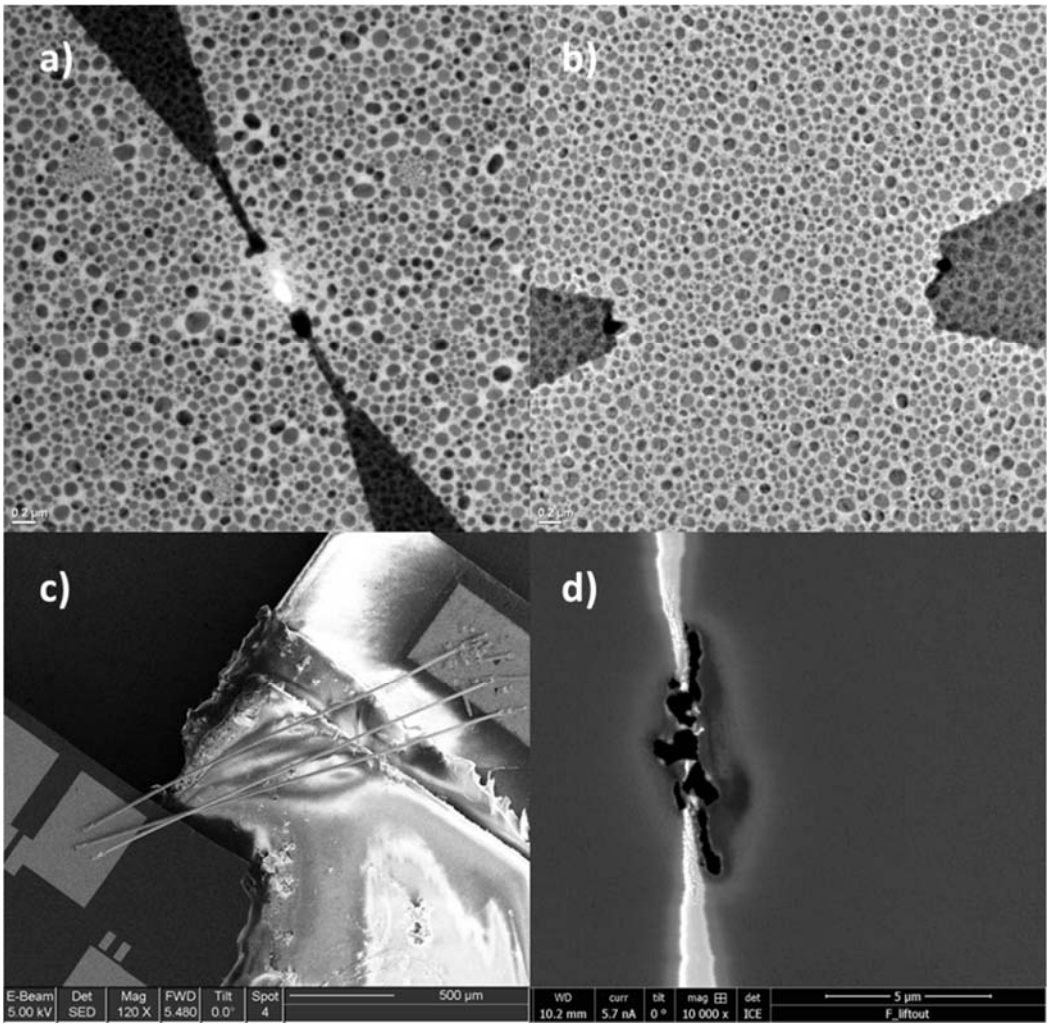

Figure 3.1.10. Images showing the problems with wire bonding. a) TEM image of a FIB fabricated heater wire that has overheated during wire bonding and melted the SiN. b) TEM image of a lithographically patterned heater wire with poor adhesion to the SiN so the entire wire disappears when exposed to high power during wire bonding. c) SEM image of the sample wire bonded to the chip carrier. d) SEM image of a FIB fabricated heater wire that has overheated during wire bonding and melted the SiN.

In summary, there are many different options for fabricating metal nanowires. The optimal method depends on the application requirements. When low, predictive resistance and minimal damage to the substrate is required, electron beam lithography and pure metal evaporation are the best options. However, if the resistance requirements are less stringent and the substrate is robust, FIB or EBID can be simpler methods. The technique that is more time-effective depends on the area that needs to be covered in

metal and the tool that is used. In general, if a wire with length on the order of single microns is desired, it will be much quicker to pattern using FIB or EBID as compared to lithography. When working with high-resistance wires and metal with poor adhesion to the substrate, successful wire bonding is difficult to achieve. However, as will be shown in the next section, the most successful electrical characterization performed *in-situ* for this project is with the STM-TEM holder, where nanostructures can be Joule-heated directly using a metal probe.

3.2. Localized graphene biasing

The electrical characterization of graphene has been performed by several other groups and with different techniques, but the results vary drastically depending on the type of graphene and the type of measurement that is used.[189] One thing that has come to light is that obtaining flat graphene is very difficult, because of the physical properties of the material. Despite many efforts to "flatten" graphene,[190] it naturally forms wrinkles and folds under most conditions, especially when transferred to a substrate.[191] Therefore, it is important to understand the effect that the wrinkles have on the transport properties of graphene. In order to look at the effect of wrinkles it is most useful to use a probe technique that allows high resolution measurements to be made.

There have been three published studies that have looked at conductance and resistance as a function of wrinkles and they all used different scanning probe techniques. The first study was performed in 2009 using scanning tunneling microscopy (STM).[192] It looks at the differential conductance at flat regions and at wrinkled regions and find that the conductance is lower at the wrinkle than at the flat regions. However, their results do not give any quantitative analysis of the difference in the conductance. The second study was published in 2011 and employed conductive atomic force microscopy (c-AFM).[193] It also simply concludes that wrinkles lead to higher resistance, but do not provide any quantitative results. One interesting comparison that they provided is that chemical vapor deposition (CVD) grown graphene has lower conductivity than exfoliated graphene. The last of these studies, published in 2013, and employed Kelvin force microscopy (KFM).[194] This study finally provided some qualitative results of the resistance induced by wrinkles, claiming that the average lower limit of wrinkle resistance in their devices is 4.5 kΩ. Their graphene, like ours, is reduced graphene oxide.[177] They conclude that wrinkles are not the limiting factor for the conductance, but rather intra-flake and inter-flake interactions, as well as structural defects.

The measurements that I perform are on reduced graphene oxide sheets that are deposited through ammonium laurate solutions onto silicon nitride membranes. A test voltage of 1 V or 2 V is applied locally using a platinum or gold STM tip using the *in-situ* STM holder. The gold contacts under the graphene are grounded. The deposition process onto silicon nitride leaves the graphene sheets very wrinkled, on the order of 10s of wrinkles per square micron, as compared to 1-2 wrinkles per square micron cited in the 2013 work discussed above. According to their conclusions, large amounts of wrinkling

should decrease the electrical conductivity. However, the results of my experiments lead to the conclusion that wrinkles are not detrimental to electronic transport; in fact the highly wrinkled sheets have very robust electrical performance.

The supported graphene sheets that I have tested are able to withstand high applied electrical power without showing any signs of degradation. Most breakdown studies have been performed on suspended graphene nanoribbons. These studies are in consensus that graphene ribbons break down at about 1-2 mW in vacuum.[195, 196, 197, 198] Here, we regularly see the graphene dissipating powers in that range without any damage. It is able to conduct electrons well, despite being very wrinkled and on a substrate. There is evidence from previous experimental work, that graphene with a low oxygen content actually has lower resistance than pure graphene.[199]

Figure 3.2.1 shows a typical TEM image of graphene flakes in contact with a gold electrode. The image is labeled with the resistance values that were measured in those locations with the STM probe. We will show that the spread in the measured resistance values for these samples is dominated by contact resistance between the probe and the graphene.

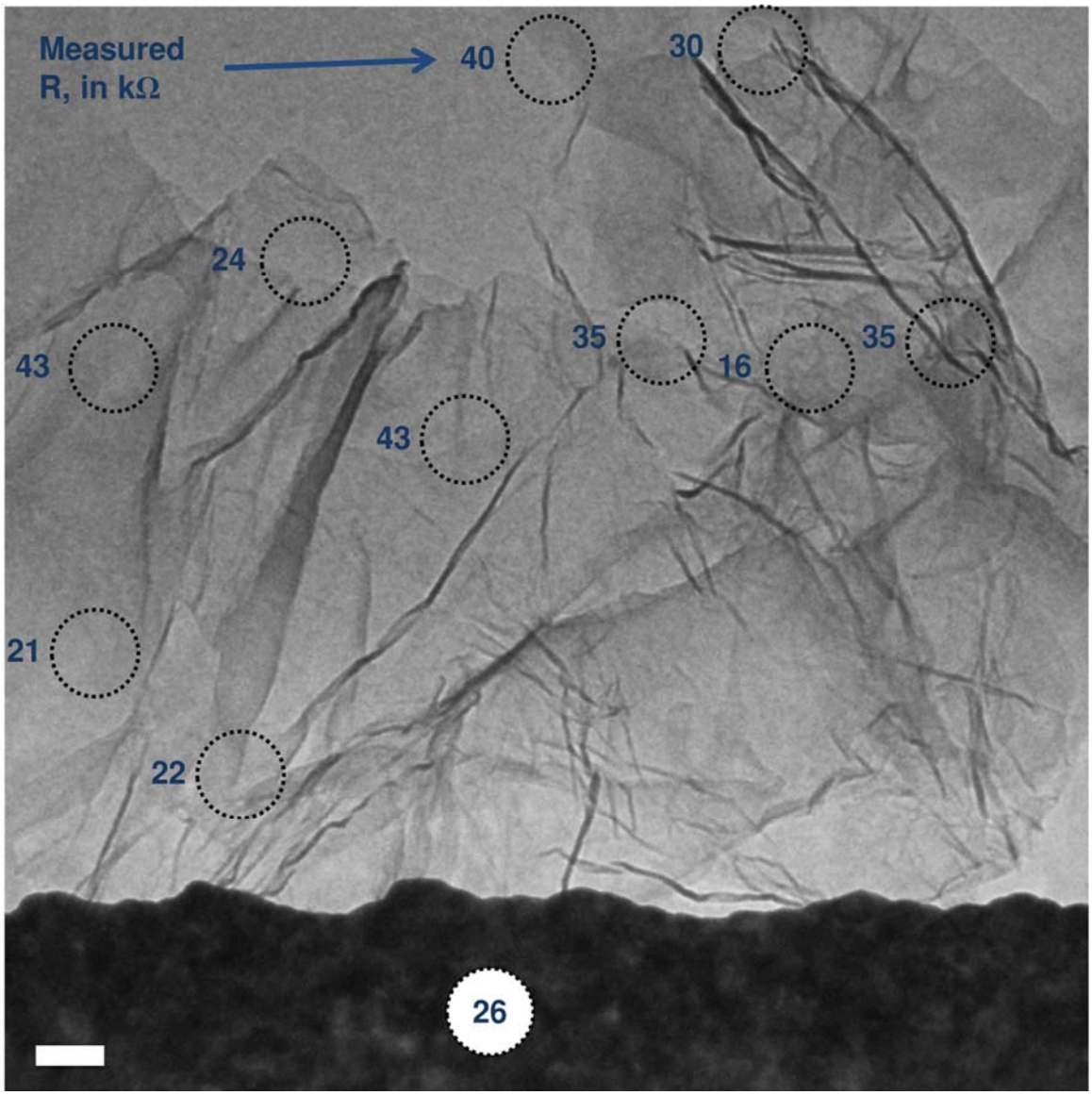

Figure 3.2.1. TEM image of graphene flakes in contact with a gold electrode at the bottom of the image. The graphene is highly wrinkled and folded. The size of the dashed circles symbolizes the uncertainty in the location of the contact point between the STM tip and the graphene. Resistance values in blue are in units of kΩ and represent the total measured resistance. Test voltage is 2 V. The scale bar is 100 nm.

Figures 3.2.2 and 3.2.3 are schematics of the experimental setup. Figure 3.2.2 shows the case where the probe contacts the graphene away from the electrode so the current travels laterally through the graphene sheet. Figure 3.2.3 shows the case where the probe contacts the graphene on top of the electrodes so the current travels directly

across the graphene sheet from the probe to the electrode. There are, of course, resistances through the metals, but they are negligible in comparison to the contact resistances and the sheet resistance of the graphene, so the total resistance becomes:

$$R_{measured} = R_{c,probe} + R_{sheet} + R_{wrinkles} + R_{c,Au}.$$

The contact resistance areas are circled in red in the schematics.

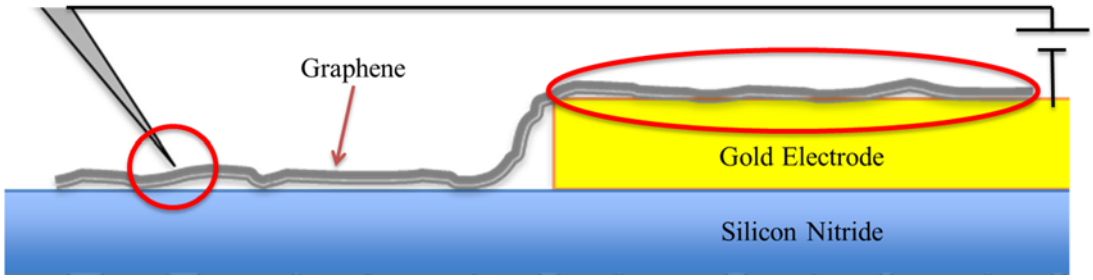

Figure 3.2.2. Schematic of the side view of the experimental set-up when the probe is contacting graphene that is lying on silicon nitride.

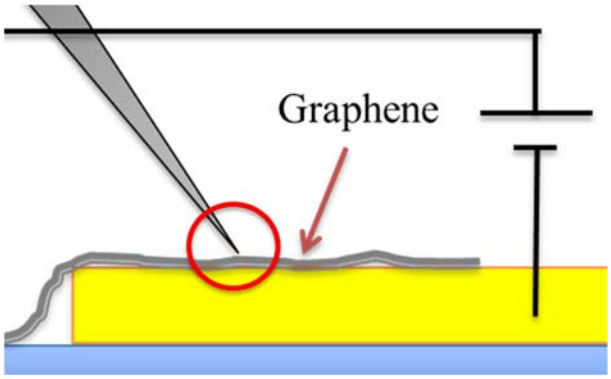

Figure 3.2.3. Schematic of the side view of the experimental set-up when the probe is contacting graphene that is lying on the gold electrode.

Our technique allows us to determine the effect of wrinkles on the measured resistance values. As can be seen in figures 3.2.4 and 3.2.5 the trend is towards lower resistance values in areas with more wrinkles. This is thanks to the fact that the texture of the wrinkles allows for more contact area to be available to make contact between the measurement probe and the graphene. Figure 3.2.4 shows a comparison of the measured values on a sheet that is highly wrinkled compared to one that is less wrinkled. Despite what might be expected from literature where wrinkles have been calculated to have high resistance,[194] we see no increase in resistance for more wrinkles. Figure 3.2.5 shows data collected on a number of different samples, with different probes and graphene geometries. However, despite the variation in the values from the different parameters involved, there is a distinguishable trend toward lower measured resistance in areas with more wrinkles. We see the opposite, that the reduction in contact resistance from the wrinkle contact area lowers the overall measured resistance. Our results do not disprove that wrinkles might be scattering sites that increase the resistance locally, but for these measurements that effect is not dominant enough to be visible.

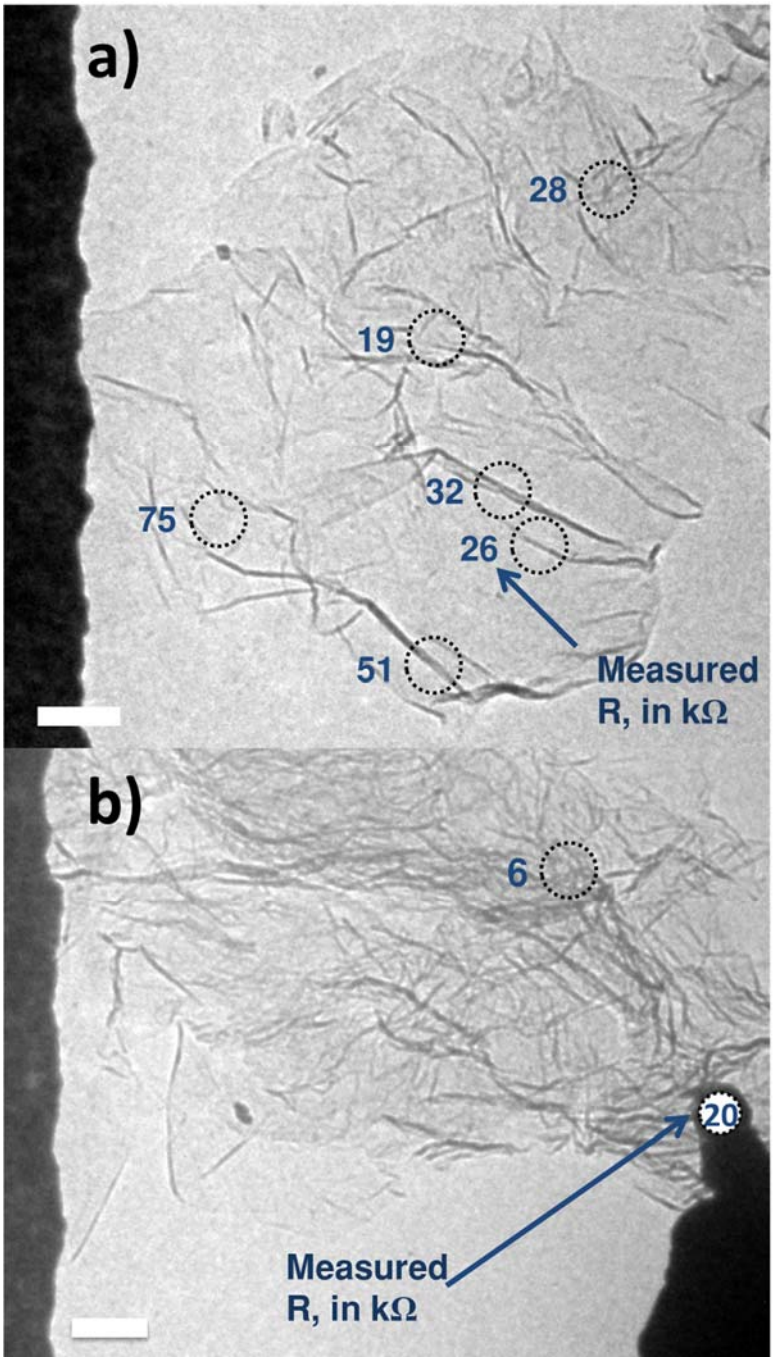

Figure 3.2.4. TEM images comparing sheets of graphene with different orders of magnitude of wrinkling. a) has less wrinkling than b) and the trend is that wrinkles contribute to lower measured resistance because the wrinkles contribute more contact area between the probe and the graphene. The size of the dashed circles symbolizes the uncertainty in the location of the contact point between the STM tip and the graphene. The resistance values labeled in blue are in kΩ. The test voltage is 1 V. The scale bar is 200 nm.

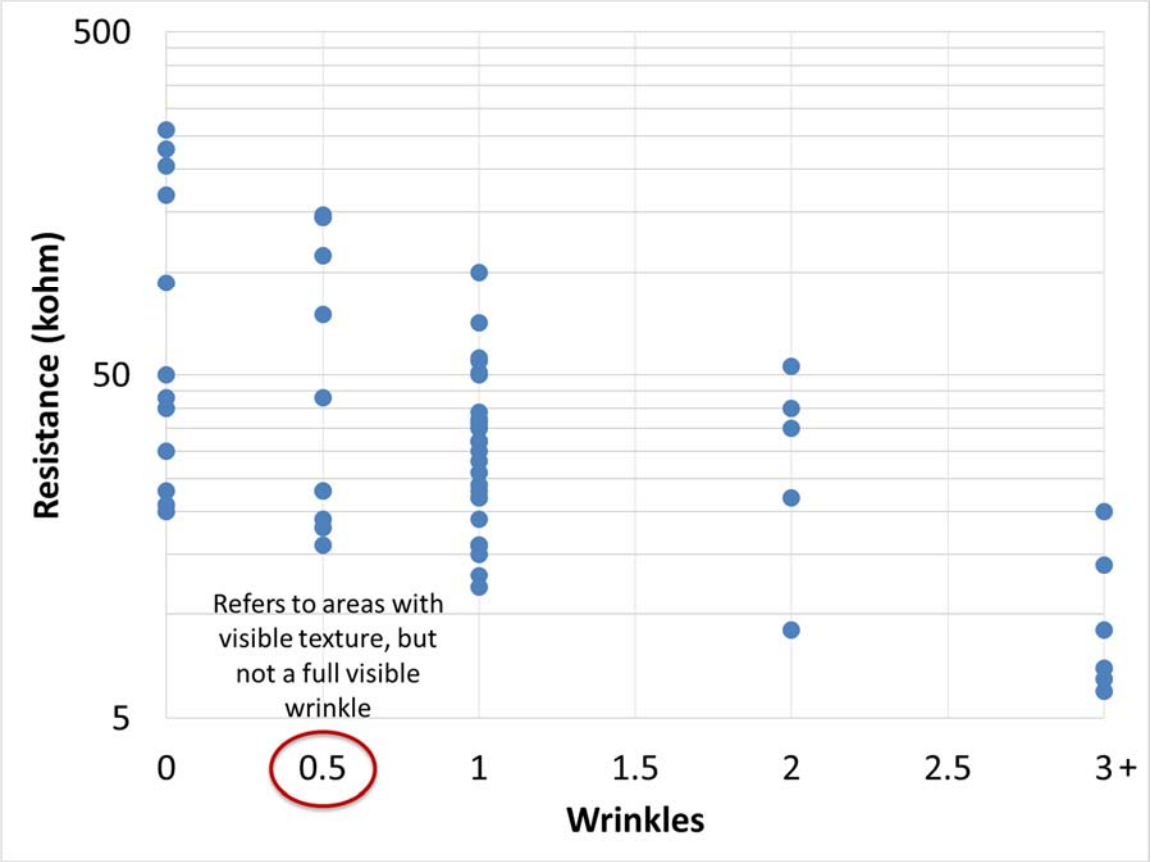

Figure 3.2.5. Measured resistance data plotted as a function of wrinkles in the probe contact area. A wrinkle values of 0.5 refers to area with visible texture, but no full visible wrinkle. The data shows a trend toward lower resistance with more wrinkles.

Since these results indicate that contact resistance with the probe is important, two methods were used to control the contact resistance in these systems. The first is to anchor the graphene, with electron beam induced deposited (EBID) platinum, both to the silicon nitride and to the gold electrode. The second is to drag the STM probe along the graphene so that more of the graphene is in contact with the probe.

Figures 3.2.6 and 3.2.7 show the platinum anchoring on the gold electrode and on the silicon nitride, respectively. Figure 3.2.7 shows that the contact resistance between the probe and the Pt is rather high (24 kΩ), higher than with the Au electrode (14 kΩ),

almost as high as with the graphene (22 kΩ). This means that no improvement in resistance can be expected with the graphene anchored by the Pt. The results shown in Figure 3.2.7 confirm these results. Both examples again show that wrinkled areas do not suffer from high resistance. All in all, the Pt deposition method was not effective for decreasing the contact resistance of the system. It may be that the EBID damaged the graphene or simply that it had high resistance due to high incorporated carbon content, as is common for EBID deposited metals.[188]

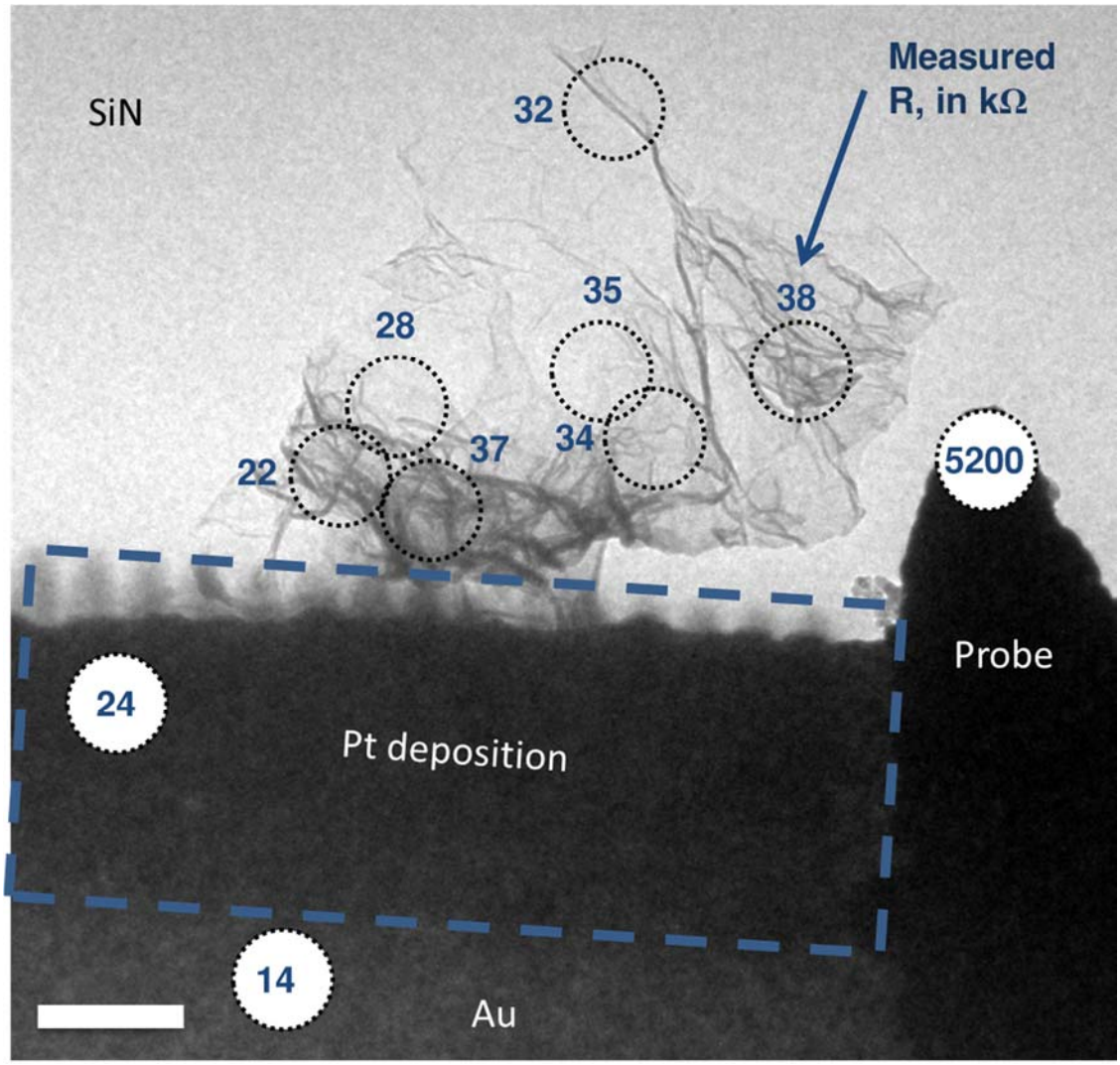

Figure 3.2.6. TEM image of graphene sheets that are anchored to the Au electrode using EBID Pt. The size of the dashed circles symbolizes the uncertainty in the location of the contact point between the STM tip and the graphene. The test voltage is 2 V. The resistance values labeled in blue are in units of kΩ. Important to note is that the resistance between the probe and the Pt is higher than the resistance between the probe and the Au. The scale bar is 500 nm.

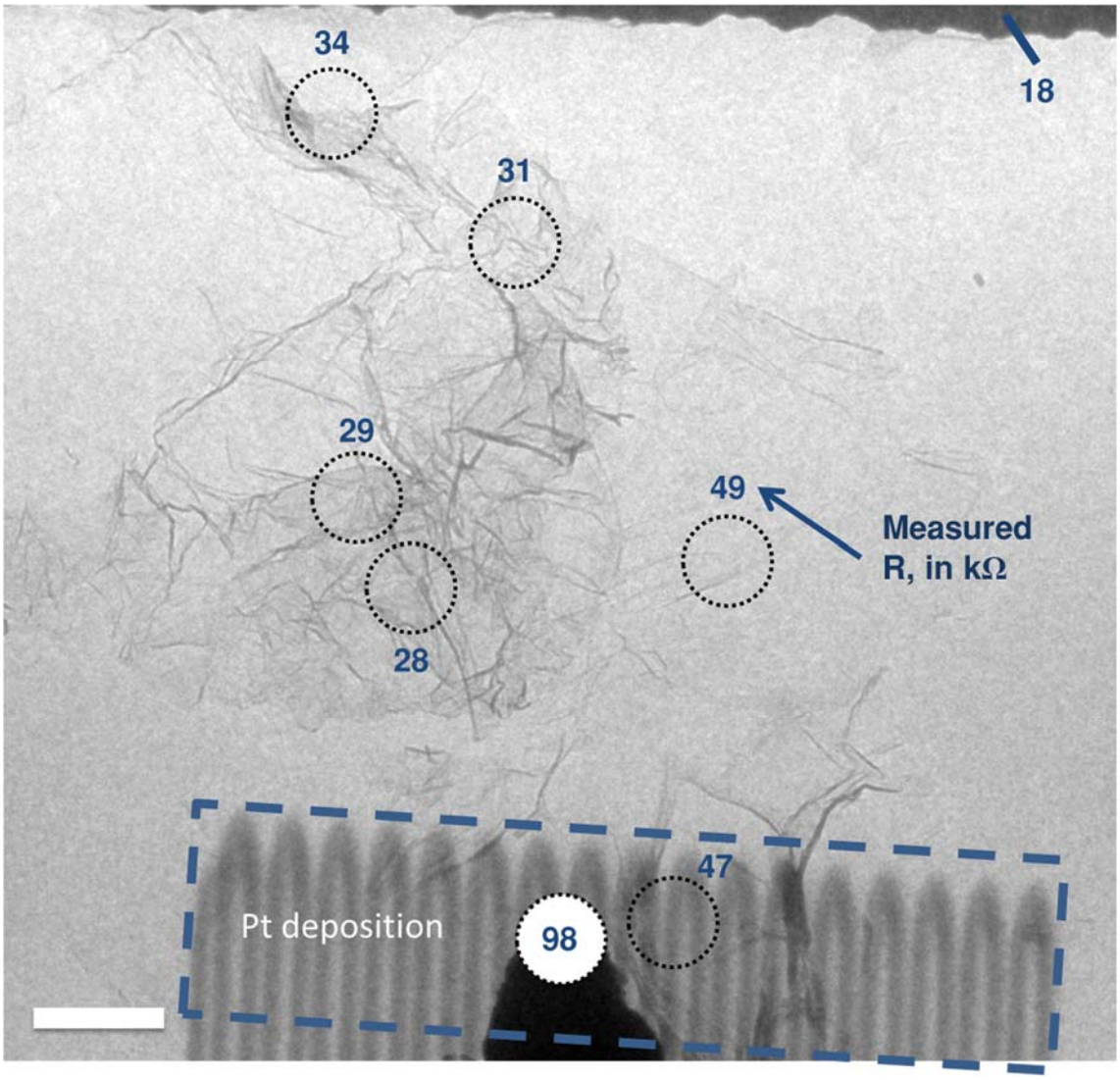

Figure 3.2.7. TEM image of graphene sheets that have been anchored to silicon nitride using EBID Pt. The size of the dashed circles symbolizes the uncertainty in the location of the contact point between the STM tip and the graphene. The resistance values labeled in blue are in units of kΩ. The test voltage is 2 V. The scale bar is 500 nm. It is important to note that the resistance between the probe and the Pt is higher than the resistance between the probe and the Au.

The second method for controlling the contact resistance; STM manipulation, is more successful. Figure 3.2.8 shows a sequence of dragging the probe against the graphene and Figure 3.2.9 shows the corresponding IV plots. The results are clear that the resistance greatly decreases as the probe increases its contact area with the graphene. The non-linear shape of the IV curves supports a conclusion of resistance change dominated by decreasing $R_{c,probe}$, at least initially, where the curves go from highly non-linear to linear. This is likely due to a semimetal tunnel junction changing to an ohmic contact. Looking at the asymmetry in current for positive and negative bias in Figure 3.2.9a, the slightly higher current for the positive bias is an indication that the graphene is p-doped which is consistent with oxygen containing graphene.[199] P-doped graphene has been found to have up to 3 times lower sheet resistance compared to un-doped graphene, perhaps explaining the low total resistance found in these experiments.[200] Nonetheless, this example again shows that the resistance is not a function of the amount of wrinkling and folds in the graphene. Even at the last steps where the graphene is starting to rip as a result of the applied force, the total resistance still decreases.

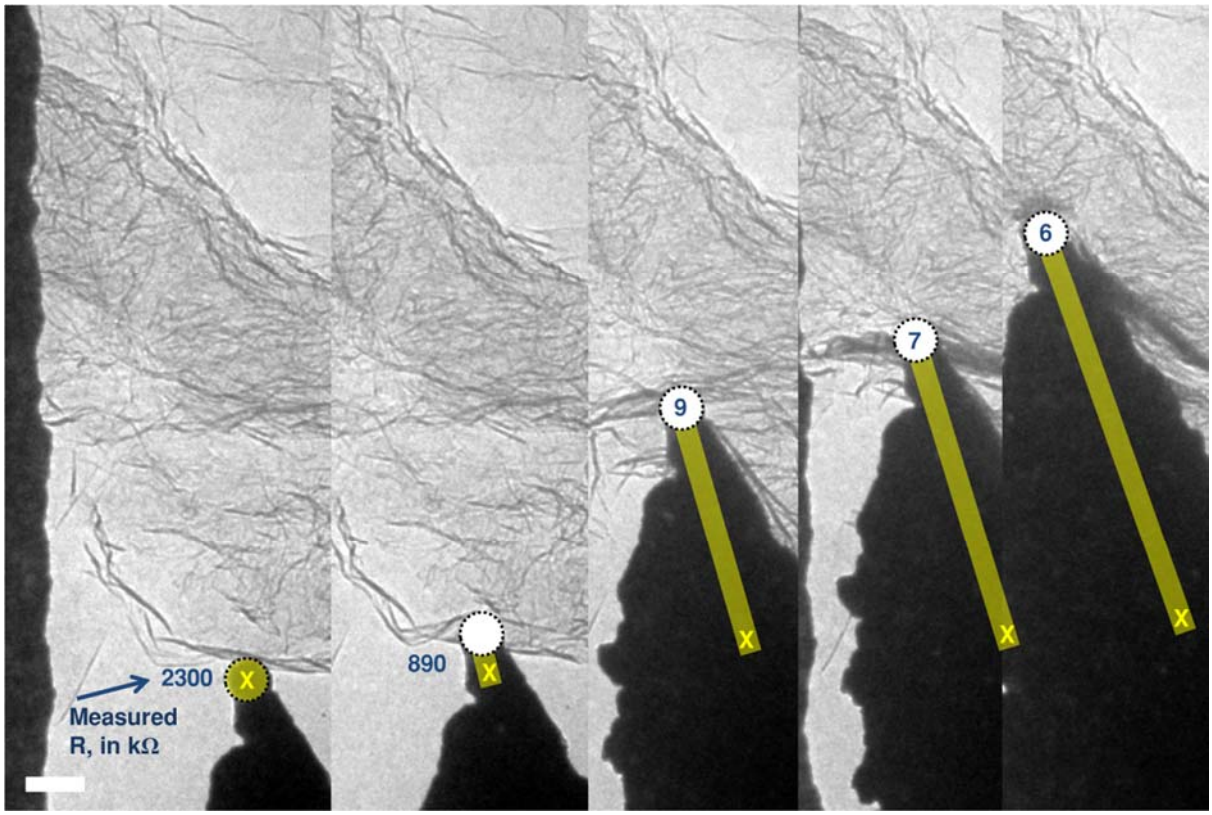

Figure 3.2.8. Sequence of TEM images of using the STM probe to drag the graphene to increase the surface area in contact with the probe. The yellow x indicates the initial contact point between the probe and the sample, the yellow line indicates the path that the probe has been pushed along the sample. The resistances are labeled at each step in unit of kΩ and the value consistently decreases despite that wrinkling, folding, and eventually tearing are induced. The corresponding IV curves are shown in the following figure. The test voltage is 1 V. The scale bar is 200 nm.

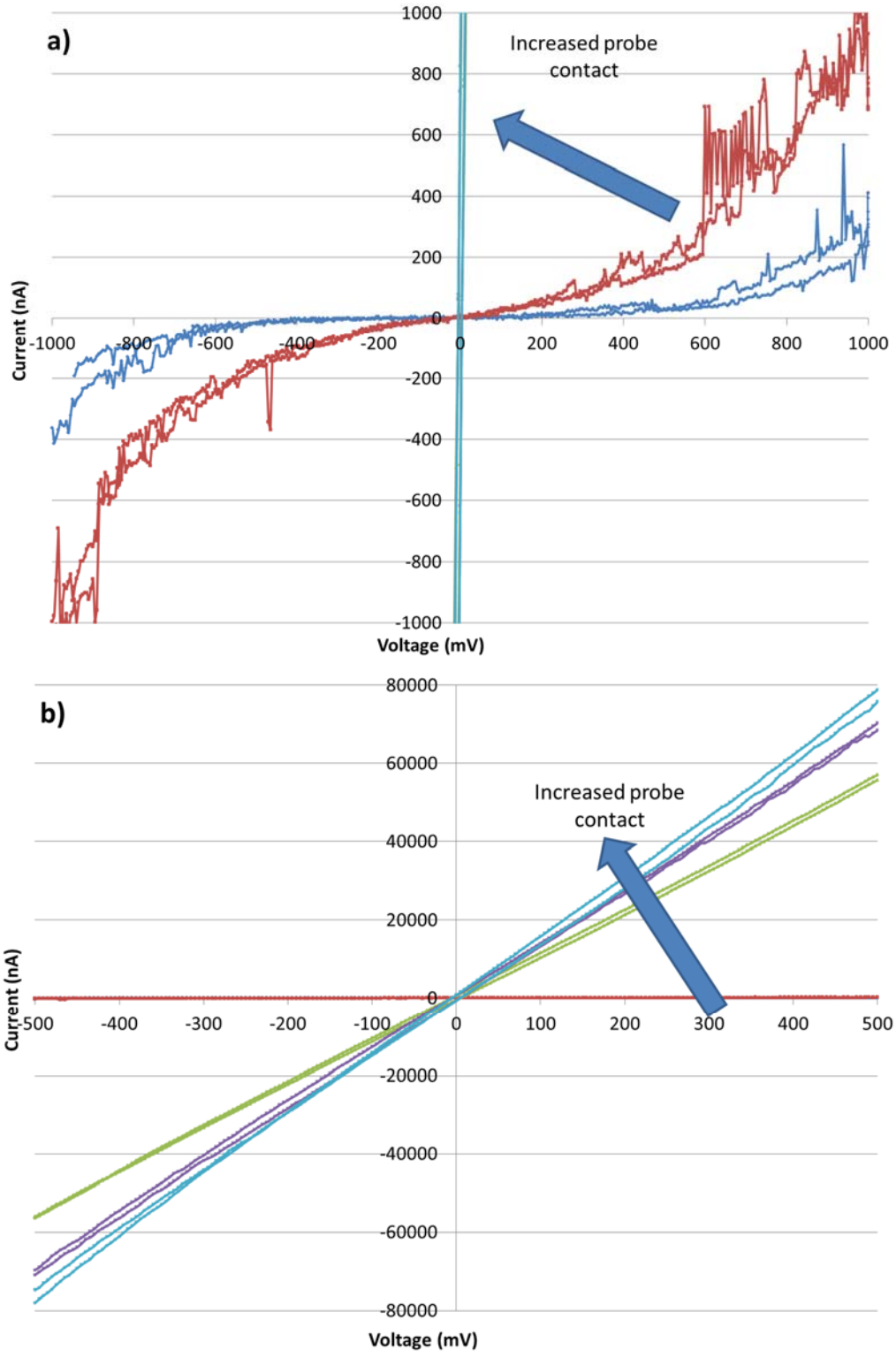

Figure 3.2.9. IV curves for the images in the previous figure showing the decrease in resistance with increased contact between the probe and the graphene sheet. a) is scaled to highlight the non-linearity of the initial measurements with poor contact while b) is scaled to highlight the linear, lower resistance cases

The next two figures, 3.2.10 and 3.2.11 show more examples of controlling the resistance with the probe contact. The first shows that the resistance at a wrinkle lowers from 50 to 15 kΩ with greater contact between the probe and the graphene. The second is a set of images of a fold interacting with the probe. The first column of images compares the resistance at different locations along the fold when the probe applies only normal contact force. The resistance varies from 32 to 71 kΩ depending on the location with no obvious correlation between structure and property. The second column, however, shows clearly that the resistance is lower if the probe is pushed to increase the contact with the graphene fold. In this case, the resistance only varies from 16 to 22 kΩ, even as the sheet tears at the last and strongest applied force. This entire resistance range is lower than all values recorded with a purely normal contact force.

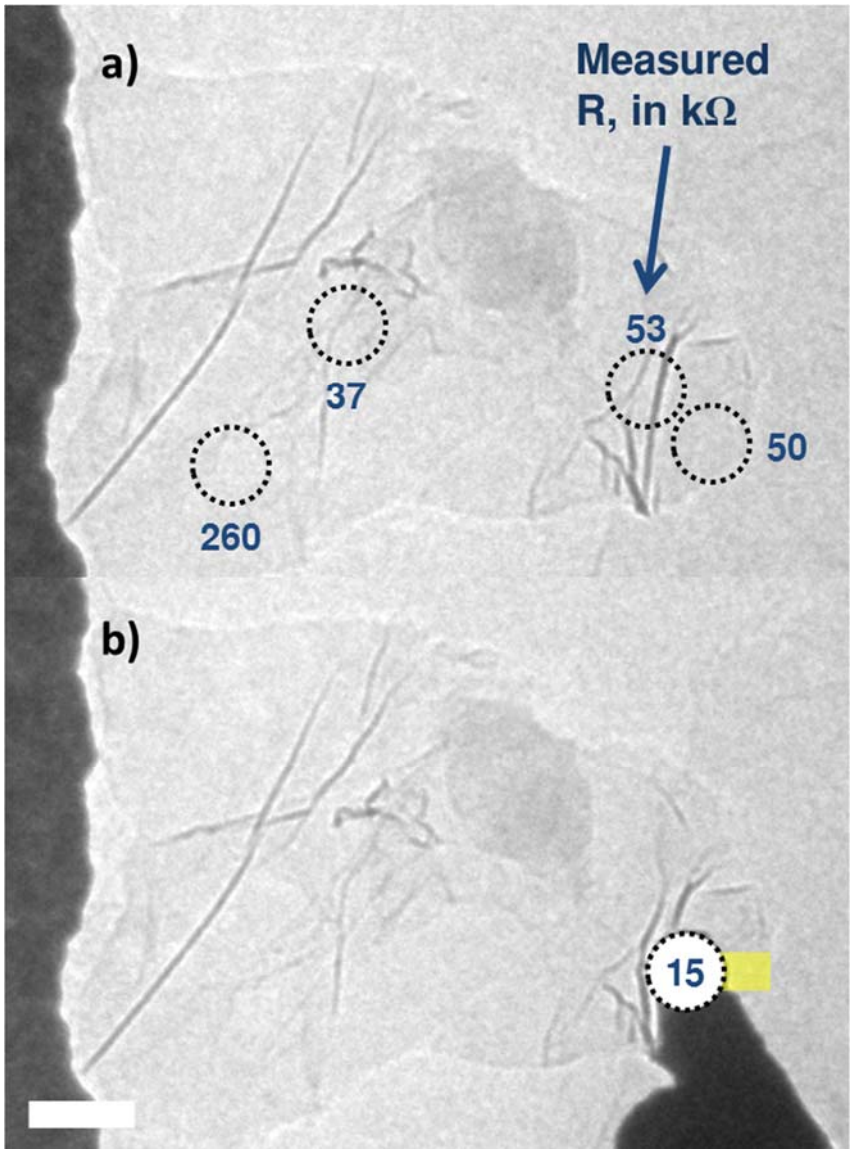

Figure 3.2.10. TEM images of another graphene flake tested for location-dependent electrical properties. The yellow x indicates the initial contact point between the probe and the sample, the yellow line indicates the path that the probe has been pushed along the sample. a) shows the case where the probe it lowered on to the graphene without any lateral motion which b) shows the case where the probe is pushed laterally along the graphene after initially touching the graphene. The results show that the resistance is lowered substantially when the probe contact area with the graphene is increased by pushing laterally. The test voltage is 1 V. The scale bar is 200 nm.

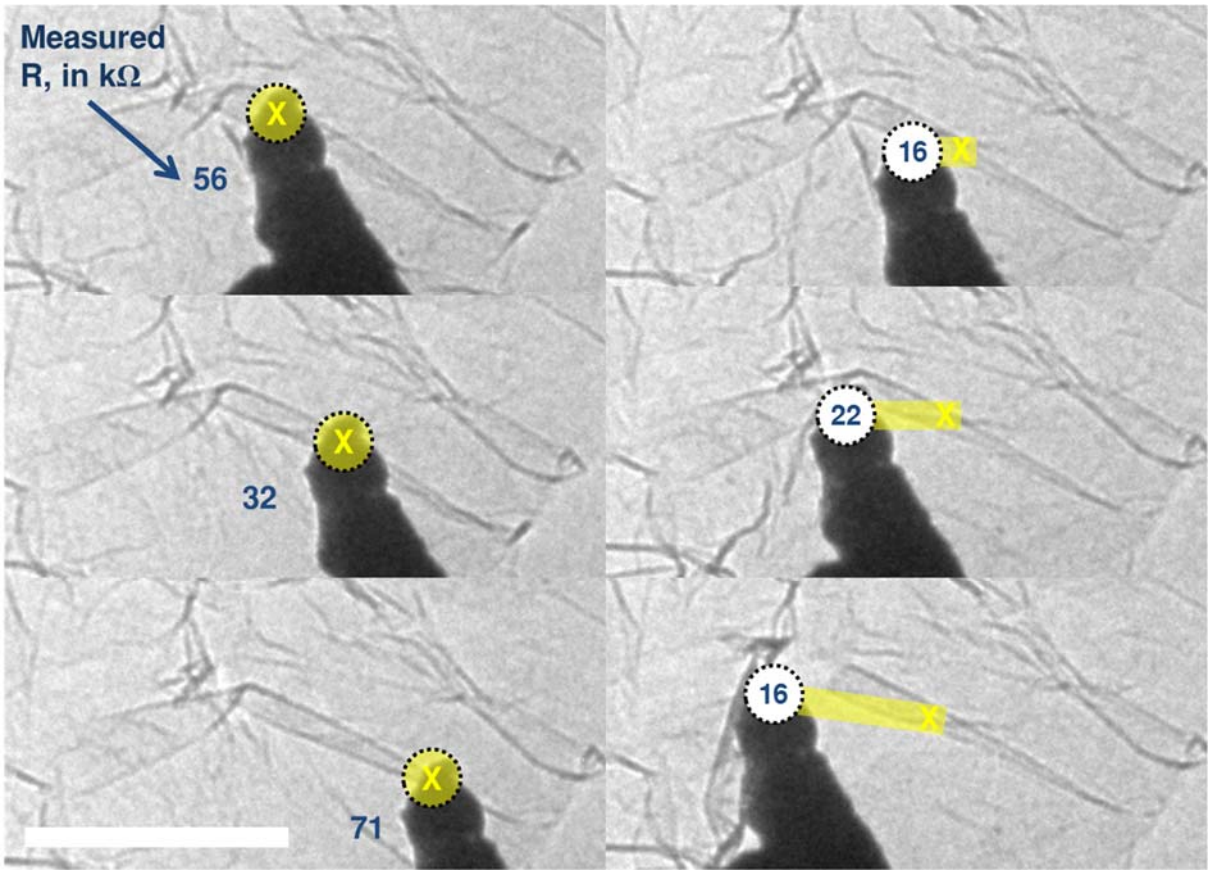

Figure 3.2.11. TEM images of a fold on a graphene sheet. The yellow x indicates the initial contact point between the probe and the sample, the yellow line indicates the path that the probe has been pushed along the sample. The first column shows the results of lowering the probe directly on to different points on the wrinkle without any lateral motion. The right column shows the results of placing the probe below on the wrinkle and then pushing it laterally long the wrinkle in order to increase the contact area between the probe and the graphene. This lowers the resistance of the system even when the applied force is high enough to tear the graphene sheet. The test voltage is 1 V. The scale bar is 500 nm.

The contact resistance between graphene has been studied previously and a summary of the results for CVD grown graphene is presented in a recent article by Asadi et al.[201] Their plot can be seen in figure 3.2.12. Generally, contact resistance can be found by comparing the resistance at different channel lengths and looking at where the line crosses the resistance axis at a channel length of 0. We show a plot of all of our measured values as a function of probe-electrode distance in figure 3.2.13. This data shows no clear

linear correlation between the resistance and the distance away from the electrode so it is not possible to extract a constant contact resisttance. If we plot on a log-log scale as can be seen in figure 3.2.14, there is an upward trend as can be expected, however it is far from linear and only fits to a 0.2 power law with a low R^2 value. Looking at the points that were obtained by dragging the probe against the sample to increase the contact area, marked by red markers, there is a decrease in the resistance and a slightly better fit to a 0.3 power law, but still far from linear correlation that can be used to back out a constant contact resistance value. This means that we can only place bounds on our contact resistance and sheet resistance as have been labeled in figure 3.2.12. The lowest measured values are 6 kΩ. Analyzing those two points, we can place upper bounds on the sheet resistance of 13 and 7 kΩ by assuming no contact resistance. However, we know from the measurements that this is not reasonable. We also know that the contact area between the graphene and the probe is around 100 nm^2 which allows us to make estimates of contact resistance for the different possible bounds on the sheet resistance. Looking at the power law fits in figure 3.2.14 we see further proof that the resistance decreases when we contact the graphene by dragging the probe against the sample to increase the contact area. The 23 kΩ decrease in base resistance as predicted by the power law makes sense if we approximately double the contact area using the drag process. This is a good approximation from the TEM images showing the graphene making contact with the sides of the probe during the dragging process.

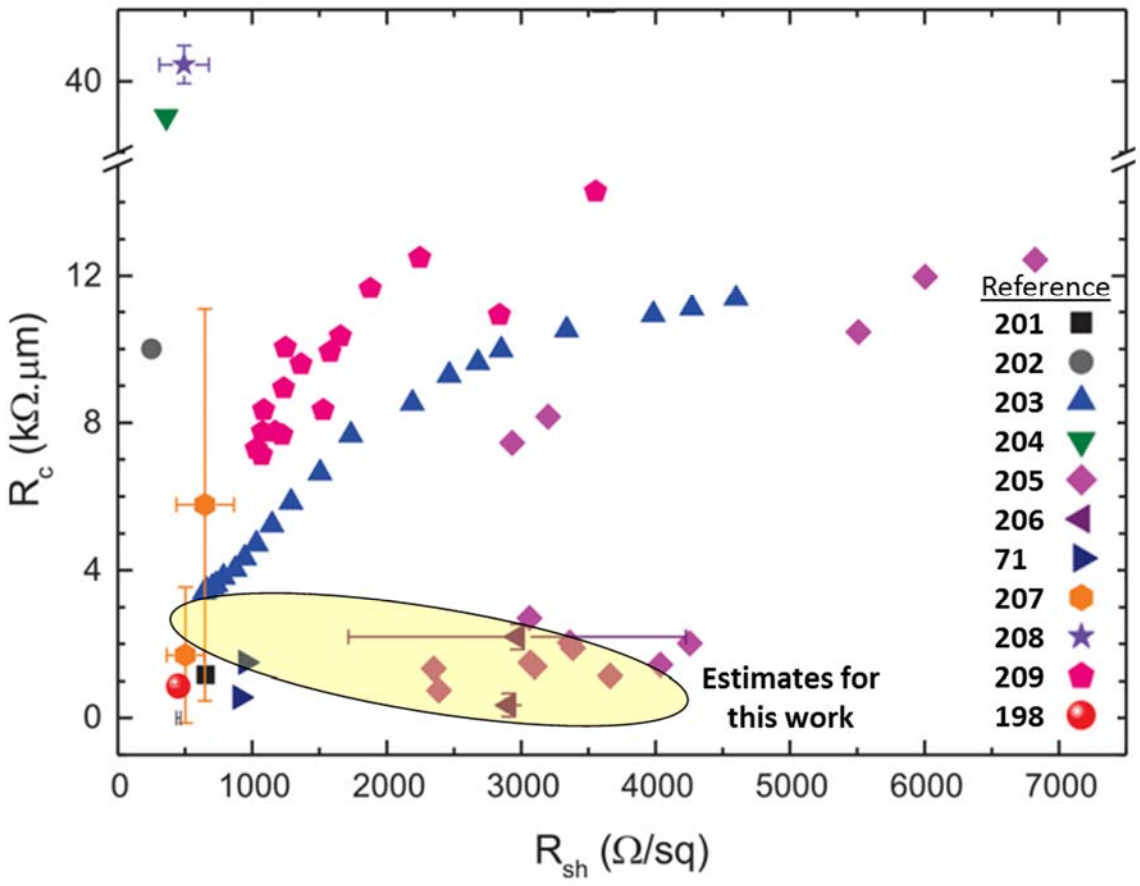

Figure 3.2.12. Plot adapted from reference[201] of contact resistances between graphene and metal as a function of sheet resistance found by different studies. The added yellow star represents the estimate that has been made for this work.

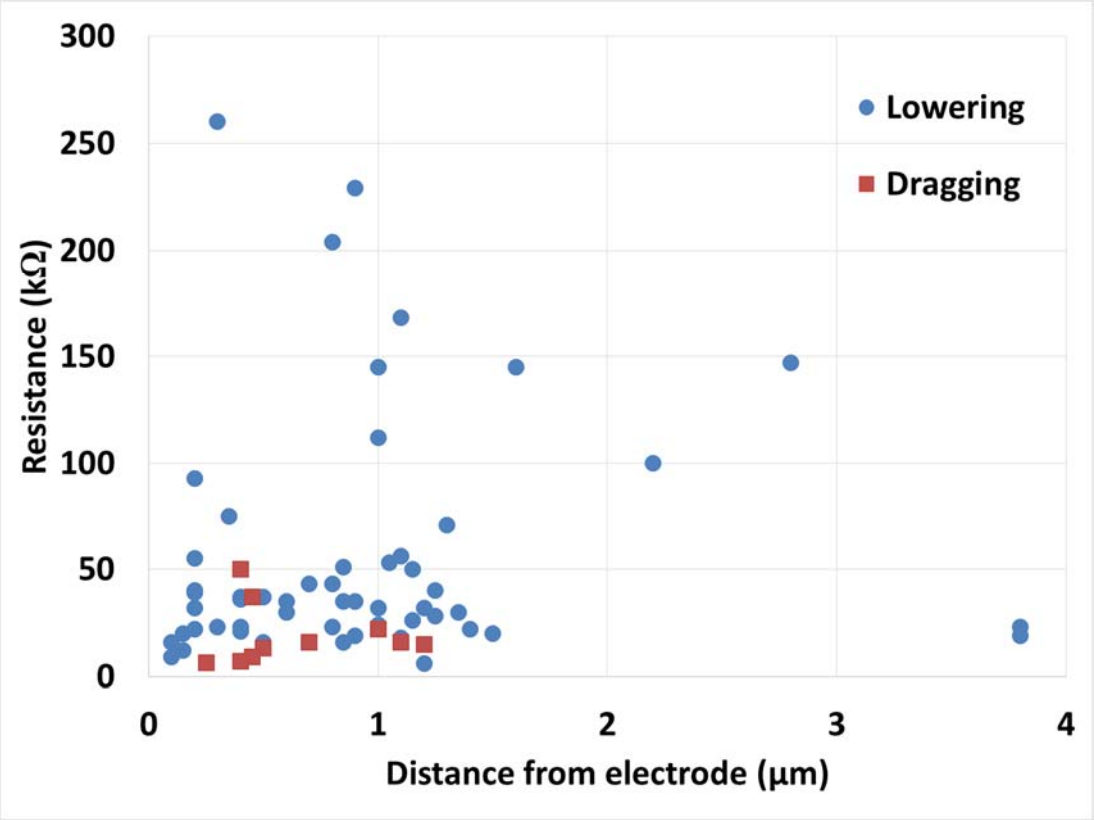

Figure 3.2.13. Plot of measured resistance as a function of distance that the probe is away from the electrode when performing the measurement. The lowering and dragging points refer to the different ways of contacting the graphene as explained above. There is no obvious linear correlation between the resistance the distance so a constant contact resistance cannot be extracted.

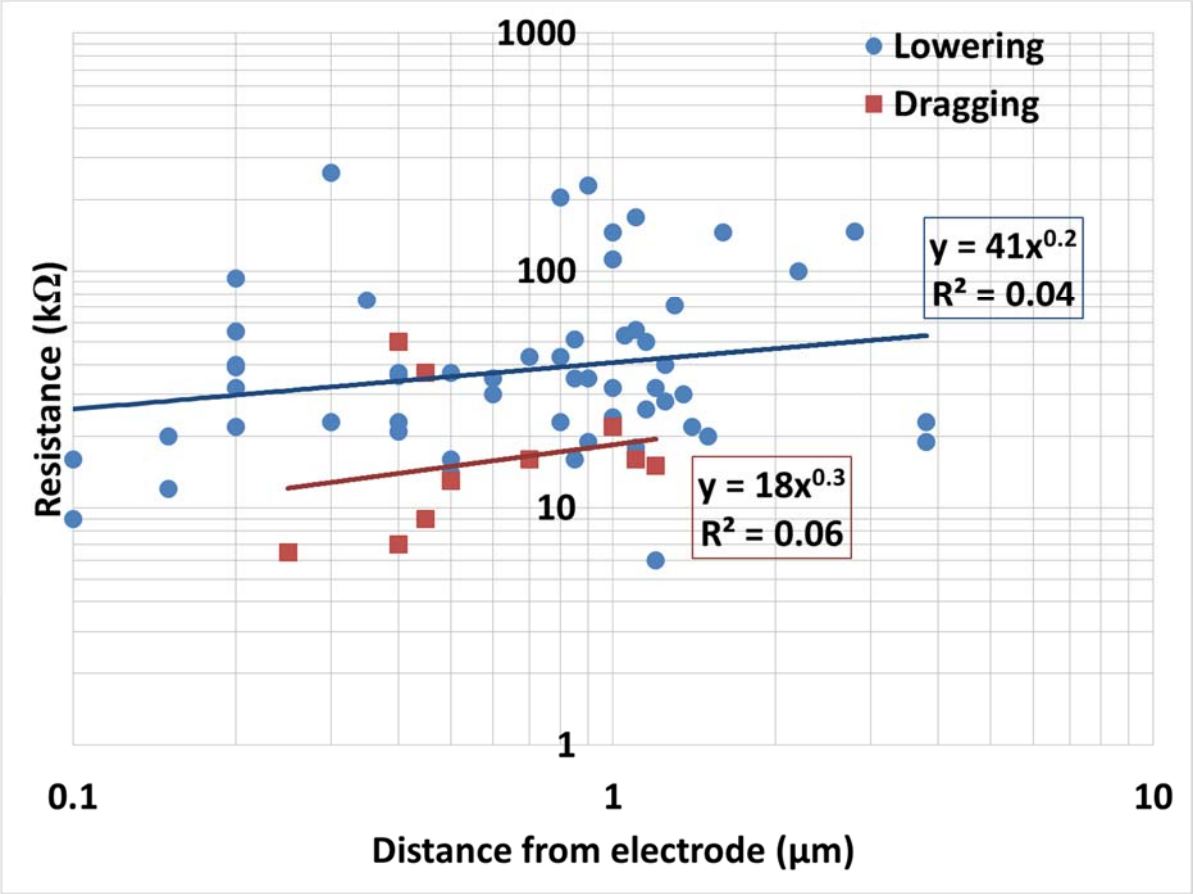

Figure 3.2.14. Log-log plot of measured resistance as a function of distance that the probe is away from the electrode when performing the measurement. The lowering and dragging points refer to the different ways of contacting the graphene as explained above. By fitting the data to a power law it is possible to see that there is no linear correlation between the distance and the resistance. Using the dragging technique to increase the contact area between the probe and the graphene causes the measured resistance to decrease by approximately 23 kΩ.

The conclusion of these experiments is that our reduced graphene sheets have a high electrical conductivity despite large amounts of wrinkling and folding. The value is to that which has been found for CVD grown graphene by several groups.[201] The Raman data and the IV data support that the graphene is slightly p-doped due to residual oxygen species.[199] These experiments have been performed on more than 20 individual sheets and with several different STM tips, both Au and Pt, and the results are reproducible so

that 4 main conclusions can be made. (1) There is never any obvious correlation between resistance and probe-electrode distance. (2) Greater amounts of wrinkles and folds does not lead to higher resistance. In fact, some cases indicate that the wrinkles may benefit the electrical transport. This can be supported by theoretical calculations on contact resistance between graphene and substrates,[202] which show that the resistance increases for rougher substrates and when the graphene conforms to the substrate surface. In our case, we have a smooth SiN substrate and rather than conform to the substrate the graphene folds and wrinkles so that it does not have as much direct contact with the substrate. (3) The overall resistance can be lowered by applying lateral force to the graphene sheets in order to induce additional contact area and force between the graphene and the STM tip. The change from non-linear to linear IV characteristics as the probe contact force is increased, backs up that the effect that we are seeing is a decrease in contact resistance. For the p-doped semimetal graphene with poor contact to the probe, the electron path between the probe and the graphene is a tunneling junction that can be overcome only at higher applied voltages which is why the IV characteristics are non-linear. Once the IV data becomes more linear the resistance starts to decrease and we are left with a low overall resistance. (4) The graphene-gold electrode contact has low contact resistance for our system. Even though the graphene is only laying on top of the Au electrodes, this contact does not seem to affect the overall resistance nearly as much as the probe graphene contact, which we show that we can control. Even when the probe is used to push down the graphene directly on top of the electrode, which would presumably improve the contact, the resistance and IV characteristics are not much different than for those when the probe is contacting the graphene away from the gold

electrode. The most important aspects of these results, is that very simple and imperfect graphene systems have high conductivities that can benefit future electronics devices. Rather than focusing on fabricating defect-free, flat graphene with close to intrinsic properties, it seems that in real-world systems, where substrates and impurities are unavoidable, slightly doped and wrinkled graphene outperforms CVD grown graphene because it is less susceptible to contact resistance losses. As I will show in the next chapter, the thermal transport seems to be equally robust through wrinkles and contact with a substrate.

Chapter 4. In-situ TEM Thermal Characterization at the Nanoscale

4.1 Methods for *in-situ* TEM heating

For more than two decades, transmission electron microscopes (TEMs) have been used to observe materials as they undergo temperature changes.[203] Today this remains an incredibly valuable method for observing phase changes and other material property modifications at the atomic scale in real time.[204] The instrumentation and approaches used for these types of experiments have evolved over time and even during this project several different *in-situ* holders and fabrication techniques have been used.

The first type of holder that has been used is a simple heating holder. Both a Philips Heating Holder PW 6592/05 as as seen in Figure 4.1.1 and a Gatan single tilt model 628 heating holder have been used for simple experiments when electrical characterization is not necessary. These types of holders use resistive wires around the sample opening on the holder in order to heat the entire sample. There are also

thermocouples that allow for temperature control. These types of holders are widely used for experiments where the main point of the research is to correlate temperature and structural changes.[205] The disadvantages are that the thermal output from the holder tells the temperature of the holder, not specific structures that are the focus of the observation. This means that the assumption of thermal equilibrium always has to be made. Especially when using SiN membranes as the substrate, this is a poor assumption to make, because of the low thermal conductivity of SiN.

Figure 4.1.1. Image of a Philips Heating Holder PW 6592/05 which can be used to increase the temperature of an entire sample through resistive wires on the holder.

In order to have more precise control of the temperature and location of heating, we have developed methods for local heating of the materials under study. The main method for doing this is to pattern heater wires or electrodes on to the nanostructure that allows for both passive and joule heating, as was explained in detail, in the previous chapter.

4.2. Indium for thermal characterization

The Cumings group has coined the term, electron thermal microscopy (EThM) to refer to a technique that involves using indium nanoislands deposited on the backside of SiN membranes as binary temperature markers.[111] The group has used this technique to characterize the thermal behavior of MWCNTs.[15, 206] The technique relies on the contrast change of indium in specific dark-field (DF) TEM conditions when it transitions from solid to liquid at 156 C. The main advantage of this technique, compared to many other thermal characterization techniques, is the high spatial resolution possible thanks to the small size of the indium nanoislands, which can be seen in Figure 4.2.1. At this time, the speed of the measurements is only limited by the microscope cameras. The measurements can be repeated many times without change to the islands because they are naturally encapsulated in an indium oxide shell which does not get damaged, unless the temperature is brought above the diffusion temperature of indium through indium oxide.

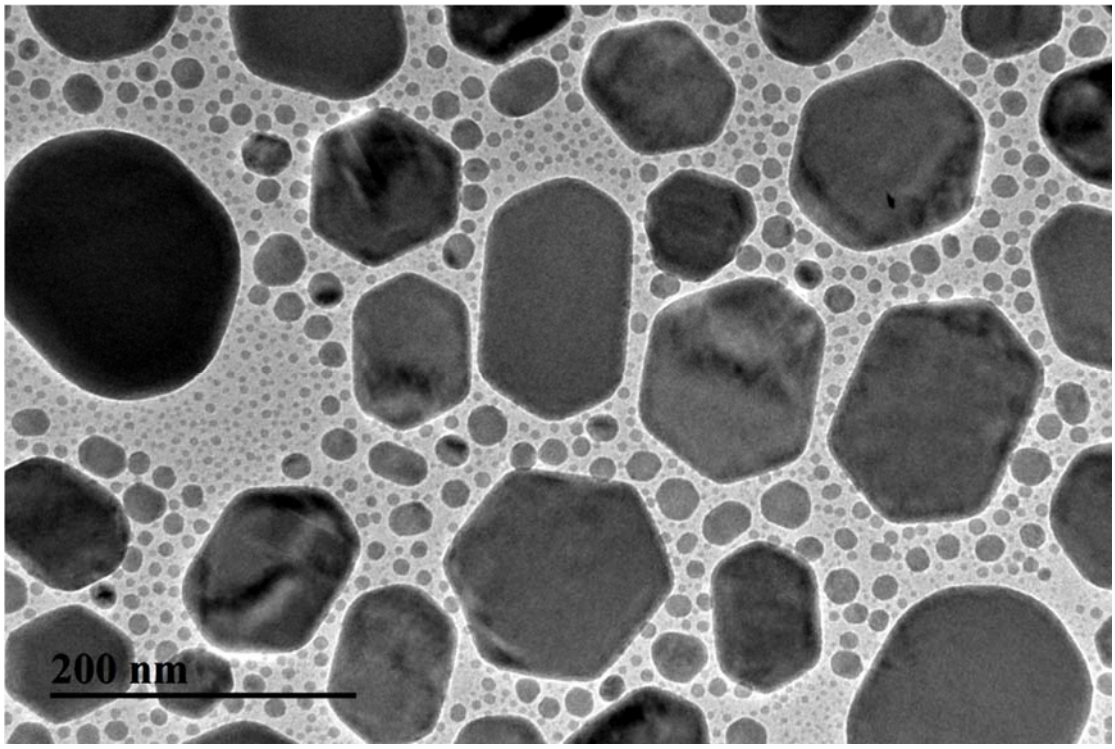

Figure 4.2.1. TEM image of indium islands encapsulated in oxide shells deposited thermally on the backside of SiN membranes.

It is always important to characterize how the measurement technique that is being used is affecting the behavior of the material being measured. Here, when looking at the thermal properties of nanostructures in TEM, it is important to understand how the electron beam is introducing heat into the system. To do this, I characterize the beam heating at two different accelerating voltages. I will show results of using the EThM technique with both a heating holder and a heater wire to look at the difference in heat introduced to the system when using different accelerating voltages.

Figures 4.2.2 and 4.2.3 demonstrate the melting of indium nanoislands on the backside of SiN membranes, at accelerating voltages of 120 kV and 200 kV respectively, as the temperature of the heating holder is increased. The temperature is held for several minutes and thermal drift is allowed to stop prior to increasing the temperature another

increment of 10 C. The first thing that is evident, is that the melting does not start at 160 C as would be expected, meaning that the thermal transport from the heater to the membrane is poor. However, this is no surprise since the thermal conductivity of silicon nitride is only 30 W/mK in the bulk state, and even lower for membranes.[207] The next thing to observe is that the change from solid to melting is much more gradual for the 200 kV case than for the 120 kV case. At 200 kV the melting can be seen already at 170 C, but does not cover the entire viewing area until 250 C. For 120 kV, on the other hand, the melting happens quicker from 220 C to 250 C. This is visible evidence that the beam is contributing more to the melting at the higher accelerating voltage. Another thing to note is that the contrast on the islands is stronger on the solid islands at 120 kV and stronger on the melted islands at 200 kV. This is most likely a result of multiple scattering effects that are stronger at 120 kV than at 200 kV.

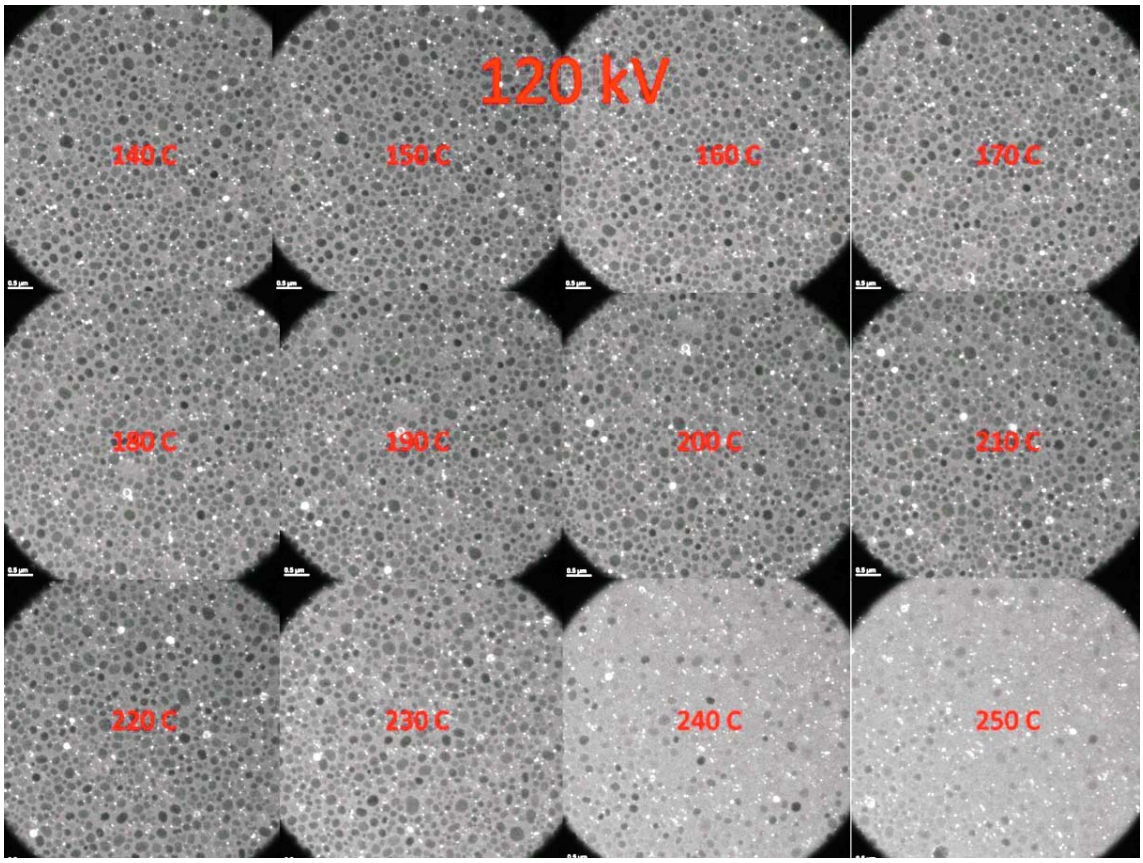

Figure 4.2.2. A series of TEM images captured at an accelerating voltage of 120 kV demonstrating the melting of indium nanoislands on the backside of SiN membranes as the temperature of a simple heating holder is increased.

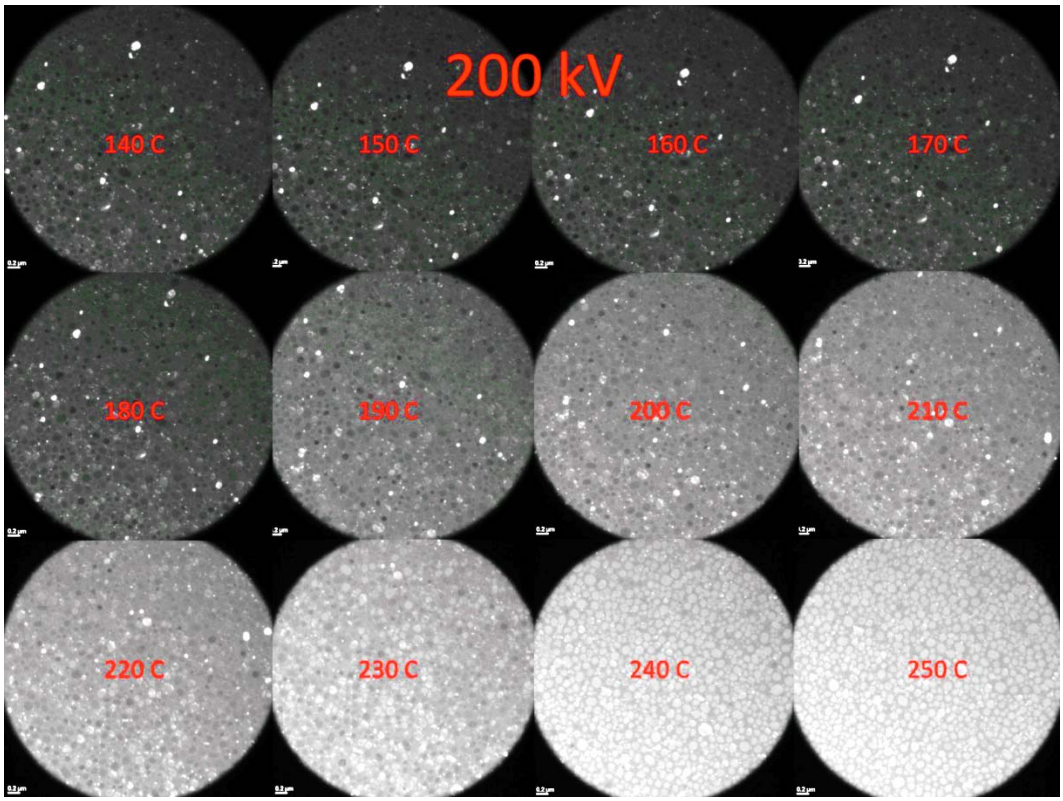

Figure 4.2.3. A series of TEM images captured at an accelerating voltage of 200 kV demonstrating the melting of indium nanoislands on the backside of SiN membranes as the temperature of a simple heating holder is increased.

For the above tests, all of the parameters including the spot size were the same. The only thing that is changed is the accelerating voltage. The next thing that I tried was keeping everything except the spot size constant. These tests were done at 200 kV. At normal imaging conditions with a spot size of 3 the electron dose hitting the screen at 200 kV is 5.4 e/nm^{2}s. If the spot size is increased to reduce the electrons coming in to contact with the sample, the dose hitting the screen is only 0.27 e/nm^{2}s. This test is performed by putting the heating holder at 200 C so that some of the islands in the field of view are melted, and some are not. All of the islands should be near the transition temperature, so small changes in temperature caused by the beam should be noticeable. The results are shown in Figure 4.2.4 and they indicate that there is no change in the melting, meaning

that the change in the dose does not affect the temperature of the sample. This leads to the conclusion that it is the energy of the electrons hitting the screen not the number of electrons that determines the temperature of the sample.

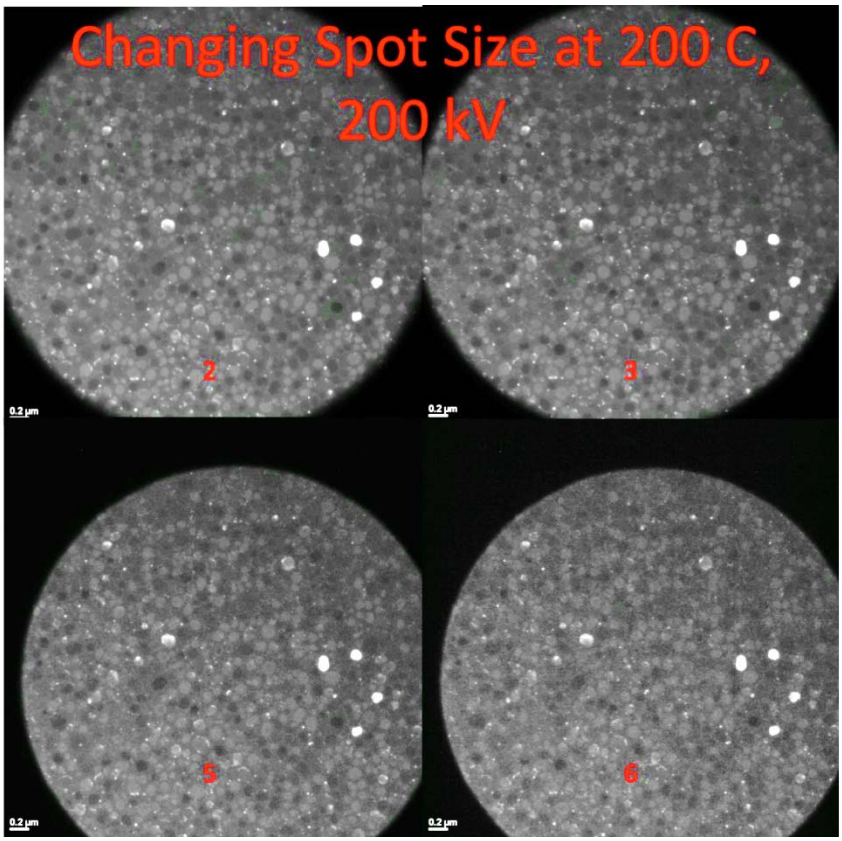

Figure 4.2.4. TEM images at 200 kV with the heating holder set to 200 C showing that some, but not all of the indium islands are melted. There is no change in the melting even as the spot size is increased, meaning that this does not lead to a change in temperature of the sample.

In order to get more quantitative results of the heating that the beam is contributing to the sample, a heater wire device was used. By comparing IV data and melting data, it is possible to extract how much power the beam is contributing between the two different accelerating voltages. Figure 4.2.5 shows the IV curves for the two different cases, and Figure 4.2.6 shows TEM images of the two different melting scenarios. A few interesting observations were made from this test. One was that the

resistance of the wire, though only by 1% (1936 Ω versus 1913 Ω), was higher for the 200 kV case versus the 120 kV case. One reason for this may be that the temperature is higher in the 200 kV case, so the metal has a different coefficient of resistance. Another explanation may be that the lower energy electrons interact more with the sample, thus adding more electrons to the system and lowering the measured resistance. The second important finding from this test is that about 5 μW of energy needed to be added to the system to cause similar melting at 120 kV compared to 200 kV. The difference was a 6.1% difference in power required. Comparing that with the 1% difference in resistance, it can be concluded that the difference in melting has to do with the temperature change in the substrate caused by the beam, more so than with the change in the resistance of the wire caused by the beam. With rough heater wire calculations, using the following equation:

$$\Delta T = \frac{V^2 L}{2RkA}$$

Where V is the applied voltage, L is the length of the wire, R is the resistance of the wire, k is the thermal conductivity of the wire, and A is the area of the wire, the change in temperature, ΔT, is about 6 C.

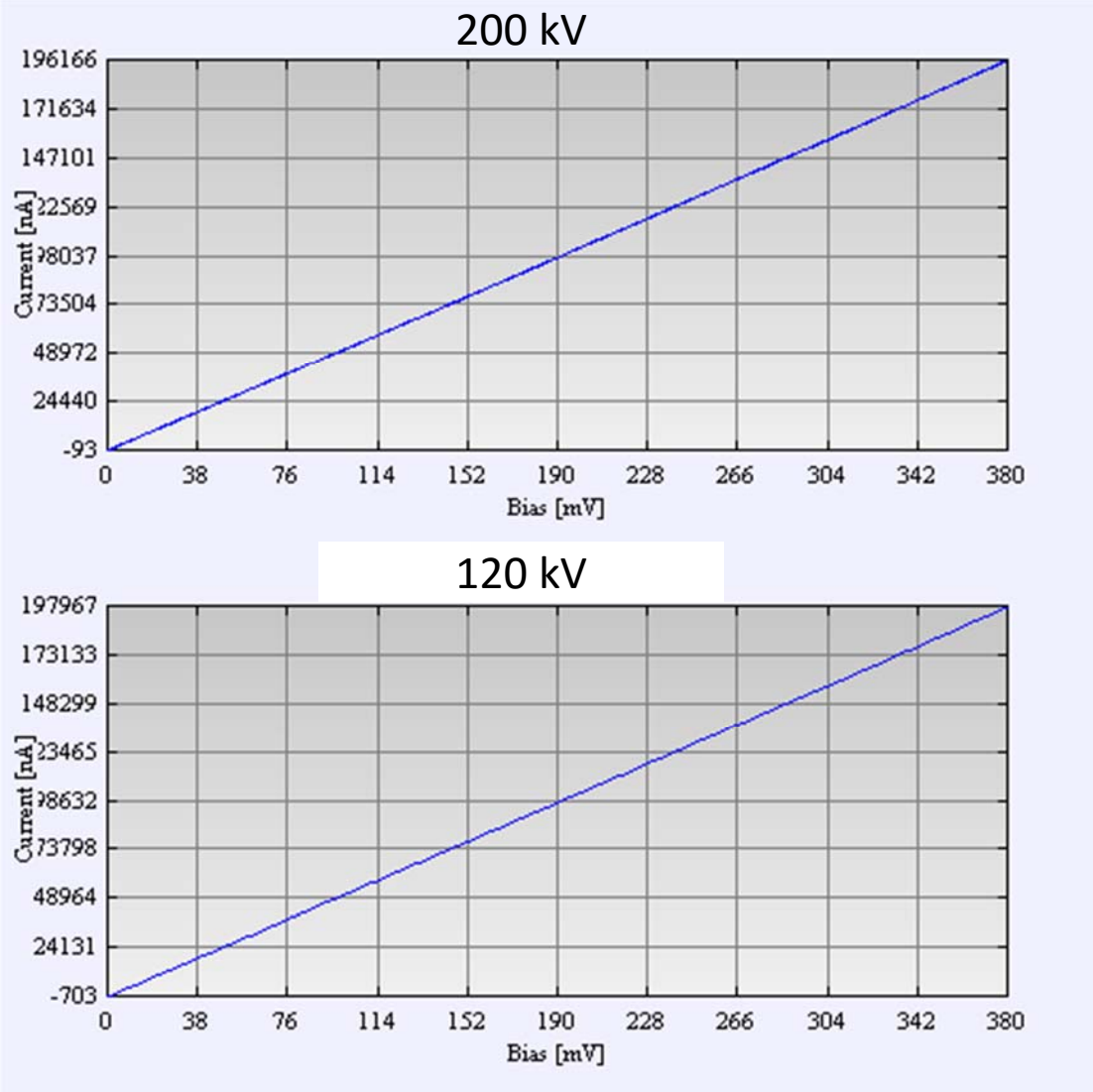

Figure 4.2.5. Plots showing the IV data for a heater wire collected under beams with different accelerating voltages. The difference in resistance is just 1%.

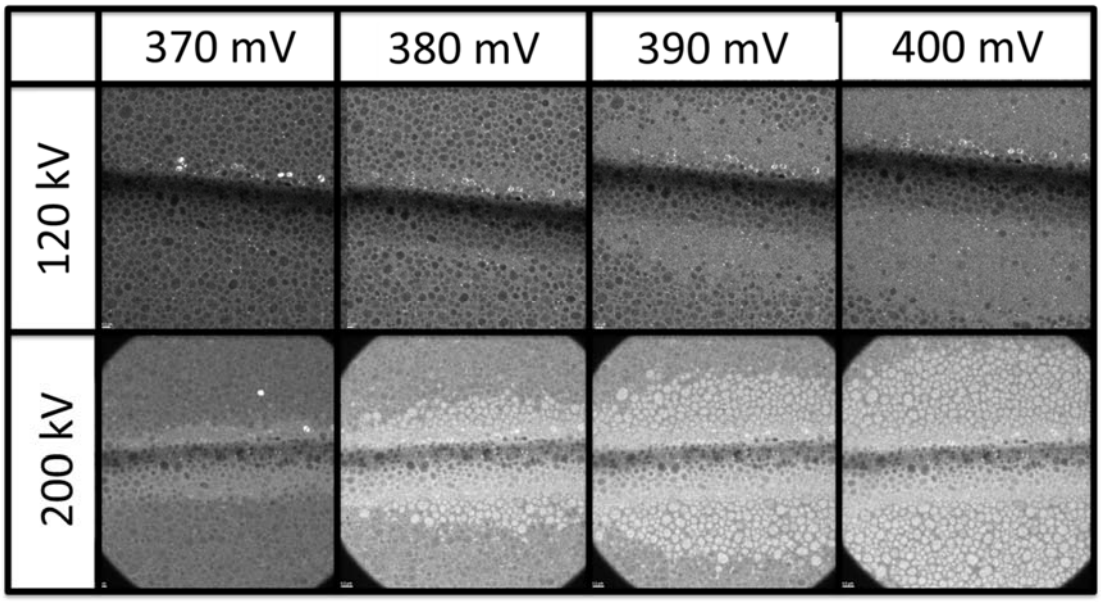

Figure 4.2.6. TEM images of island melting for the same device under different accelerating voltages. Melting begins at lower power for 200 kV than for 120 kV.

This leads to the next important issue to solve when performing these experiments; the thermal conductivity of the silicon nitride. As can be read in the doctoral thesis of Norvik Voskanian, the thermal conductivity of silicon nitride membranes has been difficult to calculate.[208] In the modeling of the devices, the results can be made to converge if a spatial or voltage dependence is added to the silicon nitride thermal conductivity. However, it is not clear what kind of physical phenomena are causing these dependencies.

In order to get a better understanding of the thermal conductivity of the SiN membranes, I have fabricated slits in the membranes and performed tests where I have better control of the heat spread through the membrane. This means that heat transport can be confined through nanostructures rather than through the substrate. I have developed two different methods for fabricating slits in the thin membranes. The first

method is a combination of electron beam lithography (EBL) and reactive ion etching (RIE).[209] The second method is FIB.

For the first method, EBL, I frequently use a pattern of 8x8 slits as can be seen in Figures 4.2.7 and 4.2.8. In order to prepare these samples, the first step is to prepare a pristine SiN membrane to be hydrophilic, preferably using a gentle oxygen plasma clean, and then spinning resist. For the slits, no metal lift-off has to be performed so the cut shape of the resist is not critical, but the thickness of the resist has to be enough that the RIE used does not go through the resist when removing the wanted amount of SiN. I found that to get through 50 nm of SiN it was enough to spin two layers of PMMA at 5000 rpm (baking them separately) to protect the rest of the membrane. Using an SF_6 and CH_4 etch, the etch rate is almost 20 times faster for PMMA than SiN so to etch through 100 nm of SiN it's necessary to protect the membrane with 2 μm of resist. Another important consideration for this technique is the exposure of the resist during alignment. Figure 4.2.8 shows an example where three corners were used to align the EBL write and too much of the resist was exposed or developed, so the etch went through to unwanted parts of the SiN. In this case, the membrane did not break, but in many cases, these types of problems lead to the membrane breaking during the etch. In order to remove the resist completely, it is generally not enough to use acetone and/or PRX, but rather requires a few iterations of oxygen plasma cleaning. Since the membranes are fragile, especially after slits have been added, I have found that it is important to perform the oxygen cleaning in steps rather than performing one long cleaning. Sample parameters that work well for removing left over resist is 4x40 seconds O_2 clean at 200 mtorr and 10 W. Each

of the 40 second etches removes approximately 50 nm of resist residue. If a longer single etch is used the membrane tends to break, most likely from thermal stress.

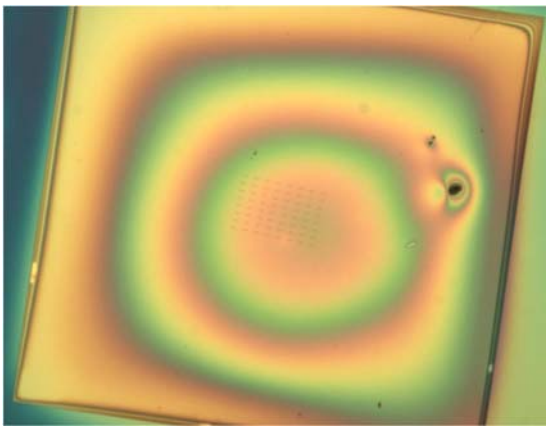

Figure 4.2.7. Image of a 250x250 μm^2 silicon nitride membrane after an EBL pattern has been developed in dual layers of PMMA.

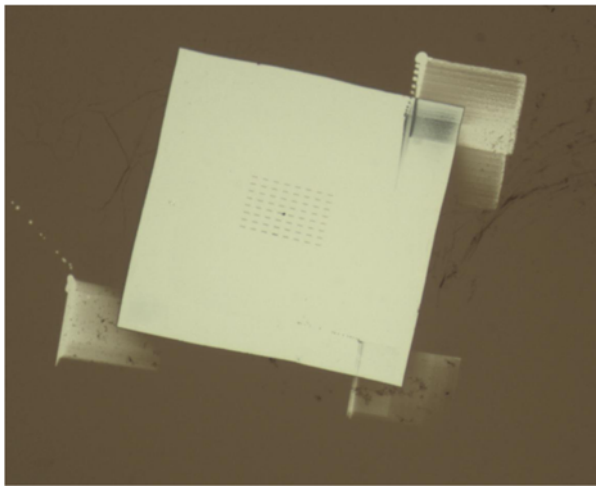

Figure 4.2.8. Image of a silicon nitride membrane after an EBL pattern has been etched out using RIE and the resist has been washed away with acetone and oxygen plasma cleaned. The corners of the membrane where the EBL alignment was performed can been seen as partially etched away.

In order to reduce stress on the membrane from adding the slits, they were kept to about 5 μm in length and 100 nm in width as can be seen in Figure 4.2.9. The image also shows that the process adds lots of residues that must be cleaned off properly before the sample can be used for experiments.

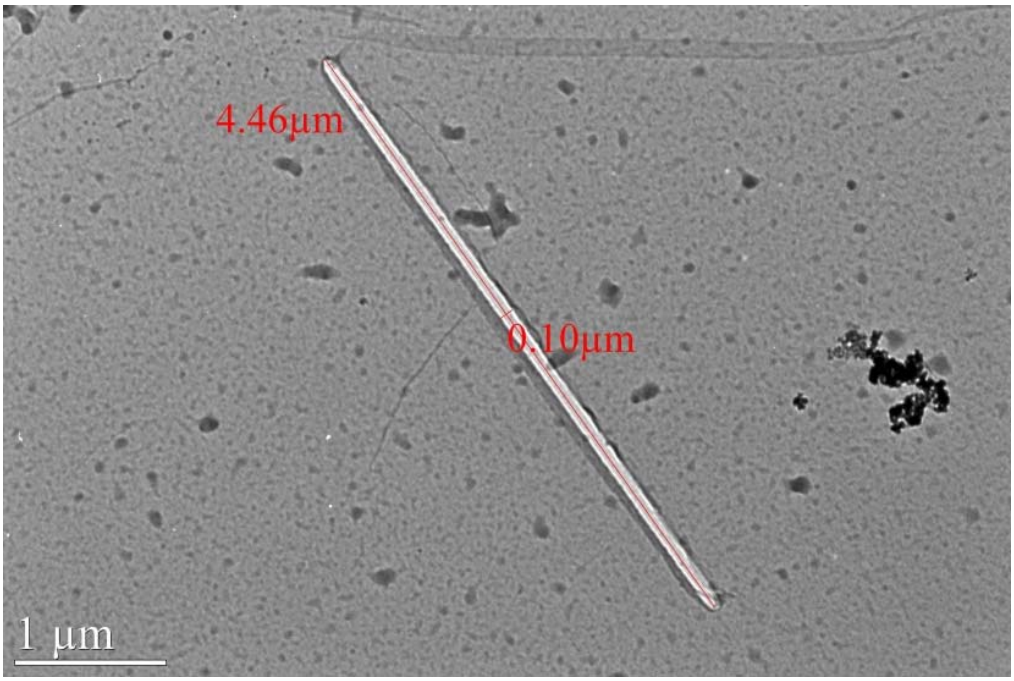

Figure 4.2.9. TEM image showing the dimensions of a slit etched via RIE.

For some applications it was preferable to have trenches rather than slits in the membrane, for example, so that indium can be deposited continuously on the backside, as can be seen in the SEM image in Figure 4.2.10. In order to have control over the trench depths, the etch rate of the RIE recipe used had to be precisely calculated. Two methods were used to characterize the depth of trenches made in the membranes; AFM and DF TEM. AFM is a straight forward and obvious choice for measuring step heights, but in this case it was not optimal because the AFM tip easily broke the fragile membranes when moving from the smooth SiN surfaces to the sometimes deep trenches.

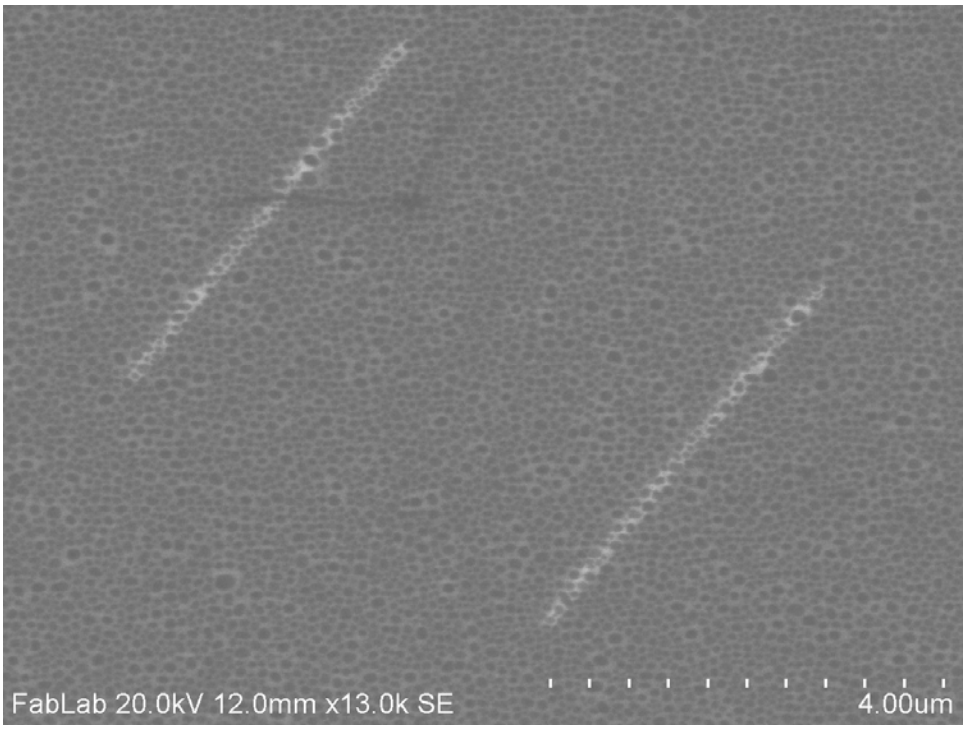

Figure 4.2.10. SEM image of 2 trenches in a SiN membrane with indium deposited on the backside of the membrane.

In order to measure more trench depths quickly and to confirm those obtained by AFM, DF TEM was used. With DF TEM it is possible to compare the intensities of the dark field scatter to calculate the thickness of the SiN material. Since the thickness of the membrane is well known from the manufacturer, it is simple to compare the intensity of the thin trench regions to estimate the thickness. An example of this can be seen in Figure 4.2.11. Using both of these techniques, I confirmed an etch rate of approximately 4 nm/sec for the recipe that was used.

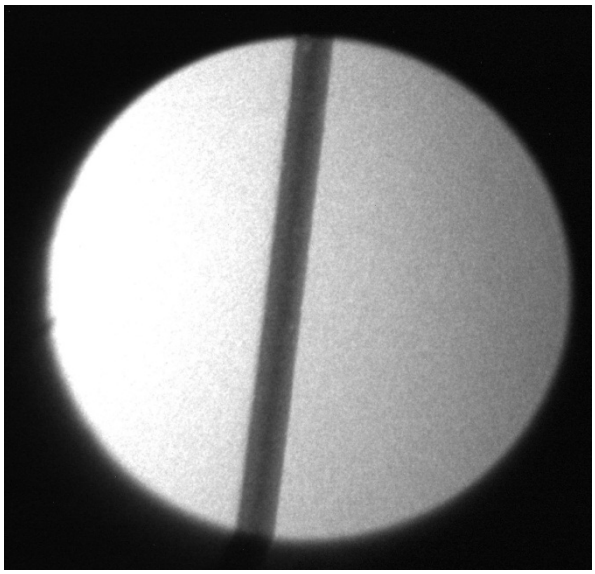

Figure 4.2.11. DF TEM image of a 100 nm wide trench in a SiN membrane. Using the correct DF conditions allows for analysis of the thickness to be made by comparing the scattering contrast of the different regions.

The second method that I used to fabricate slits was FIB. Examples of FIB created slits can be seen in Figures 4.2.12 and 4.2.13. Creating slits in this way is very simple and allows for very precise control of size and location, without adding much stress to the membrane. One downside of this method is that the gallium ions can alter the structure of the SiN near the slit, depending on the implantation depth (energy dependent). Another downside is the time of fabrication, since each slit has to be made individually. In cases where many slits are desired, this is not an optimal method.

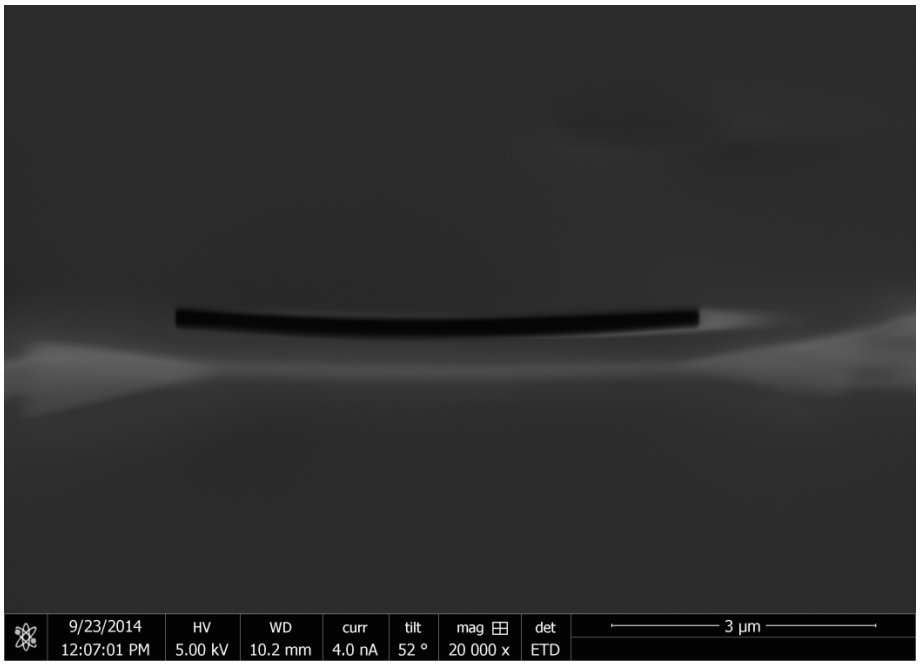

Figure 4.2.12. SEM image of a FIB fabricated slit on a SiN membrane.

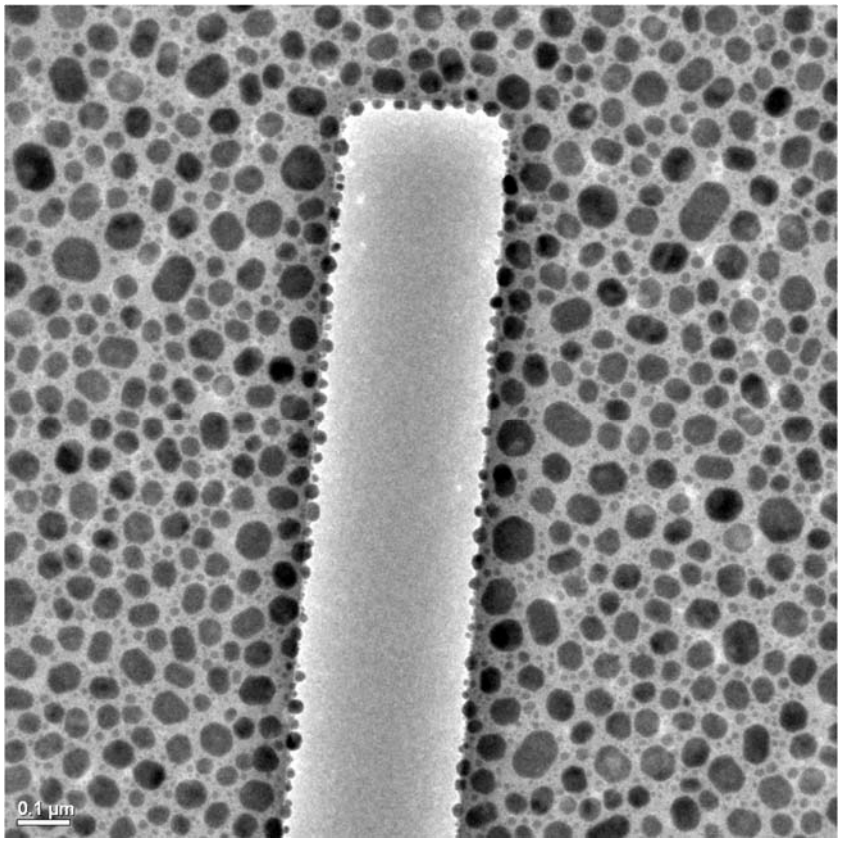

Figure 4.2.13. TEM image of a slit fabricated in SiN membranes using FIB with gallium ions. Indium has been deposited after the slit was fabricated.

The first test that was performed, after the fabrication method was developed, was to put a trench on the side of a heater wire to control the heat spread and look at the behavior of the silicon nitride thermal conductivity in these systems. Figure 4.2.14 shows a bright field image of the device that was made. A trench is chosen, rather than a slit, so that the indium layer on the back can be continuous and so that the only thing that is different on the two sides of the slit is a SiN mass change.

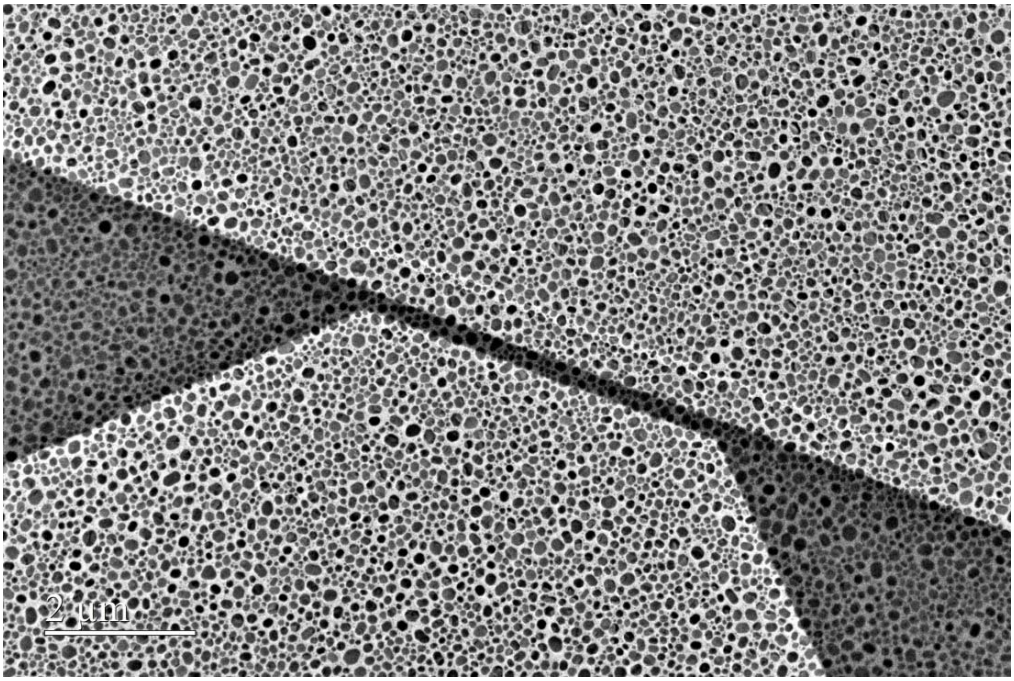

Figure 4.2.14. Bright field TEM image of a SiN membrane with a heater wire and an etch trench on the frontside and indium islands deposited on the backside.

The hope was that this device would give additional insight in to the yet not well-understood thermal transport behavior of the silicon nitride. What this device confirmed was the same phenomena that Norvik Voskanian showed in his thesis, that the thermal conductivity of silicon nitride cannot be modeled as a constant in these experiments. Traditionally, phonon mean free path has been thought of as an intrinsic property, but recent work has shown that the thermal conduction is sensitive to size and surface

parameters.[210, 211] Another promising result shows that Fourier's Law breaks down and that a two part equation is needed to account for differences in long wavelength and short wavelength phonons.[212] The conclusion of this seems to be, that at the nanoscale, long wavelength phonons at the surface dominate heat transport. This means that even though room temperature phonon mean free path is estimated to just be 5 Å, structures on the order of 100s of nms play a role in changing the thermal transport.[213] This may explain why the previous EThM results for silicon nitride thermal conductivity could be explained as a function of distance from the heat source. Figure 4.2.15 shows a plot from Norvik Voskanian's thesis with his results of thermal conductivity of silicon nitride as a function of distance from the heater wire.

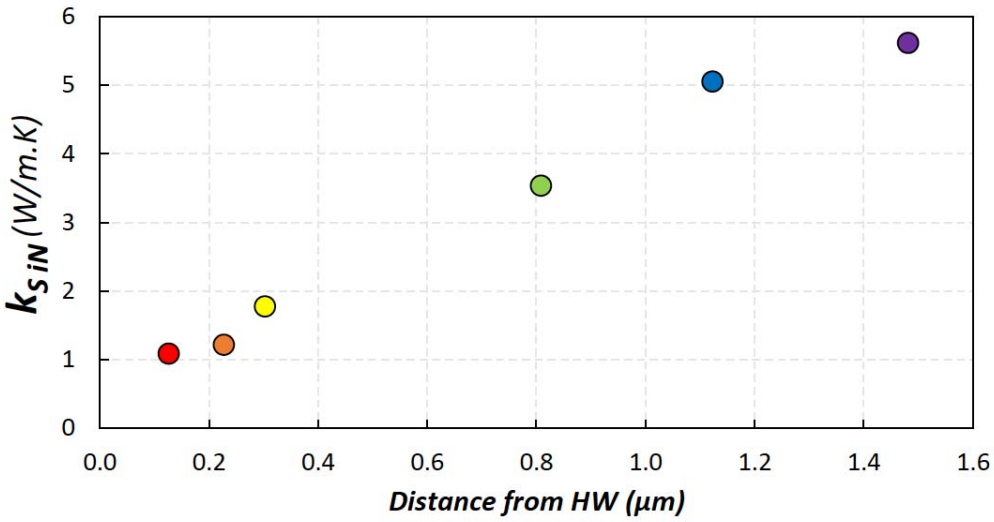

Figure 4.2.15. Results from the thesis of Norvik Voskanian showing that the thermal conductivity of the silicon nitride effectively increases further away from the heater wire.

The relation that the effective thermal conductivity increases further away from the heater wire is backed by other work, which explains long mean free path phonons as dominant in polar substrates. The results from my device show a similar trend, as can be

seen in Figure 4.2.16. The thermal conductivity is hampered close to the heat source, and then quickly increases about a micron away, before showing some signs of leveling out.

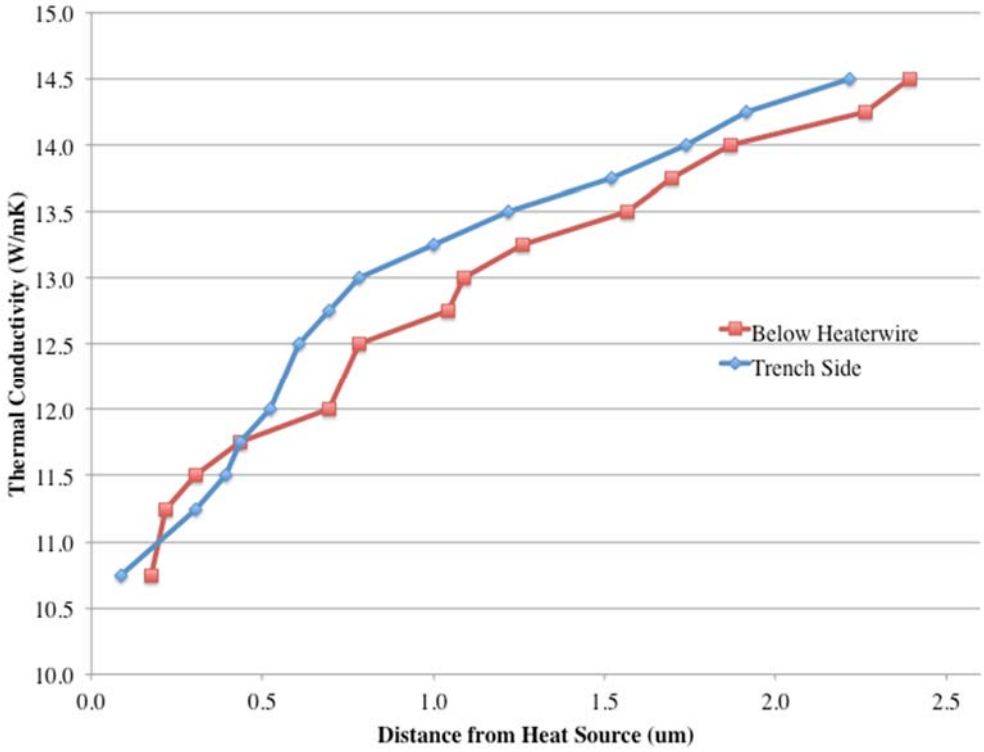

Figure 4.2.16. Plot of the change in the effective thermal conductivity of the silicon nitride as a function of distance from the heater wire shown in Figure 4.2.12.

Images of the melting and COMSOL modeled melting can be seen in Figure 4.2.17. It is clear that with the exception of the changing thermal conductivity, discussed above, that the modeling matches well with the physical results of the experiment. The plots in Figure 4.2.18 show just how well the model and the results match. The significant contribution of this device, as compared to those in Novik Voskanian's thesis, is the trench. In all cases, it was possible to model the trench thermal conductivity as one fourth of the thermal conductivity of the rest of the silicon nitride. The trench is 25 nm of silicon nitride, while the rest of the membrane is 50 nm. This means that a reduction in

mass by 50% led to a reduction in thermal conductivity by 75%, proving that there are surface effects that contribute to the thermal conduction that are disrupted by the introduction of the trench. Recently, other groups working with silicon nitride, have come to similar conclusions about surface effect and thermal transport.[210]

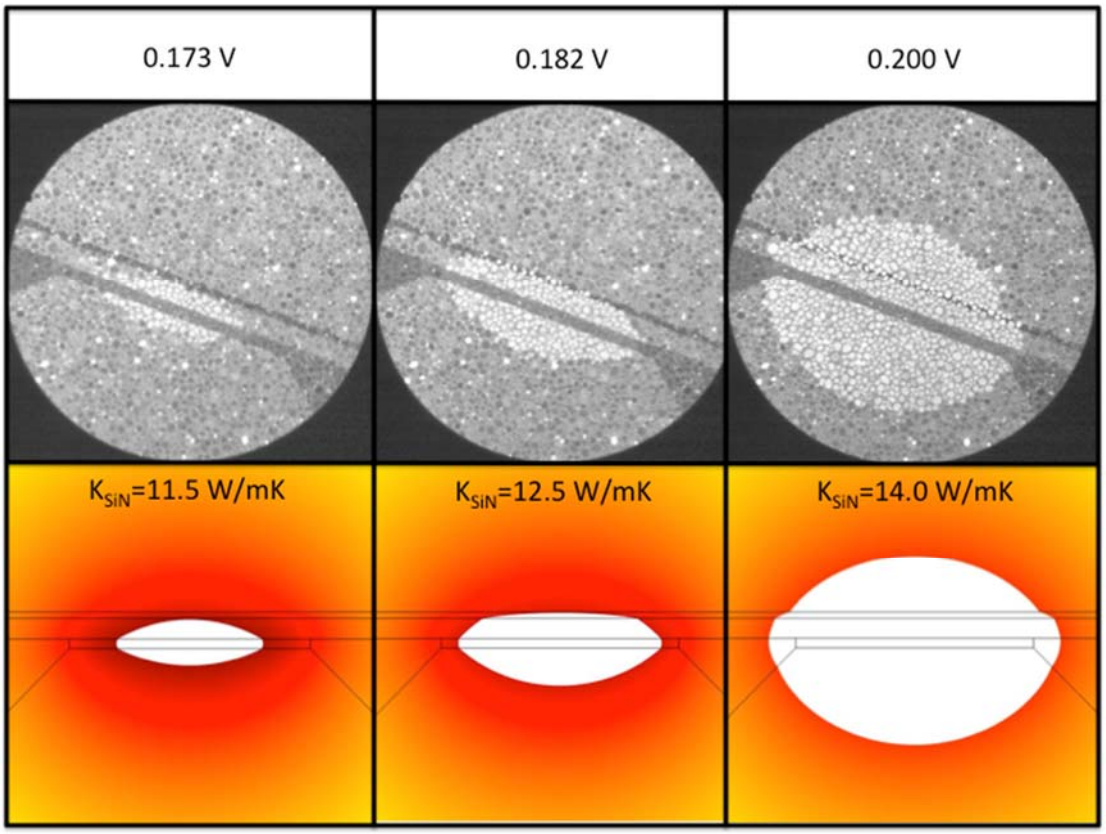

Figure 4.2.17. Three examples of TEM images and COMSOL modeled results for different melting scenarios caused by changing the voltage applied to the heater wire.

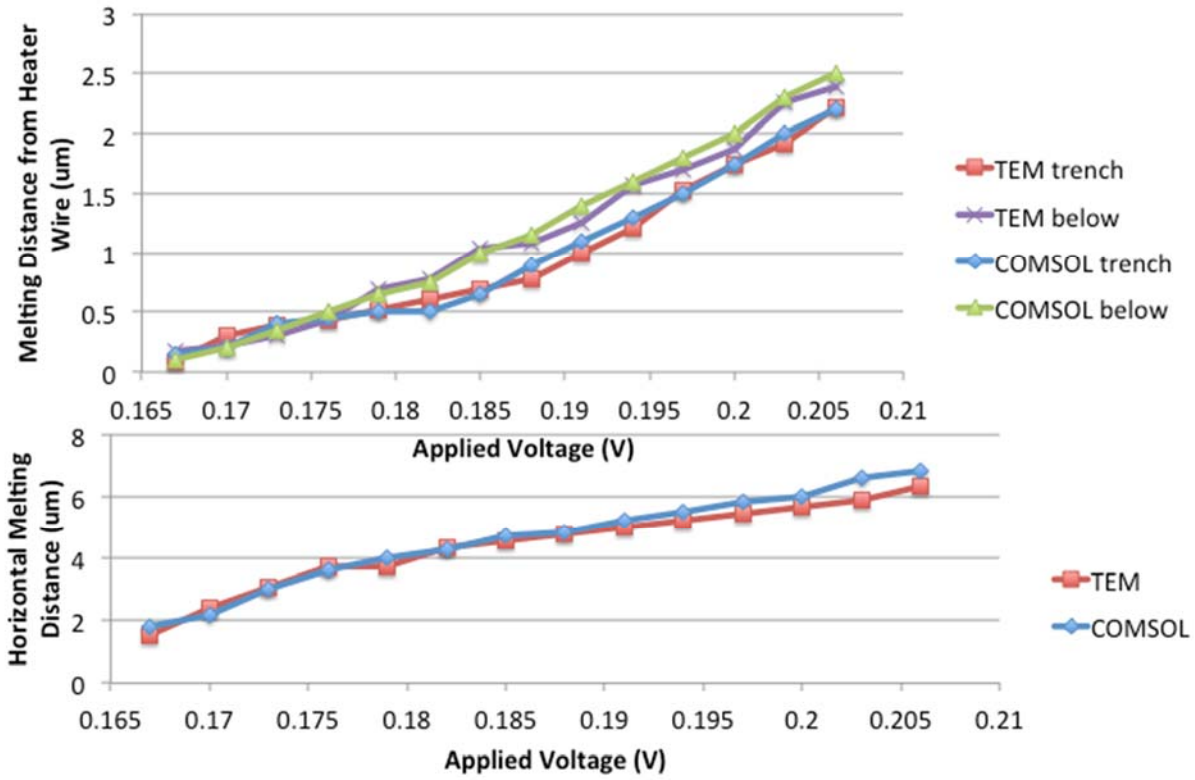

Figure 4.2.18. Plots showing the agreement between the *in-situ* melting results and the COMSOL modeled results. There is very good agreement between the two.

4.3 BNNTs

As was outlined in the introduction, BNNTs have promising thermal properties for heat management in electronics.[214, 215] Theoretically, the thermal conductivity is as high as 6,00 W/mK.[52] The problem is that there are few experimental studies, and those that exist have varying results ranging from tens to hundreds of W/mK.[54, 214] When using nanomaterial in real life systems, it does not matter if they have amazing intrinsic properties, if contact resistances hinder them from performing effectively.

The study that I perform focuses on the effective thermal conductivity of a single BNNT deposited on a SiN substrate. EThM as described in the previous section is used to measure the temperature profile of the substrate during the experimentation. The fabrication steps required to make this testing device are as follows:

1. Perform electron lithography to pattern lines in two layers of resist on pristine 50 nm SiN membranes
2. Use reactive ion etching (RIE) to etch slits through the SiN membrane
3. Remove remaining resist using acetone and then plasma clean surface
4. Perform electron lithography to pattern alignment marks and large pads on to sampled
5. Deposit 3 nm Cr and 27 nm Au
6. Lift-off unwanted metal and resist with acetone and then plasma clean surface
7. Spin cast solution suspended BNNTs on to the membranes
8. Use TEM to locate desirable BNNTs
9. Create an electron lithography pattern to contact the desired BNNT
10. Perform electron lithography to place heater wire onto BNNT and metal pads on ends to anchor the tube
11. Deposit 30 nm Pd
12. Lift-off unwanted metal with acetone
13. Deposit indium nanoislands on the back side of the membrane to serve as temperature probes

Figure 4.3.1 shows a TEM image of the device at step 8 in the above list, where a desired BNNT, nicely-suspended over a slit, has been located. Au alignment marks are also visible. The next step is to deposit a heater wire over the tube in order to control the heating of the tube. Metal squares are also added to the ends of the tube in order to increase the thermal contact between the tube and the substrate.[15] The slit allows for analysis to be made of how much heat is transferred through the tube as compared to through the SiN.

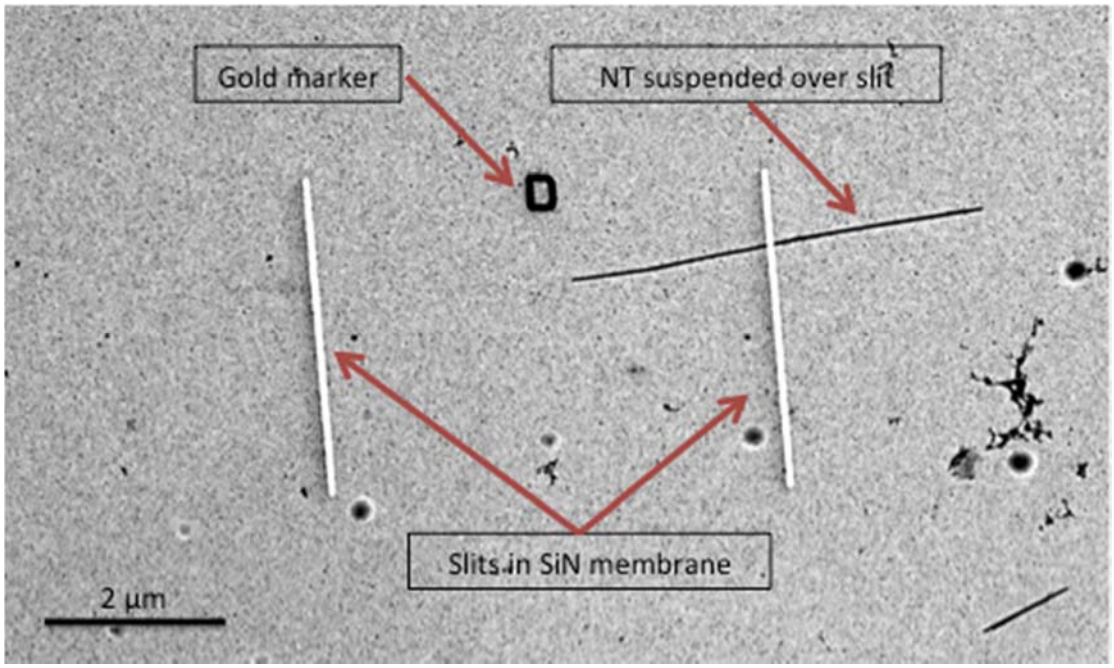

Figure 4.3.1 TEM image of a BNNT suspended over a slit in a SiN membrane.

This device is tested in the custom 4-probe holder made by the Cumings group. Figure 4.3.2 shows the completed device in dark field prior to the beginning of melting. The BNNT that is tested is about 56 nm in diameter and 7.4 µm long. The heater wire is placed parallel to the slit in order to prevent heat spread through the SiN, and instead,

forcing it to go through the BNNT to the other side of the slit. In dark field, the slit appears dark and the BNNT is not visible.

	Diameter [nm]	Length [µm]
BNNT	~56	~7.4
Slit	~137	~5
Pd heater wire	~350	~6.5

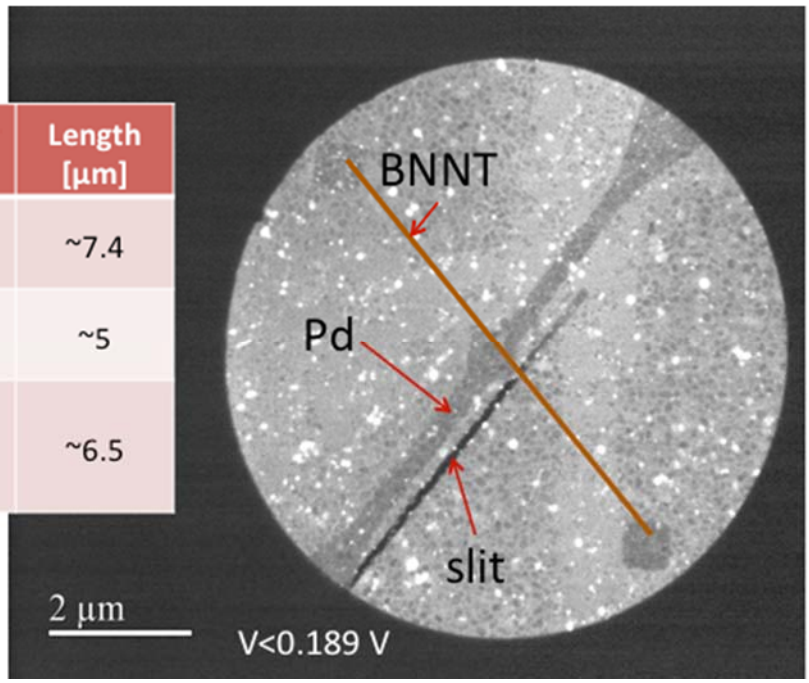

Figure 4.3.2. Dark field TEM image of the completed device including the measurements of each of the structures in the image.

Current is passed through the heater wire slowly and carefully until melting can be seen in the center of the wire. Since the slit is not completely at the center of the heater wire, the melting is not symmetrical. It is evident from the results in Figure 4.3.3, that the melting mostly travels around the top of the slit rather than over the slit through the BNNT. This would not be the case if the BNNT effective thermal conductivity was as high as the intrinsic thermal conductivity. Even with the metal anchors at the ends of the tube, the thermal contact resistance is preventing the BNNT from fully spreading the heat away from the heater wire.

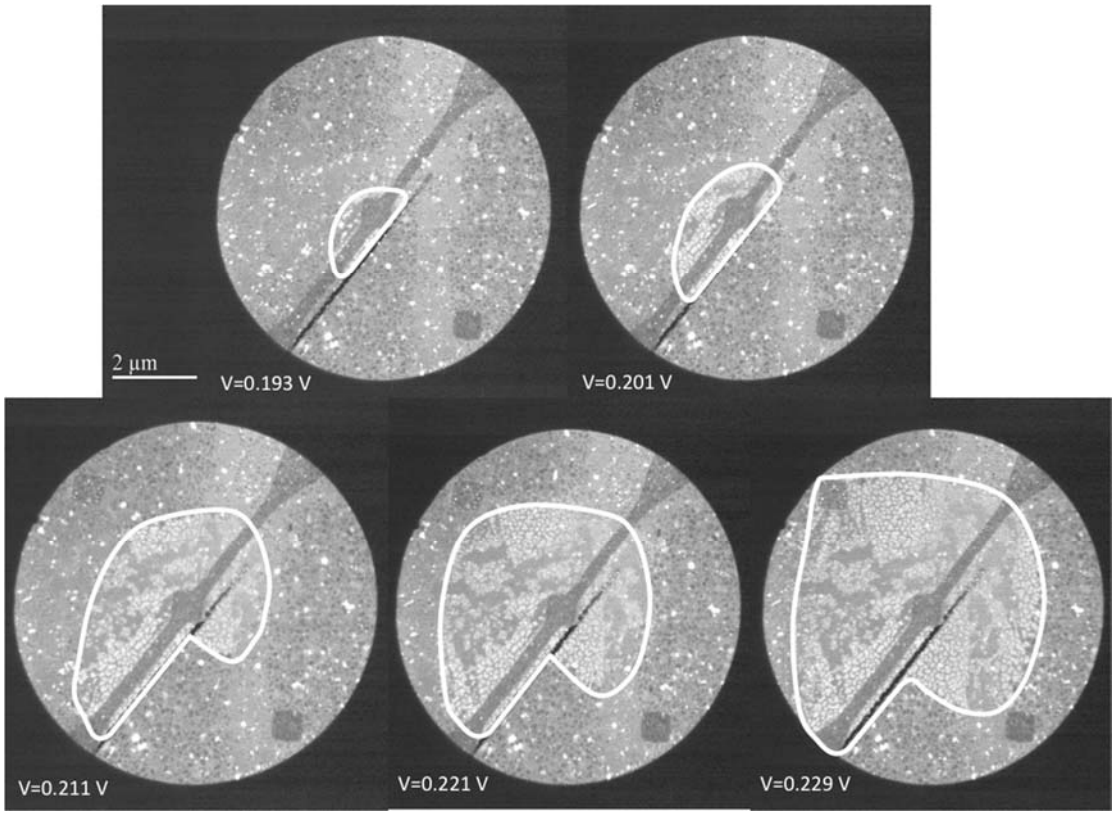

Figure 4.3.3. Sequence of dark field TEM images of the device as the voltage across the wire is increased to induce heating and melting of the indium islands on the backside of the membrane.

In order to extract quantitative results from the *in-situ* results, it is necessary to use finite element analysis, in this case, COMSOL to model the properties of the system. By fitting different effective thermal conductivities of the BNNT to the model, it is possible to compare the shape of the melting profile at each voltage to most accurately find the effective thermal conductivity of the BNNT in this system. Figure 4.3.4 shows a CAD drawing of the modeled system.

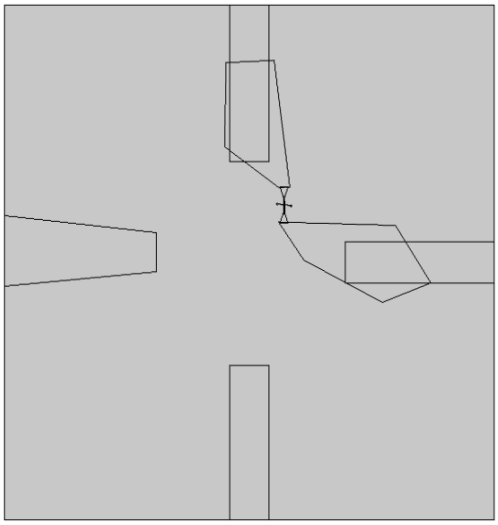

Figure 4.3.4. CAD drawing of the system as modeled in COMSOL.

The values that were used in this model were:

Property	Value
d_{Pd} [nm]	30
d_{CrAu} [nm]	30
d_{mem} [nm]	70
r_{BNNT} [nm]	28
T_0 [°C]	10
T_{edge} [°C]	23
ρ_{0_Pd} [Ωm]	2E-7
ρ_{0_CrAu} [Ωm]	2E-8
ρ_{0_SiN} [Ωm]	1E14
α_{Pd} [1/K]	0.0015
α_{CrAu} [1/K]	0.0034
κ_{mem} [W/mK]	9.5

The main assumptions that were made in the modeling were:

1. That the electrical conductivity of metals has a temperature dependence as follows:

$$\sigma = \frac{1}{(\rho_o(1 + \alpha(T - T_o)))}$$

2. That the thermal conductivity of the metals has a temperature dependence according to the Wiedermann-Franz Law:

$$\kappa = L_o T \sigma$$

3. That the total power dissipation of the heater wire determines the heating of the system according to:

$$-\nabla \cdot (\kappa \nabla T) = Q_{dc}$$

The results of the modeling with different effective thermal conductivities at a bias of 0.229 V are shown in Figure 4.3.5. The first model shows what the melting profile would look like if the effective thermal conductivity was 18 W/mK as Tang et al.[214] found it to be in their work. Comparing to the last TEM image in the previous figure, it is clear that the effective thermal conductivity is higher than that. The BNNT is contributing more to the transfer of heat than a wire with only 18 W/mK would. One the other end of the spectrum, looking at the far right simulation in Figure 4.3.5, assuming that the BNNT's effective thermal conductivity is as high as its intrinsic thermal conductivity, it is obvious that this also does not describe the system accurately. If the BNNT was that effective at spreading heat, the BNNT would have caused melting at the right metal pad

already at 0.229 V. The middle image shows the simulation thermal conductivity, 350 W/mK, which matches well, but the optimized effective thermal conductivity for this sample is 500 W/mK. This value is in line with what was found by Chang et el., both for BNNTs and MWCNTs.[54]

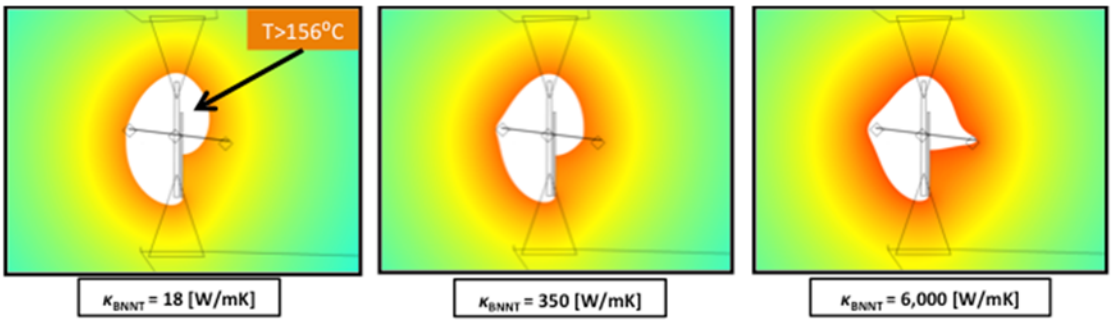

Figure 4.3.5. Images of the FEA modeled results of the tested device with different effective thermal conductances for the BNNT. The value in the middle, 350 W/mK most closely matches the experimental melting profile.

4.4 Thermal Stability of MWCNTs

Before carbon nanotubes (CNTs) can be integrated in new technologies it is important to understand their stability at high temperatures, especially for electronic applications, where they are proposed as a possible solution for heat management at hot-spots. It is well known that amorphous carbon starts to burn already at 350 C, however ordered carbons such as multi-walled CNTs (MWCNTs) should be stable at much higher temperatures. There is a large difference between the thermal stability of CNTs in vacuum and in air because the main breakdown mechanism for CNTs is the oxidation of the outer layers of the tubes.[115] High purity arc-discharge MWCNTs have previously been found to oxidize quickly in air at temperatures above 700 C.[216] The MWCNTs used

in all of this work are also high purity arc-discharge fabricated, but heating in air of these tubes does not show as high resistance to oxidation. The hope here was that the surfactant residues deposited alongside the MWCNTs would burn before damage to the CNTs occurred; however this was not successful. The study instead confirmed that unstructured graphitic particles burn much earlier than MWCNTs and that the ends of the MWCNTs are more susceptible to burning.

A tube furnace is used to heat SiN membranes deposited with high-density MWCNT surfactant solutions. They are imaged using TEM, before and after annealing in air for 2 hours at temperatures ranging from 475 to 575 C. Figure 4.4.1 shows the result of this test. The left images are of the samples prior to annealing, the middle is after, and the right is after at higher magnification showing the structure of the MWCNTs after oxidation. At the lower temperatures there is still plenty of graphitic sot and surfactant left on the sample, but some MWCNTs show clear damage to the outer walls, likely where defects existed prior to the annealing treatment. For each temperature increase, the amount of residue and unwanted particles decreases, but the damage to the MWCNTs increases.

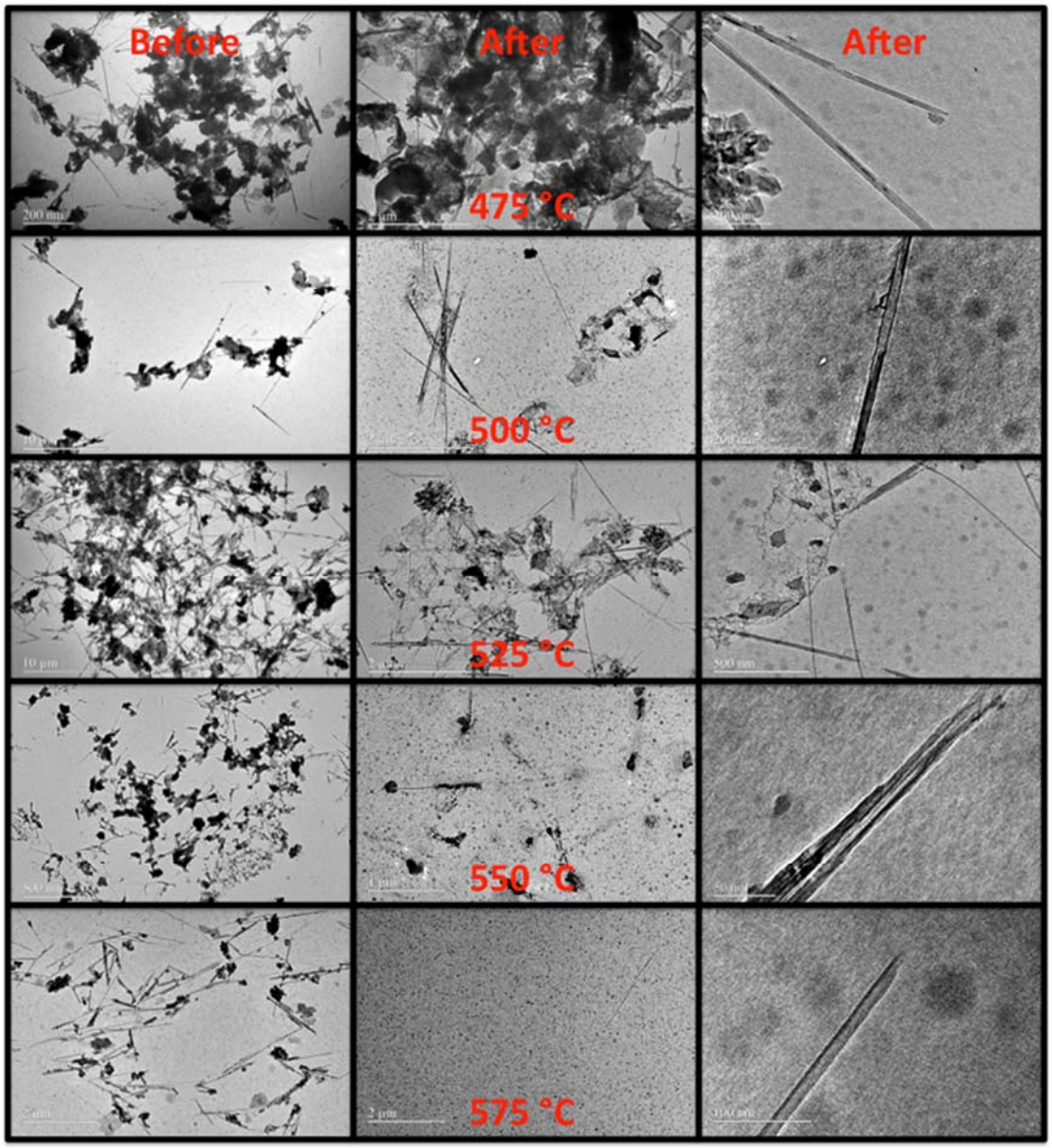

Figure 4.4.1. TEM images of MWCNTs before and after annealing at different temperatures. The first column is low magnification images before the annealing. The middle column is low resolution images after the annealing and the right column is high resolution images after the annealing showing the damage to the MWCNTs from the heat treatment.

4.5. Graphene

Shortly after it was first isolated by Novoselov and Geim, graphene was proposed as a heat spreading material for future electronic applications.[217] It not only has a high theoretical thermal conductivity, but also high experimental measurements reported up to 5,000 W/mK.[77] However, the measured values vary depending on the measurement technique used and the type of graphene measured.[78] One trend that is agreed upon, but not completely understood is that the thermal conduction is suppressed by about an order of magnitude when the graphene is resting on a substrate as compared to when it is freely suspended.[75, 81] This effect seems to be caused by phonon leakage across the support interface into low velocity modes and suppression of phonon flexural modes (*ZA*) at the interface.[218, 219] However, the amount of suppression is dependent on the type of substrate and recent results indicate that the transport can be enhanced by functionalization between the graphene and the substrate.[220, 221]

I have created an experimental set-up that allows for direct visualization of heat spreading in graphene and its substrate with high spatial resolution by combining the EThM technique with an *in-situ* STM-TEM holder. The graphene used in these experiments was AL-suspended reduced graphene oxide few-layer flakes, described in Chapter 2 Section 4. The results of the experiments are that this type of graphene is a very effective heat spreader, even on a substrate, despite, or perhaps thanks to the large amount of wrinkling. Schematics of the setup can be seen in Figures 4.5.1 and 4.5.2. The graphene is deposited onto SiN membranes with 8 Au electrodes that are all grounded to the holder. The graphene tends to land near or on the electrodes making it easy to conduct

STM biasing experiments. STM tips of both Pt and Au were used, using the circuit shown in figure 4.5.2.

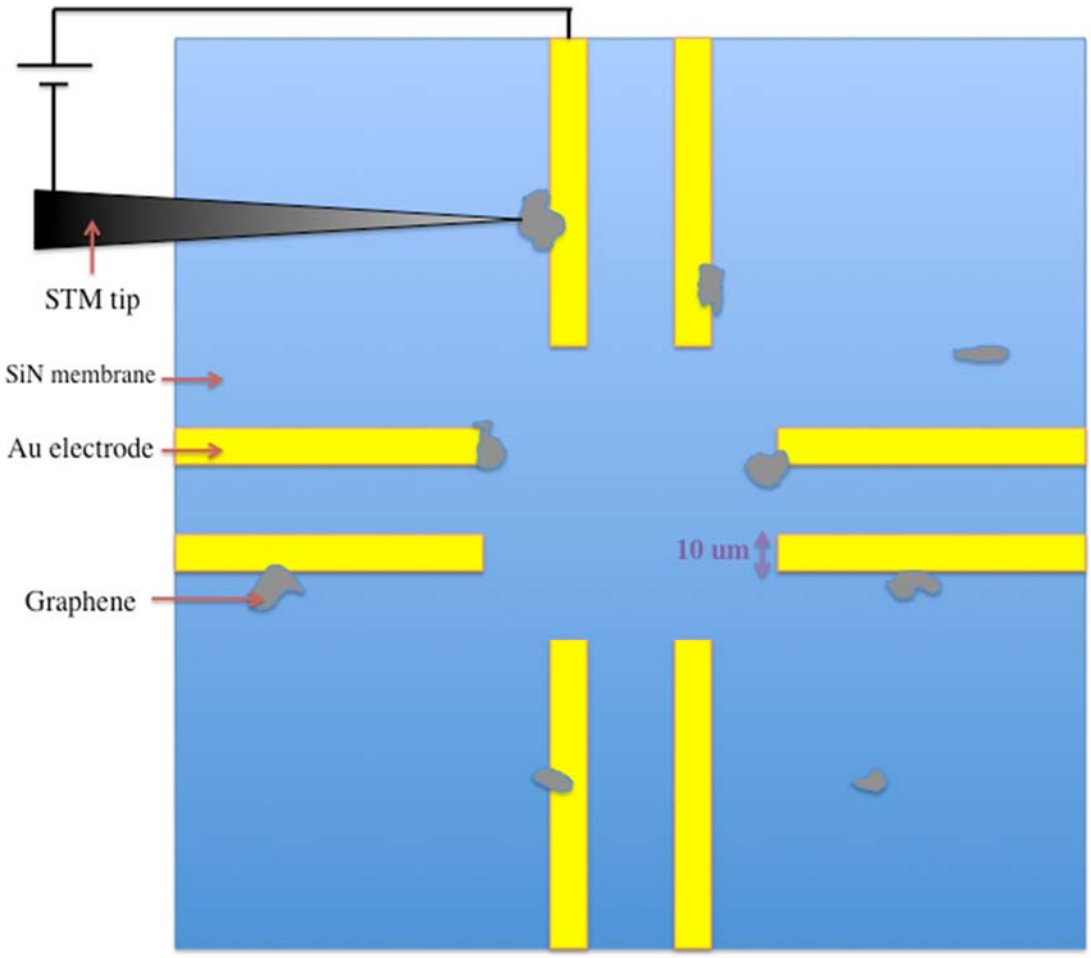

Figure 4.5.1. Top-down view of the experimental set-up showing graphene deposited on a SiN membrane with Au electrodes. The STM tip can be moved to make contact with the graphene from the side and to apply a bias to the grounded sample.

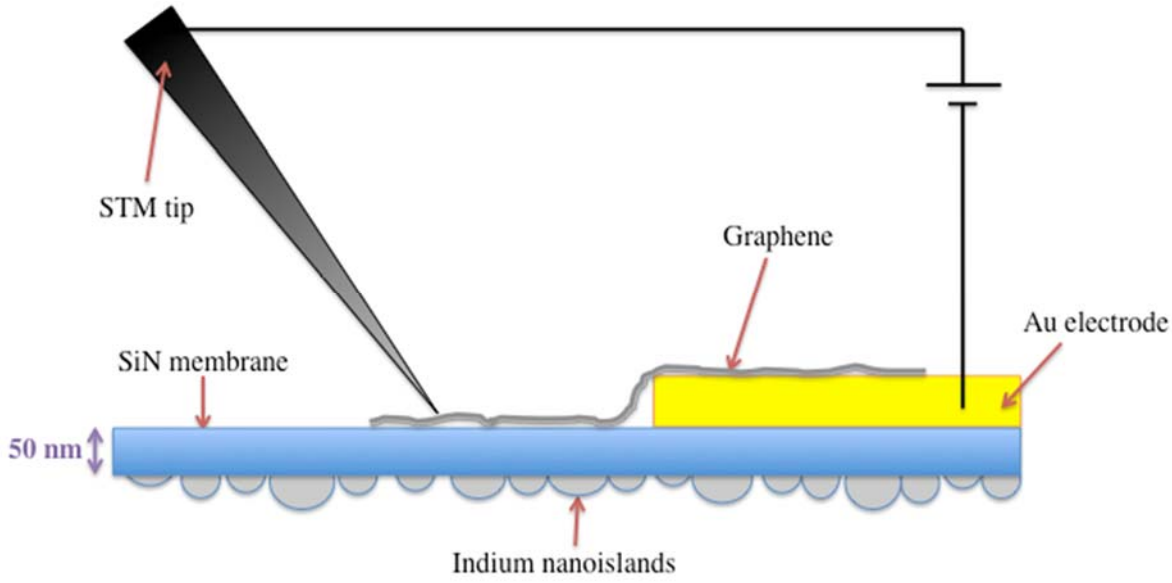

Figure 4.5.2. Side view of the experimental set-up showing graphene deposited on a SiN membrane with Au electrodes. Indium is deposited on the backside of the membrane so that thermal characterization can be performed.

If the STM tip is used to bias the Au electrode directly, without any graphene, the electrode acts as a heater wire and approximately the center of the electrode becomes the hottest point, as can be seen in figure 4.5.3. If the STM is used to apply bias to the SiN substrate, without any graphene, heating does not occur because the electrons do not reach the electrode since SiN is electrically insulating. However, if the graphene is between the STM and the electrode, the contact point between the graphene and the STM becomes the hottest point of the sample because of the high electrical contact resistance, as shown in the previous chapter. The high phonon heat conduction in the graphene then spreads the heat from the probes and heats the SiN below.

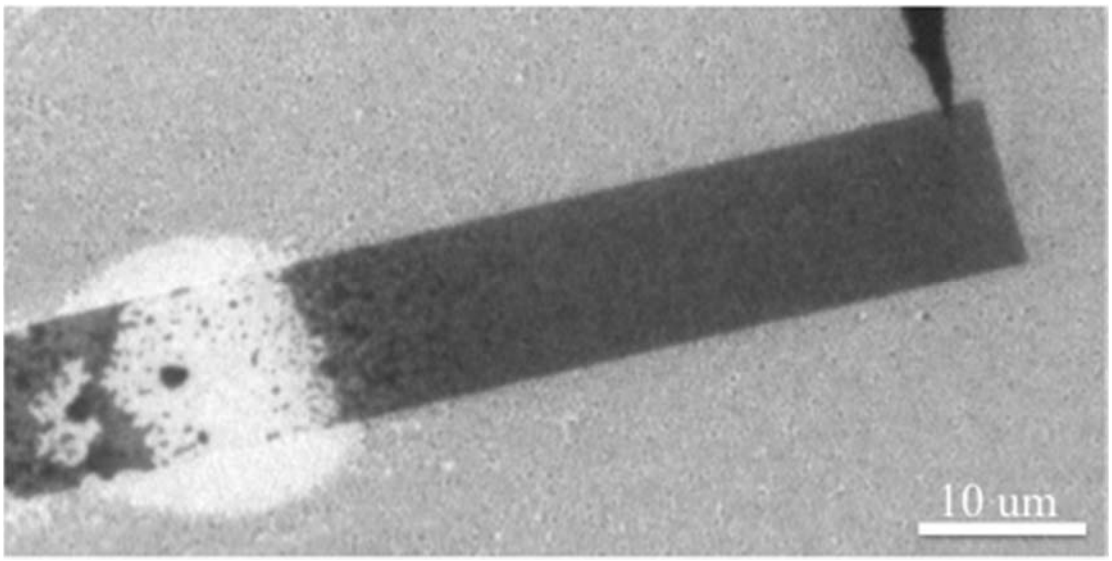

Figure 4.5.3. STM probe used to bias a large Au electrode. The electrode acts as a heater wire and somewhere near the middle of the electrode become the hottest point.

Figures 4.5.4 shows the STM tip making contact with a piece of graphene directly on top of a gold electrode. The lines indicate the order of the melting contours caused by the graphene spreading heat from the STM probe. In this image it is clear that the area where graphene fold and wrinkles are most visible, is where the melting starts first, meaning that this graphene has the best heat spreading ability. The areas that show melting, in this image, have no current flow, so the heating is not a function of Joule heating.

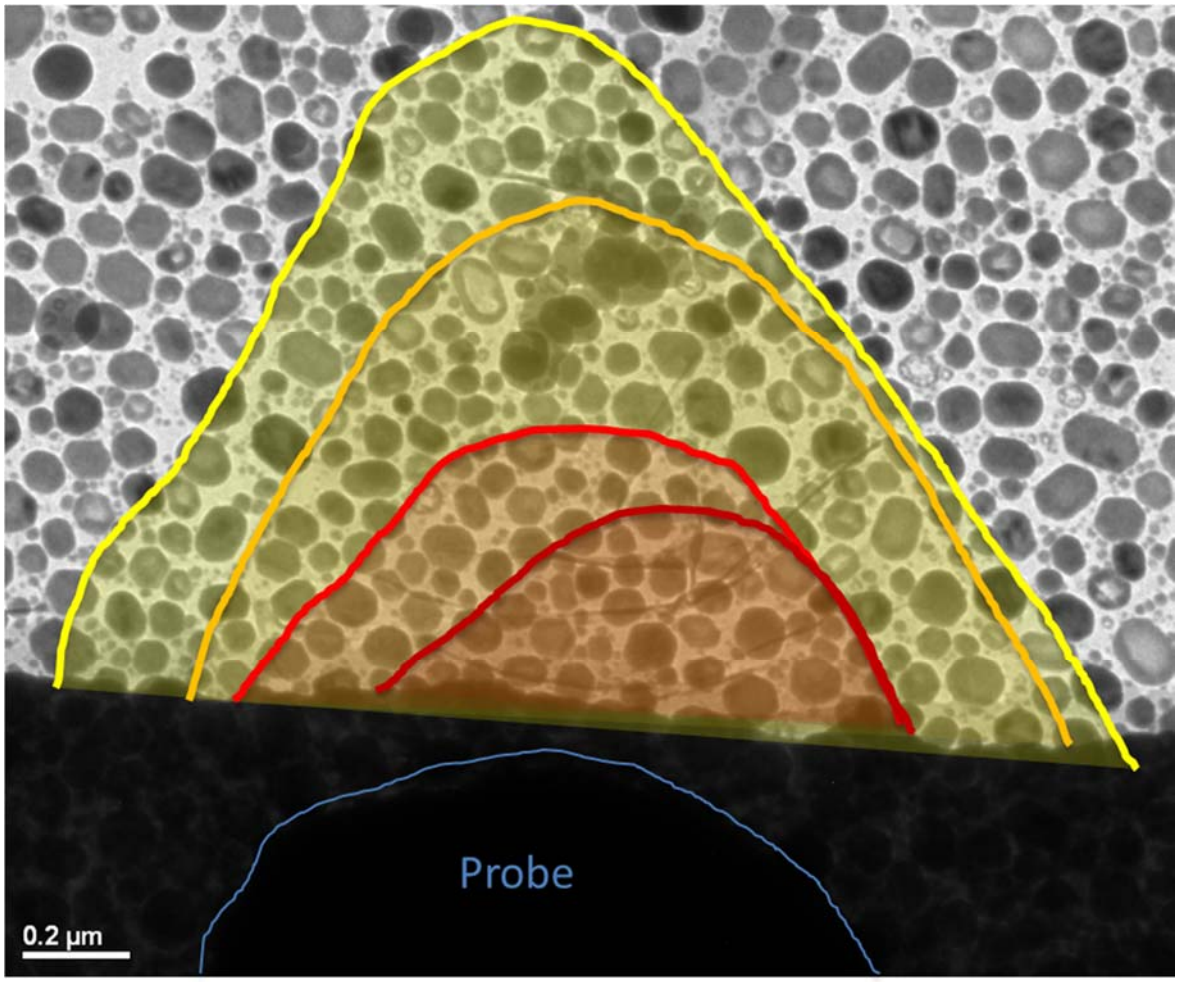

Figure 4.5.4. Bright field TEM image with overlaid melting contours showing that the melting starts at the probe contact point and then spreads out underneath the graphene. The graphene is effectively spreading the heat away from the electrode even though the current is not passing through the graphene shown in the image.

Figure 4.5.5 shows an example where ~1 µm of graphene is Joule heated. As evident by the melting contours, the region under the probe heats up first, but then, rather than following the Joule heating path, the heat spreads through the graphene and is transferred from the graphene to the substrate. The melting is not symmetric with the probe showing that the graphene is indeed controlling the heat spread. This figure is strong evidence that phonon heat conduction in graphene is high, and that graphene can effectively transfer heat to a substrate that it rests on. These results are not in agreement

with recent theoretical results that show that Joule self-heating should be dominant, especially when graphene is on a low thermal conductivity substrate.[222] However, recent experimental results have shown a trend of decreased thermal resistance with thickness for supported graphene.[223] Our results are direct evidence that areas with thicker graphene wrinkles and folds transfer heat more effectively than areas with less graphene mass.

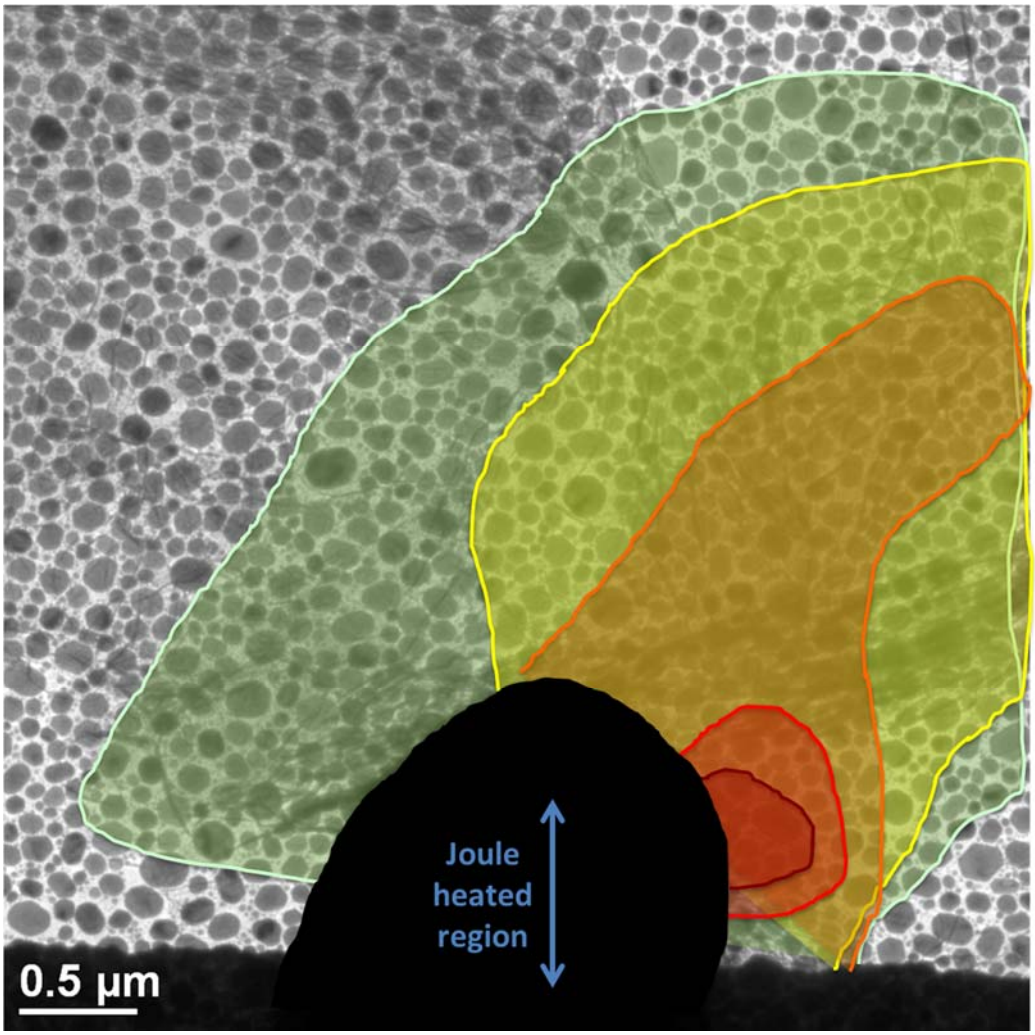

Figure 4.5.5. Bright field TEM image with overlaid melting contours showing that the melting starts at the probe contact point and then spreads out underneath the graphene. The graphene is effectively spreading the heat away from the electrode even in the areas that are not current carrying.

The last example is of a mostly-Joule heated graphene area. This example also shows how the contour lines in the examples above are obtained. Figure 4.5.6 shows first a bright field image followed by a sequence of dark field images where the bias is increasing. Figure 4.5.7 shows subtracted dark field images to clarify the island melting path. Finally, figure 4.5.8 shows a bright field image with the overlaid melting contour lines. The heating first starts at the probe contact point and is transferred through the graphene into the substrate, towards the electrode. However, before reaching the electrode, the heating spreads out underneath the graphene areas into regions that likely have low current density. This is again evidence that Joule heating of graphene is not the dominant heating mechanism, but instead that phonon conduction from the graphene to the substrate is the main type of heat transport for this system.

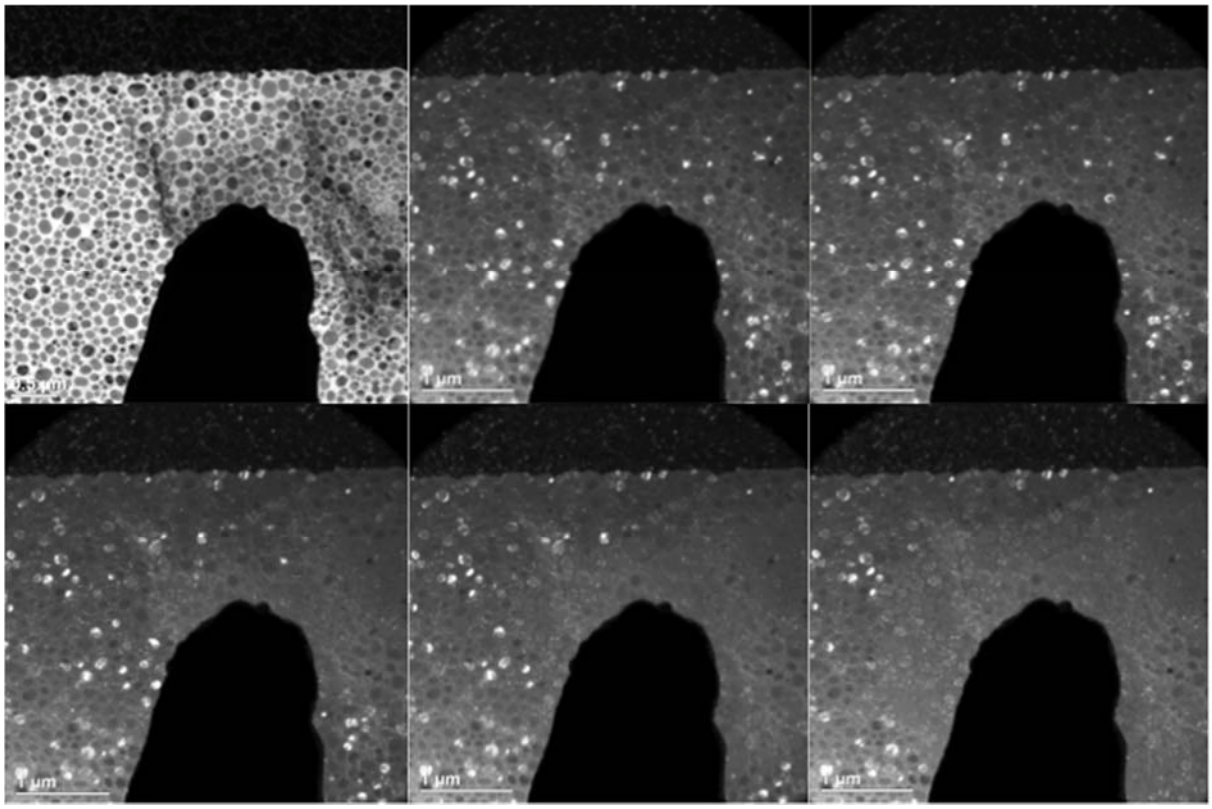

Figure 4.5.6. STM probe used to bias graphene in contact with a grounded Au electrode. The first image is a bright field TEM image of the system. The following are dark field TEM images at increasing bias so the sample is heating as evidenced by the melting of the indium islands.

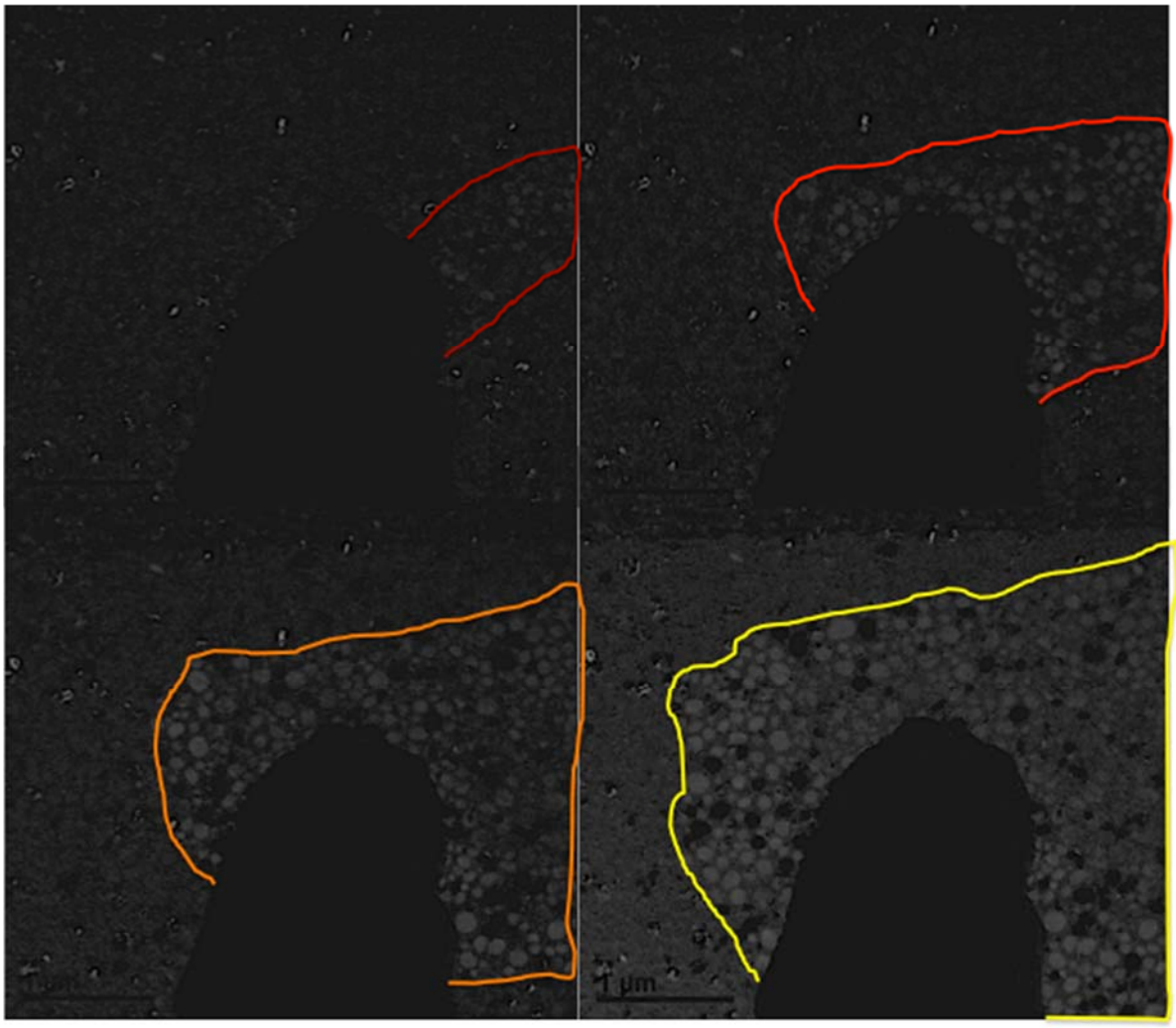

Figure 4.5.7. Subtracted dark field TEM images to clarify the path of the melting islands. The melting follows a path from the probe towards the electrode, but then spreads out underneath the graphene effectively keeping the electrode cool.

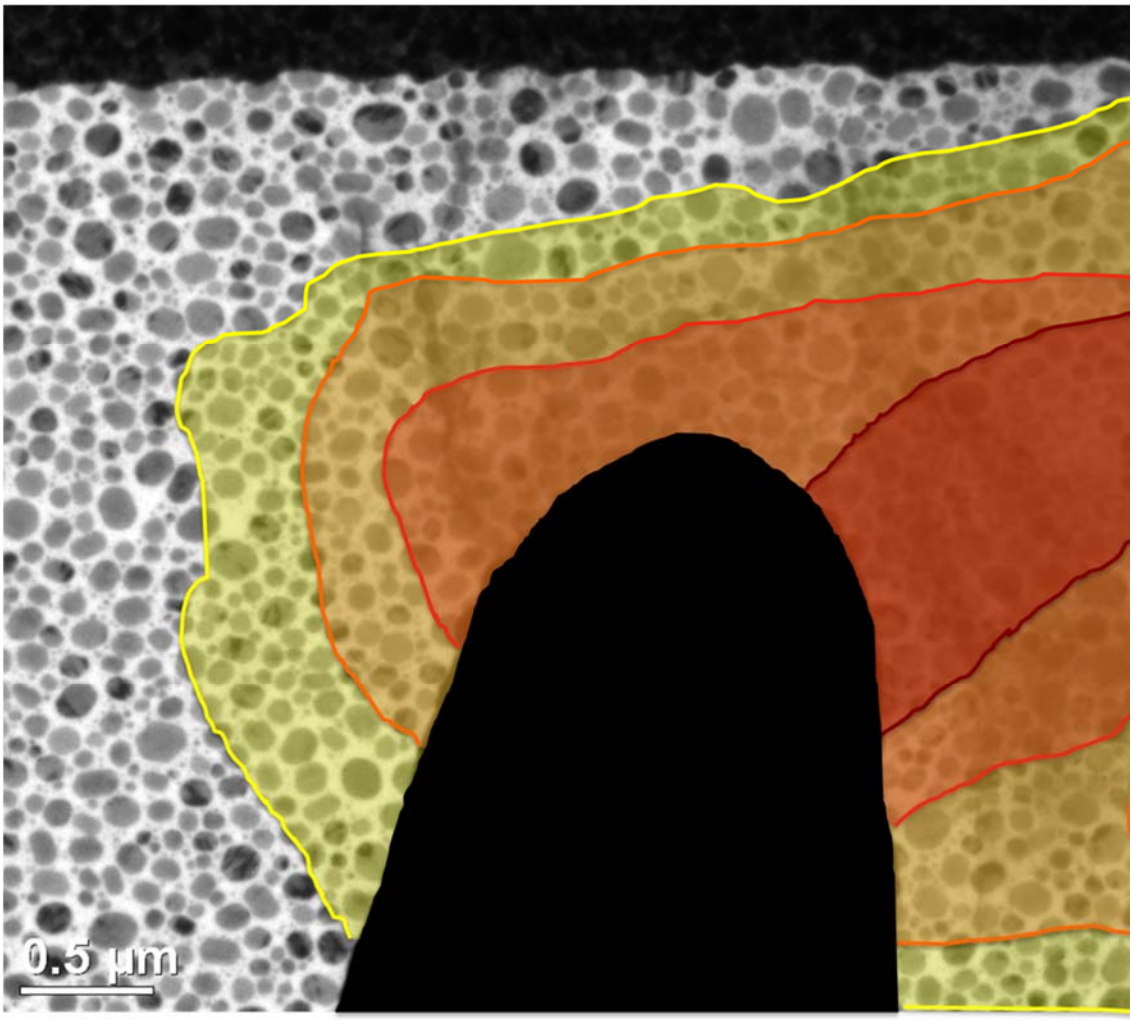

Figure 4.5.8. Bright field TEM image with overlaid melting contours showing that the melting starts at the probe contact point and then follows the graphene out towards the electrode, but then spreads out underneath the graphene instead, effectively keeping the electrode cool.

The graphene shown in these examples is highly wrinkled, leading to an expectation from recent molecular dynamic (MD) calculations[224] and analytical calculations,[225] that phonon scattering increases and limits the thermal conductivity. However, other MD simulations show that graphene wrinkles limit the graphene thermal conductivity only across the wrinkles, and not along the wrinkling direction.[226] When simple COMSOL models are made of this system, as described previously in section 4.3, the graphene must be modeled with an effective thermal conductivity in the thousands of

W/mK to obtain reasonable agreement. This model is 2D, so all of the layers, wrinkles, and interface resistances are summed in to one effective thermal conductivity. Figure 4.5.9 shows a result of the modeled system with the graphene effective thermal conductivity modeled as 3,000 W/mK. The behavior shown by this model closely resembles the results shown in the TEM images. This value is 5 times higher than previously measured for supported graphene.[193]

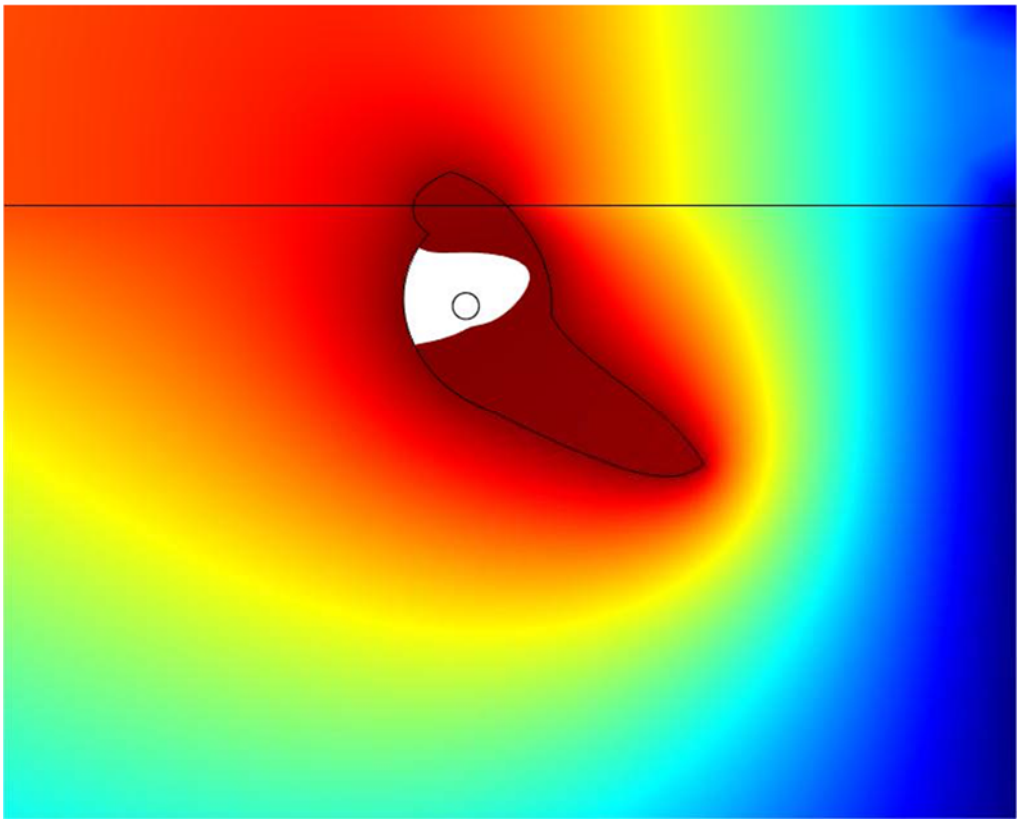

Figure 4.5.9. COMSOL model similar to the tested graphene joule heated systems. For this model the graphene is modeled with a thermal conductivity if 3,000 W/mK and it behaves similarly to the results that can be seen in the earlier figures from the *in-situ* experiments.

Another possibility is that the wrinkles are actually improving the thermal transport by counteracting the substrate reduction of the thermal transport,[218, 219] by keeping the majority of the graphene from having contact with the substrate, leading to a

semi-suspended transport case. There is support for this in recent MD calculations that show that graphene that conforms less to the substrate roughness has higher thermal conductivity.[227] There is also recent MD support that graphene with some defects, as compared to defect free graphene, have lower thermal interface resistance across the plane, even if the conduction along the plane reduces with defects.[228] This means that our, reduced graphene oxide, which has defects, may be more suited to transport heat into a substrate, than pristine graphene.

In conclusion, as with the electrical characterization, the thermal characterization of the samples leads to the conclusion that supported, wrinkled, reduced graphene oxide sheets have high thermal conduction properties. More than 10 sheets were thermally characterized and all showed evidence that the graphene spreads the heat from the probe out and in to the substrate, leaving us with three main conclusions. (1) As has been shown in calculations, but until now, not verified with experiments, wrinkled graphene has low interface resistance with substrates because it does not conform to the substrate. (2) Joule heating does not dominate thermal transport in graphene. (3) Lastly, simple COMSOL calculations show that in order for the heat spread to be visible in our system, the effective thermal conductivity of the graphene system is on the order of 1000s of W/mK. These conclusions are very promising for the future of graphene as a heat spreader in nanoscale electronic systems. Our results shows that graphene does not need to be defect and wrinkle-free in order to have high thermal conductivity, in fact, in real-life systems with substrates, the thermal transport is more robust without conformity.

4.6. Thermal Stability of Graphene

Another conclusion that can be drawn from the thermal characterization experiments of graphene is that graphene is stable at high temperatures, which is an important consideration when choosing materials for heat spreading in electronic devices. Figures 4.6.1-2 show examples where the sample has become warm enough to migrate and recrystallize the indium and the gold, while the graphene is left completely intact. Figure 4.6.2 shows that the gold right under the graphene sheet has migrated indicating that it is the hottest point. The exact temperatures that the samples have reached are unclear, but we know that it is above the recrystallization temperature of both the indium oxide and the gold. This temperature varies for different materials, but it is generally accepted that it is 30-70% of the melting temperature.[229] Based off of this we believe that the gold recrystallizes around 660 C and the indium oxide slightly below 1000 C. We can also estimate the temperature from the power generated by joule heating. It has previously been established that freely-suspended graphene nanoribbons with a diameter of 66 nm and length of 315 nm reach over 2000 C at a power dissipation of less than half a microwatt.[230] The cases shown in figures 4.6.1-2 reached powers of 630 μW and 980 μW respectively. The dimensions of our sheets are larger than the ribbons in the previously cited study, but this is gives us another indication that our samples are reaching around 1000 C.

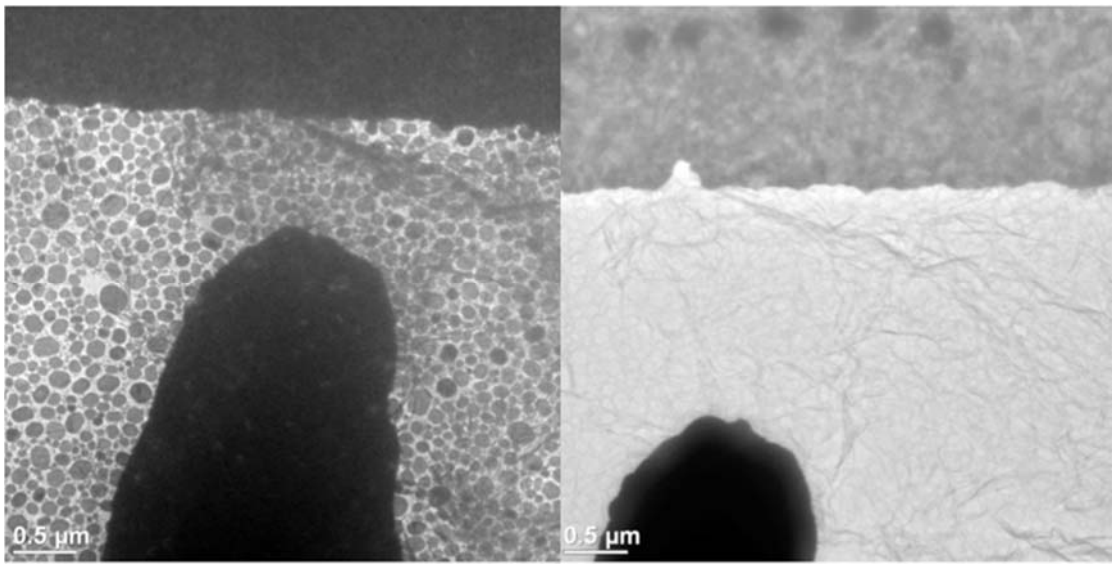

Figure 4.6.1. TEM images of a graphene sheet before and after biasing to high enough temperatures to cause migration of indium and gold.

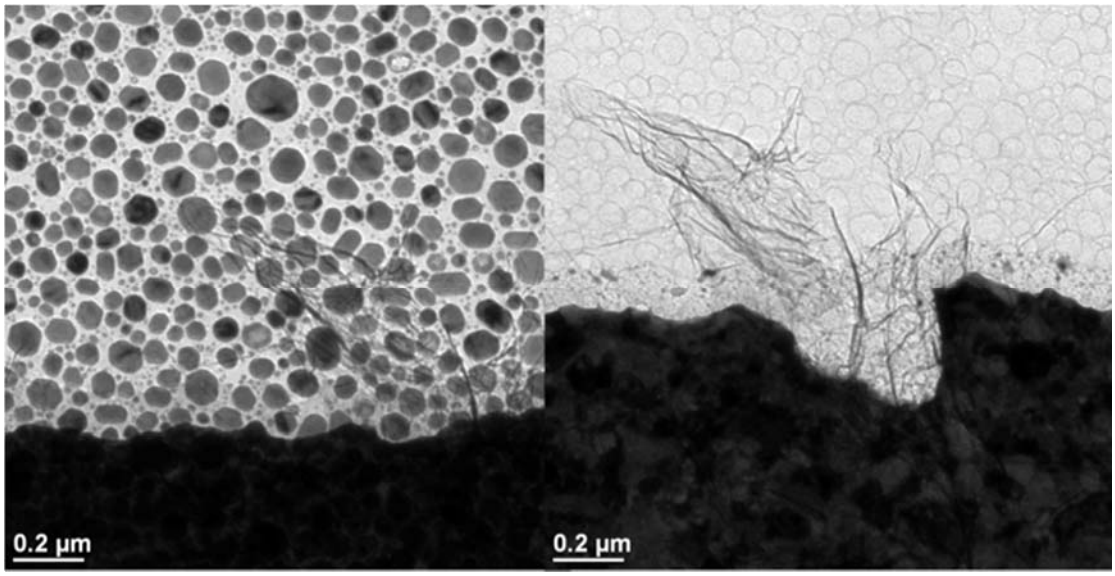

Figure 4.6.2. TEM images of a graphene sheet before and after biasing to high enough temperatures to remove the indium and recrystallize the gold.

Chapter 5: Summary and future work

This thesis presents three main projects that deal with preparing and characterizing nanostructures. The projects each have specific challenges, approaches, and measurement metrics which were presented in three different chapters. The most important characterization results came from novel *in-situ* TEM experimental techniques, but other techniques such as AFM, SEM, and Raman spectroscopy were also utilized for various parts of the project. The results that were obtained for graphene were most significant from the standpoint of understanding the behavior of nanostructures. This chapter will expand on these points and also outline the future plans for each part of this project.

Ammonium laurate (AL) was developed as a better alternative to sodium dodecyl sulfate (SDS) for aqueous processing of nanostructures. The first part of the work was to use AL to suspend and deposit individual MWCNTs. As compared to SDS, the results were that AL was more stable for storing the MWCNTs in solution and the depositions were much cleaner and showed selectivity toward deposition of unbundled individual MWCNTs over unwanted graphitic particles. This work was completed and published in

Langmuir.[231] The work with SWCNTs in AL again shows clean deposition and selective deposition, this time towards certain chiralities. The solution work for BNNTs showed that ethanol was sufficient for making individual, clean depositions of BNNTs for characterization purposes. The latest surfactant work was using the AL surfactant both to suspend reduced graphene oxide and to fabricate graphene from pristine graphite in AL through mechanical exfoliation. This work shows promising initial results; again stable solutions and clean depositions containing graphene with desirable properties. The initial results from the exfoliation fabrication of graphene in AL show promise that it is possible to fabricate high quality graphene using simple and environmentally friendly methods. However many things can be optimized further to improve the current results; including sonication time and power, surfactant concentration, and centrifugation time and speed. The significance of this chapter is that a new surfactant has been developed that can replace the currently used surfactant for processing carbon nanostructures. The thorough characterization of the surfactant performance is important for allowing others to use and to further develop applications for this surfactant.

The electrical characterization goals led to progress in fabrication methods. Electron beam lithography, FIB, and EBID were investigated for their suitability to make metal nanowires with different parameters. *In-situ* TEM STM electrical probing of reduced graphene oxide on SiN led to conclusions that supported, wrinkled, p-doped, multilayer-sheets have high electron conductivity. Wrinkles were found to decrease the measured resistance by increasing the contact area available to contact the measurement probe. The contact between the probe and the graphene was found to be very important, but also controllable by moving the probe to contact larger areas of graphene. The

significance of these results is to provide local measurement results of wrinkle reduced graphene oxide resting on a substrate. It is important that the measurements show that the natural wrinkles and oxide content do not prevent the graphene from conducting well. This points to that effort does not need to be spent on learning how to “flatten” wrinkled graphene and that RGO is a viable candidate in electronic applications.

The last chapter presents projects that were focused on thermal characterization. Work was performed on deposited metal heater wires, BNNTs, MWCNTs, and graphene. The most significant results were for graphene, where for the first time, we experimentally show that graphene can be an effective heat spreader despite wrinkles and support on a substrate. In fact, we conclude that the wrinkles can aid in preventing transport dampening by the substrate. The largest significance of these experiments is that the EThM technique allows for direct visualization of how the heat is spread through the graphene and down to the substrate below. From an industrial application standpoint, the graphene results show promise that it is possible to take advantage of both the electrical and thermal properties of graphene in actual device settings. Interesting future work would be to develop surface treatments and functionalizations that will enhance the thermal spread between the graphene and the substrate further.

References

(1) Krohn, V. E.; Ringo, G. R. THE FEASIBILITY OF ACHIEVING 15 NANOMETER RESOLUTION WITH A SCANNING MICRO PROBE USING A LIQUID GALLIUM ION SOURCE. *Parsons, Donald F. (Ed.). Annals of the New York Academy of Sciences, Vol. 306. Short Wavelength Microscopy. Workshop. New York, N.Y., USA, Feb. 23-25, 1977. 339p. Illus. the New York Academy of Sciences: New York, N.Y., USA. Isbn 0-89072-062-2* **1978**, 200-202.

(2) Bethune, D. S.; Meijer, G.; Tang, W. C.; Rosen, H. J.; Golden, W. G.; Seki, H.; Brown, C. A.; Devries, M. S. VIBRATIONAL RAMAN AND INFRARED-SPECTRA OF CHROMATOGRAPHICALLY SEPARATED C60 AND C70 FULLERENE CLUSTERS. *Chemical Physics Letters* **1991**, *179*, 181-186.

(3) Iijima, S. HELICAL MICROTUBULES OF GRAPHITIC CARBON. *Nature* **1991**, *354*, 56-58.

(4) Zhao, X. Y.; Wei, C. M.; Yang, L.; Chou, M. Y. Quantum confinement and electronic properties of silicon nanowires. *Physical Review Letters* **2004**, *92*.

(5) Parvathi, M. M.; Arivazhagan, V.; Rajesh, S. Quantum size effect on the layer by layer assembly of PbTe-InSe multilayer nanocomposite structures. *Journal of Alloys and Compounds* **2015**, *646*, 96-100.

(6) Foot, R.; Lew, H.; Volkas, R. R. ELECTRIC-CHARGE QUANTIZATION. *Journal of Physics G-Nuclear and Particle Physics* **1993**, *19*, 361-372.

(7) Mohammad, S. N. Understanding quantum confinement in nanowires: basics, applications and possible laws. *Journal of Physics-Condensed Matter* **2014**, *26*.

(8) Su, W. B.; Chang, C. S.; Tsong, T. T. Quantum size effect on ultra-thin metallic films. *Journal of Physics D-Applied Physics* **2010**, *43*.

(9) Fujiwara, A.; Zimmerman, N. M.; Ono, Y.; Takahashi, Y. Current quantization due to single-electron transfer in Si-wire charge-coupled devices. *Applied Physics Letters* **2004**, *84*, 1323-1325.

(10) Likharev, K. K. Single-electron devices and their applications. *Proceedings of the Ieee* **1999**, *87*, 606-632.

(11) Ouyang, Y.; Guo, J. Heat dissipation in carbon nanotube transistors. *Applied Physics Letters* **2006**, *89*.
(12) D'Agosta, R.; Sai, N.; Di Ventra, M. Local electron heating in nanoscale conductors. *Nano Letters* **2006**, *6*, 2935-2938.
(13) Vashaee, D.; Shakouri, A. Improved thermoelectric power factor in metal-based superlattices. *Physical Review Letters* **2004**, *92*.
(14) Leonard, F.; Talin, A. A. Electrical contacts to one- and two-dimensional nanomaterials. *Nature Nanotechnology* **2011**, *6*, 773-783.
(15) Baloch, K.; Voskanian, N.; Cumings, J. Controlling the thermal contact resistance of a carbon nanotube heat spreader. *Applied Physics Letters* **2010**, *97*, -.
(16) Chai, Y.; Hazeghi, A.; Takei, K.; Chen, H.-Y.; Chan, P. C. H.; Javey, A.; Wong, H. S. P. Low-Resistance Electrical Contact to Carbon Nanotubes With Graphitic Interfacial Layer. *Ieee Transactions on Electron Devices* **2012**, *59*, 12-19.
(17) Guo, Z.-Y. Thermomass Theory for Non-Fourier Heat Conduction. *Theoretical and Experimental Studies on Non-Fourier Heat Conduction Based on Thermomass Theory* **2014**, 21-54.
(18) Lee, J.; Lim, J.; Yang, P. Ballistic Phonon Transport in Holey Silicon. *Nano Letters* **2015**, *15*, 3273-3279.
(19) Shiomi, J.; Maruyama, S. Non-Fourier heat conduction in a single-walled carbon nanotube: Classical molecular dynamics simulations. *Physical Review B* **2006**, *73*.
(20) Cimmelli, V. A.; Carlomagno, I.; Sellitto, A. Non-Fourier Heat Transfer with Phonons and Electrons in a Circular Thin Layer Surrounding a Hot Nanodevice. *Entropy* **2015**, *17*, 5157-5170.
(21) Cahill, D. G.; Braun, P. V.; Chen, G.; Clarke, D. R.; Fan, S.; Goodson, K. E.; Keblinski, P.; King, W. P.; Mahan, G. D.; Majumdar, A.; Maris, H. J.; Phillpot, S. R.; Pop, E.; Shi, L. Nanoscale thermal transport. II. 2003-2012. *Applied Physics Reviews* **2014**, *1*.
(22) Young, D. A.; Maris, H. J. LATTICE-DYNAMICAL CALCULATION OF THE KAPITZA RESISTANCE BETWEEN FCC LATTICES. *Physical Review B* **1989**, *40*, 3685-3693.

(23) Stevens, R. J.; Zhigilei, L. V.; Norris, P. M. Effects of temperature and disorder on thermal boundary conductance at solid-solid interfaces: Nonequilibrium molecular dynamics simulations. *International Journal of Heat and Mass Transfer* **2007**, *50*, 3977-3989.
(24) Polidori, G.; Fohanno, S.; Nguyen, C. T. A note on heat transfer modelling of Newtonian nanofluids in laminar free convection. *International Journal of Thermal Sciences* **2007**, *46*, 739-744.
(25) Li, L.; Zheng, H.; Talke, F. E. Investigation of Nanoscale Heat Transfer and Flying Characteristics in Thermal Flying Height Control Sliders Considering Near-Field Radiation. *Tribology Letters* **2015**, *59*.
(26) Ottens, R. S.; Quetschke, V.; Wise, S.; Alemi, A. A.; Lundock, R.; Mueller, G.; Reitze, D. H.; Tanner, D. B.; Whiting, B. F. Near-Field Radiative Heat Transfer between Macroscopic Planar Surfaces. *Physical Review Letters* **2011**, *107*.
(27) Song, B.; Ganjeh, Y.; Sadat, S.; Thompson, D.; Fiorino, A.; Fernandez-Hurtado, V.; Feist, J.; Garcia-Vidal, F. J.; Carlos Cuevas, J.; Reddy, P.; Meyhofer, E. Enhancement of near-field radiative heat transfer using polar dielectric thin films. *Nature Nanotechnology* **2015**, *10*, 253-258.
(28) Song, B.; Fiorino, A.; Meyhofer, E.; Reddy, P. Near-field radiative thermal transport: From theory to experiment. *Aip Advances* **2015**, *5*.
(29) Hu, L.; Narayanaswamy, A.; Chen, X.; Chen, G. Near-field thermal radiation between two closely spaced glass plates exceeding Planck's blackbody radiation law. *Applied Physics Letters* **2008**, *92*.
(30) Shen, S.; Narayanaswamy, A.; Chen, G. Surface Phonon Polaritons Mediated Energy Transfer between Nanoscale Gaps. *Nano Letters* **2009**, *9*, 2909-2913.
(31) Bai, Y.; Jiang, Y.; Liu, L. Enhanced near-field radiative heat transfer between a nanosphere and a hyperbolic metamaterial mediated by coupled surface phonon polaritons. *Journal of Quantitative Spectroscopy & Radiative Transfer* **2015**, *158*, 61-68.
(32) Thostenson, E. T.; Ren, Z. F.; Chou, T. W. Advances in the science and technology of carbon nanotubes and their composites: a review. *Composites Science and Technology* **2001**, *61*, 1899-1912.

(33) Berber, S.; Kwon, Y.; Tomanek, D. Unusually high thermal conductivity of carbon nanotubes. *Physical Review Letters* **2000**, *84*, 4613-4616.
(34) Saito, R.; Fujita, M.; Dresselhaus, G.; Dresselhaus, M. S. ELECTRONIC-STRUCTURE OF CHIRAL GRAPHENE TUBULES. *Applied Physics Letters* **1992**, *60*, 2204-2206.
(35) Chen, J.; Liu, H. Y.; Weimer, W. A.; Halls, M. D.; Waldeck, D. H.; Walker, G. C. Noncovalent engineering of carbon nanotube surfaces by rigid, functional conjugated polymers. *Journal of the American Chemical Society* **2002**, *124*, 9034-9035.
(36) Saito, S. Carbon nanotubes for next-generation electronics devices. *Science* **1997**, *278*, 77-78.
(37) Radushkevich, L. V.; Lukyanovich, V. M. About the structure of carbon formed by thermal decomposition of carbon monoxide on iron substrate. *J. Phys. Chem.(Moscow)* **1952**, *26*, 88-95.
(38) Rubio, A.; Corkill, J. L.; Cohen, M. L. Theory of graphitic boron nitride nanotubes. *Physical Review B* **1994**, *49*, 5081.
(39) Chopra, N. G.; Luyken, R.; Cherrey, K.; Crespi, V. H.; Cohen, M. L.; Louie, S. G.; Zettl, A. Boron nitride nanotubes. *Science* **1995**, *269*, 966-967.
(40) Loiseau, A.; Willaime, F.; Demoncy, N.; Hug, G.; Pascard, H. Boron nitride nanotubes with reduced numbers of layers synthesized by arc discharge. *Physical review letters* **1996**, *76*, 4737-4740.
(41) Saito, Y.; Maida, M.; Matsumoto, T. Structures of boron nitride nanotubes with single-layer and multilayers produced by arc discharge. *Japanese journal of applied physics* **1999**, *38*, 159.
(42) Altoe, M.; Sprunck, J.; Gabriel, J.-C.; Bradley, K. Nanococoon seeds for BN nanotube growth. *Journal of materials science* **2003**, *38*, 4805-4810.
(43) Golberg, D.; Bando, Y.; Eremets, M.; Takemura, K.; Kurashima, K.; Yusa, H. Nanotubes in boron nitride laser heated at high pressure. *Applied Physics Letters* **1996**, *69*, 2045-2047.
(44) Laude, T.; Matsui, Y.; Marraud, A.; Jouffrey, B. Long ropes of boron nitride nanotubes grown by a continuous laser heating. *Applied Physics Letters* **2000**, *76*, 3239-3241.

(45) Arenal, R.; Ferrari, A.; Reich, S.; Wirtz, L.; Mevellec, J.-Y.; Lefrant, S.; Rubio, A.; Loiseau, A. Raman spectroscopy of single-wall boron nitride nanotubes. *Nano letters* **2006**, *6*, 1812-1816.
(46) Chen, Y.; Fitz Gerald, J.; Williams, J.; Bulcock, S. Synthesis of boron nitride nanotubes at low temperatures using reactive ball milling. *Chemical Physics Letters* **1999**, *299*, 260-264.
(47) Li, Y.; Zhou, J. e.; Zhao, K.; Tung, S.; Schneider, E. Synthesis of boron nitride nanotubes from boron oxide by ball milling and annealing process. *Materials Letters* **2009**, *63*, 1733-1736.
(48) Lourie, O. R.; Jones, C. R.; Bartlett, B. M.; Gibbons, P. C.; Ruoff, R. S.; Buhro, W. E. CVD growth of boron nitride nanotubes. *Chemistry of materials* **2000**, *12*, 1808-1810.
(49) Kim, M. J.; Chatterjee, S.; Kim, S. M.; Stach, E. A.; Bradley, M. G.; Pender, M. J.; Sneddon, L. G.; Maruyama, B. Double-walled boron nitride nanotubes grown by floating catalyst chemical vapor deposition. *Nano letters* **2008**, *8*, 3298-3302.
(50) Tang, C.; Bando, Y.; Sato, T.; Kurashima, K. A novel precursor for synthesis of pure boron nitride nanotubes. *Chem. Commun.* **2002**, 1290-1291.
(51) Smith, M. W.; Jordan, K. C.; Park, C.; Kim, J.-W.; Lillehei, P. T.; Crooks, R.; Harrison, J. S. Very long single-and few-walled boron nitride nanotubes via the pressurized vapor/condenser method. *Nanotechnology* **2009**, *20*, 505604.
(52) Xiao, Y.; Yan, X. H.; Xiang, J.; Mao, Y. L.; Zhang, Y.; Cao, J. X.; Ding, J. W. Specific heat of single-walled boron nitride nanotubes. *Applied physics letters* **2004**, *84*, 4626-4628.
(53) Golberg, D.; Bando, Y.; Kurashima, K.; Sato, T. Synthesis and characterization of ropes made of BN multiwalled nanotubes. *Scripta materialia* **2001**, *44*, 1561-1566.
(54) Chang, C. W.; Fennimore, A. M.; Afanasiev, A.; Okawa, D.; Ikuno, T.; Garcia, H.; Li, D.; Majumdar, A.; Zettl, A. Isotope effect on the thermal conductivity of boron nitride nanotubes. *Physical review letters* **2006**, *97*, 085901.
(55) Ajayan, P. M. Nanotubes from carbon. *Chemical Reviews* **1999**, *99*, 1787-1799.
(56) Kharlamova, M. V.; Volykhov, A. A.; Yashina, L. V.; Egorov, A. V.; Lukashin, A. V. Experimental and theoretical studies on the electronic properties of praseodymium

chloride-filled single-walled carbon nanotubes. *Journal of Materials Science* **2015**, *50*, 5419-5430.
(57) Kharlamova, M. V. Comparative analysis of electronic properties of tin, gallium, and bismuth chalcogenide-filled single-walled carbon nanotubes. *Journal of Materials Science* **2014**, *49*, 8402-8411.
(58) Collins, P. C.; Arnold, M. S.; Avouris, P. Engineering carbon nanotubes and nanotube circuits using electrical breakdown. *Science* **2001**, *292*, 706-709.
(59) Bachtold, A.; Strunk, C.; Salvetat, J. P.; Bonard, J. M.; Forro, L.; Nussbaumer, T.; Schonenberger, C. Aharonov-Bohm oscillations in carbon nanotubes. *Nature* **1999**, *397*, 673-675.
(60) Datta, S. *Electronic Transport in Mesoscopic Systems*; Cambridge University Press1997.
(61) Ghassemi, H. M.; Lee, C. H.; Yap, Y. K.; Yassar, R. S. Field emission and strain engineering of electronic properties in boron nitride nanotubes. *Nanotechnology* **2012**, *23*.
(62) Terrones, M.; Golberg, D.; Grobert, N.; Seeger, T.; Reyes-Reyes, M.; Mayne, M.; Kamalakaran, R.; Dorozhkin, P.; Dong, Z. C.; Terrones, H. Production and State-of-the-Art Characterization of Aligned Nanotubes with Homogeneous BCxN ($1 \leq x \leq 5$) Compositions. *Advanced Materials* **2003**, *15*, 1899-1903.
(63) Chen, H.; Zhang, H.; Fu, L.; Chen, Y.; Williams, J. S.; Yu, C.; Yu, D. Nano Au-decorated boron nitride nanotubes: Conductance modification and field-emission enhancement. *Applied Physics Letters* **2008**, *92*, 243105-243105-243103.
(64) Yu, Y.; Chen, H.; Liu, Y.; Li, L. H.; Chen, Y. Humidity sensing properties of single Au-decorated boron nitride nanotubes. *Electrochemistry Communications* **2013**.
(65) Thiyagarajan, K.; Saravanakumar, B.; Mohan, R.; Kim, S.-J. Thickness-Dependent Electrical Transport Properties of Graphene. *Science of Advanced Materials* **2013**, *5*, 542-548.
(66) Ghosh, S.; Calizo, I.; Teweldebrhan, D.; Pokatilov, E. P.; Nika, D. L.; Balandin, A. A.; Bao, W.; Miao, F.; Lau, C. N. Extremely high thermal conductivity of graphene: Prospects for thermal management applications in nanoelectronic circuits. *Applied Physics Letters* **2008**, *92*.

(67) Lee, C.; Wei, X.; Kysar, J. W.; Hone, J. Measurement of the elastic properties and intrinsic strength of monolayer graphene. *Science* **2008**, *321*, 385-388.
(68) Novoselov, K. S.; Geim, A. K.; Morozov, S. V.; Jiang, D.; Zhang, Y.; Dubonos, S. V.; Grigorieva, I. V.; Firsov, A. A. Electric field effect in atomically thin carbon films. *Science* **2004**, *306*, 666-669.
(69) Subrahmanyam, K. S.; Panchakarla, L. S.; Govindaraj, A.; Rao, C. N. R. Simple Method of Preparing Graphene Flakes by an Arc-Discharge Method. *Journal of Physical Chemistry C* **2009**, *113*, 4257-4259.
(70) Sun, J.; Cole, M. T.; Lindvall, N.; Teo, K. B. K.; Yurgens, A. Noncatalytic chemical vapor deposition of graphene on high-temperature substrates for transparent electrodes. *Applied Physics Letters* **2012**, *100*.
(71) Lin, Y.-C.; Jin, C.; Lee, J.-C.; Jen, S.-F.; Suenaga, K.; Chiu, P.-W. Clean Transfer of Graphene for Isolation and Suspension. *Acs Nano* **2011**, *5*, 2362-2368.
(72) Hofmann, M.; Chiang, W.-Y.; Nguyn, T. D.; Hsieh, Y.-P. Controlling the properties of graphene produced by electrochemical exfoliation. *Nanotechnology* **2015**, *26*.
(73) Coleman, J. N. Liquid Exfoliation of Defect-Free Graphene. *Accounts of Chemical Research* **2013**, *46*, 14-22.
(74) Saini, A. EU Graphene Flagship project aims for technological breakthroughs. *Mrs Bulletin* **2014**, *39*, 393-394.
(75) Chen, J.; Jang, C.; Xiao, S.; Ishigami, M.; Fuhrer, M. Intrinsic and extrinsic performance limits of graphene devices on SiO2. *Nature Nanotechnology* **2008**, *3*, 206-209.
(76) Sreeprasad, T. S.; Berry, V. How Do the Electrical Properties of Graphene Change with its Functionalization? *Small* **2013**, *9*, 341-350.
(77) Balandin, A.; Ghosh, S.; Bao, W.; Calizo, I.; Teweldebrhan, D.; Miao, F.; Lau, C. Superior thermal conductivity of single-layer graphene. *Nano Letters* **2008**, *8*, 902-907.
(78) Balandin, A. A. Thermal properties of graphene and nanostructured carbon materials. *Nature Materials* **2011**, *10*, 569-581.
(79) Cai, W.; Moore, A. L.; Zhu, Y.; Li, X.; Chen, S.; Shi, L.; Ruoff, R. S. Thermal Transport in Suspended and Supported Monolayer Graphene Grown by Chemical Vapor Deposition. *Nano Letters* **2010**, *10*, 1645-1651.

(80) Jauregui, L. A.; Yue, Y. N.; Sidorov, A. N.; Hu, J. N.; Yu, Q. K.; Lopez, G.; Jalilian, R.; Benjamin, D. K.; Delk, D. A.; Wu, W.; Liu, Z. H.; Wang, X. W.; Jiang, Z. G.; Ruan, X. L.; Bao, J. M.; Pei, S. S.; Chen, Y. P. Thermal Transport in Graphene Nanostructures: Experiments and Simulations. *Graphene, Ge/Iii-V, and Emerging Materials for Post-Cmos Applications 2* **2010**, *28*, 73-83.
(81) Seol, J. H.; Jo, I.; Moore, A. L.; Lindsay, L.; Aitken, Z. H.; Pettes, M. T.; Li, X. S.; Yao, Z.; Huang, R.; Broido, D.; Mingo, N.; Ruoff, R. S.; Shi, L. Two-Dimensional Phonon Transport in Supported Graphene. *Science* **2010**, *328*, 213-216.
(82) Renteria, J. D.; Nika, D. L.; Balandin, A. A. Graphene Thermal Properties: Applications in Thermal Management and Energy Storage. *Applied Sciences-Basel* **2014**, *4*, 525-547.
(83) Nika, D. L.; Pokatilov, E. P.; Askerov, A. S.; Balandin, A. A. Phonon thermal conduction in graphene: Role of Umklapp and edge roughness scattering. *Physical Review B* **2009**, *79*.
(84) Nika, D. L.; Askerov, A. S.; Balandin, A. A. Anomalous Size Dependence of the Thermal Conductivity of Graphene Ribbons. *Nano Letters* **2012**, *12*, 3238-3244.
(85) Feng, T.; Ruan, X.; Ye, Z.; Cao, B. Spectral phonon mean free path and thermal conductivity accumulation in defected graphene: The effects of defect type and concentration. *Physical Review B* **2015**, *91*.
(86) Krasavin, S. E.; Osipov, V. A. Effect of Stone-Wales defects on the thermal conductivity of graphene. *Journal of Physics-Condensed Matter* **2015**, *27*.
(87) Aksamija, Z.; Knezevic, I. Thermal transport in graphene nanoribbons supported on SiO2. *Physical Review B* **2012**, *86*.
(88) Lindsay, L.; Broido, D. A.; Mingo, N. Flexural phonons and thermal transport in graphene. *Physical Review B* **2010**, *82*.
(89) Rho, H.; Lee, S.; Bae, S.; Kim, T.-W.; Lee, D. S.; Lee, H. J.; Hwang, J. Y.; Jeong, T.; Kim, S.; Ha, J.-S.; Lee, S. H. Three-Dimensional Porous Copper-Graphene Heterostructures with Durability and High Heat Dissipation Performance. *Scientific Reports* **2015**, *5*.
(90) Du, F.-p.; Yang, W.; Zhang, F.; Tang, C.-Y.; Liu, S.-p.; Yin, L.; Law, W.-C. Enhancing the Heat Transfer Efficiency in Graphene-Epoxy Nanocomposites Using a

Magnesium Oxide-Graphene Hybrid Structure. *Acs Applied Materials & Interfaces* **2015**, *7*, 14397-14403.
(91) Ruska, E. THE DEVELOPMENT OF THE ELECTRON-MICROSCOPE AND OF ELECTRON-MICROSCOPY. *Reviews of Modern Physics* **1987**, *59*, 627-638.
(92) Ercius, P.; Boese, M.; Duden, T.; Dahmen, U. Operation of TEAM I in a User Environment at NCEM. *Microscopy and Microanalysis* **2012**, *18*, 676-683.
(93) Bell, D. C.; Mankin, M.; Day, R. W.; Erdman, N. Successful application of Low Voltage Electron Microscopy to practical materials problems. *Ultramicroscopy* **2014**, *145*, 56-65.
(94) Jinschek, J. R. Advances in the environmental transmission electron microscope (ETEM) for nanoscale in situ studies of gas-solid interactions. *Chemical Communications* **2014**, *50*, 2696-2706.
(95) Williams, D. B.; Carter, C. B. Transmission electron microscopy: a textbook for materials science. 2009. Springer US.
(96) Reimer, L. *Transmission electron microscopy: physics of image formation and microanalysis*; Springer2013; Vol. 36.
(97) Fultz, B.; Howe, J. M. *Transmission electron microscopy and diffractometry of materials*; Springer Science & Business Media2012.
(98) Meister, S.; Schoen, D. T.; Topinka, M. A.; Minor, A. M.; Cui, Y. Void Formation Induced Electrical Switching in Phase-Change Nanowires. *Nano Letters* **2008**, *8*, 4562-4567.
(99) Allard, L. F.; Overbury, S. H.; Bigelow, W. C.; Katz, M. B.; Nackashi, D. P.; Damiano, J. Novel MEMS-Based Gas-Cell/Heating Specimen Holder Provides Advanced Imaging Capabilities for In Situ Reaction Studies. *Microscopy and Microanalysis* **2012**, *18*, 656-666.
(100) Ticey, J. CARBON-SULFUR NANOCOMPOSITES
FOR LITHIUM-SULFUR BATTERIES. Doctor of Philosophy, University of Maryland2015.
(101) Demczyk, B. G.; Wang, Y. M.; Cumings, J.; Hetman, M.; Han, W.; Zettl, A.; Ritchie, R. O. Direct mechanical measurement of the tensile strength and elastic modulus

of multiwalled carbon nanotubes. *Materials Science and Engineering a-Structural Materials Properties Microstructure and Processing* **2002**, *334*, 173-178.
(102) Gu, M.; Li, Y.; Li, X.; Hu, S.; Zhang, X.; Xu, W.; Thevuthasan, S.; Baer, D. R.; Zhang, J.-G.; Liu, J.; Wang, C. In Situ TEM Study of Lithiation Behavior of Silicon Nanoparticles Attached to and Embedded in a Carbon Matrix. *Acs Nano* **2012**, *6*, 8439-8447.
(103) Cahill, D. G.; Ford, W. K.; Goodson, K. E.; Mahan, G. D.; Majumdar, A.; Maris, H. J.; Merlin, R.; Phillpot, Sr. Nanoscale thermal transport. *Journal of Applied Physics* **2003**, *93*, 793-818.
(104) Majumdar, A. Scanning thermal microscopy. *Annual review of materials science* **1999**, *29*, 505-585.
(105) Pumarol, M.; Rosamond, M. C.; Tovee, P. D.; Petty, M. C.; Zeze, D. A.; Falko, V. I.; Kolosov, O. V. Direct nanoscale imaging of ballistic and diffusive thermal transport in graphene nanostructures. *Nano Letters* **2012**.
(106) Mohammed, O. F.; Samartzis, P. C.; Zewail, A. H. Heating and cooling dynamics of carbon nanotubes observed by temperature-jump spectroscopy and electron microscopy. *Journal of the American Chemical Society* **2009**, *131*, 16010-16011.
(107) Tessier, G.; Hole, S.; Fournier, D. Quantitative thermal imaging by synchronous thermoreflectance with optimized illumination wavelengths. *Applied Physics Letters* **2001**, *78*, 2267.
(108) Hsu, I. K.; Kumar, R.; Bushmaker, A.; Cronin, S. B.; Pettes, M. T.; Shi, L.; Brintlinger, T.; Fuhrer, M. S.; Cumings, J. Optical measurement of thermal transport in suspended carbon nanotubes. *Applied Physics Letters* **2008**, *92*, 063119-063119-063113.
(109) Begtrup, G.; Ray, K.; Kessler, B.; Yuzvinsky, T.; Garcia, H.; Zettl, A. Probing nanoscale solids at thermal extremes. *Physical Review Letters* **2007**, *99*, -.
(110) Koga, K.; Ikeshoji, T.; Sugawara, K. Size-and temperature-dependent structural transitions in gold nanoparticles. *Physical review letters* **2004**, *92*, 115507.
(111) Brintlinger, T.; Qi, Y.; Baloch, K.; Goldhaber-Gordon, D.; Cumings, J. Electron thermal microscopy. *Nano Letters* **2008**, *8*, 582-585.

(112) Reguer, A.; Bedu, F.; Nitsche, S.; Chaudanson, D.; Detailleur, B.; Dallaporta, H. Probing the local temperature by in situ electron microscopy on a heated Si3N4 membrane. *Ultramicroscopy* **2009**, *110*, 61-66.
(113) Wei, X.; Wang, M. S.; Bando, Y.; Golberg, D. Thermal stability of carbon nanotubes probed by anchored tungsten nanoparticles. *Science and Technology of Advanced Materials* **2011**, *12*, 044605.
(114) Costa, P. M. F. J.; Gautam, U. K.; Bando, Y.; Golberg, D. Direct imaging of Joule heating dynamics and temperature profiling inside a carbon nanotube interconnect. *Nature Communications* **2011**, *2*, 421.
(115) Santini, C.; Vereecken, P.; Volodin, A.; Groeseneken, G.; De Gendt, S.; Haesendonck, C. V. A study of Joule heating-induced breakdown of carbon nanotube interconnects. *Nanotechnology* **2011**, *22*, 395202.
(116) Baloch, K. H.; Voskanian, N.; Bronsgeest, M.; Cumings, J. Remote Joule heating by a carbon nanotube. *Nature Nanotechnology* **2012**.
(117) Mecklenburg, M.; Hubbard, W. A.; White, E. R.; Dhall, R.; Cronin, S. B.; Aloni, S.; Regan, B. C. Nanoscale temperature mapping in operating microelectronic devices. *Science* **2015**, *347*, 629-632.
(118) Vendelbo, S. B.; Kooyman, P. J.; Creemer, J. F.; Morana, B.; Mele, L.; Dona, P.; Nelissen, B. J.; Helveg, S. Method for local temperature measurement in a nanoreactor for in situ high-resolution electron microscopy. *Ultramicroscopy* **2013**, *133*, 72-79.
(119) Wu, X.; Hull, R. A novel nano-scale non-contact temperature measurement technique for crystalline materials. *Nanotechnology* **2012**, *23*.
(120) Wu, X.; Hull, R. The material dependence of temperature measurement resolution in thermal scanning electron microscopy. *Applied Physics Letters* **2013**, *102*.
(121) Zhao, S.; Miyata, Y.; Shinohara, H.; Kitaura, R. Direct observation of zipper-like wall-to-wall coalescence of double-wall carbon nanotubes. *Carbon* **2014**, *71*, 159-165.
(122) Singh, M. K.; Titus, E.; Goncalves, G.; Marques, P.; Bdikin, I.; Kholkin, A. L.; Gracio, J. J. A. Atomic-scale observation of rotational misorientation in suspended few-layer graphene sheets. *Nanoscale* **2010**, *2*, 700-708.
(123) Liu, J.; Casavant, M. J.; Cox, M.; Walters, D.; Boul, P.; Lu, W.; Rimberg, A.; Smith, K.; Colbert, D. T.; Smalley, R. E. Controlled deposition of individual single-

walled carbon nanotubes on chemically functionalized templates. *Chemical Physics Letters* **1999**, *303*, 125-129.
(124) Furtado, C. A.; Kim, U. J.; Gutierrez, H. R.; Pan, L.; Dickey, E. C.; Eklund, P. C. Debundling and dissolution of single-walled carbon nanotubes in amide solvents. *Journal of the American Chemical Society* **2004**, *126*, 6095-6105.
(125) Hernandez, Y.; Nicolosi, V.; Lotya, M.; Blighe, F. M.; Sun, Z.; De, S.; McGovern, I. T.; Holland, B.; Byrne, M.; Gun'ko, Y. K.; Boland, J. J.; Niraj, P.; Duesberg, G.; Krishnamurthy, S.; Goodhue, R.; Hutchison, J.; Scardaci, V.; Ferrari, A. C.; Coleman, J. N. High-yield production of graphene by liquid-phase exfoliation of graphite. *Nature Nanotechnology* **2008**, *3*, 563-568.
(126) Zheng, M.; Jagota, A.; Semke, E. D.; Diner, B. A.; McLean, R. S.; Lustig, S. R.; Richardson, R. E.; Tassi, N. G. DNA-assisted dispersion and separation of carbon nanotubes. *Nature Materials* **2003**, *2*, 338-342.
(127) Davis, V. A.; Parra-Vasquez, A. N. G.; Green, M. J.; Rai, P. K.; Behabtu, N.; Prieto, V.; Booker, R. D.; Schmidt, J.; Kesselman, E.; Zhou, W.; Fan, H.; Adams, W. W.; Hauge, R. H.; Fischer, J. E.; Cohen, Y.; Talmon, Y.; Smalley, R. E.; Pasquali, M. True solutions of single-walled carbon nanotubes for assembly into macroscopic materials. *Nature Nanotechnology* **2009**, *4*, 830-834.
(128) Madni, I.; Hwang, C. Y.; Park, S. D.; Choa, Y. H.; Kim, H. T. Mixed surfactant system for stable suspension of multiwalled carbon nanotubes. *Colloids and Surfaces a-Physicochemical and Engineering Aspects* **2010**, *358*, 101-107.
(129) Bai, Y.; Park, I. S.; Lee, S. J.; Bae, T. S.; Watari, F.; Uo, M.; Lee, M. H. Aqueous dispersion of surfactant-modified multiwalled carbon nanotubes and their application as an antibacterial agent. *Carbon* **2011**, *49*, 3663-3671.
(130) Yu, J. R.; Grossiord, N.; Koning, C. E.; Loos, J. Controlling the dispersion of multi-wall carbon nanotubes in aqueous surfactant solution. *Carbon* **2007**, *45*, 618-623.
(131) Jiang, L. Q.; Gao, L.; Sun, J. Production of aqueous colloidal dispersions of carbon nanotubes. *Journal of Colloid and Interface Science* **2003**, *260*, 89-94.
(132) Yeon, C.; Yun, S. J.; Lee, K.-S.; Lim, J. W. High-yield graphene exfoliation using sodium dodecyl sulfate accompanied by alcohols as surface-tension-reducing agents in aqueous solution. *Carbon* **2015**, *83*, 136-143.

(133) Paton, K. R.; Varrla, E.; Backes, C.; Smith, R. J.; Khan, U.; O'Neill, A.; Boland, C.; Lotya, M.; Istrate, O. M.; King, P.; Higgins, T.; Barwich, S.; May, P.; Puczkarski, P.; Ahmed, I.; Moebius, M.; Pettersson, H.; Long, E.; Coelho, J.; O'Brien, S. E.; McGuire, E. K.; Sanchez, B. M.; Duesberg, G. S.; McEvoy, N.; Pennycook, T. J.; Downing, C.; Crossley, A.; Nicolosi, V.; Coleman, J. N. Scalable production of large quantities of defect-free few-layer graphene by shear exfoliation in liquids. *Nature Materials* **2014**, *13*, 624-630.
(134) Matsumoto, M.; Saito, Y.; Park, C.; Fukushima, T.; Aida, T. Ultrahigh-throughput exfoliation of graphite into pristine 'single-layer' graphene using microwaves and molecularly engineered ionic liquids. *Nature Chemistry* **2015**, *7*, 730-736.
(135) Hilding, J.; Grulke, E. A.; Zhang, Z. G.; Lockwood, F. Dispersion of carbon nanotubes in liquids. *Journal of Dispersion Science and Technology* **2003**, *24*, 1-41.
(136) Lau, Y.-T. R.; Yamaguchi, M.; Li, X.; Bando, Y.; Golberg, D.; Winnik, F. M. Facile and Mild Strategy Toward Biopolymer-Coated Boron Nitride Nanotubes via a Glycine-Assisted Interfacial Process. *Journal of Physical Chemistry C* **2013**, *117*, 19568-19576.
(137) Zhi, C. Y.; Bando, Y.; Tang, C. C.; Golberg, D. Specific heat capacity and density of multi-walled boron nitride nanotubes by chemical vapor deposition. *Solid State Communications* **2011**, *151*, 183-186.
(138) Rank, D. H. ON THE POLARIZATION OF RAYLEIGH SCATTERING AS AN AID TO DETERMINE MOLECULAR CONFIGURATION IN LIQUIDS. *Journal of Chemical Physics* **1951**, *19*, 511-511.
(139) Obrien, R. W.; Midmore, B. R.; Lamb, A.; Hunter, R. J. ELECTROACOUSTIC STUDIES OF MODERATELY CONCENTRATED COLLOIDAL SUSPENSIONS. *Faraday Discussions* **1990**, *90*, 301-312.
(140) Li, X.; Zhi, C.; Hanagata, N.; Yamaguchi, M.; Bando, Y.; Golberg, D. Boron nitride nanotubes functionalized with mesoporous silica for intracellular delivery of chemotherapy drugs. *Chemical Communications* **2013**, *49*, 7337-7339.
(141) Golberg, D.; Costa, P. M. F. J.; Lourie, O.; Mitome, M.; Bai, X.; Kurashima, K.; Zhi, C.; Tang, C.; Bando, Y. Direct force measurements and kinking under elastic

deformation of individual multiwalled boron nitride nanotubes. *Nano Letters* **2007**, *7*, 2146-2151.
(142) Dumee, L.; Sears, K.; Schuetz, J.; Finn, N.; Duke, M.; Gray, S. Influence of the Sonication Temperature on the Debundling Kinetics of Carbon Nanotubes in Propan-2-ol. *Nanomaterials* **2013**, *3*, 70-85.
(143) Bystrzejewski, M.; Huczko, A.; Lange, H.; Gemming, T.; Buchner, B.; Rummeli, M. H. Dispersion and diameter separation of multi-wall carbon nanotubes in aqueous solutions. *Journal of Colloid and Interface Science* **2010**, *345*, 138-142.
(144) Li, L. H.; Chen, Y.; Glushenkov, A. M. Synthesis of boron nitride nanotubes by boron ink annealing. *Nanotechnology* **2010**, *21*.
(145) Kim, Y. L.; Jung, H. Y.; Kar, S.; Jung, Y. J. Cleaning organized single-walled carbon nanotube interconnect structures for reduced interfacial contact resistance. *Carbon* **2011**, *49*, 2450-2458.
(146) Shimauchi, H.; Ohno, Y.; Kishimoto, S.; Mizutani, T. Suppression of hysteresis in carbon nanotube field-effect transistors: Effect of contamination induced by device fabrication process. *Japanese Journal of Applied Physics Part 1-Regular Papers Brief Communications & Review Papers* **2006**, *45*, 5501-5503.
(147) Gahng, S.; Ra, C. H.; Cho, Y. J.; Kim, J. A.; Kim, T.; Yoo, W. J. Reduction of metal contact resistance of graphene devices via CO2 cluster cleaning. *Applied Physics Letters* **2014**, *104*, 223110.
(148) Joiner, C.; Roy, T.; Hesabi, Z.; Chakrabarti, B.; Vogel, E. Cleaning graphene with a titanium sacrificial layer. *Applied Physics Letters* **2014**, *104*, 223109.
(149) Rosca, I. D.; Watari, F.; Uo, M.; Akaska, T. Oxidation of multiwalled carbon nanotubes by nitric acid. *Carbon* **2005**, *43*, 3124-3131.
(150) Balasubramanian, K.; Burghard, M. Chemically functionalized carbon nanotubes. *Small* **2005**, *1*, 180-192.
(151) Frolov, A. I.; Arif, R. N.; Kolar, M.; Romanova, A. O.; Fedorov, M. V.; Rozhin, A. G. Molecular mechanisms of salt effects on carbon nanotube dispersions in an organic solvent (N-methyl-2-pyrrolidone). *Chemical Science* **2012**, *3*, 541-548.
(152) Premkumar, T.; Mezzenga, R.; Geckeler, K. E. Carbon Nanotubes in the Liquid Phase: Addressing the Issue of Dispersion. *Small* **2012**, *8*, 1299-1313.

(153) Rastogi, R.; Kaushal, R.; Tripathi, S. K.; Sharma, A. L.; Kaur, I.; Bharadwaj, L. M. Comparative study of carbon nanotube dispersion using surfactants. *Journal of Colloid and Interface Science* **2008**, *328*, 421-428.
(154) Choi, K.; Bourgoin, J.; Auvray, S.; Esteve, D.; Duesberg, G.; Roth, S.; Burghard, M. Controlled deposition of carbon nanotubes on a patterned substrate. *Surface Science* **2000**, *462*, 195-202.
(155) Ebbesen, T. W.; Ajayan, P. M. Large-scale synthesis of carbon nanotubes. *Nature* **1992**, *358*, 220-222.
(156) Flavel, B. S.; Moore, K. E.; Pfohl, M.; Kappes, M. M.; Hennrich, F. Separation of Single-Walled Carbon Nanotubes with a Gel Permeation Chromatography System. *ACS Nano* **2014**, *8*, 1817-1826.
(157) Smith, L. A.; Hammond, R. B.; Roberts, K. J.; Machin, D.; McLeod, G. Determination of the crystal structure of anhydrous sodium dodecyl sulphate using a combination of synchrotron radiation powder diffraction and molecular modelling techniques. *Journal of Molecular Structure* **2000**, *554*, 173-182.
(158) Heise, H. M.; Kuckuk, R.; Ojha, A. K.; Srivastava, A.; Srivastava, V.; Asthana, B. P. Characterisation of carbonaceous materials using Raman spectroscopy: a comparison of carbon nanotube filters, single- and multi-walled nanotubes, graphitised porous carbon and graphite. *Journal of Raman Spectroscopy* **2009**, *40*, 344-353.
(159) Kroto, H. W.; Heath, J. R.; Obrien, S. C.; Curl, R. F.; Smalley, R. E. C-60 - BUCKMINSTERFULLERENE. *Nature* **1985**, *318*, 162-163.
(160) Liu, X.; Pichler, T.; Knupfer, M.; Golden, M. S.; Fink, J.; Kataura, H.; Achiba, Y. Detailed analysis of the mean diameter and diameter distribution of single-wall carbon nanotubes from their optical response. *Physical Review B* **2002**, *66*.
(161) Okazaki, T.; Saito, T.; Matsuura, K.; Ohshima, S.; Yumura, M.; Iijima, S. Photoluminescence mapping of "as-grown" single-walled carbon nanotubes: A comparison with micelle-encapsulated nanotube solutions. *Nano Letters* **2005**, *5*, 2618-2623.
(162) Finnie, P.; Kaminska, K.; Homma, Y.; Austing, D. G.; Lefebvre, J. Charge contrast imaging of suspended nanotubes by scanning electron microscopy. *Nanotechnology* **2008**, *19*.

(163) Strano, M. S.; Huffman, C. B.; Moore, V. C.; O'Connell, M. J.; Haroz, E. H.; Hubbard, J.; Miller, M.; Rialon, K.; Kittrell, C.; Ramesh, S.; Hauge, R. H.; Smalley, R. E. Reversible, band-gap-selective protonation of single-walled carbon nanotubes in solution. *Journal of Physical Chemistry B* **2003**, *107*, 6979-6985.
(164) O'Connell, M. J.; Bachilo, S. M.; Huffman, C. B.; Moore, V. C.; Strano, M. S.; Haroz, E. H.; Rialon, K. L.; Boul, P. J.; Noon, W. H.; Kittrell, C.; Ma, J. P.; Hauge, R. H.; Weisman, R. B.; Smalley, R. E. Band gap fluorescence from individual single-walled carbon nanotubes. *Science* **2002**, *297*, 593-596.
(165) Bachilo, S. M.; Strano, M. S.; Kittrell, C.; Hauge, R. H.; Smalley, R. E.; Weisman, R. B. Structure-assigned optical spectra of single-walled carbon nanotubes. *Science* **2002**, *298*, 2361-2366.
(166) Fagan, J. A.; Khripin, C. Y.; Batista, C. A. S.; Simpson, J. R.; Haroz, E. H.; Walker, A. R. H.; Zheng, M. Isolation of Specific Small-Diameter Single-Wall Carbon Nanotube Species via Aqueous Two-Phase Extraction. *Advanced Materials* **2014**, *26*, 2800-2804.
(167) Fagan, J. A.; Haroz, E. H.; Ihly, R.; Gui, H.; Blackburn, J. L.; Simpson, J. R.; Lam, S.; Walker, A. R. H.; Doorn, S. K.; Zheng, M. Isolation of > 1 nm Diameter Single-Wall Carbon Nanotube Species Using Aqueous Two-Phase Extraction. *Acs Nano* **2015**, *9*, 5377-5390.
(168) Subbaiyan, N. K.; Parra-Vasquez, A. N. G.; Cambre, S.; Cordoba, M. A. S.; Yalcin, S. E.; Hamilton, C. E.; Mack, N. H.; Blackburn, J. L.; Doorn, S. K.; Duque, J. G. Bench-top aqueous two-phase extraction of isolated individual single-walled carbon nanotubes. *Nano Research* **2015**, *8*, 1755-1769.
(169) Brintlinger, T.; Chen, Y. F.; Durkop, T.; Cobas, E.; Fuhrer, M. S.; Barry, J. D.; Melngailis, J. Rapid imaging of nanotubes on insulating substrates. *Applied Physics Letters* **2002**, *81*, 2454-2456.
(170) Homma, Y.; Suzuki, S.; Kobayashi, Y.; Nagase, M.; Takagi, D. Mechanism of bright selective imaging of single-walled carbon nanotubes on insulators by scanning electron microscopy. *Applied Physics Letters* **2004**, *84*, 1750-1752.

(171) Zhang, R. Y.; Wei, Y.; Nagahara, L. A.; Amlani, I.; Tsui, R. K. The contrast mechanism in low voltage scanning electron microscopy of single-walled carbon nanotubes. *Nanotechnology* **2006**, *17*, 272-276.
(172) Hsieh, A. G.; Korkut, S.; Punckt, C.; Aksay, I. A. Dispersion Stability of Functionalized Graphene in Aqueous Sodium Dodecyl Sulfate Solutions. *Langmuir* **2013**, *29*, 14831-14838.
(173) Alanyalioglu, M.; Jose Segura, J.; Oro-Sole, J.; Casan-Pastor, N. The synthesis of graphene sheets with controlled thickness and order using surfactant-assisted electrochemical processes. *Carbon* **2012**, *50*, 142-152.
(174) Li, W.; Liu, J.; Yan, C. Reduced graphene oxide with tunable C/O ratio and its activity towards vanadium redox pairs for an all vanadium redox flow battery. *Carbon* **2013**, *55*, 313-320.
(175) Parvez, K.; Wu, Z. S.; Li, R. J.; Liu, X. J.; Graf, R.; Feng, X. L.; Mullen, K. Exfoliation of Graphite into Graphene in Aqueous Solutions of Inorganic Salts. *Journal of the American Chemical Society* **2014**, *136*, 6083-6091.
(176) Li, D.; Muller, M. B.; Gilje, S.; Kaner, R. B.; Wallace, G. G. Processable aqueous dispersions of graphene nanosheets. *Nature Nanotechnology* **2008**, *3*, 101-105.
(177) Stankovich, S.; Dikin, D. A.; Piner, R. D.; Kohlhaas, K. A.; Kleinhammes, A.; Jia, Y.; Wu, Y.; Nguyen, S. T.; Ruoff, R. S. Synthesis of graphene-based nanosheets via chemical reduction of exfoliated graphite oxide. *Carbon* **2007**, *45*, 1558-1565.
(178) Szabo, T.; Berkesi, O.; Forgo, P.; Josepovits, K.; Sanakis, Y.; Petridis, D.; Dekany, I. Evolution of surface functional groups in a series of progressively oxidized graphite oxides. *Chemistry of Materials* **2006**, *18*, 2740-2749.
(179) Xu, Z.; Bando, Y.; Liu, L.; Wang, W. L.; Bai, X. D.; Golberg, D. Electrical Conductivity, Chemistry, and Bonding Alternations under Graphene Oxide to Graphene Transition As Revealed by In Situ TEM. *Acs Nano* **2011**, *5*, 4401-4406.
(180) Ferrari, A. C. Raman spectroscopy of graphene and graphite: Disorder, electron-phonon coupling, doping and nonadiabatic effects. *Solid State Communications* **2007**, *143*, 47-57.
(181) Saito, R.; Hofmann, M.; Dresselhaus, G.; Jorio, A.; Dresselhaus, M. S. Raman spectroscopy of graphene and carbon nanotubes. *Advances in Physics* **2011**, *60*, 413-550.

(182) Cancado, L. G.; Pimenta, M. A.; Neves, B. R. A.; Dantas, M. S. S.; Jorio, A. Influence of the atomic structure on the Raman spectra of graphite edges. *Physical Review Letters* **2004**, *93*.
(183) Hernandez, Y.; Lotya, M.; Rickard, D.; Bergin, S. D.; Coleman, J. N. Measurement of Multicomponent Solubility Parameters for Graphene Facilitates Solvent Discovery. *Langmuir* **2010**, *26*, 3208-3213.
(184) Haar, S.; Ciesielski, A.; Clough, J.; Yang, H. F.; Mazzaro, R.; Richard, F.; Conti, S.; Merstorf, N.; Cecchini, M.; Morandi, V.; Casiraghi, C.; Samori, P. A Supramolecular Strategy to Leverage the Liquid-Phase Exfoliation of Graphene in the Presence of Surfactants: Unraveling the Role of the Length of Fatty Acids. *Small* **2015**, *11*, 1691-1702.
(185) Ferrari, A. C.; Meyer, J. C.; Scardaci, V.; Casiraghi, C.; Lazzeri, M.; Mauri, F.; Piscanec, S.; Jiang, D.; Novoselov, K. S.; Roth, S.; Geim, A. K. Raman spectrum of graphene and graphene layers. *Physical Review Letters* **2006**, *97*.
(186) Giancoli, D. C. *Physics for scientists and engineers*; Prentice hall Upper Saddle River, NJ2000; Vol. 3.
(187) Reguer, A.; Bedu, F.; Tonneau, D.; Dallaporta, H.; Prestigiacomo, M.; Houel, A.; Sudraud, P. Structural and electrical studies of conductive nanowires prepared by focused ion beam induced deposition. *Journal of Vacuum Science & Technology B* **2008**, *26*, 175-180.
(188) Fang, J.-Y.; Qin, S.-Q.; Zhang, X.-A.; Liu, D.-Q.; Chang, S.-L. Annealing effect of platinum-incorporated nanowires created by focused ion/electron-beam-induced deposition. *Chinese Physics B* **2014**, *23*.
(189) Novoselov, K. S.; Fal'ko, V. I.; Colombo, L.; Gellert, P. R.; Schwab, M. G.; Kim, K. A roadmap for graphene. *Nature* **2012**, *490*, 192-200.
(190) Mun, J. H.; Oh, J. G.; Bong, J. H.; Xu, H.; Loh, K. P.; Cho, B. J. Wrinkle-free graphene with spatially uniform electrical properties grown on hot-pressed copper. *Nano Research* **2015**, *8*, 1075-1080.
(191) Zhang, K.; Arroyo, M. Understanding and strain-engineering wrinkle networks in supported graphene through simulations. *Journal of the Mechanics and Physics of Solids* **2014**, *72*, 61-74.

(192) Xu, K.; Cao, P.; Heath, J. R. Scanning Tunneling Microscopy Characterization of the Electrical Properties of Wrinkles in Exfoliated Graphene Monolayers. *Nano Letters* **2009**, *9*, 4446-4451.
(193) Ahmad, M.; Han, S. A.; Tien, D. H.; Jung, J.; Seo, Y. Local conductance measurement of graphene layer using conductive atomic force microscopy. *Journal of Applied Physics* **2011**, *110*.
(194) Ladak, S.; Ball, J. M.; Moseley, D.; Eda, G.; Branford, W. R.; Chhowalla, M.; Anthopoulos, T. D.; Cohen, L. F. Observation of wrinkle induced potential drops in biased chemically derived graphene thin film networks. *Carbon* **2013**, *64*, 35-44.
(195) Lu, Y.; Merchant, C. A.; Drndic, M.; Johnson, A. T. C. In Situ Electronic Characterization of Graphene Nanoconstrictions Fabricated in a Transmission Electron Microscope. *Nano Letters* **2011**, *11*, 5184-5188.
(196) Murali, R.; Yang, Y. X.; Brenner, K.; Beck, T.; Meindl, J. D. Breakdown current density of graphene nanoribbons. *Applied Physics Letters* **2009**, *94*.
(197) Liao, A. D.; Wu, J. Z.; Wang, X.; Tahy, K.; Jena, D.; Dai, H.; Pop, E. Thermally Limited Current Carrying Ability of Graphene Nanoribbons. *Physical Review Letters* **2011**, *106*.
(198) Xia, F.; Perebeinos, V.; Lin, Y.-m.; Wu, Y.; Avouris, P. The origins and limits of metal-graphene junction resistance. *Nature Nanotechnology* **2011**, *6*, 179-184.
(199) Yuan, J.; Ma, L.-P.; Pei, S.; Du, J.; Su, Y.; Ren, W.; Cheng, H.-M. Tuning the Electrical and Optical Properties of Graphene by Ozone Treatment for Patterning Monolithic Transparent Electrodes. *Acs Nano* **2013**, *7*, 4233-4241.
(200) Kasry, A.; Kuroda, M. A.; Martyna, G. J.; Tulevski, G. S.; Bol, A. A. Chemical Doping of Large-Area Stacked Graphene Films for Use as Transparent, Conducting Electrodes. *Acs Nano* **2010**, *4*, 3839-3844.
(201) Asadi, K.; Timmering, E. C.; Geuns, T. C. T.; Pesquera, A.; Centeno, A.; Zurutuza, A.; Klootwijk, J. H.; Blom, P. W. M.; de Leeuw, D. M. Up-Scaling Graphene Electronics by Reproducible Metal-Graphene Contacts. *Acs Applied Materials & Interfaces* **2015**, *7*, 9429-9435.
(202) Lee, D.; Kwon, G. D.; Kim, J. H.; Moyen, E.; Lee, Y. H.; Baik, S.; Pribat, D. Significant enhancement of the electrical transport properties of graphene films by

controlling the surface roughness of Cu foils before and during chemical vapor deposition. *Nanoscale* **2014**, *6*, 12943-12951.
(203) Ross, F. M.; Hull, R.; Bahnck, D.; Bean, J. C.; Peticolas, L. J.; King, C. A. CHANGES IN ELECTRICAL DEVICE CHARACTERISTICS DURING THE INSITU FORMATION OF DISLOCATIONS. *Applied Physics Letters* **1993**, *62*, 1426-1428.
(204) Agarwal, R.; Zakharov, D. N.; Krook, N. M.; Liu, W.; Berger, J. S.; Stach, E. A.; Agarwal, R. Real-Time Observation of Morphological Transformations in II-VI Semiconducting Nanobelts via Environmental Transmission Electron Microscopy. *Nano Letters* **2015**, *15*, 3303-3308.
(205) Li, Y.; Liao, Z.; Fang, F.; Wang, X.; Li, L.; Zhu, J. Significant increase of Curie temperature in nano-scale BaTiO3. *Applied Physics Letters* **2014**, *105*.
(206) Baloch, K. H.; Voskanian, N.; Bronsgeest, M.; Cumings, J. Remote Joule heating by a carbon nanotube. *Nature Nanotechnology* **2012**, *7*, 315-318.
(207) Stojanovic, N.; Yun, J.; Washington, E. B. K.; Berg, J. M.; Holtz, M. W.; Temkin, H. Thin-film thermal conductivity measurement using microelectrothermal test structures and finite-element-model-based data analysis. *Journal of Microelectromechanical Systems* **2007**, *16*, 1269-1275.
(208) Voskanian, N. Heat dissipation in current carrying multiwalled carbon nanotubes. Doctor of Philosophy, University of Maryland, College Park2014.
(209) Amar, A.; Lozes, R.; Sasaki, Y.; Davis, J.; Packard, R. Fabrication of submicron apertures in thin membranes of silicon nitride. *Journal of Vacuum Science & Technology B: Microelectronics and Nanometer Structures* **1993**, *11*, 259-262.
(210) Sultan, R.; Avery, A. D.; Underwood, J. M.; Mason, S. J.; Bassett, D.; Zink, B. L. Heat transport by long mean free path vibrations in amorphous silicon nitride near room temperature. *Physical Review B* **2013**, *87*.
(211) Johnson, J. A.; Maznev, A. A.; Cuffe, J.; Eliason, J. K.; Minnich, A. J.; Kehoe, T.; Sotomayor Torres, C. M.; Chen, G.; Nelson, K. A. Direct Measurement of Room-Temperature Nondiffusive Thermal Transport Over Micron Distances in a Silicon Membrane. *Physical Review Letters* **2013**, *110*.

(212) Ramu, A. T.; Ma, Y. An enhanced Fourier law derivable from the Boltzmann transport equation and a sample application in determining the mean-free path of nondiffusive phonon modes. *Journal of Applied Physics* **2014**, *116*.
(213) Zink, B. L.; Hellman, F. Specific heat and thermal conductivity of low-stress amorphous Si-N membranes. *Solid State Communications* **2004**, *129*, 199-204.
(214) Tang, C.; Bando, Y.; Liu, C.; Fan, S.; Zhang, J.; Ding, X.; Golberg, D. Thermal conductivity of nanostructured boron nitride materials. *The Journal of Physical Chemistry B* **2006**, *110*, 10354-10357.
(215) Zhi, C.; Bando, Y.; Terao, T.; Tang, C.; Kuwahara, H.; Golberg, D. Towards thermoconductive, electrically insulating polymeric composites with boron nitride nanotubes as fillers. *Advanced Functional Materials* **2009**, *19*, 1857-1862.
(216) Ajayan, P. M.; Ebbesen, T. W.; Ichihashi, T.; Iijima, S.; Tanigaki, K.; Hiura, H. OPENING CARBON NANOTUBES WITH OXYGEN AND IMPLICATIONS FOR FILLING. *Nature* **1993**, *362*, 522-525.
(217) Subrina, S. Thermal Transport in Graphene and its Application in Chip Cooling. *Journal of Nanoelectronics and Optoelectronics* **2013**, *8*, 317-336.
(218) Qiu, B.; Ruan, X. L. Reduction of spectral phonon relaxation times from suspended to supported graphene. *Applied Physics Letters* **2012**, *100*.
(219) Ong, Z. Y.; Pop, E. Effect of substrate modes on thermal transport in supported graphene. *Physical Review B* **2011**, *84*.
(220) Li, M.; Zhang, J.; Hu, X.; Yue, Y. Thermal transport across graphene/SiC interface: effects of atomic bond and crystallinity of substrate. *Applied Physics a-Materials Science & Processing* **2015**, *119*, 415-424.
(221) Zhang, Y.; Han, H.; Wang, N.; Zhang, P.; Fu, Y.; Murugesan, M.; Edwards, M.; Jeppson, K.; Volz, S.; Liu, J. Improved Heat Spreading Performance of Functionalized Graphene in Microelectronic Device Application. *Advanced Functional Materials* **2015**, *25*, 4430-4435.
(222) Lee, K.; Moon, J.-S.; Oh, T.; Kim, S.; Asbeck, P. Analysis of heat dissipation of epitaxial graphene devices on SiC. *Solid-State Electronics* **2014**, *101*, 44-49.

(223) Menges, F.; Riel, H.; Stemmer, A.; Dimitrakopoulos, C.; Gotsmann, B. Thermal Transport into Graphene through Nanoscopic Contacts. *Physical Review Letters* **2013**, *111*.
(224) Shen, H. Wrinkling and thermal conductivity of one graphene sheet under shear. *Molecular Simulation* **2015**, *41*, 231-236.
(225) Chu, K.; Li, W.-s.; Tang, F.-l. Flatness-dependent thermal conductivity of graphene-based composites. *Physics Letters A* **2013**, *377*, 910-914.
(226) Wang, C.; Liu, Y.; Li, L.; Tan, H. Anisotropic thermal conductivity of graphene wrinkles. *Nanoscale* **2014**, *6*, 5703-5707.
(227) Lee, Y.; Pak, A. J.; Paek, E.; Hwang, G. S. Principal Role of Contact-Force Distribution in Determining the Thermal Conductivity of Supported Graphene. *Physical Review Applied* **2015**, *4*.
(228) Liu, Y.; Hu, C. Z.; Huang, J. S.; Sumpter, B. G.; Qiao, R. Tuning interfacial thermal conductance of graphene embedded in soft materials by vacancy defects. *Journal of Chemical Physics* **2015**, *142*.
(229) Callister, W. D.; Rethwisch, D. G. *Materials science and engineering: an introduction*; Wiley New York2007; Vol. 7.
(230) Jia, X.; Hofmann, M.; Meunier, V.; Sumpter, B. G.; Campos-Delgado, J.; Romo-Herrera, J. M.; Son, H.; Hsieh, Y.-P.; Reina, A.; Kong, J.; Terrones, M.; Dresselhaus, M. S. Controlled Formation of Sharp Zigzag and Armchair Edges in Graphitic Nanoribbons. *Science* **2009**, *323*, 1701-1705.
(231) Nilsson, H. M.; Meany, B.; Ticey, J.; Sun, C.-F.; Wang, Y.; Cumings, J. Ammonium Laurate Surfactant for Cleaner Deposition of Carbon Nanotubes. *Langmuir* **2015**, *31*, 6948-6955.